Hydrogen Peroxide Sensing

with Microstructured Optical Fibres

Fuel, Wine & Babies

by

Erik Peter Schartner

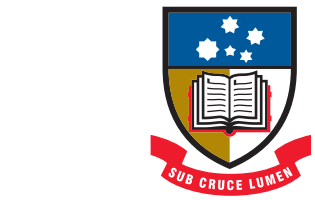

THE UNIVERSITY
of ADELAIDE

A thesis submitted for the degree of

Doctor of Philosophy

in the

Faculty of Sciences
School of Chemistry & Physics

April 2012

To Megan

I am among those who think that science has great beauty. A scientist in his laboratory is not only a technician: he is also a child placed before natural phenomena which impress him like a fairy tale.

— Marie Curie

CONTENTS

LIST OF FIGURES

LIST OF TABLES

ACRONYMS

AR Amplex Red

ARD Amplex Red Derivative

AUR Amplex Ultrared

CE Coupling Efficiency

EDC 1-Ethyl-3-(3-dimethylaminopropyl)carbodiimide

F2/F2HT Lead silicate soft glasses

FCF Fluorescence capture fraction

FMOC Fluorenylmethyloxycarbonyl chloride

FOM Figure of Merit

FWHM Full Width Half Maximum

HRP Horseradish Peroxidase

IR Infra-red

IVF In Vitro Fertilisation

MCVD Modified Chemical Vapour Deposition

MOF Microstructured Optical Fibre

NA Numerical Aperture

NHS N-Hydroxysuccinimide

OD Outer Diameter

OSA Optical Spectrum Analyser

PBGF Photonic Band Gap Fibre

PBS Phosphate Buffered Saline

PCF Photonic Crystal Fibre

PF Power Fraction

PMT Photomultiplier Tube

Qdot Quantum Dot

SEM Scanning Electron Microscope

TEM Transmission Electron Microscope

TLC Thin Layer Chromatography

WW(F) Wagon-Wheel (Fibre)

PUBLICATIONS

The material in this thesis is based largely on the following publications

Journal Papers

- Erik P. Schartner , Heike Ebendorff-Heidepriem , Stephen C. Warren-Smith , Richard T. White and Tanya M. Monro, 'Driving down the Detection Limit in Microstructured Fiber-Based Chemical Dip Sensors,' Sensors, **11**(3), 2961-2971, 2011
- Tanya M. Monro, Stephen Warren-Smith, Erik P. Schartner, Alexandre François, Sabrina Heng, Heike Ebendorff-Heidepriem, Shahraam Afshar V., 'Sensing with suspended-core optical fibers,' Optical Fiber Technology, **16**, 343-356, 2010

Additionally, the original work on Quantum dot detection in fibres was work done for my honours project. The main achievements of this work are contained within

- Yinlan Ruan, Erik P. Schartner, Heike Ebendorff-Heidepriem, Peter Hoffmann, and Tanya M. Monro, 'Detection of quantum-dot labelled proteins using soft glass microstructured optical fibers,' Optics Express, **15**(26), 17819-17826 (2007)

Conference papers

- Erik P. Schartner, Heike Ebendorff-Heiepriem, Tanya M. Monro, Markus Pietsch, Chris Hulston and Claire Davis, 'Fuel Degradation Sensing Using Small-Cored Microstructured Optical Fibres,' AIP congress, Adelaide, Australia 2008.
- Erik P. Schartner, Tanya M. Monro, Heike Ebendorff-Heiepriem, Markus Pietsch, Chris Hulston and Claire Davis,' Fuel degradation sensing using microstructured optical fibres,' Structural Health Monitoring Workshop, Melbourne, Australia 2008.
- Erik P. Schartner, Heike Ebendorff-Heiepriem, Markus Pietsch and Tanya M. Monro, 'A hydrogen peroxide fibre optic dip sensor for aqueous solutions,' ACOLS/ACOFT, Adelaide, Australia, 2009.
- Erik P. Schartner, Richard T. White, Stephen C. Warren-Smith and Tanya M. Monro, 'Practical sensitive fluorescence sensing with microstructured fibres,' Optical Fibre Sensors, Edinburgh, UK, 2009

- Florian V. Englich, Erik P. Schartner, Dominic F. Murphy, Heike Ebendorff-Heidepriem, and Tanya M. Monro, 'Fusion Splicing Soft-Glass Suspended Core Fibers to Solid Silica Fibers for Optical Fiber Sensing,' ACOFT, Melbourne, Australia, 2010
- Erik P. Schartner, Heike Ebendorff-Heidepriem and Tanya M. Monro, 'Sensitive fluorescence detection with microstructured optical fibers,' SPIE Defense, Security & Sensing, Orlando, USA, 2011
- Erik P. Schartner, Dominic F. Murphy, Heike Ebendorff-Heidepriem & Tanya M. Monro, 'A low-volume microstructured optical fiber hydrogen peroxide sensor,' SPIE Defense, Security & Sensing, Orlando, USA, 2011
- Erik P Schartner, Heike Ebendorff-Heidepriem and Tanya M Monro, 'Driving down the detection limit in microstructured fiber-based chemical dip sensors,' Optical Fiber Sensors, Ottawa, Canada, 2011
- Erik P Schartner, Dayong Jin, Heike Ebendorff-Heidepriem, Jim A. Piper, Tanya M Monro, 'Lanthanide upconversion nanocrystals within microstructured optical fibres; a sensitive platform for biosensing and a new tool for nanocrystal characterisation,' Asia Pacific Optical Sensors, Sydney, 2012 (In press)

ABSTRACT

The capacity to measure the concentration of hydrogen peroxide in solution is critical for many disparate application areas, including wine quality sensing, aviation fuel monitoring and embryology. This thesis covers work related to the development of a low-volume hydrogen peroxide sensor, utilising microstructured optical fibres to perform measurements on small (<20 µL) sample volumes.

This work has used the interaction between the guided light and fluorescent molecules within the holes of microstructured optical fibres to perform detection. This interaction has been used firstly to optimise the sensing architecture, using photostable Quantum dots as a characterisation tool. This work also has potential biosensing applications, using the Quantum dots was fluorescent labels for antibody reactions. This thesis covers work related to lowering the effective detection limit using microstructured optical fibres to detect fluorescent molecules, utilising novel glasses and implementing a theoretical model to reduce the amount of background signal that is generated within the fibre. New candidates for fluorescent molecules in fibre are also examined, resulting in a further reduction of the minimum detectable concentration.

The second use of this interaction with the guided light involved the use of fluorophores that react with hydrogen peroxide to produce an increase in fluorescence. This increase in fluorescence can then be observed by monitoring the signal from either end of the fibre. By establishing a calibration curve that gives an expected fluorescence signal for a given hydrogen peroxide concentration it is then possible to correlate the observed fluorescence with the concentration of hydrogen peroxide present within the sample.

Additionally this thesis presents practical improvements to microstructured fibre dip sensors, including splicing the sensing fibres to commercial optical fibres as well as methods for mixing low volumes of liquids to enable rapid detection of target molecules.

DECLARATION

This work contains no material which has been accepted for the award of any other degree or diploma in any university or other tertiary institution to Erik Schartner and, to the best of my knowledge and belief, contains no material previously published or written by another person, except where due reference has been made in the text.

I give consent to this copy of my thesis, when deposited in the University Library, being made available for loan and photocopying, subject to the provisions of the Copyright Act 1968.

The author acknowledges that copyright of published works contained within this thesis (as listed earlier) resides with the copyright holder(s) of those works.

I also give permission for the digital version of my thesis to be made available on the web, via the University's digital research repository, the Library catalogue, the Australasian Digital Theses Program (ADTP) and also through web search engines, unless permission has been granted by the University to restrict access for a period of time.

Adelaide, April 2012

Erik Peter Schartner

ACKNOWLEDGMENTS

It is a pleasure to thank the many people who made this thesis possible.

Firstly, I would like to thank my supervisors, Tanya Monro, Heike Ebendorff-Heidepriem and Shahraam Afshar. Their passion for physics is what has driven me to become the researcher I am today. Special thanks must go to Tanya Monro for setting up the vast array of collaborations that have driven this research along its somewhat windy road. I don't think any of us had any idea that this project would end up where it did, but I sincerely hope that we've all enjoyed the journey. Thanks also Heike Ebendorff-Heidepriem for all your support throughout this time; no matter how busy you are it always seemed that your door was open and were available to help me with a problem.

I acknowledge the support of DSTO, and specifically Claire Davis for the funding support and initial motivation for this project. Thanks also to Chris Hulston, for providing the aviation fuel samples, and Christy-Anne Stansfield, for the hydroperoxide titration method.

Many people have worked with me on various projects during the course of my thesis: Dominic Murphy, Richard White, Alexandre François, Daniel White, & Stephen Warren-Smith. Thank you to all of you; your help and assistance with all aspects of my project, and the many discussions we've had has been of great assistance.

I would also like to thank the chemists who have provided the synthesis for the peroxide sensing section of this project; Markus Pietsch, Andrew Abell, Sabrina Heng and Ondrej Zvarec. The seemingly endless chain of compounds always gave me something to do in the lab. Many thanks to Alastair Dowler, Blair Middlemiss and Trevor Waterhouse for their timely technical support. Every time I managed to break something you were always on hand to help me out. Thanks also to Kevin Kuan and Tze Foo, who were always on hand to help me further my understanding of the chemical aspects of my project.

On a personal note, I would also like to thank my parents for their love and support during this period - one cannot underestimate the effect that a guaranteed home-cooked meal and a self-cutting lawn has. Thanks also to my Mum for her help proof reading and finalising my thesis. To those of you who have been my office & lab mates for the last 3 years, thank you; the mix of procrastination and motivation that you've provided was invaluable.

And last, but most definitely not least, I would like to thank my darling wife, Megan. I'm still not sure how you've put up with me during some of the most stressful periods of my life, but I don't think

you'll ever know just how thankful I am for your understanding, support and encouragement over these past years.

I love deadlines. I like the whooshing sound they make as they fly by.

— Douglas Adams

SUMMARY

This thesis covers work related to the development of a low-volume hydrogen peroxide sensor. This work has used the interaction between the guided light and fluorescent molecules within the holes of microstructured optical fibres to perform detection. This has been used firstly for potential biosensing applications, by detecting Quantum dots which can be used as fluorescent labels for antibody reactions. The second application involves a fluorophore that reacts with hydrogen peroxide or hydroperoxides to produce an increase in fluorescence. This increase in fluorescence can then be observed by monitoring the fluorescence from either end of the fibre. By establishing a calibration curve that gives an expected fluorescence signal for a given hydrogen peroxide concentration it is then possible to correlate the observed fluorescence with the concentration of hydrogen peroxide present within the sample.

Chapter 1 reviews the literature on optical fibre based sensing methods, exploring both unstructured core-clad fibres, as well as microstrutured fibres with transverse holes through their cross-sections. The main focus of this chapter is on fluorescent techniques, but alternative methods are also examined.

Chapter 2 documents progress during this PhD project towards lowering the effective detection limit using microstructured optical fibres to detect fluorescent molecules. This work begins with sensing using small, nanoscale core fibres, using quantum dots as the fluorophore for detection. Here, some basic theoretical models are also established to gain an understanding about how the parameters of the fibre geometry affect the sensing performance. This chapter proceeds with a detailed examination of the autofluorescence from different soft glasses, culminating in the fabrication of a microstructured optical fibre from the glass showing the lowest fluoresence signal. This work then moves on to utilising doped nanoparticles for detection, using an infra-red source and upconversion fluorescence signals to perform detection. Several types of nanoparticles are examined, including particles doped with both Erbium and Thulium. An extension of this work is included in Appendix A, looking at the fabrication of a novel fibre geometry to attempt to reduce the effects of glass fluorescence in these types of sensors.

Chapter 3 examines practical improvements to the currently used methods, that would act to improve the usability of these types of sensors in real world scenarios. This is an attempt to move these systems out of the laboratory, and develop them to a point at which they could potentially be deployed in the field. This covers work to splice

these to conventional silica fibres, including both practical results for splicing as well as a basic theoretical model to explore what would be required to improve the efficiency of these splices. This work also develops a novel temperature sensor, which is integrated with the fluorescent sensors discussed earlier.

Chapter 4 explores work on the use of microfluidic mixing techniques to attempt to circumvent the requirements for surface attachment, while preserving the low-volume characteristics that are inherent in sensing using these microstructured fibres. This allows easier changes to new fluorophores, as commercially available molecules can be used without the requirement of modifications to attach them to the surface. This includes work on relatively large scale microfluidic chips, moving on to development of a cost-effective mixing system utilising in-house made capillaries and a simple micro-T mixing chamber.

Chapter 5 delves into work on fabricating microstructured optical fibres from a new type of soft glass with an improved UV transmission. The motivation behind this work is to open up new possibilities for fluorescent molecules by increasing the transmission window of these fibres into a range which is suitable for more of these molecules. This chapter investigates work on extruding these types of preforms, and the subsequent fibre fabrication and characterisation.

Chapter 6 investigates work towards practical fuel degradation sensing, specifically looking for hydroperoxides, again using a fluorescent method which a literature survey shows to be the method most suitable for use in a microstructured fibre. The motivation for this work is the desire to fabricate a quick, effective sensor that can give an immediate indication as to the degradation state of a sample of aviation fuel. This chapter primarily looks at characterisation of fluorophores synthesised at the University of Adelaide to determine their viability for use in the optical fibres.

Chapter 7 looks at an extension to this work, where the focus has shifted from sensing in fuel to work on detection of hydroperoxides in aqueous solutions. This initially begins with wine sensing as the application, but it becomes apparent that the ideal application for this type of low-volume sensor is in the detection of hydrogen peroxide around embryos in In vitro fertilisation (IVF). This chapter again primarily focuses on fluorophore characterisation, looking both at the performance of the fluorophore in cuvette as well as in fibre. This covers both commercially available fluorophores, as well as characterisation of several fluorophores synthesised at Adelaide.

This chapter culminates with work on the functionalisation of one of these synthesised fluorophores on the internal surfaces of the microstructured fibres. This exploress progress towards developing a new method for functionalisation in the fibres, as well as characteri-

sation and progressive development of the performance of the fluorophore itself.

Part I

MICROSTRUCTURED OPTICAL FIBRES

1 INTRODUCTION

1.1 FIBRE SENSING BACKGROUND

1.1.1 *Introduction*

Although the historic focus of optical fibre research was in communications applications [2], fibres have also found many applications in sensing techniques [3]. Traditionally fibre sensors have mainly been used to monitor stress, strain or temperature or merely used to transmit the data from a conventional sensor to a receiver [3]. Arising from both improved traditional fibre designs and new novel microstructured designs, fibres have found many more applications in recent years [4]. These have found use in fields ranging from monitoring pressure, displacements or liquid levels, rotational positions to measuring current and voltage or detecting gas, chemical or biological molecules. Fibres have a number of advantages over traditional sensing methods: they are light, flexible, generally chemically inert, immune to electromagnetic interference, and also carry no current, and as such are usable in hazardous or volatile environments as there is no risk of them producing a spark [3]. Optical fibres also have the desirable characteristic that the sensor can be placed at one location, and the data analysed in a different location a considerable distance away [5]. This enables fibres to be placed in locations that would be otherwise inaccessible to traditional sensors. Fibres also enable the use of multiplexing, as many sensors can be monitored from a single location. They also lend themselves to distributed sensing, in that a single fibre can be used to monitor a variable along a considerable distance [5].

The following section will explore various methods that have been used in the past for sensing using optical fibres. This section is focused on sensing using interactions with the evanescent field. The more commonly used applications such as sensing for stress or strain are not explored, nor are methods for measuring the refractive index for reasons which will be discussed in Chapter 6.

1.1.2 *Modal overlap sensing*

1.1.2.1 *Absorption*

One common method of fibre sensing utilises interactions between the propagating electromagnetic field that extends outside of the fi-

bre, sometimes known as the evanescent field, and the surrounding medium [6].

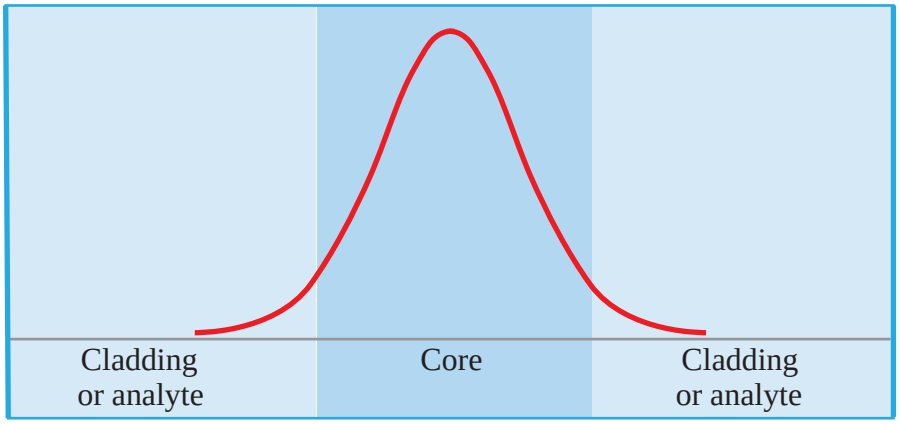

Figure 1: Basic schematic of modal (evanescent) overlap in an optical fibre.

In broad terms several methods can be utilised to exploit this field; covering methods looking at absorption features, and methods involving excitation and subsequent recapture of fluorescent light. This type of sensing can be further separated into two fields, consisting of indirect and direct methods. This requires interaction of the molecules, with the guided light within the fibre. Methods to obtain this will be discussed in the following sections.

For direct methods, one seeks to observe a specific property of our target analyte such as its refractive index or absorption spectra. For the latter example, this is particularly useful when we seek to detect a gas possessing strong absorption peaks, such as acetylene [7] or methane [8–10]. To obtain a measurement of the concentration of the gas firstly a spectrum is obtained without the target gas present. This can be done either using a white light source, or alternatively a tunable laser is a somewhat better method, as it generally enables much higher powers to be coupled into the fibre. A spectrum is then taken with the target gas present, and the difference between this result and the first result is then the absorption spectrum [8]. The concentration of the gas can be determined using the Beer-Lambert Law as long as the other values required in the equation are known [11].

1.1.2.2 *Fluorescence*

The alternative to seeking to observe absorption spectra is to instead look for the emission spectra of a fluorophore, or even of the target molecule itself if it possesses its own distinct fluorescence emission spectra. The fundamental concept behind this type of sensing is similar to that that which is used in absorption sensing, in that both utilise interactions between the evanescent and our target molecule/antibody [3]. However, rather than taking the absorption spectra as was

described previously, one instead aims to excite and recapture fluorescent light from molecules outside the core of the fibre.

Figure 2 shows the general schematic used for this type of sensing. A mode is guided within the fibre, as shown in Figure 2 (1). This mode excites fluorescent light from the fluorophores surrounding the core (2). The fluorescence is emitted in all directions, and a portion of this fluorescence is recaptured into both a forward (3b) and backward (3a) propagating fluorescent mode in the fibre, which can then be detected at either end [12].

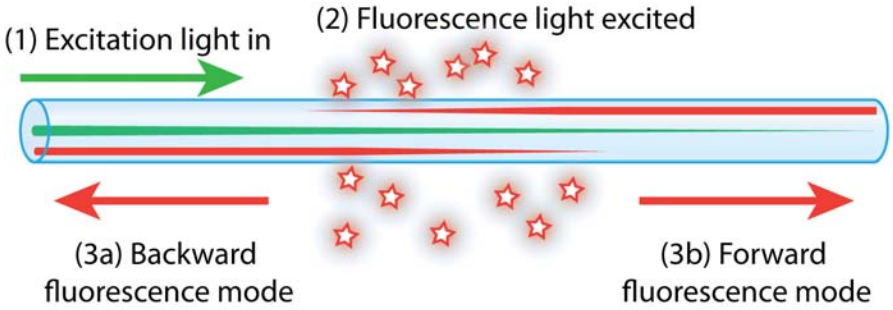

Figure 2: Schematic of fluorescence excitation and subsequent recapture in to the guided mode in an optical fibre, both in the forward and backward directions.

Fluorophores can also be used as labels, which may be attached to the molecules, proteins or bacteria of interest [13]. Specific detection of biomolecules is typically performed through an antibody/antigen reaction, which allows selectivity to be introduced to the sensor [14].

1.1.3 *Fibre Sensing Geometries*

1.1.3.1 *Basic Evanescent Sensors*

The simplest form of an evanescent sensor, commonly referred to as an "air suspended rod" or "unclad fibre," is fundamentally a core-clad fibre in which either the entire cladding or a length of the cladding is removed. This can also be referred to as a bare fibre, i.e. it only consists of a core with no structure or lower refractive index material providing a solid cladding. This has two major effects, the first is that the light becomes more strongly confined to the core due to the increased index contrast, but the second and much more useful (for sensing anyway) property is that a portion of the light overlaps into the air as an evanescent field.

Paul et al. [15] first demonstrated this principle using a 50µm core fibre in which the cladding had been stripped using chemical techniques. This region was immersed in a liquid with strong absorption features, (Rhodamine 6G was used) and the increase in loss at 514 nm recorded. The concentration of the fluid can then be determined by analysing the loss and using known values for the power fraction

overlapping with the analyte and the coefficient of absorption at the desired wavelength.

However this design of fibre is extremely susceptible to damage, both through breakage due to the small (relative to conventional fibre diameters) dimensions of the core and surface contamination caused by the core being directly exposed to the surrounding medium. However both of these issues can be at least partially overcome with the use of permeable coatings [16]. Rather than completely removing the cladding of the fibre and simply using it as a bare fibre, a permeable layer (eg. a polymer) is coated on to the fibre. This layer acts to protect the fibre, while still allowing molecules of the analyte to penetrate through to the evanescent field where they can be detected.

DeGrandpre et al. [17] demonstrated a polymer coated fibre using this principle, as the polymer coating over the core of the fibre acted both to protect the fibre from damage as well as enabling the fluorophore to interact with the evanescent field of the fibre. Preejith et al. [18] demonstrated a protein sensor based on this concept using a multimode fibre coated with a porous cladding layer around the core of the fibre. In this layer fluorescent dye was immobilized, enabling simple detection of the reaction of proteins with the dye. Scorsone et al. [19] also showed that this type of configuration could be used for gas sensing, by detecting ammonia and HCl using a plastic clad silica fibre with an electrochromic polymer immobilised in the cladding.

Cao et al. [20] showed that a similar type of plastic clad silica fibre could be used as an oxygen deficiency sensor in that the oxygen content in the air surrounding the fibre could be recorded at concentrations between 0.6% and 20.9%. This was performed using an oxygen-sensitive organic dye (methylene blue) immobilised in the cladding using a sol-gel method, which gave a logarithmic response of the recorded light absorption for increasing oxygen concentration.

1.1.3.2 *U-Shaped fibres*

A slight alteration to this concept involves the use of U-shaped fibres. In this configuration the fibre is bent through 180 °, which has the effect of extending the evanescent field of the fibre in the region on the outside of the bend. Bending the fibre shifts the refractive index profile, such that more light is guided within the cladding on the outer surface of the bend [21]. Khijwania et al. [22] states that the sensitivity of a scheme involving a U-shaped fibre generally increased with decreasing bend radius, as well as that there exists an ideal bend radius for a given core size. Below this radius the bend loss of the fibre starts to become significant, and any gains in sensitivity with the increase in the evanescent field overlap are removed by an increase in the overall loss of the system.

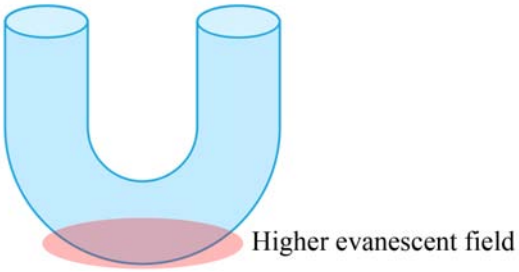

Figure 3: U Fibre. For this type of fibre the evanescent overlap typically increases with decreasing bend radius.

This type of fibre was also used by Gupta et al. [21] to create a pH sensing fibre. By taking a fibre, bending the sensing area, and using a sol-gel coating to immobilise three different pH sensitive fluorophores on the surface it was possible to measure the pH of a solution from 2-12. Again results showed that the sensitivity of the system increased with decreasing bend radius of the fibre. A similar scheme was used by Choudhury et al. [23] using a bent multimode fibre and patent blue as the pH sensitive fluorophore and was successfully shown to be able to record changes in pH from 3 to 13.

This type of sensing geometry has also found use as a liquid-level sensor [24] as the change in the refractive index of the water from that of air induces a change in the transmission of the fibre, enabling the use of the fibre as a rather simple on/off liquid level sensor.

1.1.3.3 *D-Shaped Fibres*

One extension of the air-suspended rod design is known as a D-fibre. This type of fibre typically consist of a conventional silica fibre, of which a portion of the cladding is removed either before or after drawing [10]. This has the effect that the evanescent field extends out a small distance into this region. This field can then be used for evanescent field sensing, as described earlier. One of the primary advantages of D-fibres is that the detection length can be extremely long, unlike that of alternative geometries such as the U-fibres or tapers which are intrinsically limited to short lengths. This should enable this type of fibre to find uses in distributed sensing [10].

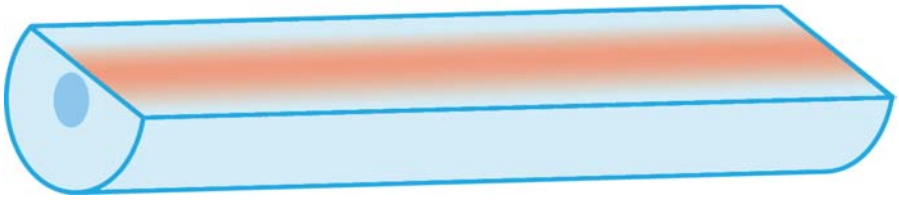

Figure 4: D fibre. The evanescent overlap is increased where the cladding is removed.

There are two main limitations with this type of fibre sensor, the first of that is that the field overlap is typically limited, typically in the order of 0.1% depending on how close to the core the flat face is, and secondly, due to the design of the fibre it cannot be easily coated and as such is comparatively fragile when compared to a standard coated fibre. Some work has been done however on the use of permeable coatings to overcome this. Stewart et al. [10] explored the possibility of using a permeable sol-gel coating on the fibre to improve its strength while still enabling target molecules to penetrate through to the evanescent field.

These fibres have found applications primarily in gas sensing, including gases such as methane etc [10]. Due to the absorption method that is used by this type of fibre, this geometry could be used for any gas or liquid that has strong absorption features in the visible or infrared spectrums.

1.1.3.4 *Microwires/Nanowires*

The tapering optical of fibres to create microwires increase the interaction with the evanescent field presents an alternative method to those described above. By reducing the outer diameter of an optical fibre the modal overlap between the guided light and the external environment begins to increase. This process has been used for evanescent field absorption measurements by tapering a single mode optical fibre to approximately 1 µm [11]. This showed that the tapered fibre had both good sensitivity to target fluorophores and a linear response to increasing concentrations.

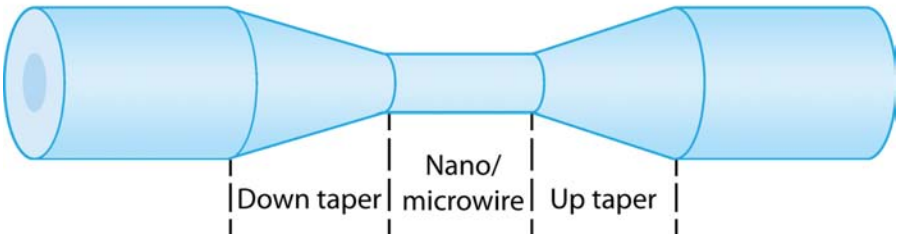

Figure 5: Tapered fibre, showing down & up taper regions.

Fundamentally, a nanowire is a standard solid core index guiding fibre, whose dimensions have been reduced such that the diameter of the fibre is typically smaller than that of the light itself [25]. Fabrication is generally performed by heating a fibre of standard dimensions with a laser or open flame, and then stretching the fibre such that the diameter is reduced. By carefully controlling both the amount of heating and the rate of stretching the dimensions of the fibre can be controlled [26]. The result of this altered geometry is that unlike the traditional methods discussed above, a large portion of the field can travel outside of the glass and interact with any analyte surround-

ing the nanowire [27]. Tong et al. [26] demonstrated that over 20% of the field propagated outside the confines of the glass in a silica fibre with a diameter of 450nm. As would be expected the field overlap is shown to increase with decreasing nanowire diameter [28].

Warken et al. [28] demonstrated another phenomena that cannot be seen in conventional fibres, in that due to the small dimensions of the nanowires an enhancement of the evanescent field intensity is seen at the glass-air interface. Even in an ideal case where 100% evanescent field overlap is achieved, the practicality of using a nanowire to measure the absorption spectra of a gas or liquid surrounding the wire is limited. Due to the short interaction length inherent with nanowires, and considering that the evanescent field absorption will never exceed that of free space techniques for volumetric absorption measurements with an identical path length nanowires may not be the ideal geometry for this type of measurement. Due to their small diameter nanowires are inherently flexible with a low bend loss so it is possible for them to be tightly coiled to increase their interaction length, or alternatively knotted to create ring resonators [25]. This allows the apparent path lengths to be increased, as well as allowing measurements of quantities such as the refractive index to be performed using the resonator [25].

The practical usage of nanowires is limited primarily due to their limited interaction length, as well as their fragility. This is primarily caused by the difficulty in fabricating nanowires with lengths greater than several millimetres, but additionally even if these could be overcome then they also have comparatively high losses of 10dB/m [28] to 100dB/m [26] for nanowires with small (<100 nm) diameters. The loss of the nanowire has been shown to scale with the inverse of the diameter of the wire [29], so the diameter of the nanowire must be chosen to satisfy both the desired diameter as well as practical usable length. It has also been shown that the surface quality degrades over time, resulting in a large increase in the loss requiring protection of the surface to allow practical use as sensors [25].

Much like the D-shaped fibres, nanowires also possess the property that the surface of the core is easily accessed, so processes involving functionalising the surface are greatly simplified over fibres whose core is not easily accessible.

1.1.3.5 *Discussion*

So although the methods described above make good use of sensing with fibres, the use of unstructured optical fibres limits the flexibility of the sensors. The primary issue is the apparent trade off between the high evanescent overlaps possible using nanowires, and the robustness & long interaction lengths possible using D-fibres. There is no possibility to blend the two to create an ideal sensor with a high evanescent overlap, over a long distance with a relatively strong fibre.

One of the main fields of research to attempt to resolve these issues involves microstructured fibres, which will be discussed in the next section.

1.2 SENSING WITH MICROSTRUCTURED OPTICAL FIBRES

1.2.1 *Introduction*

Microstructured optical fibres (MOFs) have found extensive use in sensing applications. They present an alternative to the other geometries and methods discussed earlier in Section 1.1.3 which present some distinct advantages over more conventional methods.

A large variety of microstructured fibres are available, fabricated both from the more standard silica glass, as well as polymers and more exotic glasses. These typically comprise of a lattice formed through stacking of capillary tubes, into which a defect is introduced for light guidance [30]. This defect can either be in the form of a solid rod to introduce index guiding, which if parameters are controlled correctly can result in endlessly single mode guidance within the fibre [30]. An example of this type of fibre is shown in Figure 6a.

This type of fibre is analogous to standard core-clad silica fibres, in that the light is guided down a central core, with the index contrast between the core and the cladding maintaining confinement of the light within the fibre. However, rather than the index contrast being supplied by two glasses with different refractive indices the lower-index cladding arises from the effective index (n_{eff}) of the holes and glass surrounding the core.

A second category of MOFs are the Photonic Bandgap Fibres (PBGF). Air-cored versions of these consist of a large central hole, surrounded by a periodic hexagonal lattice as seen in Figure 6c. This creates a bandgap in the cladding lattice structure through which certain wavelengths of light are forbidden from propagating, thus confining them to the core [33, 35]. Again this type of fibre lends itself to evanescent field sensing as it is relatively easy to fill the holes with a liquid or gas for interaction to occur. This has found a multitude of uses, including acetylene, methane [36, 37] or hydrogen cyanide sensing [7].

A variation on this design is commonly known as a "Bragg fibre," of which an example is shown in Figure 6b. This type of design consists of concentric rings of materials with alternating refractive indices such that interference is generated at a range of wavelengths, confining light to the central hole. This type of fibre had first been proposed as early as 1978 [32], but complicated fabrication requirements meant it was not successfully realised until 2000 [38].

1.2.2 *Sensing applications*

Many applications have been demonstrated using MOFs, including gas sensing [7, 39, 40], biological species detection [13, 14, 41], or refractive index monitoring. The methods utilised for detection using

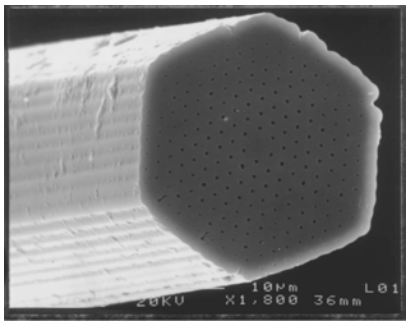

(a) First fabricated single mode MOF [31].

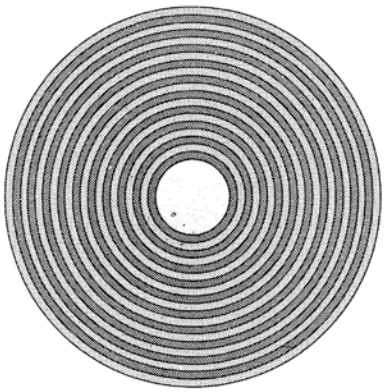

(b) Bragg fibre schematic. The principle is similar to that of (c), where the light is confined to the central region through anti resonance effects [32].

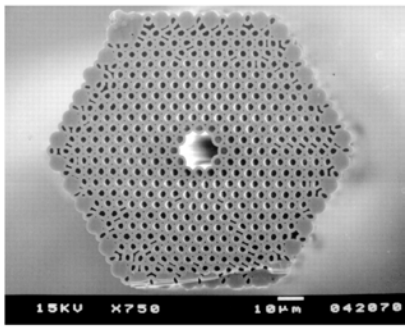

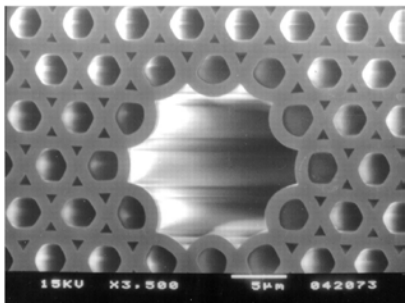

(c) First Photonic bandgap fibre (PBGF) [33] The light is guided within the central air region of the fibre using band gaps that effectively prevent propagation of certain frequencies within the cladding.

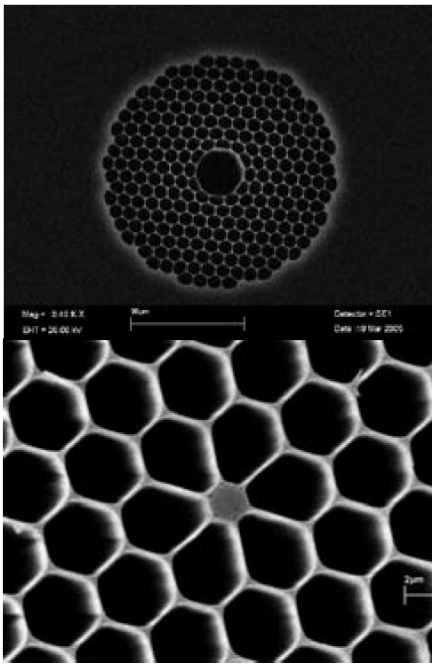

(d) (top) PBGF [34] (bottom) Highly nonlinear MOF [34].

Figure 6: Different types of microstructured optical fibres (MOFs).

MOFs are similar to those discussed previously using conventional fibres, however the use of MOFs opens up new possibilities for detection methods.

Konorov et al. [42] demonstrated a scheme in which a double-clad MOF was used both as an excitation source for molecules located within an external container, and a collection device to collect the fluorescence they emitted. This fluorescent light then travelled back along the fibre, and was then reflected using a dichroic mirror to a camera for detection.

Yu et al. [43] expanded on the concept of utilising MOFs for sensing by introducing a small defect to the core of their fibre. This had the effect of creating a localised region of high intensity along the walls of the fibre, and they were able to successfully detect relatively low concentrations of cobalt chloride via an absorption method, even though the overlap of the field was less than 0.4%.

Jensen et al. [13] demonstrated the usage of a PBGF in absorption sensing, although in this case the guidance method was not via a bandgap, instead the entire lattice area was illuminated at the input end of the fibre. This had the effect that each of the junctions in the lattice acted almost like a fibre themselves, with most of the light guided in the centre of the junction and an evanescent field extending out into the holes. The overlap using this particular implementation of this technique was 5.7%. The fibre was then filled with Cy-5 labelled DNA molecules, the end face illuminated with a tungsten halogen light and the absorption spectra obtained. The detection limit of this system was found to be 100 nM.

1.2.3 *Exposing the fibres*

One of the issues with using MOFs for sensing applications is the filling or diffusion times required to perform measurements on liquids and gases respectively. The most obvious solution to this problem is to insert holes into the sides of the fibres enabling the analyte to more easily enter the fibre. However, especially with MOFs, the internal structure of the fibre is of small dimensions, and the holes must be fabricated to exactly the right depth to avoid damage to the structure [44]. Any damage to the structure typically increases the loss of the fibre. Numerous solutions have been proposed to solve this problem with varying degrees of success, including 193nm laser ablation [45], femtosecond lasers combined with etching [46] or focused ion beam milling [47]. Alternatively, drilling [48] or direct fabrication of structured preforms [49] have also been used to successfully fabricate polymer and glass optical fibres respectively with exposed cores.

These methods allow distributed sensing to be performed, as if the fibre is mounting in a structure or aircraft optical time domain

reflectometry techniques can be used to determine the location from which a fluorescent signal originates [49].

1.2.4 *Tapering for modal overlap*

An alternative method to overcome the issue of filling times of MOFs is to avoid filling fibres at all. Lize et al. [50] demonstrated a technique of tapering microstructured index guiding fibres similar to those in Figure 6 are tapered from an initial diameter of approximately 125 µm down to as small as 2.7 µm. The effect of this is that the mode of the fibre transitions from being strongly confined to within the core region of the fibre to a mode where a large portion of the light exists as an evanescent field. This then enables direct interaction of the light with external material in the tapered region without the time-consuming process of filling the fibre. In addition to this, outside of the tapered region, the fibre is almost completely insensitive to external conditions, making this type of fibre suitable for remote sensing applications.

A similar configuration was used by Mägi et al. [51] to create a 11 µm taper with the primary difference being that unlike Lize, a second "post-processing" tapering was performed to collapse the internal structure of the fibre to create a completely solid tapered region. This work showed that the majority of the fibre exhibited low bend loss (<0.05 dB/m with 125 µm bend radius) due to the presence of the large air holes while allowing a strong overlap with the surrounding medium in the tapered region.

Minkovich et al. [52] demonstrated that this technique could also be applied to MOFs similar to that shown in Figure 6. However this type of fibre displayed a significantly changed transmission spectra to that of the original fibre, in that beats were seen in the spectra, with the transmission varying to as little as 10% of the original value in some of the troughs of the beats. Experimental validation of the sensing properties of the fibres was performed by coating the fibre with a thin layer of palladium, which reacts with hydrogen resulting in a change in the dielectric constant of the layer and thus changing the transmission properties of the fibre. Using this configuration it was found to be possible to easily detect hydrogen concentrations in the order of 1%.

Tapering MOF structures allows the novel guidance characteristics to be maintained over the majority of the fibre length, with only small sections tapered to allow interaction with the surrounding medium. However this method still has the same drawbacks as tapering solid core-clad fibres, in that the tapered regions are susceptible to damage and the lengths over which they can practically be fabricated are limited.

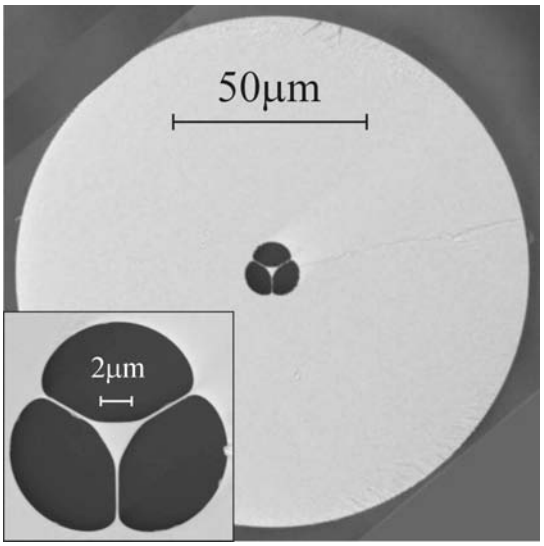

Figure 7: Wagon-wheel fibre.

1.2.5 *Sensing with wagon-wheel fibres*

An alternative to the MOF designs discussed in Section 1.2.1 is to attempt to create a suspended nanowire design, commonly referred to as a "Wagon Wheel" (WW) or "Steering Wheel" design. This design, an example of which is shown in Figure 7, combines the controllable field overlap of the nanowire design with the long interaction lengths and robustness of a conventional fibre. These fibres have been manufactured with a number of different strut designs, ranging from three [48, 53, 54] to six or more [13] and from materials including silica [55], polymers [14, 48, 56] or soft glasses [57, 58].

This type of fibre lends itself to sensing applications, as the holes can be filled with fluids or gases [53, 59, 60] without any implications to shifting bandgaps that may result from using the same technique in bandgap fibres.

The large holes possible with this type of fibre lend themselves to evanescent sensing [54, 55, 61] while still allowing the small cores required for nonlinear techniques [58]. Fabrication is generally simpler than MOFs, which are commonly fabricated via stacking [31] with techniques including extrusion [57, 62] or drilling [55] having been used previously.

Previous work [14] using a fluorescence method in an index-guiding MOF of fibre involved illuminating the side of the fibre with a laser, exciting the fluorophores (in this case Cy3 molecules) that are located in the holes of the microstructured fibre. This particular example was done using a polymer MOF using a Cy3 fluorescent dye, with a 7 cm interaction length and the output of the fibre butt coupled into a standard multi-mode fibre. This particular example also utilised surface functionalisation, as described earlier, and successfully showed

that the fibre was able to differentiate between two different strands of DNA. This demonstrated that it was indeed possible for the fluorescence emitted by fluorophores in the holes of the fibre to be recaptured by the fibre, and detected at the output face. Other work using similar fibres by Frosz et al. [63] has demonstrated successful measurements of the refractive index of aqueous solutions using four wave mixing in silica MOFs with a sensitivity of 6×10^{-6} refractive index units.

Fibres of this design have also found applications detecting analytes such as antibodies [64], acetylene [55], or labeled proteins [61]. Detection of biomolecules attached to fluorescent labels has previously been demonstrated in wagon-wheel fibres, yielding a detection sensitivity down to 1 nM for antibodies labelled with quantum dots (Qdots) [41].

1.3 FABRICATION TECHNIQUES

1.3.1 *Silica optical fibre fabrication*

Standard optical fibres are generally made by first fabricating a preform, and then drawing this preform down into a fibre [65]. The methods to make this preform are varied, but conventional silica core-clad fibres are typically made through modified chemical vapour deposition (MCVD) [66, 67]. This process enables extremely high purity preforms to be fabricated, and in addition this technique allows the addition of dopants [68]. These can be used simply to modify the refractive index, typically using germanium or alternatively the dopants can introduce a gain medium such as erbium which is required for fibre lasers or amplifiers.

This technique however cannot be directly used to fabricate MOFs, since it is unable to fabricate complex geometries. Several possible methods have found extensive use in the past, with the two most widely used being stacking, and drilling.

In the stacking and drawing technique high purity silica capillaries are first drawn down to approximately 1 mm diameter. These capillaries are then stacked together to form a macroscopic version of the desired final fibre structure, and then pulled using a drawing tower into optical fibres. Controlling the diameter and wall thickness of the capillaries enables the pitch and hole diameter to be altered to the desired geometry. By omitting capillaries one can fabricate defects suitable for photonic bandgaps [33] or by adding a solid rod in place of a capillary index-guiding MOFs can be made [31, 69, 70].

This technique has two main drawbacks - firstly, it is restricted to circular (or hexagonal) geometries, and it can be difficult to precisely control the pressures to obtain the desired results. Secondly it is extremely time-consuming and labour intensive to fabricate fibres using

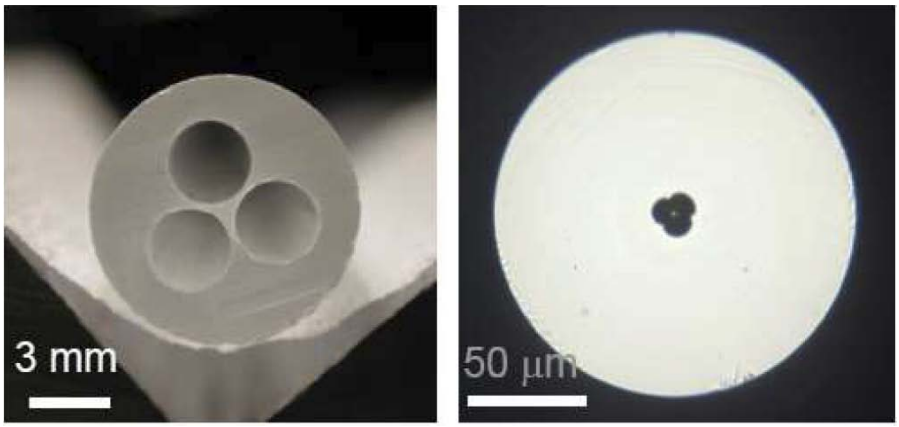

Figure 8: Drilled preform (left) and final fabricated silica wagon-wheel fibre (right) [71]. A two-step drawing process was used for this fibre. In this case the holes were drilled into the preform such that they were large enough to be subsequently manually polished to improve the internal surface quality of the preform.

this method, and it can take several weeks to fabricate a single preform [55]. Typically this also requires clean-room conditions, as any contamination during the stacking process can introduce additional loss into the final fibre.

An alternative method is to directly drill holes into the glass preforms using an ultrasonic drill. This method has been used in the past to fabricate various geometries including wagon-wheel fibres [55, 71] as well as more complicated MOF structures [72]. This process however results in a poor surface quality inside the preform, leading to the requirement that the preform is either mechanically polished [71] or etched to reduce the surface roughness and remove surface contaminants. The length of the preforms is also restricted to lengths of the order of 10 cm when drilling compared to what can be fabricated using other techniques.

The earliest fibres [31] used a mix of both stacking and drilling to obtain the fibre shown in Figure 6a, however in this case the drilling was used to fabricate the capillaries which were then stacked to form the final structure. A two-step process was used to make this fibre, wherein the preform is first drawn down to an intermediate size, and then re-drawn to obtain the final fibre dimensions.

1.3.2 *Soft glasses and their applications*

While silica fibres have found good use in the telecommunications industry due to their durability and low transmission loss, they have several limitations which prevent their effective use in certain applications. For example the transmission window of silica extends only to approximately 2 µm [73], meaning that sensing or lasing applications in the mid-IR are not feasible using silica glasses.

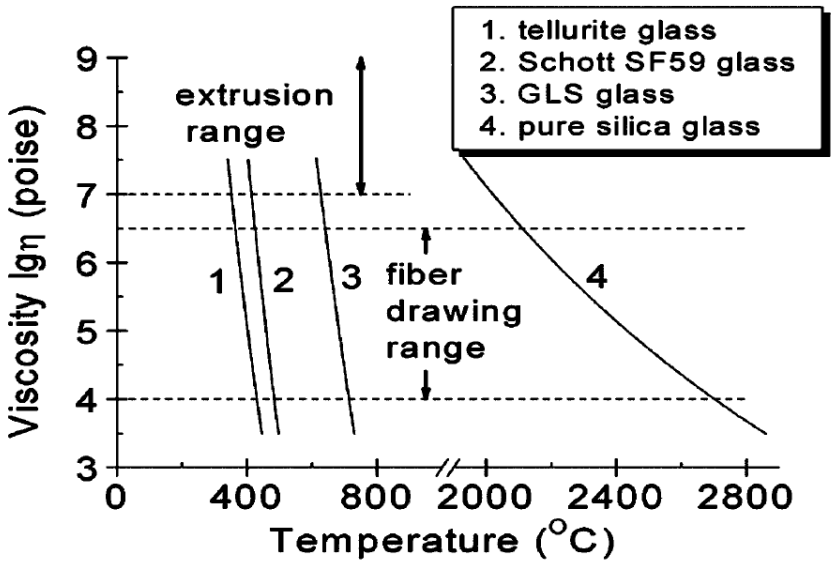

Figure 9: Differing viscosity profiles for several soft glasses.[72] The high temperatures required for the viscosity of silica to reach the 'extrusion range' silica makes silica extrusion a challenging prospect.

Over recent years alternatives to standard silica glass have been investigated, including such glasses as tellurite [74, 75], fluoride [76], chalcogenides [77–79] and lead-silicates [60, 80–85] have been examined. These glasses broadly fall under the umbrella of "soft-glasses," which encompasses glasses that have a melting temperature significantly lower than silica (see Figure 9) and consist of a number of chemical components [73]. Due to the lower phonon energies of these glasses compared to silica they display improved infra-red transmission properties, with transmission out to 8 µm possible using chalcogenide glass.

This improved transmission window enables both the use of mid-IR laser sources [78, 86], or alternatively these glasses have found common use as fibre optic sensors. Since the fundamental absorptions in the mid-IR of various molecules are typically stronger than their harmonics in the near-ir/visible, higher sensitivity can generally be obtained by looking at the fundamental absorption. The use of soft-glasses makes possible these otherwise inaccessible wavelengths [77, 87] for both chemical and biosensing applications.

In addition to the improved IR transmission characteristics, soft-glasses also possess higher nonlinearities than silica glasses [71, 84, 85, 88]. Soft glasses have significantly higher nonlinear indices than silica glass, leading to higher total nonlinearities in fibre. The nonlinearity of a standard SMF28 fibre is $\gamma = 1\,W^{-1}km^{-1}$ and microstructured silica fibres can have in the order of $\gamma = 70\,W^{-1}km^{-1}$, as the nonlinearity γ is a function of both the nonlinear refractive index n_2 as well as the transverse size of the mode A_{eff} [89]. However it has

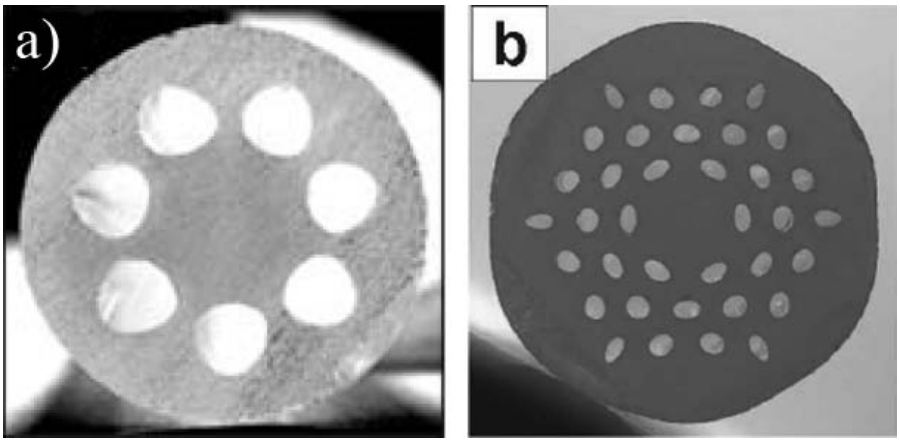

Figure 10: Extruded preforms (a) ZBLAN [76] (b) Bismuth [62].

been demonstrated that nonlinearities of at least $\gamma = 9300\,W^{-1}km^{-1}$ can be obtained using soft glasses, in this case with a chalcogenide core and tellurite cladding [90].

For some applications, such as data transmission, nonlinearity is generally a detrimental property since it increases losses and reduces bandwidth, but for certain fields nonlinearity is a critical parameter. One of these is supercontinuum generation. This is a complex process of nonlinear interactions, in which a relatively narrow linewidth laser pulse is converted into a broadband spectra while still maintaining good spatial coherence. This process can generate a spectra spanning up to 3 µm [91], while still maintaining high beam qualities.

Soft glasses have found good use in supercontinuum generation [91–93] as this is an application which combines both high nonlinearity for efficient generation of the signal, but also good IR transmission such that the supercontinuum can extend further out than would be possible using a silica fibre.

1.3.3 *Extrusion*

The use of soft glasses or polymers [94–96] opens up new opportunities for fabrication techniques that are not possible with standard silica glass. One such technique is extrusion [57, 58, 62, 97–99], in which the glass/polymer is heated to its softening point, and forced through a metal die whose exit is effectively the inverse of the desired structure. Depending on the initial size of the glass billet, these preforms can be in excess of a metre long, enabling multiple trials from a single preform.

Since there are constraints in the scale of the features that can be extruded and drawn, it is not generally possible to fabricate the final structure in a single step, and for this reason a two-step fabrication process is employed. To obtain the small core sizes required for evanescent sensing applications this preform is then caned down from its

initial diameter of 10-15 mm to ≈1 mm and then inserted into an outer jacket. This process is known as the "cane-in-tube" method [98]. The choice of the ratio between the inner and outer diameters determines the size of the core, and as such, the strength of the evanescent field interaction with the fluid of interest that fills the holes (see Sections 2.2 & 2.11). This assembly is then pulled into a fibre using a drawing tower. By controlling the tension and drawing temperature, stable structures can be fabricated with lengths of up to several hundred metres being obtainable from a single draw.

The extrusion technique presents several advantages over the stacking or drilling methods discussed earlier. It allows virtually arbitrary structures to be generated, rather than being restricted to circular holes as with drilling or hexagonal lattice structures as typically would occur with stacking [62]. Figure 10 gives some examples of geometries that have been fabricated using extrusion. The surface quality of extruded preforms is typically better than observed directly after drilling a preform, although this can be mitigated somewhat by etching the preform before it is drawn into a fibre.

As can be seen in Figure 9 the temperature required to reach $\log\eta$=7-9 for silica is 1500°C, while the same viscosity can be achieved in soft glasses at temperatures as low as approximately 300°C [74, 75] or 100-150°C for polymers [96]. This large differential in required temperatures means that the die materials that have been used to date such as stainless-steel [62, 98] or graphite [76] cannot be used for silica extrusions. Steel for example melts at 1325-1530°C while graphite will oxidise at temperatures over approximately 500°C. As such the extrusion technique is currently limited to soft-glasses or polymers, although alternative die materials for higher temperature extrusions are currently being examined.

2

LOW-CONCENTRATION SENSING USING WAGON-WHEEL FIBRES

This chapter documents progress during this PhD project towards lowering the effective detection limit using microstructured optical fibres to detect fluorescent molecules. Sections of this work have been collaborative efforts with others. Section 2.2 is based on FEM code originally written by Kris Rowland, and further modified by Shahraam Afshar and Stephen Warren-Smith. Section 2.5.1 builds on work from both my honours project, comprising the initial work on the detection of Qdots in fibre, which was then continued by Dr Yinlan Ruan. Section 2.7 was work performed with Dr Richard White, which lead to a conference paper (OFS 2009) as well as the basis for a journal paper. The work in Section 2.11 builds on code written by Stephen Warren-Smith for the OFS 2009 paper. The basis for this work is the fluorescence recapture theory developed by Shahraam Afshar and Stephen Warren-Smith, adapted to look at different integration regions compared to the standard case with the fluorophore in the cladding. Analysis of loss measurement data in later sections is performed with the assistance of code written by Mr Matt Henderson. Section 2.12 comprises work performed at Adelaide in collaboration with Dr Jin Dayong from Macquarie University. Some of these experiments, such as the red:green fluorescence work were performed with the technical assistance of Ms Mai-Chi Nguyen, with the Thulium nanoparticles measurements also being performed with Mr Tim Zhao from Macquarie University. In fibre lifetime measurements were performed by the author, with calculations and comparison values in bulk solutions provided by Dr Dayong.

2.1 INTRODUCTION

The extremely small transverse structures that are possible in MOFs (~420 nm [98]) allow small samples to be measured, with total volumes of less than 10 nL being easily obtainable with practical (~20 cm) lengths of fibre with a hole diameter of 4.5 µm. Through the use of fluorescent molecules that interact with target species these fibres can be applied to diverse applications including hydrogen peroxide detection (Section 6) or aluminum detection [100]. The detection of biomolecules attached to fluorescent labels has recently been demonstrated in suspended core MOFs [13, 61], yielding a detection sensitivity down to 1 nM for antibodies labelled with Qdots. The aim of the work in the following chapter is to determine the factors currently re-

stricting the detection limit in this type of sensor and to improve this sensing architecture to increase the sensitivity of the dip sensor.

The fluorescence-detection approach is attractive because of its simplicity. When one end of the fibre is dipped into the sample, capillary forces draw the liquid into the voids within the fibre. The overlapping field of the pump light excites the fluorescent labels and a portion of the fluorescence is captured by the fibre core and propagates to the fibre tips. Captured fluorescence can be detected at either end of the fibre, although backward detection provides the convenience of single-ended devices and an improved signal-to-pump ratio [12] as only a small portion of pump light is transmitted to the detector compared to sensing from the opposite end.

Measurements can either be performed on labelled biomolecules in solution [13, 61], or, if specificity is required, by attaching recognition antibodies to the internal fibre surface [14, 41]. In the latter case, fluorescence is detected when antigens bind to their corresponding immobilized antibodies and non-bound antigens are flushed out of the fibre. In either case, efficient fluorescence-based MOF sensors require a large modal overlap with the fibre holes, such as in band-gap fibres, liquid-core fibres or suspended core fibres.

Suspended-core fibres are clearly a powerful platform both for chemical and biological sensing [101]. The aim of this work is determine the factors currently restricting the detection limit in this type of sensor and to improve this sensing architecture to increase the sensitivity of the dip sensor. To facilitate this modifications will be made to both the existing fibre geometry, as well as the glass used for its fabrication. Through the use of theoretical models it is possible to gain a better understanding of the source of the limitations to the sensitivity of this system, as well as investigating possible approaches to reduce the minimum detectable concentrations of fluorophores.

2.2 MODAL OVERLAPS - THEORETICAL BACKGROUND

As discussed earlier, fluorescence sensing using optical fibres relies on the modal overlap between the guided mode in the core of the fibre, and the fluorescent molecules within the holes of the fibre. The amount of overlap is determined by the refractive index contrast, and the geometry of the fibre. To gain an understanding of how various parameters of the fibre geometry affect sensing performance some preliminary modelling was performed. The aim of this was to examine how the sensing parameters are influenced by changing the core size of the fibre to optimise the fibre geometry such that the fluorophore concentration required for detection is minimised.

The amount of fluorescence emission that is generated is strongly dependent on the overlap of the guided laser light and the holes [102], hereafter referred to as the power fraction (PF_{clad}). Here we define this

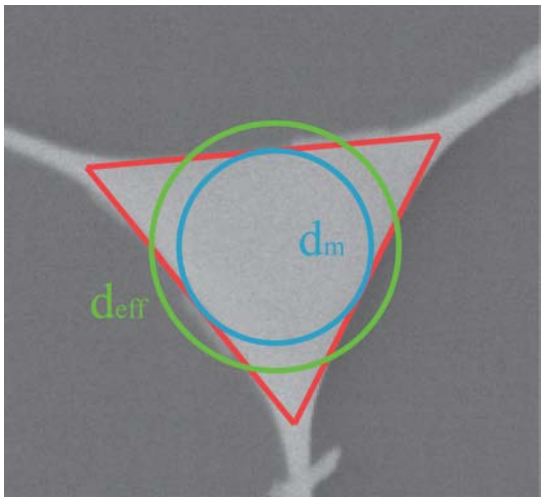

Figure 11: Core size definitions from Ebendorff-Heidepriem et al. [98] overlaid over the SEM image of a wagon-wheel fibre. d_{eff} is defined as the diameter of a circle with the equivalent area as that of the largest triangle which can be wholly contained within the core structure. d_m is defined as the diameter of the largest circle which can be wholly contained within the core. The conversion between these two is $d_{eff} = 1.286 \times d_m$.

as the fraction of the total power in the z direction of the Poynting vector [102, 103] within the cladding relative to the total power.

The modal overlap in a wagon-wheel fibre is governed by three main parameters - the refractive indices of the core and cladding, (n_{core} and n_{clad}) the wavelength of the excitation source (λ_{ex}) and the core size of the fibre (d_{eff}). d_{eff} is defined as the diameter of a circle with the equivalent area to that of a triangle which can be wholly contained within the core of the wagon-wheel fibre [98]. This is shown pictorially in Figure 11. An alternative definition d_m is also used, generally during fabrication where it is too time-consuming to perform the measurement of d_{eff}. These two parameters have a conversion factor of $d_{eff} = 1.286 \times d_m$.

The geometry of a typical wagon-wheel fibre was modelled in the commercial finite element model (FEM) simulation package COMSOL [104]. Analysis was performed using the equations from [102] to give an indication of the how changing fibre parameters affects the sensing properties of the fibre. The initial parameters here were limited to F2 [1] glass (see Section 1.3.2) rather than alternative glasses, as this had previously been fabricated into wagon-wheel fibres with good results. The wavelengths and cladding refractive index were picked as these corresponded to the initial fluorophore choice, which will be discussed in detail in Section 6.6.

Figure 12 demonstrates how this power fraction varies with the core size of the fibre. However, the excitation efficiency is only one part of the calculation of how much fluorescence will actually be re-

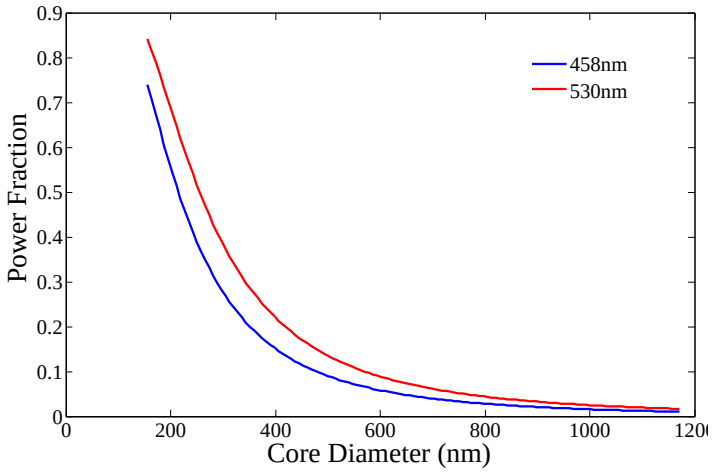

Figure 12: Power fraction (PF_{clad}) for an F2 wagon-wheel fibre with toluene ($n \approx 1.4969$) filled within the holes, for both 458 nm and 530 nm. Core size refers to the equivalent core diameter of an F2 wagon-wheel fibre as shown in Figure 11. 458 nm and 530 nm wavelengths are chosen to represent the excitation and emission of an example fluorophore dissolved in toluene.

captured by the fibre core, and this will be explored in more detail in Section 2.11. As expected, as the core size of the fibre decreases more light is guided in the cladding, which in the case of the wagon-wheel fibre is the holes within the fibre. PF_{clad} also behaves in the same manner with increasing wavelength, as the variation in refractive index with wavelength is relatively small in these glasses. So a fibre with a smaller core size results in a larger modal overlap within the holes of the fibre, and an increased generation of fluorescence from molecules within those holes. For a fibre with a core size of 400 nm, the smallest fabricated in F2 to date [98], this corresponds to a modal overlap of 15% at 458 nm and 22% at 530 nm.

Here the assumption is made that only the fundamental mode of the excitation light generates a fluorescence signal. This assumption is made even though the fibre is multi-mode across the majority of this spectra. However, it was noted during preliminary experiments that by choosing a lens such that the theoretical spot size of the laser is close to that of the mode field diameter, and carefully adjusting the coupling into the fibre that the fundamental mode could be preferentially excited over other higher order modes in the fibre.

The optimum length of the fibre is another important parameter that can easily be modelled. This parameter arises from the increased loss of the fibre induced by the fluorophore. Details of this optimum length parameter can be found in Afshar et al. [102]. This creates a maximum fibre length beyond which any gains in fluorescence from additional fluorophores are cancelled out by increases in the fibre loss, causing the actual detected signal to reduce with longer fibre lengths.

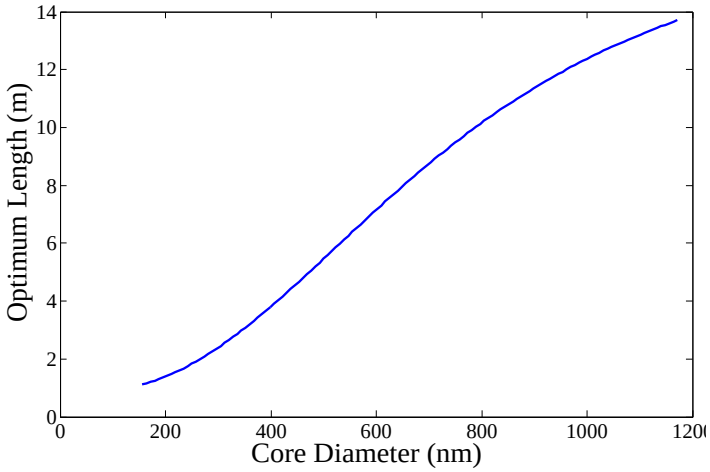

Figure 13: Optimum length for various core sizes of an F2 wagon-wheel fibre. The excitation wavelength is 458 nm, emission 530 nm. Fluorophore parameters are concentration, fibre loss 2 dB/m = 10 nM, extinction coefficient = 19000 $cm^{-1}M^{-1}$.

This parameter considers the effects of losses in the fibre, arising from both the material/waveguide losses as well as from absorption from the fluorophore. These losses act to reduce the measured fluorescence intensity. Up to this optimum length value the fluorescence signal increases as more fluorescence is generated from the fluorophores within the holes of the fibre. However, once the fibre reaches a critical length the losses in the fibre counteract any gains, and the measured fluorescence intensity decreases. It should be noted that this optimum length is only relevant when collecting the fluorescence from the opposite end of the fibre from where the excitation light is coupled in [12] which was the intended method for initial experiments. See Section 2.5.3 for more details.

The results in Figure 13 show that at a moderate fluorophore concentration of 10 nM that the optimum length is greater than the intended fibre length for all core sizes. Although it is theoretically possible to use fibre lengths longer than those shown here, the time required to fill the fibre becomes prohibitive. This suggests that the fibre length will more be governed by the fill time required for a practical sensor, rather than being limited by this optimum length parameter. This optimum length decreases with concentration as the absorption arising from the fluorophore increases, although the effect is minimal for the desired concentration range up to 10 µM.

With this preliminary modelling data it was decided to first attempt measurements using a fibre with a core size of 500-700 nm as a compromise between the higher loss and poor coupling efficiency into small-core fibres [98] and the increased power fraction that is obtained at smaller core sizes.

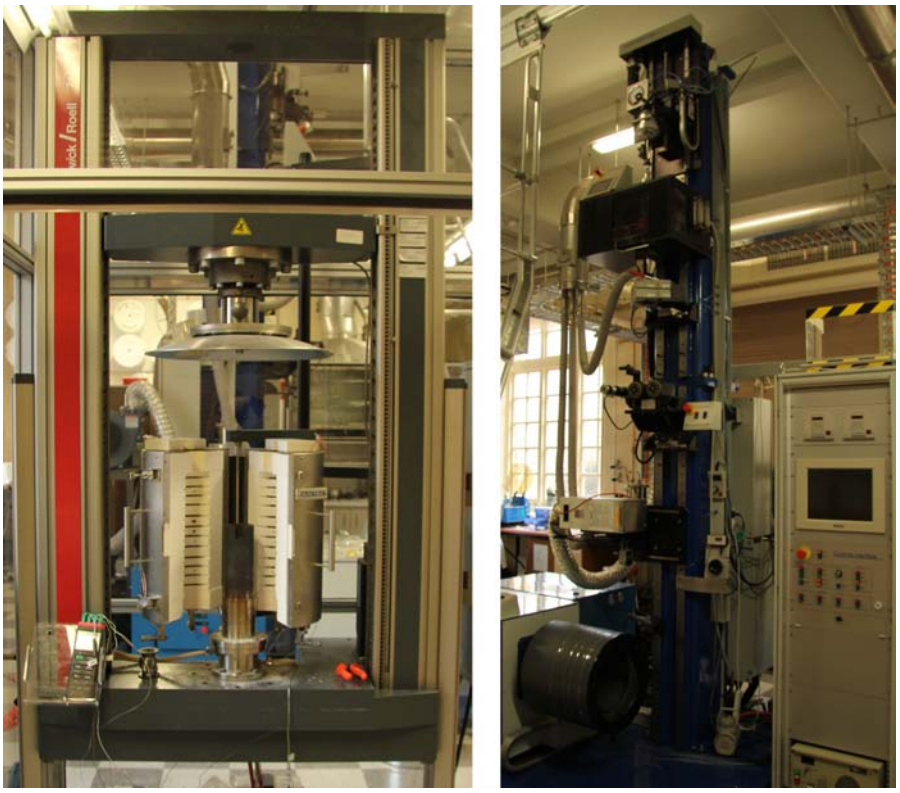

Figure 14: Fabrication machinery (left) Extrusion machine (right) Drawing tower.

2.3 FIBRE FABRICATION

2.3.1 *Methods*

Wagon-wheel fibres with core sizes from 500-700 nm were fabricated in house, using the extrusion method described in Section 1.3.1 and the equipment shown in Figure 14. A pictorial representation of the fabrication process of an F2 wagon-wheel fibre is shown in Figure 15.

Initially fabrication commences with a billet of glass, which is then polished to remove surface imperfections as shown in Figure 15a. The extrusion process involves heating up the glass to its softening point, and then applying a force to the top of the billet (Figure 15b) such that the softened glass is pushed through the extrusion die (Figure 15c). The die is of course much larger than the final geometry, with the size of the features on the die restricted by manufacturing limitations. The minimum scale of the die features is approximately 0.2 mm, using spark erosion techniques. The die is designed such that the flow rate through all areas of the die design is approximately equal, as otherwise deformation of the structure can occur.

Once the glass billet is extruded, a preform such as that shown in Figure 15e is obtained. This typically has an outer diameter in the range of 8-20 mm. As mentioned earlier to facilitate the fabrication

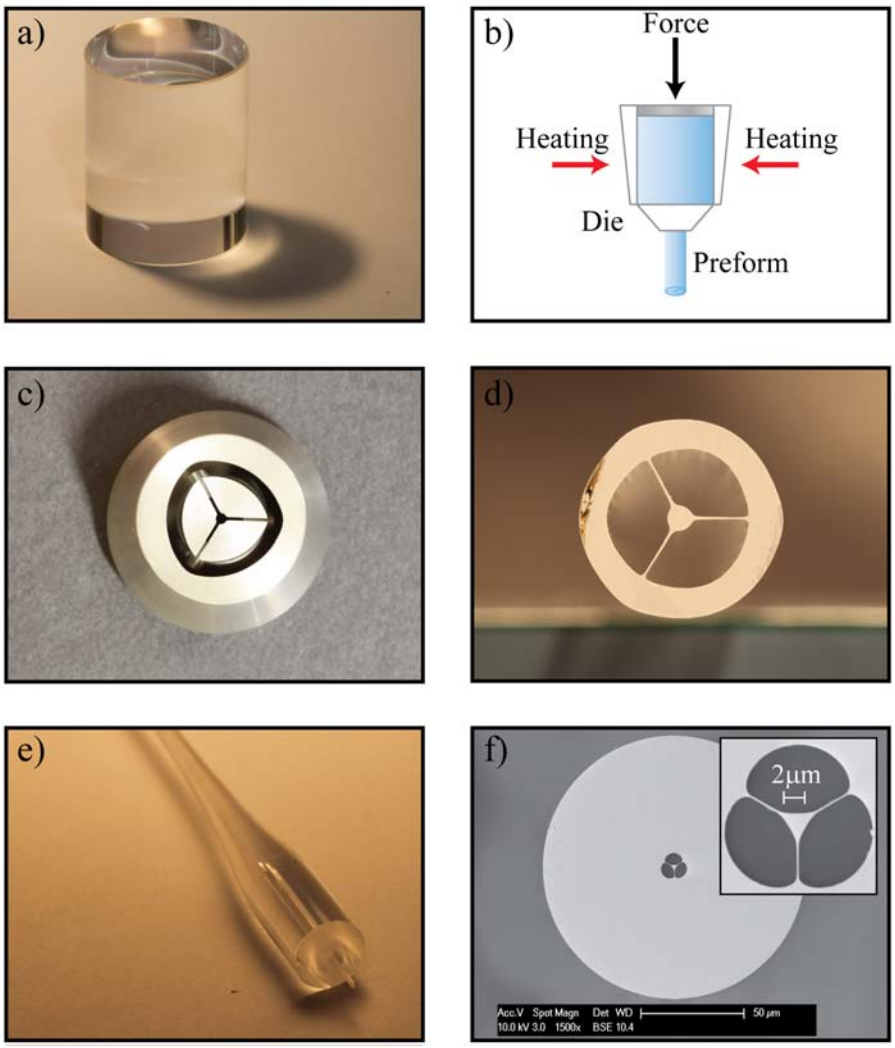

Figure 15: Extrusion a) F2 Glass Billet b) Schematic of extrusion scheme c) Example extrusion die used for F2 suspended core preform fabrication d) Preform after cutting e) First section of fibre draw, showing cane of the preform in d) inserted into a 10 mm tube. The diameter of the structure tapers rapidly in the initial stages of the drawing process f) Final fabricated fibre.

of small scale features in the final fibre a two-step process is used. This process involves first caning down this preform to 0.5-2 mm diameter, and inserting this into an extruded tube. The ratio of the cane diameter- tube outer diameter determines the final core size of the fibre. Generally the cane is fabricated such that the gap between the cane and tube inner is minimised so that it is easier to close the interface gap between the two during the draw. Typically this is aided by self-pressurisation, where the cane is flame sealed at one end, and so as the draw progresses the pressure inside the cane increases pushing the cane outwards. If this is not sufficient a vacuum can then be applied to the gap between the cane and tube to ensure that any interface gaps are completely closed up.

While most wagon wheel canes are fabricated such that the cane and tube inner diameter are of similar proportions, it is sometimes desirable to make the cane smaller than this inner hole. Doing this, and applying a pressure to the cane in a process called active inflation can result in much larger holes being formed in the fibre than otherwise could be obtained using the standard self pressurisation method. This is useful when it is desirable to increase the filling rates, either if faster filling times are needed for more rapid measurements or to simplify surface functionalisation techniques (see Section 7.5).

2.3.2 *Glass choice and fibre design*

The glass chosen for this work was F2, a lead-silicate soft glass from Schott, with a refractive index of 1.62 at 532 nm. This glass has previously been used for fabrication of wagon-wheel fibres with good success [80], in addition to showing a good transmission in the visible with a bulk-glass absorption of ≈0.34 dB/m at 546 nm [1]. This was also the glass which was used to demonstrate a detection limit of 1 nM previously [61]. A number of bare fibres, i.e. a solid glass fibre with no structure or refractive index contrast, have also been fabricated from this glass so the parameters required for both extrusion and drawing of this glass are well understood.

An example of a loss measurement from a bare fibre is shown in Figure 16. This figure also shows a comparison between the manufacturer's data and the measured loss, demonstrating that the loss of the bare fibre is identical to the bulk glass loss within error.

Experience has shown that bare fibre measurements closely approximate the minimum obtainable loss for a microstructured fibre, which for an ideal case with no additional induced loss is the bulk material loss. Although the loss of the fibre can theoretically drop below the intrinsic material losses as the power fraction decreases [105, 106] in practice the increased losses arising from the effects of surface roughness outstrip the gains from the portion of the light propagating in air [98]. In addition Figure 16 also shows a comparison between an

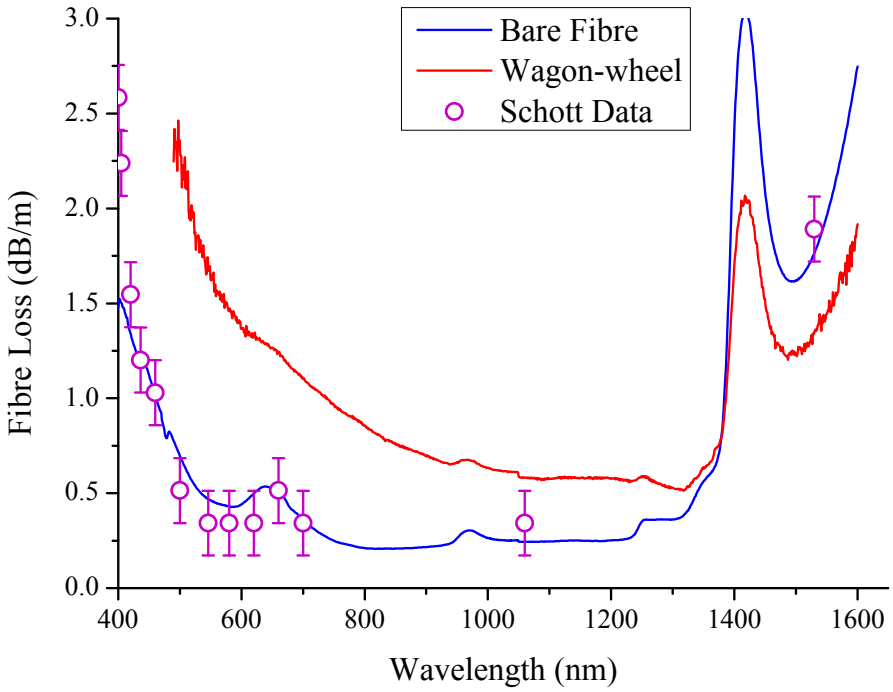

Figure 16: Comparison of manufacturer's bulk F2 glass loss data [1] and measured loss values for an F2 bare fibre and wagon-wheel fibre with a core size of 1.7 µm. The Schott data is measured from 25 mm thick samples, and the error bars shown encompass an error in transmission of 0.001.

F2 bare fibre and wagon-wheel fibre (core size 1.7 µm). It can be seen from this data that the measured values for the bare fibre agree with those given by the manufacturer within error. From this it can be concluded that, for a bare fibre at least, the fabrication process does not induce significant extra loss in the process. This is not always true for all glasses, as will be discussed in detail in Chapter 5, so this is an important result towards fabricated an effective sensing fibre.

Importantly, F2 glass is relatively strong compared to other soft glasses which can be fragile and brittle. Past experience has shown that F2 glass is much easier to work with than glasses such as tellurite [75] or fluoride [76] which is especially relevant when the goal of this work is to develop a practical dip sensor.

Initially it was decided to focus this work on small-core fibres. This decision was made to optimise the obtained signal, since the large modal overlap that arises from small-core fibres generally leads to an increase in PF_{clad} as shown in Figure 12.

2.3.2.1 *Small core fibre fabrication*

By slightly varying the parameters during the fabrication process, Ebendorff-Heidepriem et al. [98] were able to reduce the core size from the comparably large 1.2 µm in Figure 17 to as small as 420 nm

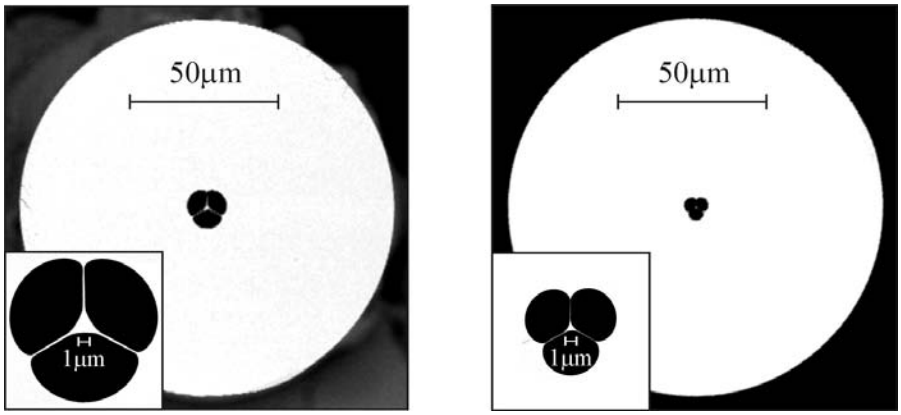

Figure 17: Comparison between typical F2 wagon-wheel fibre similar to that used in [61] (left) to small-core WW fibre (right) used for measurements in this section.

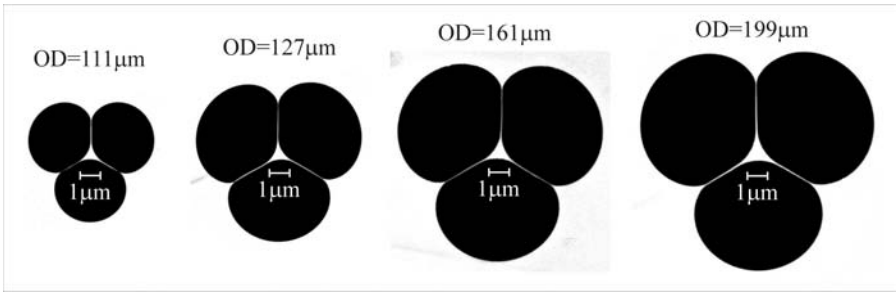

Figure 18: Range of core sizes fabricated for F2 WWs. From left to right - 420 nm, 480 nm, 590 nm, 720 nm [98].

[98]. This process involved fabricating a tube preform with a larger outer diameter than is normally used. Fabrication of wagon-wheel fibres with more conventional (1-2 µm) core sizes generally uses a tube with approximately a 10 mm outer diameter and 1 mm inner diameter. However here, to obtain a smaller core diameter, a 15 mm outer diameter 0.8 mm inner diameter tube was used. Since the final fabricated fibre dimensions generally scale relatively well with the initial preform dimensions, the ratio of the outer diameter to inner diameter has a strong influence on the final core size. This immediately suggests that this should reduce the core size of the fibre by approximately 45% by changing the initial preform from a 10:1 ratio to a 15:0.8 ratio.

In addition to this change, the wagon-wheel die itself was modified such that the strut length compared to the core size was increased significantly, with this ratio almost doubling compared to previous WW trials [98]. The effect of these combined changes can be seen in Figure 17, where although the outer diameters of the two fibres shown here are comparable, the resultant core size is significantly decreased.

As is shown in Figure 18, a range of core sizes were fabricated. The outer diameter of the fibre was varied during the draw resulting in core sizes from 420 nm to 720 nm. This range of core sizes allows the core size of the sensing fibre to be changed if desired.

2.4 FLUOROPHORE CHOICES

The next major goal was to select a fluorophore for the initial characterisation trials. This required evaluation of the performance of conventional fluorophores, as well as examinations into possible alternatives that overcome some of the shortfalls of these fluorophores.

The majority of the previous work on fibre-based fluorescence sensing has focussed on organic fluorophore molecules [13, 14, 102, 107, 108]. However this method has two primary drawbacks -

1. In conventional organic fluorophores, the separation between the excitation and emission wavelengths is relatively limited. As can be seen in Figure 19 the peak absorption of Rhodamine B, a common fluorescent molecule, is 542 nm while the emission peak is only at 565 nm. This limited separation requires results in a requirement for either good optical filters to ensure that residual laser light is not detected during measurements, or alternatively a source away from the peak absorption wavelength can be used. However this naturally reduces the amount of excitation light that is absorbed, and thus reduces the emitted fluorescence signal

2. The other drawback of organic molecules is that they suffer from photobleaching [109–111]. This is a mechanism in which a fluorophore when exposed to light will reduce its emitted fluorescence intensity. This can occur either rapidly (seconds to minutes), after the molecule has only emitted a small number of photons, or may occur after many tens of thousands of photons have been emitted by the molecule. Photobleaching itself refers to the process where a molecule undergoes permanent photochemical destruction, resulting in a reduction of the emitted fluorescence intensity [112]. One of the basic mechanisms is that the fluorophore is excited by an incoming photon from a singlet state to a triplet state [113]. From this state the molecule can interact covalently with other molecules, resulting in the effective quenching of that molecule since it will no longer emit fluorescent photons. Oxygen has been shown to play at least some part in the photobleaching process, with higher concentrations of oxygen in solution showing higher photobleaching rates for organic molecules [112, 114]. The photobleaching rate varies depending on that particular fluorophore, though regardless of the choice of fluorophore all molecules experience this

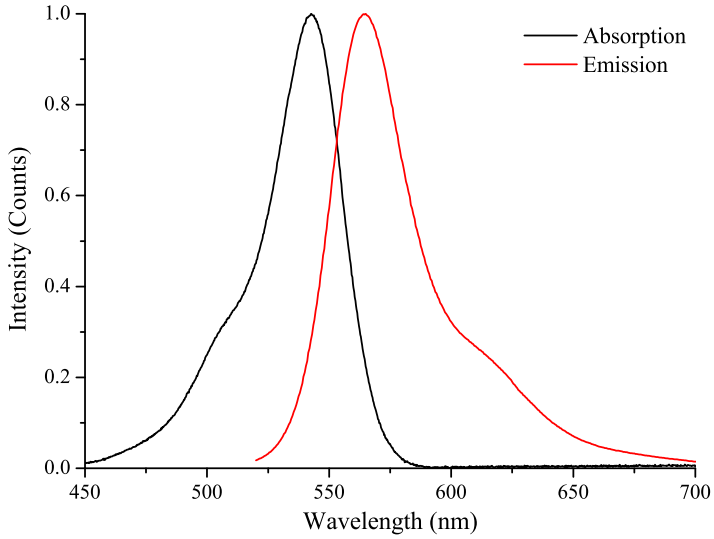

Figure 19: Absorption and emission spectra for Rhodamine B in ethanol [116].

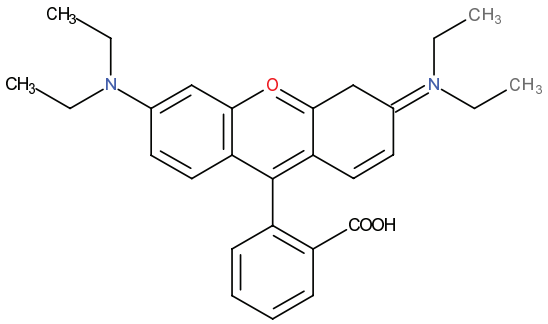

Figure 20: Chemical structure of Rhodamine B.

to some extent [115]. Depending on the excitation source used, photobleaching can occur in as short as a few microseconds using a laser or over a seconds to minutes using a lamp for excitation [112].

In bulk solutions photobleaching is somewhat compensated for by diffusion in the solution [112]. At room temperatures this rate is significant enough that molecules can move in and out of the excitation field. Since some forms of photobleaching are recoverable this process results in a general decrease in the photobleaching rate, and indeed if the diffusion rate is high enough compared to the photobleaching rate then no measurable reduction in the fluorescence intensity will be observed.

The photobleaching rate is an especially important parameter in fibre, since fibres generally exacerbate the effects of the photobleaching. In a fibre the liquid is confined within the micron-scale holes, and the amount of fluorophore molecules available for the diffusion related recovery of photobleaching to occur are relatively limited. Ad-

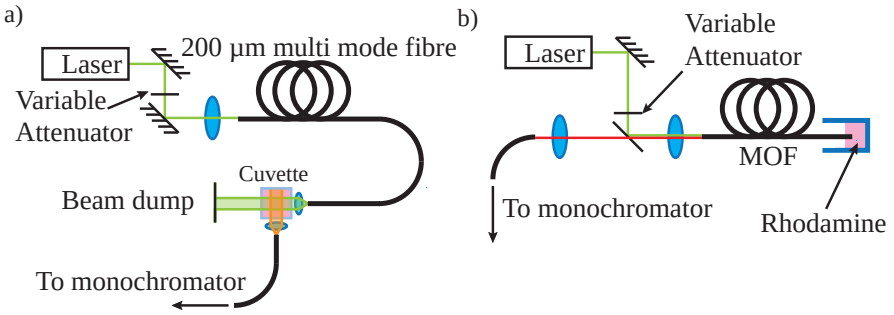

Figure 21: Experimental schematics for photobleaching measurements a) Cuvette measurement b) Microstructured optical fibre measurement.

ditionally, the peak intensity of the light within the fibre is orders of magnitude higher than what is typically used for bulk cuvette measurements which significantly increases the photobleaching rate. This increased rate of photobleaching, combined with the lack of recovery of the fluorescence signal from diffusion processes leads to a photobleaching rate that is several orders of magnitude higher in fibre than in bulk cuvette measurements.

Where photobleaching may be observed over the course of tens of minutes to hours in a cuvette measurement, coupling a similar power into an optical fibre filled with the same fluorophore will result in photobleaching in the order of minutes.

The fluorescence signal was monitored using a cuvette holder and an iHR 320 spectrometer, as shown in Figure 21. This fluorescence signal was then integrated across the wavelength range shown in Figure 22a and normalised to the initial intensity.

For this experiment a 1 µM solution of Rhodamine B was used, whose excitation and emission spectra are shown in Figure 19 and structure is shown in Figure 20. The majority of the Rhodamine B solution was placed in a cuvette and illuminated with 1 mW of 532 nm light for 1 hour using an attenuated 25 mW diode-pumped solid state source.

This measurement was then repeated using a microstructured optical fibre, with the experimental configuration shown in Figure 21b. The fibre was placed on an XYZ translation stage, with approximately 20 mm of the output end of the fibre hanging over the edge of the v-groove mount. This enabled the fibre to be filled without having to remove the fibre from the stage by placing the Rhodamine in a small container held horizontally. Using a 100 µL sample enabled surface tension to keep the fluid in the container ever when held horizontally.

A 30 cm length of fibre was used, and the fibre filled for 5 minutes. This only filled approximately $\frac{3}{5}$ths of the fibre. This was chosen to maximise coupling stability over the course of the measurement, as when the fibre is fully filled it can induce additional fluctuations in the coupling efficiency. The meniscus of the liquid moves constantly

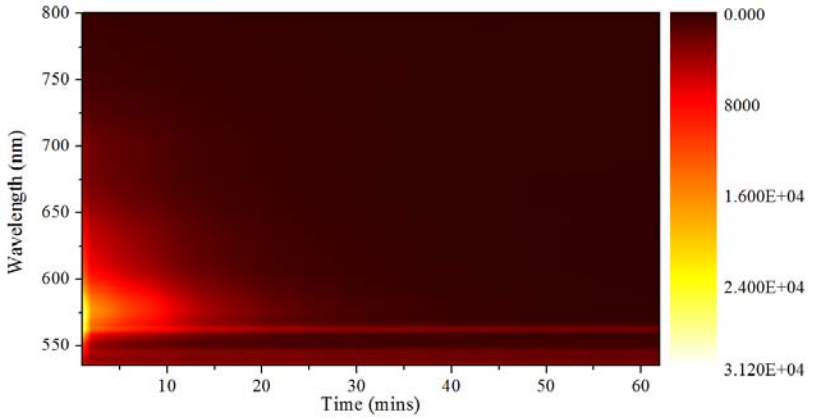

(a) Time series of scans of in-fibre photobleaching. Time is displayed along the x axis, with z showing the intensity in arbitrary units.

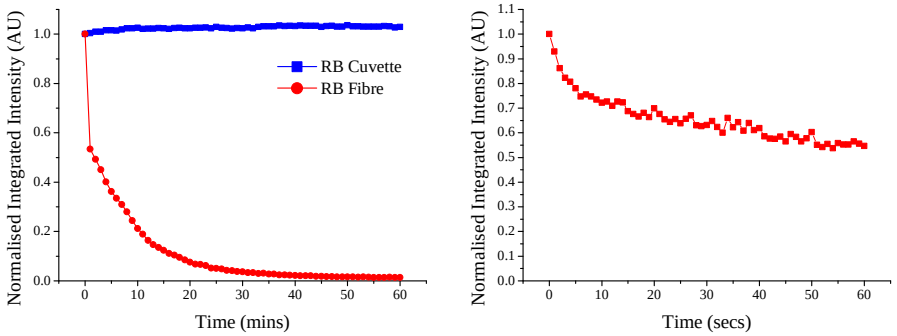

(b) Left) Normalised fluorescence intensities over 1 hour, with 1 scan per minute. Right) In-fibre normalised photobleaching with 1 scan per second over 1 minute.

Figure 22: Photobleaching kinetics of Rhodamine B in ethanol. 532 nm excitation was used for both samples. The total laser power in the bulk measurement was 1 mW, and the coupled laser power for the fibre measurement was approximately 1 mW.

due to air currents, so only partially filling the fibre ensures this can not significantly affect measurements.

Figure 22 shows the extent of the photobleaching observed in wagon-wheel fibres. Figure 22a shows the spectral evolution over time over the region that is integrated to obtain the plots in Figure 22b. Figure 22b shows that the fluorescence intensity over the course of an hour for a cuvette sample remains approximately constant, with the small variations most likely due to slight changes in the coupling over the course of an hour. However the situation for the fibre measurement is markedly different, with significant reductions in the power noted almost immediately with only a few percent of the initial signal still present after 1 hour of illumination. When this measurement is repeated with only a 1 minute duration and a much more rapid scanning speed this behaviour can be properly observed, with the fluorescence power reducing to approximately half its intensity over the duration of this measurement.

The time-dependent effect induced by photobleaching complicates characterisation measurements, as it introduces an extra variable which must be carefully controlled to ensure consistency between measurements. A number of modifications can be made to the experimental design to counteract the effects of photobleaching, however for the initial characterisation of the system another approach was taken which will be discussed in the next section.

Two alternatives to organic fluorophores have found use in recent years, Qdots and nanoparticles. Both of these are attractive because they are much less susceptible to the effects of photobleaching than organic fluorophores.

Previous work [61] on fluorescence detection utilised Qdots to overcome some of the issues with photobleaching discussed earlier. Qdots consist of a central semiconductor core of radius 1-25 nm [117], often with an outer cladding of a different semiconductor material to enhance the optical properties [118]. A schematic of a commercial Qdot is shown in Figure 23. These colloidal nanocrystals possess quantum confinement in all three directions due to the scale of the molecule being comparable to that of the exciton Bohr radius [119]. They display broad excitation spectra, and discrete emission that is typically well separated from the excitation source.

The emission wavelength of the Qdots scales with the size of the particle, with larger particles emitting longer wavelength light. This arises due to the method in which the Qdots produce fluorescence, which does not use internal conversions between energy levels to produce the emission. Instead photons are created via Coulomb correlated electron-hole pairs. The energy of these photons is inversely dependent on the size of the semiconductor structure explaining the size dependence on the emission wavelength.

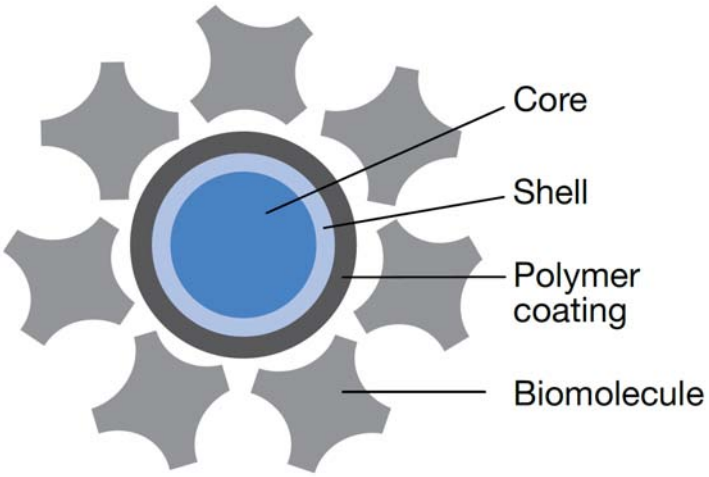

Figure 23: Schematic of Qdot from Invitrogen [118].

Qdots have been shown to be significantly more photostable than organic fluorophores [120–122]. This property makes measurements using Qdots simpler, as they can be illuminated for a longer duration without bleaching occurring. Since the absorption of Qdots is typically much higher than with organic fluorophores (compare Figures 19 & 32) they generally produce a higher fluorescence signal at identical concentrations.

Qdots can be used as biolabels in a similar way to conventional organic fluorophores [122–125]. By coating the semiconductor particles with a polymer layer the dots become water soluble [122]. This polymer coating can then be functionalised with a compound such as streptavidin/avidin [123] and then used as a fluorescent label with standard techniques. This combination of the high quantum efficiency and photostability of Qdots with standard labelling techniques means that these dots can be used as more sensitive fluorescent labels since their signal is more readily distinguished above the background autofluorescence of the samples [123].

More recently developments have been made in utilising rare-earth doped nanoparticles for sensing applications [126–131]. These particles consist of small (5-100 nm) diameter crystals doped with rare earth ions. These particles can then be functionalised [127] using standard techniques such that they can then be bound to conventional antibodies. Once this process has been completed the nanoparticles can then act as a conventional fluorescent label.

Nanoparticles have a number of advantages over standard organic molecules -

1. Excitation requirements. For erbium-doped nanoparticles the excitation source used is in the NIR, and thus the autofluorescence from the sample is greatly reduced compared to visible or UV excitation [132–134].

2. Stability. Nanoparticles are virtually immune to photobleaching effects [135].

3. Lifetime. The lifetime of these particles is much longer than organic fluorophores (10-100s µs for nanoparticles, ~ns for organic fluorophores). This means that by using time gating techniques a large amount of the background autofluorescence can be removed, as the autofluorescence is typically has a shorter lifetime than that of the nanoparticles [129].

Both of these alternatives to conventional fluorophores will be investigated in later sections.

2.5 INITIAL EXPERIMENTS

2.5.1 *Qdots*

For the initial characterisation of the system it was decided to use Qdot® 800 ITK™, a commercially available CdSe Qdot from Invitrogen [118]. These are unconjugated Qdots in decane, as the concentration of these is more accurately known than conjugated versions in aqueous solutions. 800 nm was chosen to allow easy integration with existing laser sources used for excitation of Rhodamine B dyes, while maximising both the absorption coefficient of the dye at this wavelength.

When Qdots in aqueous solutions are used, they are typically suspended in buffers such as Phosphate Buffered Saline (PBS) or Tris-Buffered Saline (TBS). This creates issues when the fibres are filled, as when the liquid reaches the end of the fibre it can evaporate from the tip. PBS solutions for example have relatively high concentrations of salts (0.14 M $NaCl$, 0.0027 M KCl, 0.01 M PO_4^{3-} for pH 7.4 solution) [136] leading to deposits forming on the tip of the fibre. An example of this is shown in Figure 24 where extensive salt deposits are seen to have formed on the tip of the fibre [61].

The Qdot ITK differs from the conjugated version by not having antibodies or functional groups attached to the surface, and is suspended in decane rather than an aqueous solution. This in particular is also advantageous compared to Qdots in aqueous solutions, as when the solvent evaporates no additional precipitates are formed apart from the Qdots themselves.

As the liquid evaporates from the first 1-5 mm of the fibre after it is removed from the liquid, we believe from the experiments described below that similar deposits are formed along the length of the fibre. While the deposits on the tip significantly reduce the coupling efficiency, the deposits along this length inside the holes of the fibre would significantly increase the losses due to scattering. This evaporation occurs relatively rapidly, with visible changes in the loca-

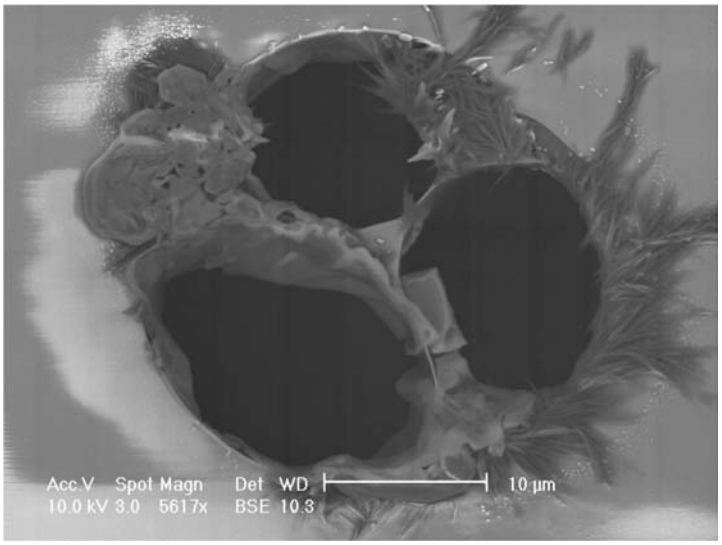

Figure 24: Scanning electron microscope (SEM) image of fibre tip with salt deposits from PBS buffer [61].

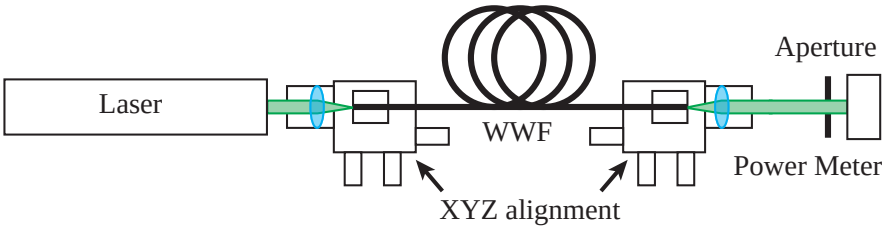

Figure 25: Experimental configuration for degradation measurements.

tion of the meniscus observed using a microscope within the first few seconds of the fibre's removal from the solution.

To examine the effects of salt deposits on the fibre an experiment was performed. This experiment utilised two 18 cm long pieces of F2 WW fibre with a core size of approximately 1.5 µm. A 532 nm laser was used as the input source, attenuated to approximately 200 µW. Each fibre was aligned to its maximum possible intensity of 70 µW $\pm$ 5 µW before being de-tuned from its peak intensity by moving the fibre longitudinally away from the focal point. Each fibre was detuned using the same method to 18 µW $\pm$ 0.2 µW. This was performed to increase the stability of the fibre over the duration of the filling to ensure that drift in the output power due to variations in coupling was minimised.

Care was taken to ensure that only the light guided within the core was being measured, as this detuning method does couple additional light into cladding modes. A variable diameter aperture was used directly in front of the power meter, and the output from the fibre imaged on to this aperture. The diameter of the aperture was then reduced until only the core light was allowed through to the power meter. This is possible using a wagon-wheel fibre as the air holes sur-

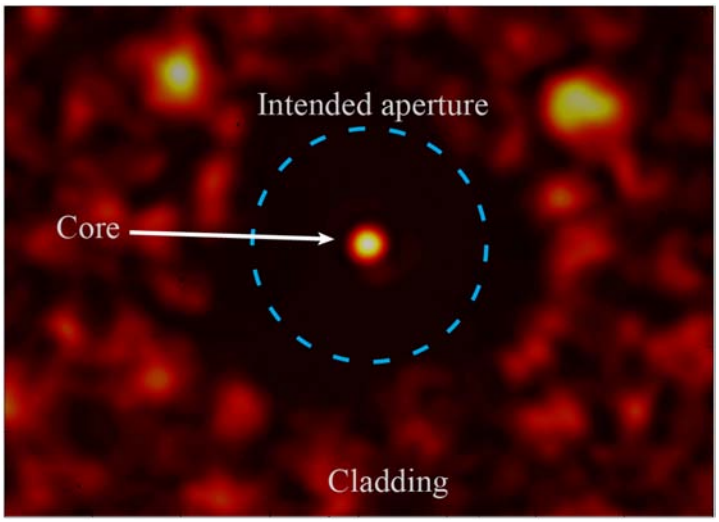

Figure 26: Composite image of the core modes and cladding modes guided within an F2 wagon-wheel fibre. The three holes in the wagon-wheel fibre can be resolved just outside of the dashed circle marked "Intended aperture".

rounding the core of the fibre create a dark region around the core area, as shown in Figure 26. To obtain this data the laser was first optimised in the core, and the output of the fibre imaged directly on to a spiricon CCD camera. No aperture was used here. The fibre was then adjusted on the stage such that the light was coupled into the cladding, and another set of data obtained. The output coupling was not changed between measurements. Two separate measurements were required here as the cladding modes are typically much dimmer than the core mode, so much so that the cladding modes are often not visible above the noise of the detector.

This measurement shows the effect this large air gap has on the mode structure within the fibre, and how it is possible to ensure that the power measured is only the power guided within the core of the fibre simply by using a small aperture to remove the cladding light.

The filling time was measured separately to these trials, and recorded as 280 s $\pm$ 10s. The fibres were allowed to fill for 300 s, then removed from the solution. The fibre end was then placed on an XYZ stage, and using a lens the output was focussed into a power meter with an aperture in place to block cladding light as shown in Figure 25. The power was then monitored for 10 minutes. At the completion of the scan the input end of the fibre was adjusted in the XY plane to improve the coupling.

These deposits significantly increase the scattering losses of the fibre as shown in Figure 27. The dashed lines at the top of the plot show the initial recorded power in each of the fibres, with the solid lines showing the power over the duration of the 10 minute scan after filling had completed. As can clearly be seen in Figure 27 the PBS

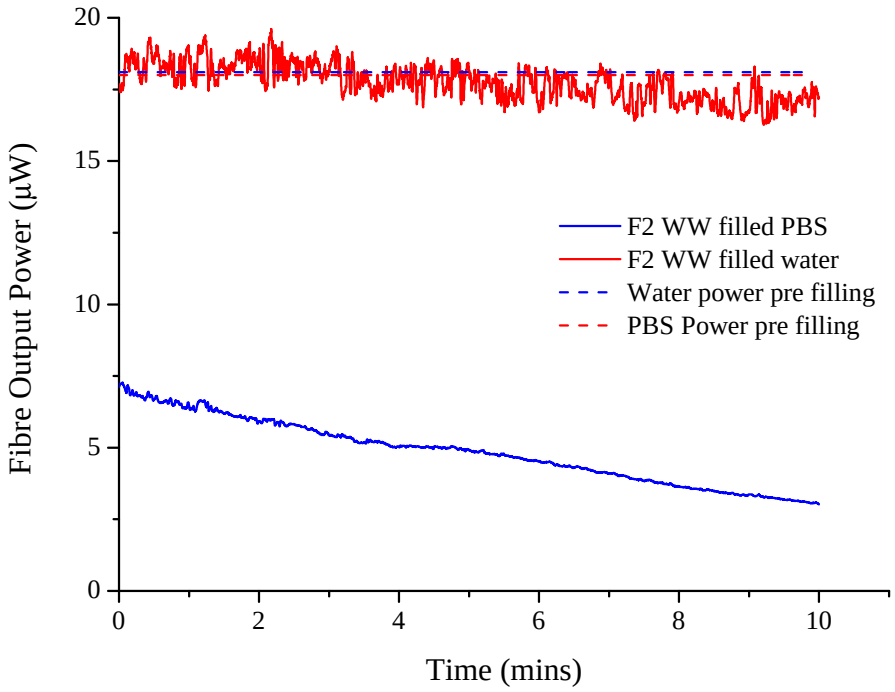

Figure 27: Reduction in fluorescence intensity due to salt-deposits forming on the tip of the fibre when using Qdot solution in PBS buffer, pH 7.4.

filled fibre has a much lower output power than the water filled fibre from the beginning of the scan, which continues to decrease over the duration of the measurement. The large drop in the signal before the scan starts is due to crystallisation either during filling or in the short duration (< 1 minute) between when the fibre was removed from the solution and when the measurement was performed.

Losses due to scattering from these salt deposits are readily differentiated from losses due to effects such as photodarkening (see Section 5.4) as virtually the full power can be recovered by cleaving the tips of the fibre and realigning the laser light into the core. The PBS filled fibre was then removed from the stage, and ≈10 mm cleaved from each end. The fibre was then replaced on the stage, and realigned using the power meter. It was found that the power could be optimised to 64 µW ± 5 µW which is the same as the initial power within experimental error. This strongly suggests that the majority of the degradation in the power is due to scattering losses caused by crystallisation of the salts in the buffer solution at the tip of the surface of the fibre.

It was noted during experiments in later sections that when this measurement was performed using Qdot 800 ITK in decane solution that the input power remained constant before and after filling. From this we can conclude that scattering losses induced by filling

this decane solution through the fibre are smaller than the variations in the coupling, and as such can be ignored for these measurements.

Being able to reliably estimate the transmitted power through the fibre after filling is important for a dip sensor, because if the coupled power decreases such as seen here with the scattering losses then the measured fluorescence intensity will be significantly lower than would otherwise have been measured. Since measurements such as those in Chapter 6 correlate the measured fluorescence intensity with a concentration of the target chemical this drop in intensity arising from increased loss could easily be interpreted as a lower concentration of the target molecule. As such, measurements demonstrating that the power transmitted through the fibre does not drop after filling are an important step towards developing a sensor which does not require the output power to be monitored for each measurement.

2.5.2 *Fibre filling*

To fabricate an effective dip sensor it is desirable to gain an understanding of what lengths of fibre can practically be used in measurements. The preliminary modelling results of the optimum fibre length when filled with a 10 nM solution of fluorophore (see Section 6.6 for details) showed that this length is in the order of 1-10 m for core sizes between 200-800 nm. However, since the fibre holes are of the order of 3-10 µm, actually using lengths of fibre beyond around 50 cm becomes impractical due to the filling times required.

For initial work, the fibres were filled simply using capillary flow. This involves dipping one end of the fibre into the desired solution, and allowing capillary forces to draw the liquid up the fibre.

The filling time can be estimated from experimental methods, such as the plot shown in Figure 28 or calculated using theoretical methods described below. To measure the filling rate experimentally, typically a high concentration of fluorophore ($\geq$ 10µM) is added to a solvent, and allowed to fill through a relatively long length of fibre. Using laser light coupled into the fibre it is possible to measure the location of the meniscus as it traverses the length of the fibre, and by monitoring this over time the fill rate for a given length of fibre can thus be estimated. A high concentration of fluorophore is used to make it easier to identify its location, since at high fluorophore concentrations it is a clearly visible spot that moves along the length of the fibre. Here longer fibre lengths than would typically be used for fluorescence measurements are employed, as the longer lengths allow the position of the meniscus to be monitored more precisely. Using short fibre lengths the liquid fills rapidly, creating a relatively large uncertainty in the position of the meniscus when the measurement is taken.

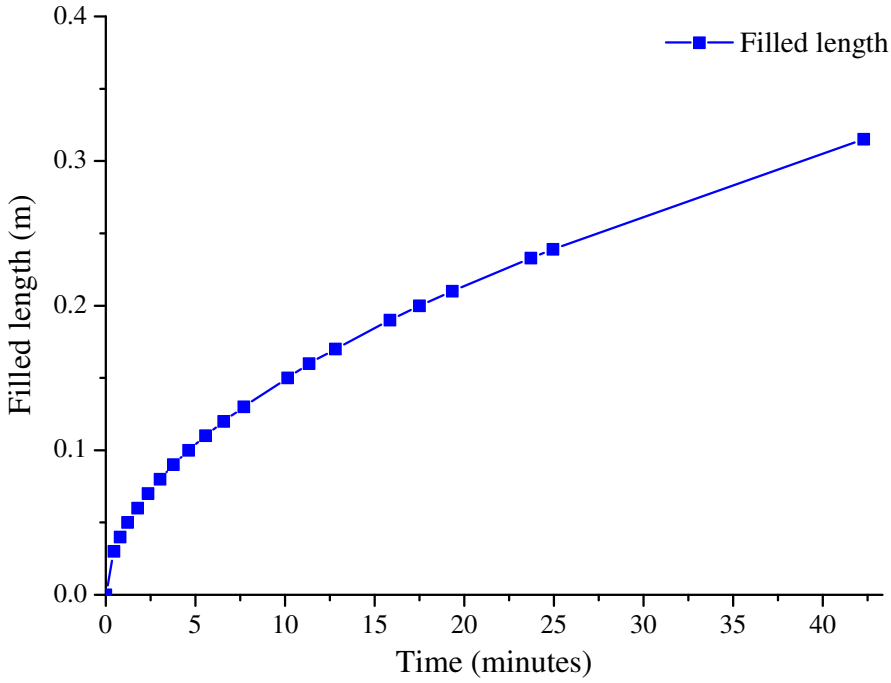

Figure 28: Filling dynamics of decane through F2 WW fibre, hole size 5 µm. Here filling is performed only using capillary action, without the application of pressure to increase the filling rate.

Since the filling rate is highly dependent on the contact angle and viscosity of the solvent the fluorophore used must be soluble in this solvent for this method to work. If this is not possible, or if the desired fluorophore emits in the infra-red then the location of the meniscus can be monitored by carefully looking for an area of increased scattering along the length of the fibre. As the fibre fills this region moves up the fibre, making it possible to estimate the filling time. The error involved in this method is naturally higher than using the fluorophore, as this region is not as prominent as when using a visible emitting fluorophore. This can also be monitored using a microscope and looking directly into the holes of the fibre, but this method is problematic for measuring the filling times for more than one or two points along the fibre.

Alternatively, the filling rate can be estimated using the capillary flow equation [137, 138] for a capillary open at both ends.

$$l^2 = \frac{(P_A + D \cdot g \cdot h + \frac{2\gamma}{r_{eff}} cos[\theta])(r_{eff}^2 + 4 \cdot \varepsilon \cdot r_{eff}) \cdot t}{4(\eta - \eta_A)} - \frac{2\eta_A l_T}{\eta - \eta_A} \cdot l \quad (2.1)$$

solving for l gives

$$l = 8lt^2\eta_A +$$

Variable	Description
l	filled length
P_A	Driving pressure
D	density
g	gravity
h	depth of tip below surface
γ	surface tension
θ	Contact angle
r_{eff}	effective hole radius
ε	coefficient of slip
η	viscosity of liquid
η_A	viscosity of air
l_T	total capillary length

Table 1: Variables for capillary flow equation.

$$\sqrt{\frac{64l_T^2\eta_A^2 - 4(4\eta - \eta_A)(-Dghr_{eff}^2 t - 4Dhr_{eff}t\varepsilon - 2r_{eff}t\gamma cos\theta - 8t\gamma\varepsilon cos\theta)}{8(\eta - \eta_A)}} \tag{2.2}$$

The results using Equation 2.2 are shown in Figure 29. Typically the contact angle is assumed to be 0° for water on clean glass. The effect of changing the contact angle in the capillary flow equations is shown in Figure 29, where the theoretical results are compared to experimental values from 0° to 50° in 10° increments for a 4 µm hole size filling with water. No external pressure differential is applied, such that the pressure is identical at both ends of the fibre. The deviation between the theoretical and experimental values is due to the holes of the fibre not being perfectly circular as the equation assumes, and approximations in the contact angle of the liquid on the glass.

2.5.3 *Forward and backward collection of fluorescence*

2.5.3.1 *Introduction*

As previously mentioned, to fabricate an effective dip sensor ideally one end of the fibre needs to be free such that the measurement can be performed with the fibre in-situ, without having to remove it from the sample and realign the output into a detector. For initial characterisation of the sensing platform both methods were explored, as will be discussed in the following section.

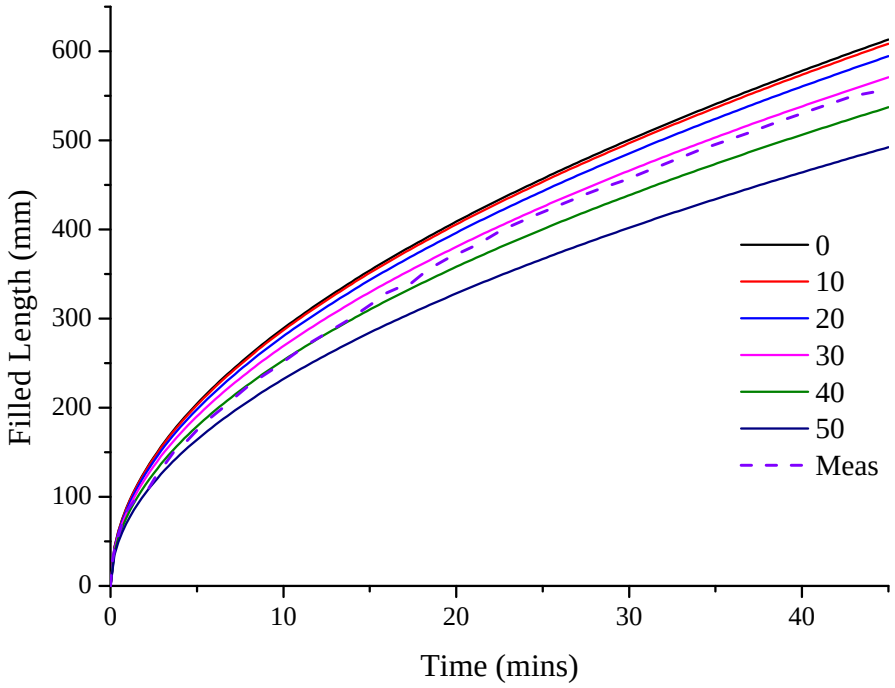

Figure 29: Comparison between experimental and theoretical calculations for F2 WW fibre with an effective hole radius of 4.0 µm filled with water.

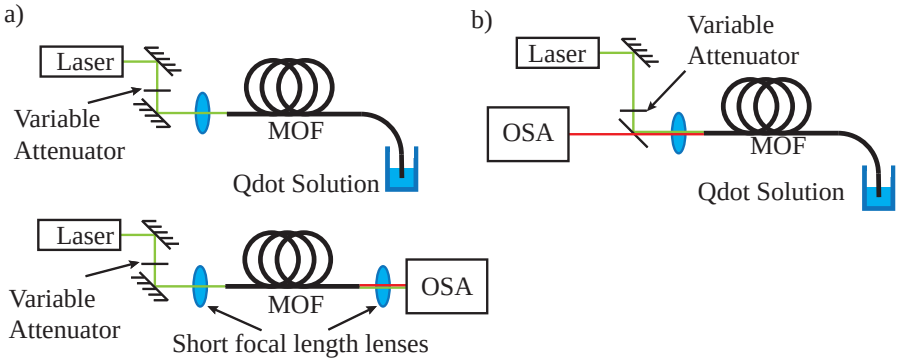

Figure 30: a) Forward detection scheme. b) Simplified backward direction scheme.

2.5.3.2 *Forward*

Several possible experimental configurations were examined for detection of the Qdots in solutions. The first, as shown in Figure 30a is a forward-based detection scheme, in which the fluorescence signal is measured from the distal end of the fibre. For clarity here we define the distal end as the fibre end opposite to that which the excitation source is coupled in, which we label as the input end. To perform a measurement using this technique the fibre is first aligned using a power meter, and then the distal tip is removed from the output XYZ stage and dipped into the Qdot solution. The fibre is allowed to fill for a set length of time, either to allow the fibre to fully fill or alternatively to allow it to fill up to a set point for each trial.

This can be calculated using capillary flow equations presented in Section 2.5.2. Once the filling is completed the fibre is removed from the solution, and again placed on to the output XYZ stage. The fibre is then realigned, and the measurement performed.

This scheme is advantageous because of its simplicity - it requires no dichroic mirrors for the measurement to be performed, as all of the output light is directly coupled into the optical spectrum analyser (OSA). However this can lead to issues if the laser power propagating from the sensing end of the fibre is significantly larger than the power of the Qdot signal, as this can easily overwhelm the measured signal. This can easily occur when using organic fluorophores whose emission wavelength is close to that of the excitation source, significantly reducing the possible signal that can be detected. This is not as prevalent when using Qdots since the emission is ≈300 nm away from the excitation source. This is also a potential issue if a sensitive detector is used, as the residual laser signal could be significantly higher than the damage threshold of the detector leading to its subsequent destruction.

Additionally, this method requires the removal of the fibre for filling, and subsequent optical realignment. At high Qdot concentrations (100 nM-1 µM) this method is relatively easy, as the OSA can be scanned at the peak of the Qdot emission enabling the coupling into the OSA to be tuned. However at low concentrations close to the noise floor of the OSA, this method becomes much more difficult as the signal becomes increasingly noisy and the scan speed decreases dramatically. The combination of these two factors make tuning of this signal a time consuming process if repeatability is desired. The repeatability of these measurements was not explored in detail. While at high Qdot concentrations alignment is relatively easy due to the large signal and rapid scan times, it becomes progressively more difficult thus increasing the uncertainty of the measurements. Thus this exact method would not find good use in measurements requiring high precision with low Qdot concentrations, which would likely be

made worse by the use of photobleachable organic fluorophores as opposed to Qdots.

It is possible to optimise the signal into the OSA based on the residual laser light, although this can lead to issues as the lenses used are not perfectly achromatic, and as such the focal points of the laser light and the peak of the fluorescent signal are not located at the same spatial position. This means that if the coupling is not perfectly aligned the signal could change in both height and spectral shape depending on exactly how the fibre is aligned.

Some of these issues can be partially or fully eliminated through the use of long pass and laser-line filters, which reduces issues arising from the spacing of the excitation and emission light. However the ratio of excitation to emission light will always be significantly higher using this method than in the backward detection scheme discussed in the next section.

2.5.3.3 *Backward*

The alternative to this forward detection method is to adjust the experimental configuration such that one of the 45° mirrors is replaced with a dichroic mirror. This mirror is chosen such that it is highly reflective at the laser wavelength while passing the majority of the fluorescence signal.

The fibre is aligned using the same method as Figure 30a), however since the fluorescence is captured in the back direction through the use of a dichroic mirror the fluorescence signal can be constantly monitored while the fibre is filling. If care is taken with the measurement the need for realignment can also be removed when using this measurement.

Using this method the residual pump signal is significantly lower than is observed using the forward direction method, primarily because the only pump light that travels in the backwards direction is the light that is reflected from the face of the cores, or scattered backwards along the length of the fibre. Both the input and output faces of the fibre core will contribute to this signal, although the input face will have a greater impact since the signal from the output face will be diminished by transmission losses. This, combined with the use of a dichroic filter that is between $OD4$ to $OD6$ (i.e. reducing the intensity by between $10,000\times$ and $1,000,000\times$) virtually removes the excitation light before the detector.

This backwards detection method has two distinct advantages over the forward detection scheme discussed in the previous section. Firstly, and most importantly only the output end of the fibre needs to be free for the measurement to be performed. This is critical for an effective dip sensor, since the fibre can be constantly monitored while the filling is being performed. This type of method also enables the fibre to be spliced to a conventional silica SMF fibre, such that the sensing

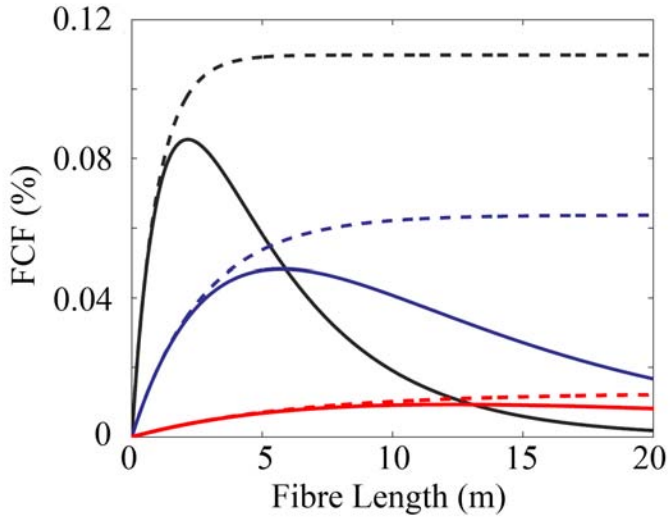

Figure 31: Comparison between maximum forward (solid) and backward (dashed) capture fraction for Bismuth (black), F2 (blue) and Silica (Red). Modelled fluorophore was 0.5 µM Rhodamine B in Isopropanol. Taken from Ref. [12].

fibre can be easily integrated with standard connectorised fibres and detectors. This will be discussed in detail in Chapter 3.

For the forward direction case it was noted that the maximum fluorescence signal obtainable decreases at long fibre lengths [12, 102]. This arises due to a combination of the intrinsic loss of the fibre, along with the additional loss caused by the absorption of the fluorophore filled within the holes.

Two separate detection methods were employed, based on an optical spectrum analyser and a photodiode for detection in forward and backward directions, respectively (see Figure 30). Advantages and disadvantages of each approach are discussed below in Sections 2.6 and 2.7.

2.6 SPECTRALLY RESOLVED RESULTS

Measurements that are able to resolve spectral features from the fluorescent signal are advantageous over those that do not as it is possible to differentiate between background/spurious signals and the actual signal from the fluorophore. This allows more certainty in the results than would be obtained such as by using a photodiode, where there is no simple confirmation of the wavelength or source of the signal. By examining the spectral output from the fibre based measurements it is possible to confirm that the signal originates from the fluorophores (in this case Qdots) and not simply from residual pump light or from other sources of fluorescence as will be discussed later in this

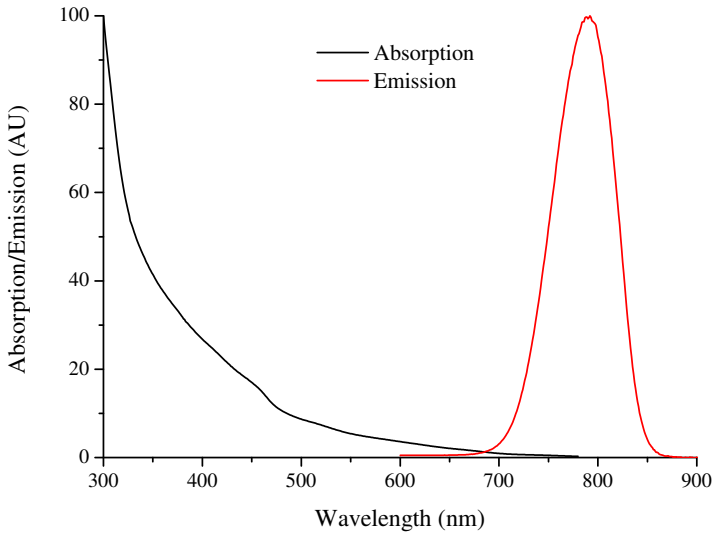

Figure 32: Absorption and Emission spectra of Qdot 800 streptavidin conjugate [118].

section. The absorption and emission spectra of Qdot800 as used here is shown in Figure 32.

The aim of this section is to examine the limitations of this type of sensor to determine what improvements can be made in terms of the detection limit compared to existing results.

Spectrally resolved measurements were obtained using the experimental schematic shown in Figure30a. These measurements were performed using a forward-collection scheme, in which the fluorescence signal was collected from the distal end of the fibre. An argon-ion laser was used, tuned to 514 nm with a maximum output power of approximately 100 mW. For collection of the fluorescence signal an Ando AQ6315E OSA was used, with a 550 nm long pass filter to reduce the residual pump intensity.

The method used for these measurements was described earlier. The input powers into the fibres were varied between 1-5 mW depending on the scenario. The fibre used here is shown on the right in Figure 17, with a fibre length of 30 cm used for these measurements.

Figure 33 shows the results obtained using forward detection by the OSA. Observe that the 0.2 nM (200 pM) concentration Qdot solution can be clearly detected, which represents a significant improvement on previous reports [61]. This result was obtained using a relatively short length (30 cm) of fibre and input powers in the range 1–5 mW.

As can be seen from this measurement, while the 1 nM signal can be clearly resolved using this method it then becomes increasingly difficult to detect lower concentrations of Qdots. The 0.2 nM signal can still be resolved over the background signal, however when the concentration is further reduced to 0.1 nM the signal becomes indistinguishable over the background.

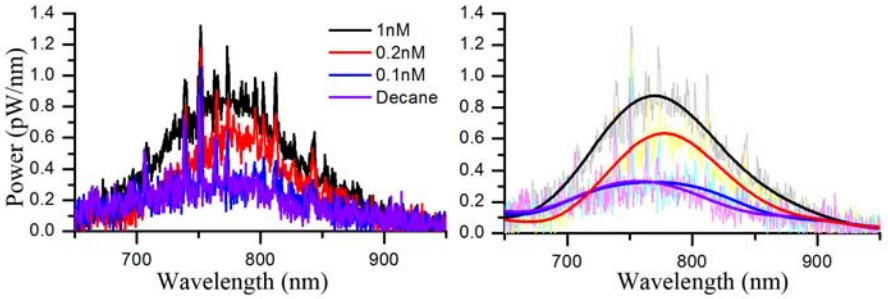

Figure 33: Spectrally resolved measurements for Qdot 800 ITK in small-core wagon-wheel fibres for various concentrations of Qdots. 'Decane' represents a fibre filled with just solvent with no Qdots present. a) Direct signals from optical spectrum analyser b) Low pass filtered measurements showing spectral shapes at various concentrations.

This work determined that the background signal shown here, labelled as "decane" in Figure 33a does not actually arise from the decane, but rather from the glass itself. This will be covered in detail later in Section 2.7. This signal is still observed with unfilled fibres, at an even higher intensity than with completely filled fibres. The reasons for this were examined theoretically, and again this will be discussed in a later section.

For clarity the obtained spectra were low-pass filtered with identical parameters to improve the usability of the data. By removing the effect of the noise, as shown in Figure 33b it is possible to estimate the peak emission wavelengths of each of the spectra. It can be noted that the peak wavelengths of both the decane and 0.1 nM signal are blue shifted compared to both the higher concentration signals, as well as the manufacturer's data shown in Figure 32. Since the peak wavelengths of the 0.1 nM and decane signals are close this strongly suggests that the signal in the 0.1 nM signal arises from the background glass, and any fluorescence from the Qdots is not observable above this background level.

Using this spectrally resolved method makes it possible to differentiate between the background signal and Qdot signal, even without a direct comparison between the two. As such this method enables analysis to be performed in more detail than the time-resolved measurements discussed in the next section. However the sensitivity of OSAs are relatively poor, with noise floors in the order of 80 dBm. At low Qdot concentrations it becomes increasingly difficult to differentiate between different concentrations due to the noise of the detector. Additionally the scan speed is extremely slow, with scans at the highest sensitivity level taking in the order of 15 minutes. While this scan is being performed the coupling into the fibre can not be adjusted.

The primary limitation encountered was background fluorescence from the F2 glass, which is believed to originate from metal impur-

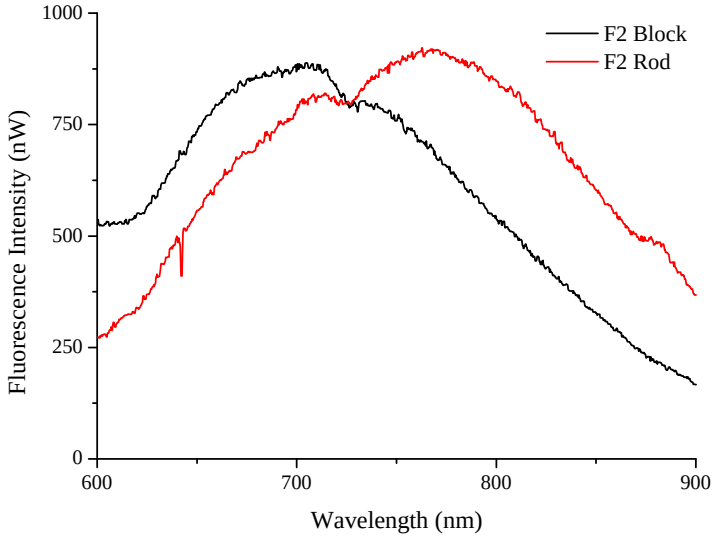

Figure 34: Comparison between glass fluorescence signal from bulk samples of F2 glass.

ities in the glass. This has previously been encountered [61] with F2 glass, and several changes from previous results have been implemented to reduce the impact of this unwanted fluorescence. Firstly, the glass composition was changed from commercially available F2 rods to bulk F2 glass, which reduced the observed glass fluorescence, as seen in Figure 34. This was measured using the experimental protocol described in Section 2.8. The most important value is the fluorescence intensity at the peak of the Qdot emission, which drops from approximately 900 counts for the F2 rod to 600 counts for the F2 block. The second change is the reduced core size of the fabricated fibre; as the core size decreases, the power fraction located within the glass decreases as shown in Figure 12.

As the glass fluorescence is related to the power within the glass, reduction of the pump power acts to decrease the recorded glass fluorescence. The advantage of the OSA detection method is that the results can be analysed in more detail than with a photodiode because the entire spectrum can be viewed. This is negated somewhat by the sensitivity of the OSA, as low concentrations are close to its noise level and differentiation between background and Qdot signals becomes difficult.

These results show clearly that these spectrally resolved measurements are close to the noise floor of the detector (Figure 33) and as such they would most likely benefit from improvements to the detection apparatus. Additionally these results demonstrate that the main restriction to lowering the detection limit is still the intrinsic glass fluorescence, even after changing the glass from an F2 rod to an F2 block reduced the amount of fluorescence generated by approximately 30%.

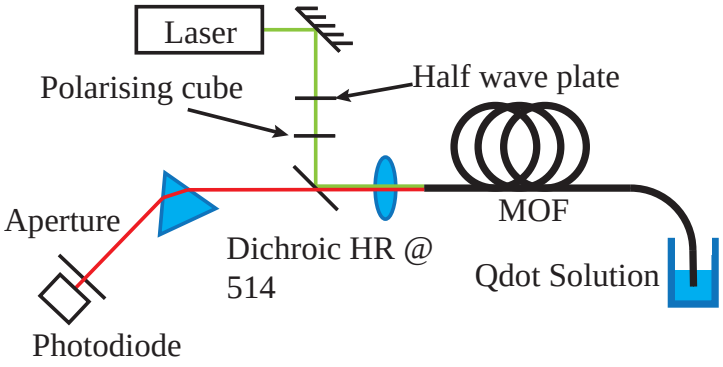

Figure 35: Experimental schematic for time-resolved Qdot detection using a high gain silicon photodiode for detection. This configuration is based on the back-detection configuration described earlier.

2.7 TIME-RESOLVED RESULTS

2.7.1 *Experimental method*

With the basic characterisation completed using the OSA a more field-deployable method was investigated. Due to the disadvantages of an OSA based method, namely the long scan times, poor sensitivity, high cost and lack of portability, alternative methods for detection were required.

To improve the stability of the coupling a slightly larger core fibre was used, and is shown in Figure 36. This fibre also had a significantly larger outer diameter, which improved the mechanical characteristics of the fibre and greatly simplified handling during experiments. The loss of this fibre was higher than that of the last trial, with a loss at 800 nm of 1.4 dB/m compared to approximately 0.9 dB/m of the earlier fibre. The reason for this increase in loss is unclear. It is possible that it was caused by contamination of the cane or variations in the fibre drawing process.

This technique, using the experimental configuration shown in Figure 35 utilised a modified version of the back detection method discussed in Section 2.5.3.3 and shown in Figure 30b. This method uses the same basic set-up as previously with a single lens for coupling and a dichroic mirror (high reflection at 514 nm, high transmission at 700 nm) to efficiently split up the fluorescent and residual excitation light. It was further improved by the addition of a prism to spatially remove any pump light that is not spectrally filtered with the dichroic filter. It is possible to do this using a prism as the spectral separation between the pump signal at 514 nm is a significant distance from the Qdot emission at 700-850 nm meaning that when the two are passed through the prism the resultant separation is big enough that an aperture can be used to block the pump light.

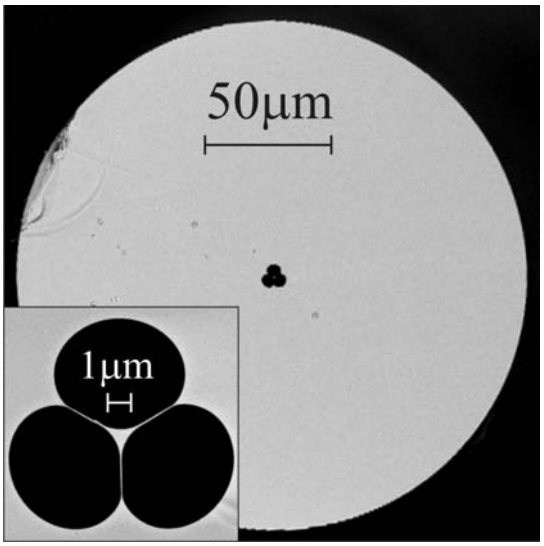

Figure 36: Wagon-wheel fibre used for these measurements, core size 0.6 µm, outer diameter 200 µm.

The dichroic filter used in this section was of a relatively poor quality, with enough 514 nm pump light transmitted through the filter that a green spot could clearly be observed to the left of the mirror. Without the prism in place this results in complete saturation of the photodiode. The use of this prism splits the green pump spot from the infra-red signal spot by 10-30 mm, so the photodiode signal does not increase from the dark signal even when the laser is operated at maximum power. An additional 550 nm long pass filter was also used directly in front of the photodiode, to further reduce the green pump light incident on the detector, whether it was passed through the fibre or scattered from another source.

Alignment was performed by optimising the coupling into the fibre using the same air cooled argon ion laser that was used in the last section. The laser was tuned to 514 nm, with a maximum power at this wavelength of 130 mW. A 633 nm HeNe laser was used for rough alignment of the back-detection system. The fibre was first aligned in the forward direction using the 514 nm laser. The HeNe beam was then coupled into the core in the backwards direction, adjusting only the stage originally used for the output of the 514 nm light. The long pass filter is then removed from the configuration, and the location of both the red HeNe spot and green 514 nm spot observed. The location of the Qdot signal can then be estimated by recording the distance between the green and red spots and extrapolating.

Once the rough alignment is complete a test fibre is used for optimisation of the signal. The fibre is aligned as described earlier, and then filled with a relatively high concentration of Qdots. Using a linear translation stage the position of the photodiode is varied along the

direction of the dispersed light from the prism until the maximum signal intensity is obtained.

The variable attenuator from the previous configuration was also changed slightly, from using a number of neutral density filters to using a half-wave plate, polariser combination. Since the argon ion is linearly polarised (250:1) rotating the half wave plate enables the power to be almost infinitely varied. Combined with the variable output power of the laser itself (variable between approximately 1 mW to 130 mW this enables much better control over the power transmitted through the fibre.

This configuration possesses the advantage of the back detection method discussed earlier, in that the signal can be monitored constantly while the fibre is filling. Although this method could be used with the OSA, real-time results would not be possible due to the long scan times (up to 15 minutes) meaning that the only advantage over the forward direction measurements would be that the signal can be measured without having to remove, replace and realign the output end of the fibre.

For these measurements the fibre was initially aligned before filling using a power meter and the 514 nm laser. The signal recorded from the photodiode in Figure 35 was then monitored for fine adjustment of the recorded power. Once the maximum power was obtained the fibre was removed from the output stage, and dipped in the liquid. While filling the signal from the photodiode was monitored constantly, and fine adjustments made to optimise the power. This power was recorded at relatively short intervals, and the results are shown in Figure 37.

2.7.2 *Results and analysis*

Results filling with 0.5 nM and 1 nM solutions were initially confusing, as the observed fluorescence signal decreased over time when the fibre was filled. Further investigations demonstrated that in addition to the Qdot signal decreasing while filling, the signal when filling with only decane also decreased. Initially it was assumed that this could be due to a decrease in power in the fibre caused by increased loss or scattering, however the transmitted power through the fibre remained almost constant (after realignment) before and after filling.

The next consideration was how filling the fibre would change the recapture of the fluorescent light. Crudely, one can look at the numerical aperture (NA) of the fibre, given by $NA = \sqrt{n_1^2 - n_2^2}$ [139] where n_1 is the refractive index of the core and n_2 is the refractive index of the cladding. In the case of an F2 wagon wheel (n=1.62) filled with decane (n=1.41) the numerical aperture shifts from 1.27 before filling to 0.798 after filling. This reduction in NA will reduce the captured fluorescence power since the collection angle of the fibre has been

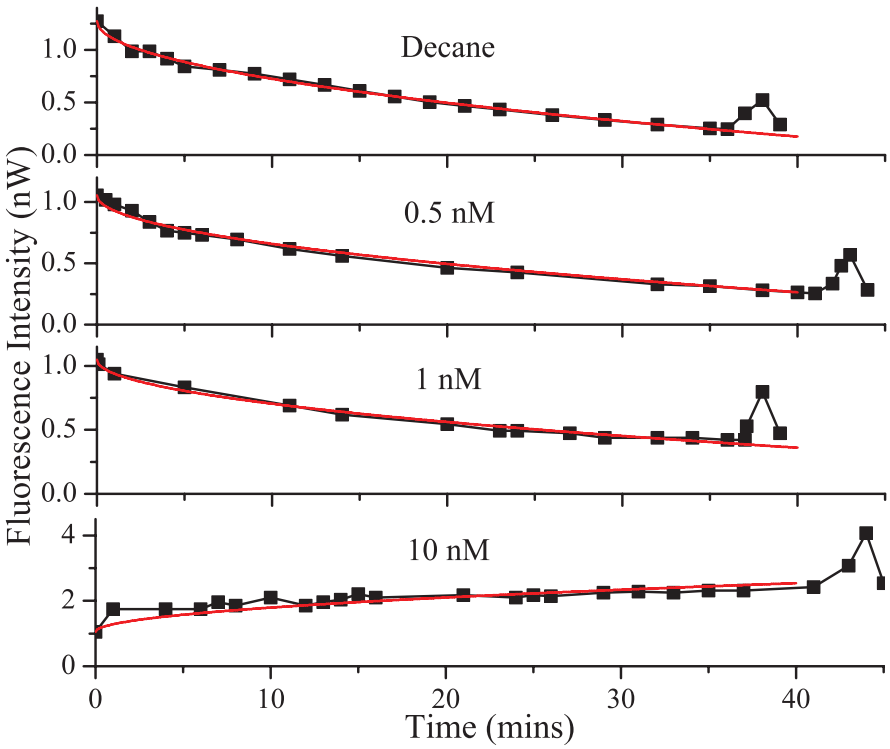

Figure 37: Photodiode measurements for varied Qdot concentrations with an initial fibre output power of approximately 230 µW through 30 cm ± 1 cm of wagon-wheel fibre. The black squares show the measured data, with the red lines showing a power fit to the obtained data.

reduced, however this does not explain the magnitude of the results observed here. This will be examined quantitatively in Section 2.11, using a fluorescence capture fraction model developed by Ref. [102].

In addition to the change in NA upon filling one expects the portion of light guided within the core of the fibre to decrease as the index contrast between the core and cladding decreases. This, combined with the change in the fluorescence capture efficiency is the cause of the reduction in fluorescence intensity from the decane sample. This will be examined theoretically in Section 2.11.

To further analyse the results, lines were fitted to the obtained data. It was observed that the fluorescence power jumped significantly when the fibre was completely filled. This was attributed to scattering or increased fluorescence from the input end of the fibre rather than from the sample vial that it was being filled from, as the fluorescence intensity did not change if the fibre was removed from the fluid during filling. However once the fibre was completely filled (where the intensity suddenly jumps at the end of the plots) if the fibre was removed from the liquid the fluorescence signal dropped to approximately that before the fibre completed filling.

Using the microscope it was observed that when the fibre is filled, the liquid reaches the very end of the fibre, however when the fibre is removed from the liquid the meniscus retreats from the end of the fibre. Although this distance is relatively short compared to the fibre length so it doesn't have a large effect on the actual amount of fluorescence generated. The liquid is observed to move back 1-2 mm over the course of 2 minutes, so for a 200 mm fibre this only changes the filled length by 1-2%.

So since the amount of fluorescence generated is not changing significantly, and since the captured fluorescence must also not change significantly this change in fluorescence intensity must be caused by the capture of the light emitted from the fibre into the spectrometer. The aperture of the lens used for excitation/capture of the fluorescent light has a NA of 0.55, so any light that is emitted from the fibre outside of this "cone" is not captured by the lens and thus is not recorded on the detector.

Consider a fluorescent mode propagating down the fibre in the backwards direction. When the fibre is completely filled (fibre still in the solution) the mode propagates to the end of the fibre, where it exits the glass with an NA of 0.798. When the fibre is removed from the liquid and the meniscus drops back there is a mode mismatch at this interface, so not all of the light from the guided mode in the liquid filled region will transfer to the mode in the air filled region. So some light will be lost to radiation modes. Finally, once this guided mode reaches the tip of the fibre it finds that the refractive index contrast is higher than for the liquid filled case, and as such the NA

is higher. As previously mentioned, the NA of the lens is only 0.55 so some of this light will be lost.

So since this large jump in fluorescence signal seemed to be caused by the NA of the fluorescence light as it exits the fibre and the mode mismatch at the air:water interface, it was decided to remove these points from the fit such that the fit was only dependent on the length of the fibre filled. All points are still shown in Figure 38, but the line of best fit is only applied to data points before this large jump in observed signal. Since this increase in signal is caused by the collection of light from the fibre and not from the actual fluorescence capture in the fibre the fits were made to data before the fibre was completely filled.

Consider only the decane-filled case. Since the lengths of fibre used in this section are relatively short, only approximately 30 cm the loss of the fibre is negligible for these measurements. As noted earlier in Section 2.5.2 the filled length l is proportional to the square root of the time. The initial fluorescence intensity A in the filled length of fibre is decreased by a factor which we define as B. So the fluorescence intensity F_{glass} from a fibre filling over time t can be described by Equation 2.3.

$$F_{glass} = A - B\sqrt{t} \tag{2.3}$$

Now consider the case of a fibre filling with a Qdot solution, with a concentration high enough that the fluorescence signal is significantly higher than that of the background glass signal, yet still low enough to not induce additional loss to the fibre. Here we assume the initial fluorescence intensity is zero, since the Qdot signal is taken to be much larger than the background. Again the filled length is proportional to $\sqrt{t}$. If we take the fluorescence intensity per unit length to be C we obtain a similar equation to that for the glass fluorescence, and is shown in Equation 2.4.

$$F_{Qdot} = C\sqrt{t} \tag{2.4}$$

If the Qdot signal is of a similar or lower intensity than the background glass signal both of these effects need to be considered, such that the total fluorescence intensity can be represented by Equation 2.5.

$$F_{total} = F_{Qdot} + F_{glass} = A + (C - B) \cdot \sqrt{t} \tag{2.5}$$

Using these equations, fits were created for each of the data sets as shown in Figure 37.

To obtain the signal arising from the Qdots the decane background signal was subtracted from the total signal. Due to the relatively high

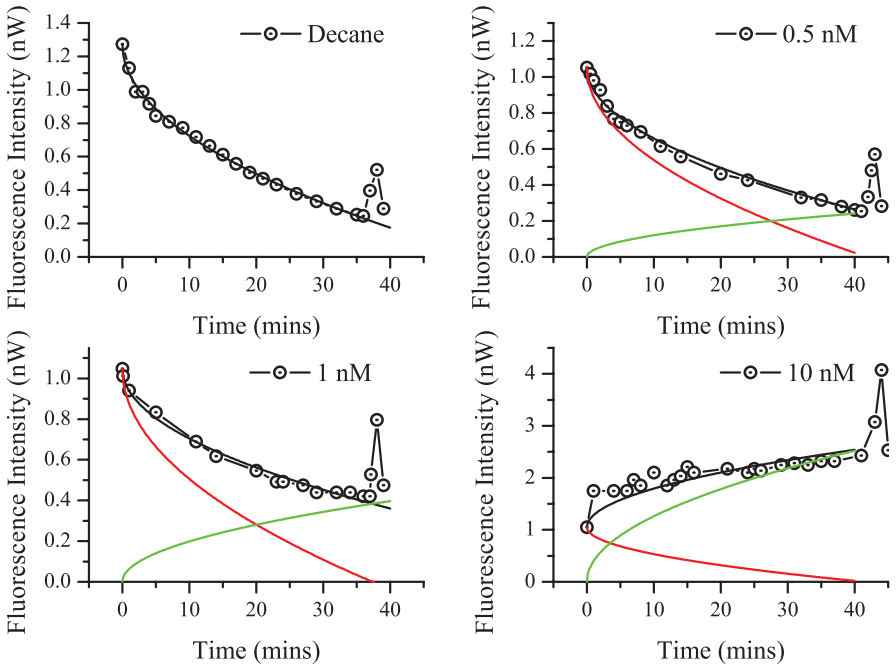

Figure 38: Time resolved data. Black circles are the original data, black line shows the power fit to the total data (F_{total}), red is the scaled fit to the background decane signal (F_{glass}), green is the subtracted signal representing only the fluorescence arising from the Qdots themselves (F_{Qdot}).

variability in the points, the subtraction was performed on the fits rather than the actual data. The decane signal was scaled to the initial intensity recorded in each of the data sets, and stretched slightly such that the filling times of the decane and Qdots were matched. The variation in filling time is due to slight variations in the diameter of the fibre along the length, as well as measurement uncertainty when the data was recorded. These fits are shown in Figure 38.

These results demonstrate that it is possible to observe signals as low as 500 pM using this method. A 200 pM sample was trialled using the same method, however was not distinguishable from the background signal within the error margin.

The reason this detection limit is slightly higher than the previous section is attributed to the ability of the OSA to visually discriminate between the Qdot signal and the background signal, by observing both the peak location and the shape of the fluorescence signal.

2.7.3 *Monitoring the excitation power*

To create an effective dip sensor only one end of the fibre can be used for coupling and collection, and the other end needs to remain free to be dipped in the desired solution. Previous results in earlier sections demonstrated this practice, however only the time-resolved

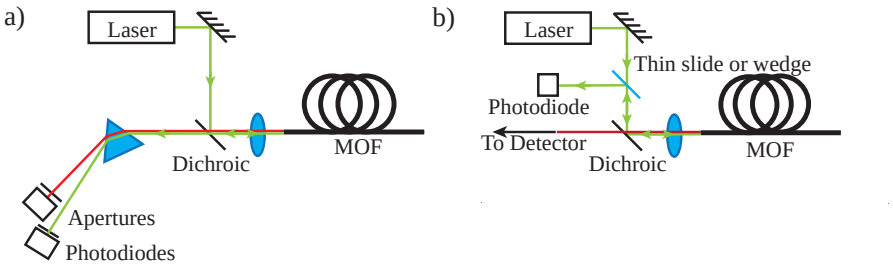

Figure 39: Methods for monitoring transmitted power through fibre using only the input end of the fibre a) Direct system using residual pump light passed through the dichroic filter after its reflection from the core of the fibre. The prism is used to split the signal (red) and pump (green) so that they can be monitored independently without interference with each other b) Insertion of thin glass slide or wedge into the beam path. The pump light is reflected off of the core of the fibre, and the majority of this is reflected upwards from the dichroic. The use of an element to split a portion of this light off enables the power to be monitored.

measurements enabled alignment in addition to the collection to be performed with a single end of the fibre.

For these results it was demonstrated that the fluorescence signal could be optimised and monitored without the use of a power meter on the distal end of the fibre. The results discussed in Section 2.7 utilised the fluorescence signal itself, and a high gain photodiode. However, for a system using an organic fluorophore this would be problematic, since the response rate of the detector is slow, and as such aligning the system takes a considerable length of time.

Alternatively the residual laser signal itself can be monitored. The general theory of this is that when the pump is incident on the tip of the fibre a small amount of the pump is returned along its direction of propagation from the Fresnel reflection of the core. When the laser spots drifts from its optimum position on the core the amount of reflected light decreases which is then recorded by the photodiode.

This would not be feasible for a conventional fibre, since the solid glass end means that the difference in reflection between the core and cladding is negligible due to the small ($\approx$ 0.35%) [89] difference in refractive indices in an SMF fibre. At 532 nm , the refractive indices of the core and cladding respectively are approximately 1.4658 and 1.4607, giving a difference in the Fresnel reflection from the surface of only 0.063% [139] (3.50% from cladding, 3.56% from the core). Even for relatively high NA solid core fibres with fluorine doped cladding the refractive index contrast is only in the order of 0.6% [140] so again this method could not be used with any great precision.

However with a wagon-wheel fibre the cladding is air, thus the power can be monitored by observing the amount of reflected light.

This signal is at a maximum when the coupling is optimised, and reduces rapidly when the core is removed from the optimum position.

If the dichroic mirror has a relatively low attenuation of the pump signal (i.e. OD3-OD4) a direct method can be used, where a prism is used to separate the pump and signal fluorescence. Rather than directing the pump light into a beam dump, it can be monitored using a photodiode. Alternatively, the pump signal can be split off using a wedge before the beam reaches the dichroic mirror. Both of these methods are shown above in Figure 39.

The direct method has the advantage that it does not introduce additional optics into the experimental configuration, thus improving both the stability and simplicity of the system. The latter gives a larger signal to monitor, since it is less attenuated when using the wedge than it is after passing through the dichroic mirror.

An example of the method passed through the dichroic mirror is shown in Figure 40. To determine how effective this method is in monitoring the actual power through the fibre, an additional photodiode was used on the distal end of the fibre to observe the transmitted power. For this trial the alignment into the fibre was optimised using the detector in the backwards direction. The power in both the forward and backward directions was monitored using separate photodetectors. Logging was started simultaneously, and the power coupled into the fibre slowly varied by adjusting the position of the translation stage. It should be noted at this point that this method was simplified here by the poor quality of the dichroic mirror providing only approximately OD3 attenuation at the laser wavelength, such that enough power was transmitted through the mirror that it could be monitored using a power meter. This method has also been demonstrated using a higher grade (OD4-6) dichroic mirror, however successful detection required the high-gain photodiode used in Section 2.7 which limits the response time of this method.

As shown in Figure 40, both the forward and backward direction show a good correlation between their detected powers, strongly suggesting that this method can be used for monitoring the power during measurements. Additionally, at the completion of the trial the coupling into the fibre was optimised using the forward direction detector which showed that the maximum obtainable power was only approximately 5% higher than was initially obtained using the backward detector. This shows that the power transmitted through the fibre can both be aligned and monitored without needing to perform measurements at the output end of the fibre.

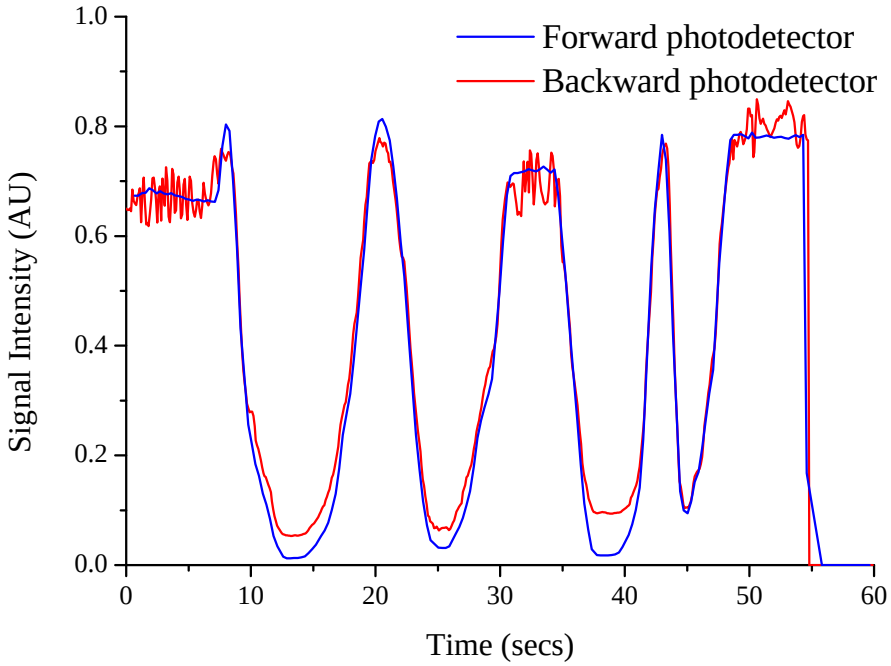

Figure 40: Trial result monitoring both the forward and backward power levels. The coupling into the wagon-wheel fibre was slowly varied, and the power from each end of the fibre monitored simultaneously using separate photodetectors.

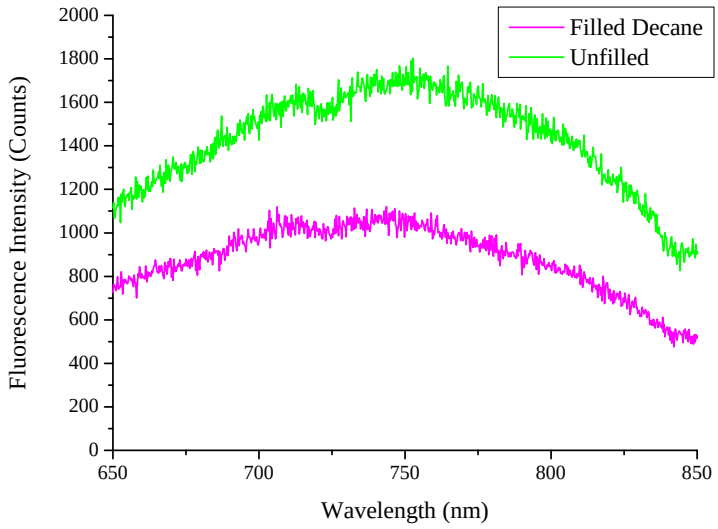

Figure 41: Background fluorescence signal for an F2 wagon wheel fibre before and after filling with decane.

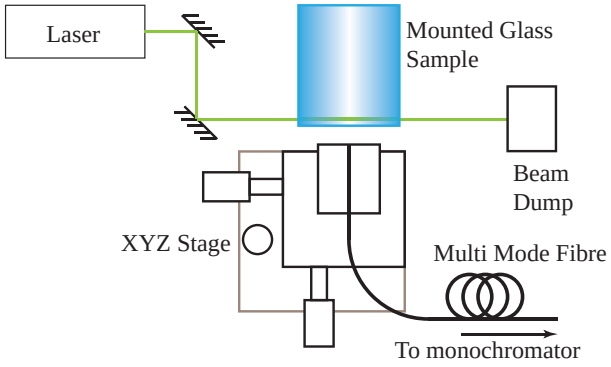

Figure 42: Experimental configuration for bulk glass fluorescence measurements. Three separate lasers wavelengths were used - Argon Ion 458 nm, Argon Ion 477 nm, Diode-pumped solid state 532 nm.

2.8 GLASS FLUORESCENCE

2.8.1 *At 532 nm*

The results obtained in Sections 1.2.1 and 2.7 clearly show that the primary limitation to the sensitivity of a fibre-based fluorescence system is the background fluorescence from the glass, as Section 2.7 showed that this signal still occurred even before the fibre was filled. Figure 41 further supports this, again showing that with a spectrally resolved measurement the signal observed after filling is a effectively the same as before filling, just reduced in intensity. As such, to optimise the sensitivity of a system such as this it is desirable to characterise this background glass fluorescence, and see how it compares between the different glasses available for extrusion.

To measure the glass background fluorescence spectra, a 25 mW 532 nm laser source was used to illuminate a range of bulk glass samples, and the fluorescence captured using a multi-mode fiber and recorded using an iHR 320 monochromator with the pump blocked with a long-pass filter.

Various glasses were examined to test their suitability as a material for fabricating sensing fibres. The initial requirement was simply that the glass could be extruded, with the possibility of fabricating microstructured fibres. As such the glass choice was restricted to soft glasses that can currently be fabricated into optical fibres through extrusion at temperatures less than 650°C, so that suspended-core fibres could be fabricated via the use of extruded preforms. These included lead-silicates previously used for wagon-wheel fibres such as F2, LLF1, SF57 or tellurite glasses in addition to a number of alternative glasses.

The results shown in Figure 43 show that the glass used for the Qdot measurements in Sections 2.6 & 2.7, F2, displays a relatively low fluorescence compared to many of the other soft-glasses that are

Glass	Supplier	Description	n	Loss
Borofloat	Schott	Borosilicate [141]	1.47	
F2	Schott	Lead Silicate [1]	1.62	~0.34
F2HT	Schott	Lead Silicate [1]	1.62	~0.34
LLF1	Schott	Lead Silicate [1]	1.51	0.51
N-FK5	Schott	[1]	1.49	1.02
N-FK51A	Schott	Fluoroborosilicate [1]	1.49	0.51
SF57	Schott	Lead Silicate [1]	1.84	1.02
SF6	Schott	Lead Silicate [1]	1.81	0.69
Tellurite	In-house	5Na 20Zn 75Te [72]	2	
Tellurite (La)	In-house	Lanthanum doped [75]	2	
ZBLAN	In-house	Fluoride [72, 76]	1.5	

Table 2: Glasses for fluorescence measurements. Both the refractive index and loss are given at 546 nm. The loss is given in dB/m, and is converted from the manufacturer's loss data for a 25 mm sample.

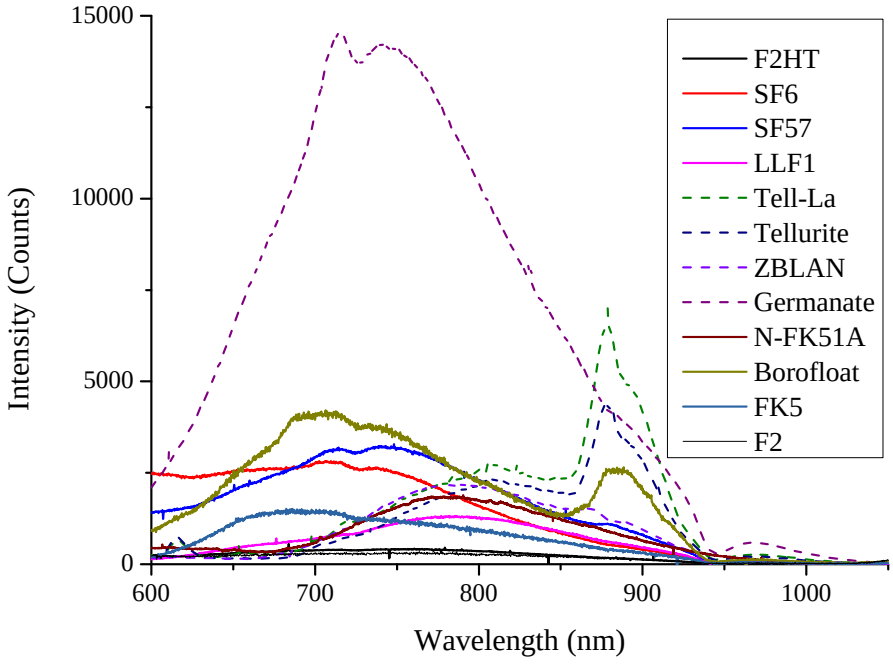

Figure 43: Glass fluorescence spectra for all glasses in Table 2 using 532 nm excitation.

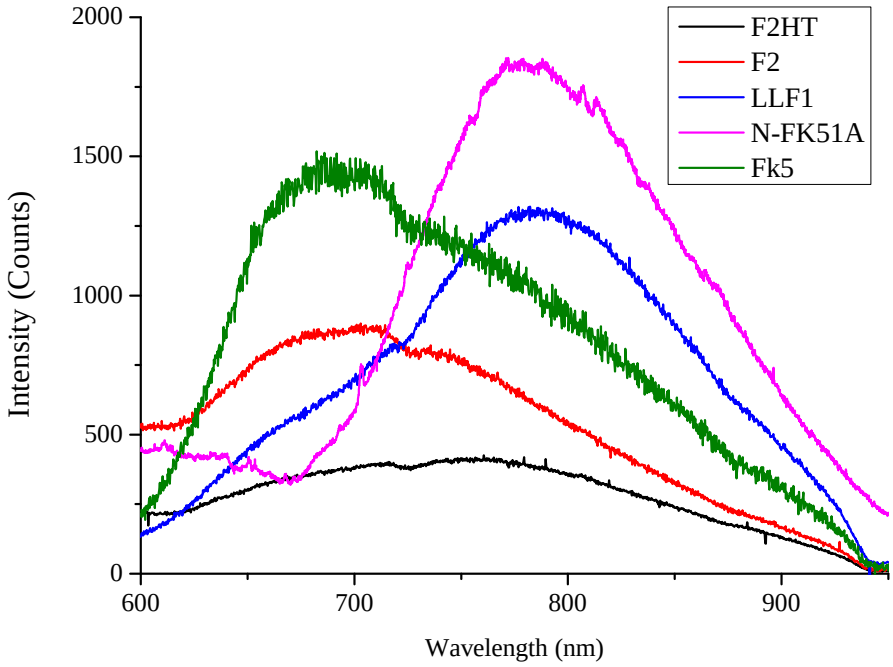

Figure 44: Soft glass samples showing the lowest bulk fluorescence signal with 532 nm excitation.

suitable for extrusion. The only glass showing a lower fluorescence than F2 at 800 nm is F2HT. This is a glass which is compositionally identical to F2, but with lower impurities and an improved UV transmission [1]. This reduction in fluorescence is shown in more detail in Figure 44.

These measurements have demonstrated that the intrinsic glass fluorescence that was the main limitation to the sensitivity in Sections 2.6 & 2.7 can be reduced in magnitude by changing from the F2 glass used for those measurements, to F2HT glass. Simply changing the glass should result in a further 30% reduction in the observed glass fluorescence at 790 nm.

2.8.2 *Varying the excitation wavelength*

To further characterise the fluorescence from the glass, the same glass samples were analysed using an argon-ion laser for excitation. This enables the excitation wavelength to be varied between 457 nm and 514 nm. This is important as the Qdot fluorescence increases with decreasing wavelength (see Figure 32) so if the glass fluorescence reduces or even remains constant as the wavelength decreases this could correlate to an increase in sensitivity.

It should be noted that these results are not directly comparable to the 532 nm data set shown above, since the alignment and collection fibres were changed between these measurements. The experimental configuration used was similar to that used in the previous section,

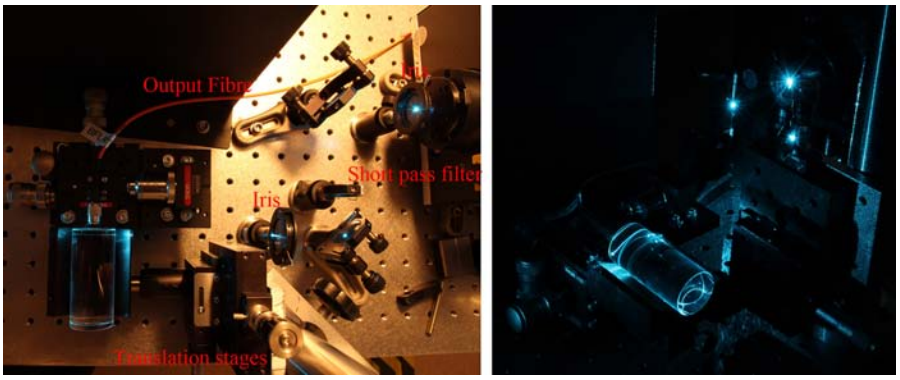

Figure 45: Experimental setup for glass fluorescence measurements using argon-ion laser.

however to improve the sample throughput the glass samples were mounted on translation stages to enable fine adjustment of the sample positions.

The experimental setup is shown in Figure 45. A short pass filter was used to block any longer wavelength light from the argon ion laser to prevent contamination of the measurements.

These results show that the fluorescence signal is always present when the wavelength range is varied from the green to the blue, however the intensity of the emission changes drastically with changing wavelength. The typical behaviour shows that the emission intensity increases with decreasing wavelength. The fluorescence spectra are visibly similar for the same glass with varied wavelength, suggesting that the absorption features causing these emissions are broad.

The sample showing the lowest emission at each of the three wavelengths (F2HT) was then examined in more detail, with the results shown in Figure 49a. All lines of the argon ion showing a minimum power of at least 8.5 mW were used for these trials. The experimental method was the same as previously used. Figure 49a shows the peak fluorescence intensity at 790 nm (the approximate peak of the Qdot emission) plotted against the wavelength of the excitation source used. The power for each of these trials was 8.5 $\pm$0.1 mW.

These results demonstrate that although the spectral shape of the fluorescence signal remains relatively constant, the magnitude of the fluorescence increases significantly with decreasing wavelength. For example, at the peak of the fluorescence emission F2HT shows approximately 1200 counts when excited with 9 mW of 472 nm light, and when excited with the same intensity of 458 nm light the fluorescence signal doubles to approximately 2400 counts. This demonstrates that although the absorption coefficient of the Qdots increases from approximately 3,400,000 cm^{-1} at 472 nm to 4,750,000 cm^{-1} at 458 nm the gain in Qdot signal fluorescence would be more than countered by the increase in background glass fluorescence. Here we define a figure of merit (FOM) as $FOM = \frac{Qdot_{absorption}}{GlassFluor}$. GlassFluor is

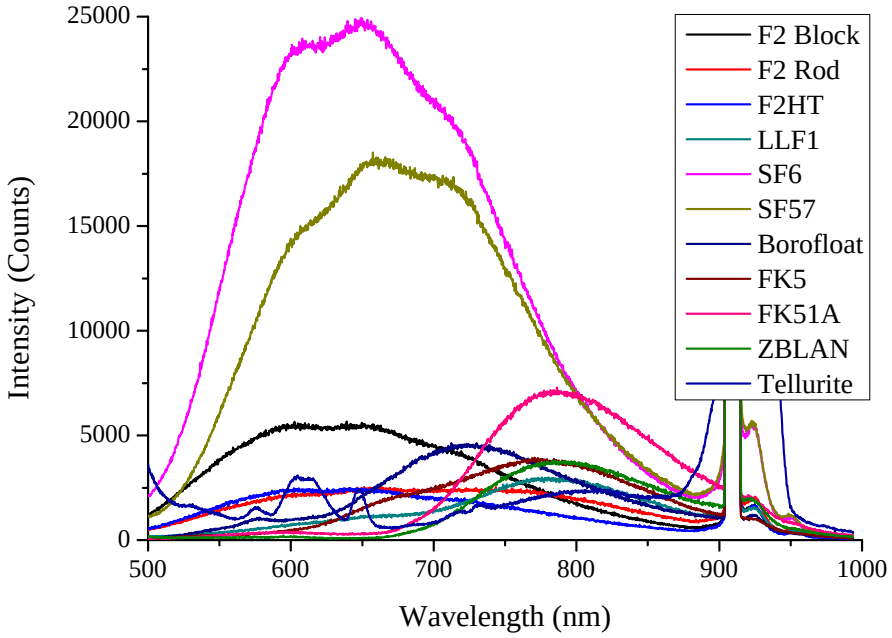

Figure 46: Bulk glass fluorescence spectra using argon ion laser, excitation power 8.5 mW. 458 nm excitation.

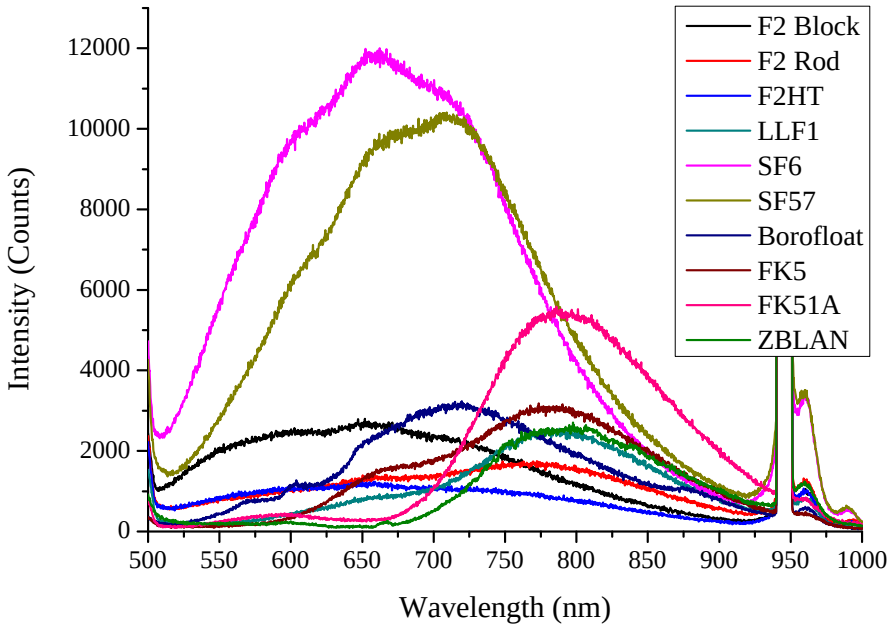

Figure 47: Bulk glass fluorescence spectra using argon ion laser, excitation power 8.5 mW. 477 nm excitation.

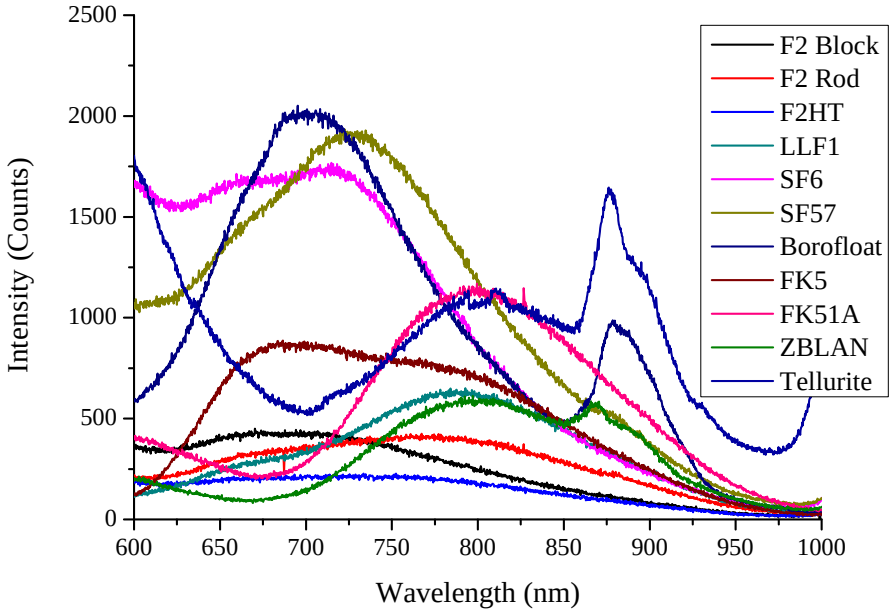

Figure 48: Bulk glass fluorescence spectra using argon ion laser, excitation power 8.5 mW. 514 nm excitation.

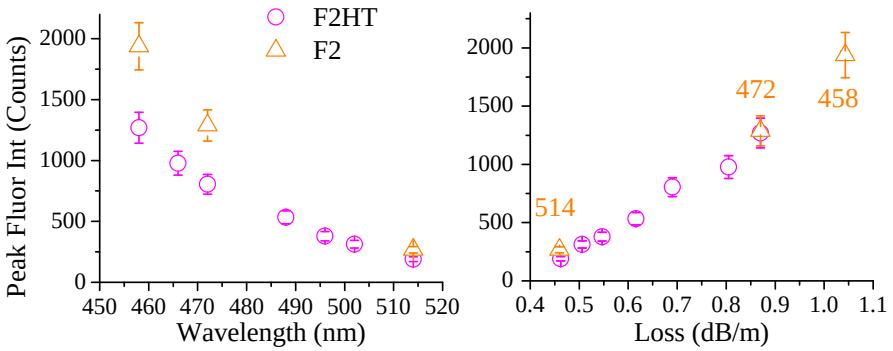

Figure 49: a) Peak fluorescence intensity at 790 nm vs excitation line for F2HT and F2 b) Peak fluorescence intensity at 790 vs approximate bulk glass loss for each of the excitation lines used in a). The error bars are set to encompass both the variability in the excitation power itself, as well as variations in maximising the fluorescence intensity from the samples. The loss is interpolated from the bulk glass loss given from the Schott catalogue [1]. The three F2 loss values are labelled with their corresponding wavelengths in orange, the values for F2HT can be read from a) reading from right to left.

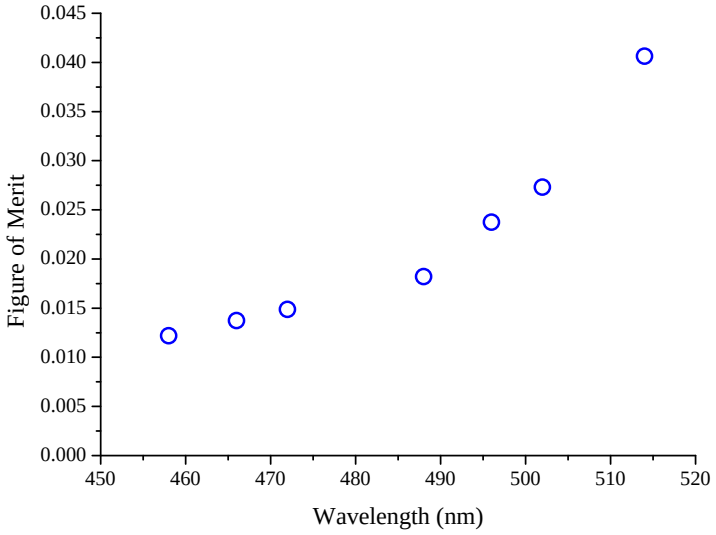

Figure 50: Figure of merit for the absorption coefficient of Qdot 800 at a given wavelength compared to the corresponding glass fluorescence from F2HT.

taken to be the intensity of the glass fluorescence emission at 790 nm in F2Ht glass. This figure of merit is plotted for various wavelengths in Figure 50.

It can be seen from this plot that the general trend is that the FOM increases with wavelength, clearly demonstrating that the increase in the fluorescence generated by the increased absorption from the Qdots is more than compensated for by the increase in the intrinsic glass fluorescence.

As such the decision was made to move to a 532 nm source, which should increase the Qdot signal relative to the glass fluorescence, as well as significantly increasing the stability of the alignment arising from the improved pointing stability of the source.

Interestingly, it was noted that the glass fluorescence intensity vs wavelength plot displayed a trend which was similar in shape to that of the bulk glass loss. The loss of the F2HT glass and F2 samples was interpolated from the bulk glass loss given in the Schott catalogue [1], and plotted against the peak wavelength in Figure 49b. As can clearly be seen the F2 glass fits the same trend as the F2 glass, even though Figure 49a shows significant variation in the peak fluorescence at a given wavelength. However when this wavelength is converted to its corresponding loss a trend emerges.

As was mentioned earlier the composition of the F2HT glass is identical to that of the standard F2 glass, with the primary difference being improved blue transmission arising from lower impurities within the glass. These impurities could include such ions as Chromium [142], Iron, Zinc or Vanadium [143–145].

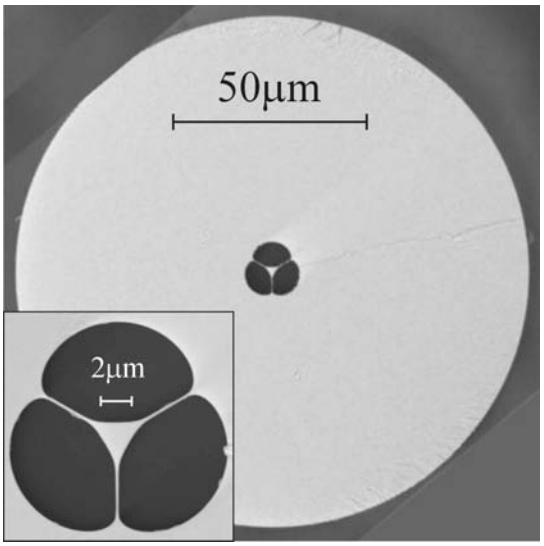

Figure 51: Scanning Electron Microscope (SEM) image of the soft glass MOF used for these experiments. The central, structured region of the fiber was made from F2HT glass, and the cladding from F2 glass.

Thus the results in Figure 49b strongly suggest that these impurities that increase the loss at shorter wavelengths are also the source of the increased glass fluorescence of the F2 glass compared to F2HT.

2.9 F2HT FIBRE CHARACTERISATION

Following the bulk glass results described above a new wagon-wheel fibre was fabricated from F2HT glass specifically to reduce the background fluorescence from the fibre. The fibre was made following the same cane-in-tube technique described earlier. Only the internal cane of the fibre was fabricated from F2HT glass due to its limited supply and increased cost compared to the standard F2 glass. The outer tube was fabricated from F2 which as mentioned earlier is essentially identical to F2HT apart from impurities. The primary difference between the two glasses is reduced impurities in the F2HT glass, leading to lower absorption at shorter wavelengths in addition to the reduced glass fluorescence shown in Figure 43.

The final fibre possessed a core size of 1.6 µm, and an outer diameter of 130 µm. This outer diameter was chosen such to make splicing to conventional silica fibres with an outer diameter of 125 µm simpler than would be the case using the diameters of 160 µm or 200 µm.

The loss of the fibre was recorded using a bulb and OSA, and is shown in Figure 52 compared to a wagon-wheel fibre fabricated entirely from F2 glass. A bulb was used for these measurements in preference to a supercontinuum source due to instabilities in the power of the supercontinuum. Since the bulb gives a large spot size, the light

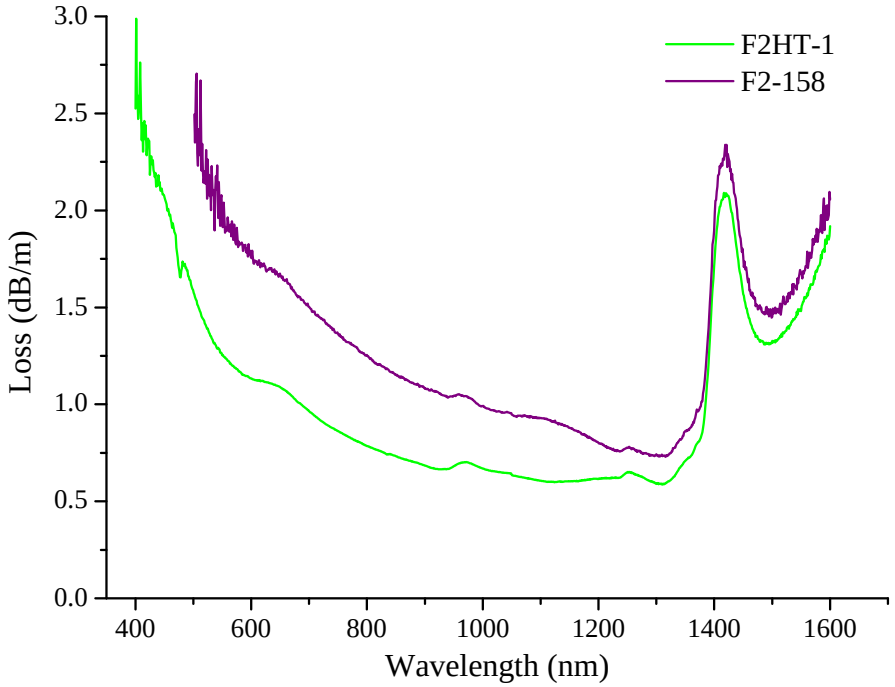

Figure 52: Loss spectra of F2HT wagon-wheel fibre (green) compared to standard F2 wagon-wheel fibre (purple). The high level noise in the F2 spectra is due to insufficient light at long fibre lengths, however the general trend of the loss of the fibre can still be observed. Points below 500 nm have been removed from this plot due to this excessive noise. The labels correspond to the draw numbers of the fibres.

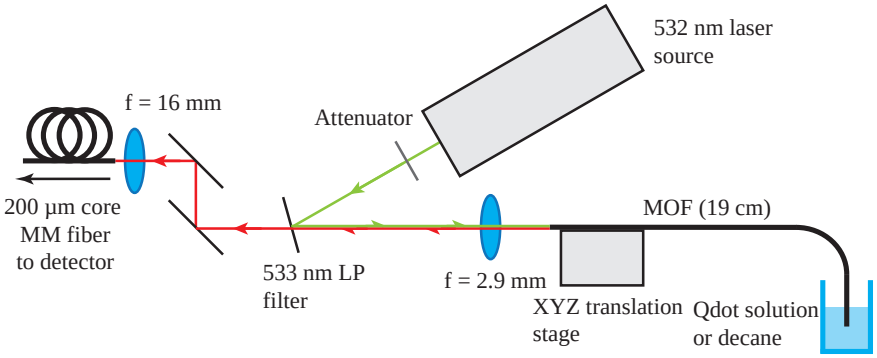

Figure 53: Modified experimental configuration using normal incidence filter and monochromator for detection.

could not be preferentially coupled into the core, and instead the majority of the light is coupled into the cladding of the fibre. To ensure that the recorded loss is that of the core of the fibre, and not that of the cladding this light is then stripped off using a coating of graphite.

2.10 LOW CONCENTRATION RESULTS

In addition to changing the fibre material to the lower-fluorescence F2HT glass, modifications were made to the experimental configuration to further improve the sensitivity and thus the minimum detectable concentrations of fluorophores.

As mentioned in Section 2.8.2 the excitation was changed to a 532 nm diode pumped solid state source. Although less power is available from this laser compared to the 514 nm argon ion line (25 mW vs 130 mW), it possesses an improved beam quality ($M^2 < 1.1$ vs 1.2) and better pointing stability (5 µrad/°C vs 30 µrad/°C) meaning that it should provide both more efficient and more stable coupling into the wagon wheel fibres.

As well as changing the source, the dichroic filter was also changed to a normal incidence raman filter, with approximately OD6 attenuation at 532 nm and 99% transmission at ≈533 nm. The improved characteristics of this dichroic make sensing with fluorophores whose emissions are close to that of the laser wavelength possible. The use of this filter required the geometry of the setup to change, since the light must be incident on the filter at 90° rather than the 45° required for the previous dichroic. As such the laser was moved such that the light was incident on the filter within 5° of normal, with only the minimum angle required to be able to couple in and out of the wagon-wheel fibre.

Finally, the detection method was changed from the optical spectrum analyser, to a Horiba iHR320 monochromator with a cooled CCD array detector. This change compared to the OSA results in both a drastically reduced signal to noise ratio, and a greatly im-

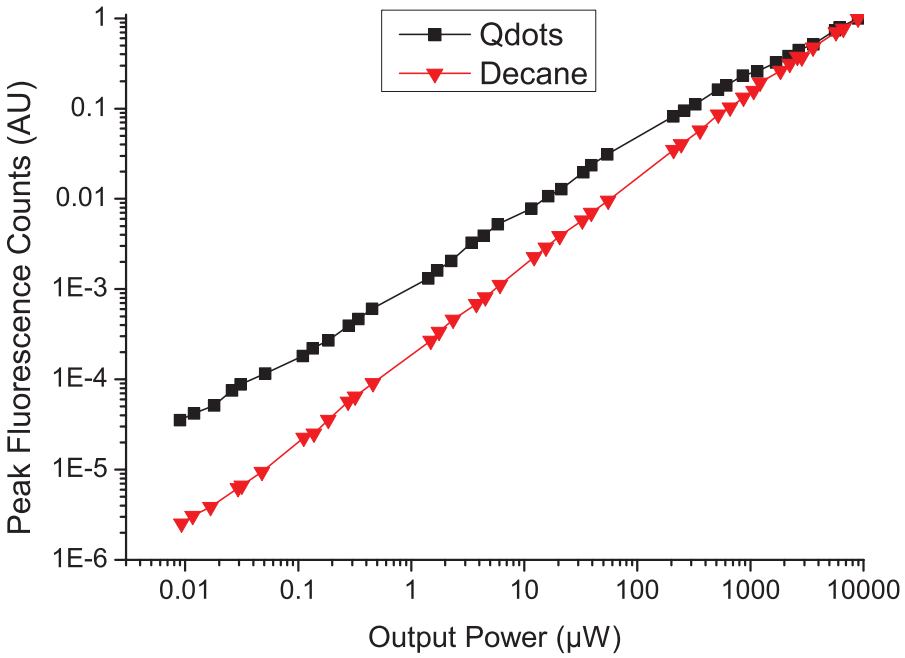

Figure 54: Peak fluorescence counts for Qdots (Black) and glass (red) in a 19 cm T190 F2 wagon-wheel fibre. 532 nm excitation, the power was varied using neutral density filters with a power meter to record the output power of the fibre. Note the logarithmic scale. Decane was used for comparison since this is the solvent the Qdots are suspended in. Filling the holes with decane rather than using an empty fibre ensures that the modal structure, power fraction and capture fraction are identical between the two samples.

proved scan time. The new detection method improves sensitivity by 3-4 orders of magnitude, while the scan times at high sensitivities are reduced from approximately 15 minutes to 1-20 seconds.

The fibre was aligned by optimising the output power. Minimising the path length of the laser ensured that the alignment stability of the light coupled into the fibre was good, with a maximum power reduction of 10% being recorded over a period of one hour.

Here we define the output power as the total pump power recorded from the distal end of the fibre. For reference the total coupling efficiency from the laser source to the core of the WW fibre is in the range 35–40%.

One aspect of the fluorescence sensing that was noted during the time resolved measurements is that the recorded Qdot fluorescence intensity is not linear with power as one might expect. This observation was again seen during the spectrally resolved results, and is shown in Figure 54. The reasons behind this behaviour are not known and were not explored in detail. It does not appear to be a saturation effect, as the slope is relatively constant across all recorded power levels.

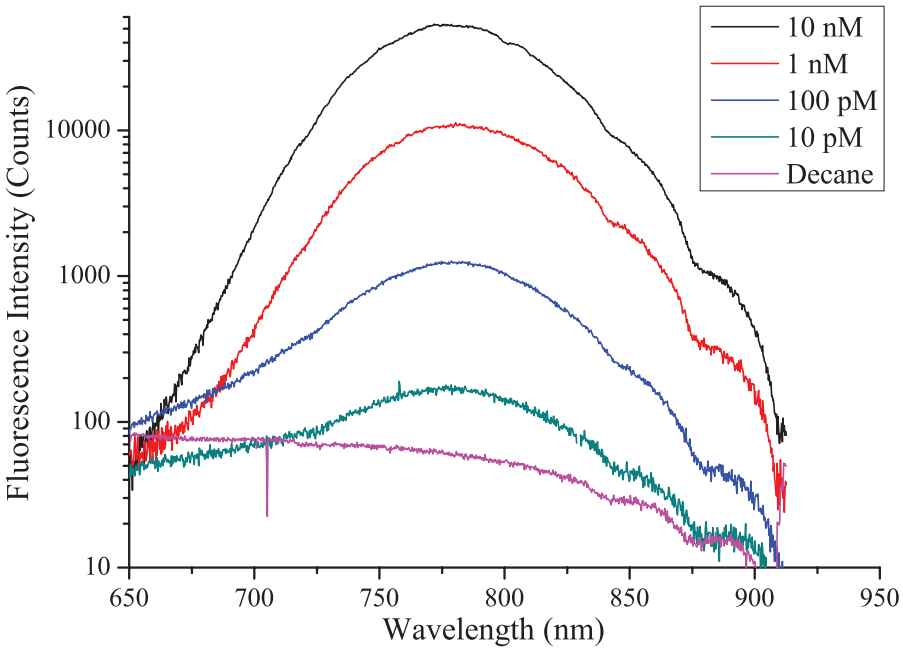

Figure 55: In-fibre fluorescence measurements with varied Qdot concentrations. As per previous results, a fibre filled with a plain decane solution was used to give a background reference signal (in this case the fluorescence comes from the glass itself).

The results in Figure 54 show that while the background glass fluorescence, as shown by the red symbols, increases almost linearly with the output power of the fibre. As might be expected, the Qdot signal is not linear with the output power (Note the logarithmic scale of the axes in Figure 54). As can be seen from Figure 54, as the power within the fibre increases, the Qdot signal decreases relative to the background glass fluorescence.

The main outcome from this result is that since the minimum detectable signal is governed by the ratio of the Qdot fluorescence to glass fluorescence, simply decreasing the power will increase this ratio. This is made possible primarily from the improvements to the detection method mentioned earlier, as the monochromator setup provides a greatly improved signal to noise ratio meaning that significantly lower laser powers can be used while maintaining a fluorescence signal above the noise level.

For the final set of measurements these improvements were put into place. The fibre was first aligned before filling. A test fibre was then filled with a relatively high concentration of Qdots, and the alignment into the monochromator adjusted using an XYZ translation stage on the input fibre. Once this optimal alignment position was found it remained fixed across all trials, as it was found that the coupling into the monochromator remained optimised when the sensing fibre was changed.

A new fibre section, cleaved using a mechanical cleaver to a length of 190 mm $\pm$ 1 mm, was used for each measurement. Before filling a spectra of the glass fluorescence was recorded to ensure consistency between samples. The fibre was aligned at a relatively high power (Input power $\approx$ 2.5 mW) with the typical output power from the wagon-wheel fibre in the range from 1-1.1 mW. If a fibre was not able to be aligned to this power level it was discarded, as the reduction in power is most likely due to a poor cleave or defects along the length of the fibre.

The filling method was also modified for these measurements, changing to a system in which the fibre could remain almost horizontal during the filling process. This limits the amount of movement required of the fibre, eliminating the possibility of moving the opposite end of the fibre (where the laser light is coupled) altering the coupling efficiency into the fibre.

The results of these measurements are shown in Figure 55. These results demonstrate that with a relatively high (compared to that shown in Figure 4) input power of 2.5 µW for all measurements, the minimum detectable Qdot signal using this configuration is 10 pM, which is a significant improvement over the 1 nM concentration previously reported in [61]. Assuming identical experimental paramaters, if this measurement were performed using antibody conjugated Qdots the minimum detectable antibody concentration would be approximately 30 pM according to the specifications from Invitrogen [118] which give a Qdot:antibody ratio of 1:3.

2.11 THEORETICAL MODELLING

To better understand the behaviour of the fluorescence signals observed from both the signal (Qdot) fluorescence and background (glass) fluorescence a theoretical model was employed. The aim of this was to be able to analyse the behaviour observed with the experimental results in the previous section, to determine if any further improvements in terms of the detection limit could be made when the theoretical model is expanded from the basic one considered in Section 2.2.

The model chosen was a step index analytical model (i.e. jacketed air-suspended rod) as opposed to a FEM primarily due to the greatly increased computational speed of the analytical model. The assumption here is that the strut and altered core shape from the actual non-circular geometry of an actual wagon-wheel fibre have minimal effects on the outcomes of the model.

$$PF = \frac{\int_{clad} S_z dA}{\int_{\infty} S_z dA} \tag{2.6}$$

The power fraction (PF) within the holes of the fibre is defined by Equation 2.6 [101], where "clad" represents integrating over the area outside of the core of the fibre. The same equation can likewise be evaluated for the power within the core by setting the top integral over the area of the core of the fibre. Both of these parameters with varied core size and glass type are shown in Figure 56. The PF represents the amount of fluorescence that is generated by the fluorophores within the fibre, and their emission is assumed to be directly proportional to the intensity of light in the cladding.

For the power fraction only the fundamental mode is considered, even though the fibre is capable of supporting higher order modes at moderately small core sizes. This decision was made since as mentioned earlier it was observed during experiments that by proper lens choice and careful alignment the laser light can be preferentially coupled into the fundamental mode of the fibre, showing little evidence of higher order modes of excitation light [103].

An example of this multi-mode fluorescence capture is shown in Figure 57. The left image shows the case where the fibre is filled with decane. This was chosen in preference to using an unfilled fibre to ensure that the modal structures of the laser source in the pump and emission images are identical. This image was obtained by filling a 1.7 µm core F2 wagon wheel fibre with decane, and carefully optimising the alignment into the fibre using an XYZ stage and power meter. The output from this fibre was then heavily attenuated and focussed on the CCD camera.

For the Qdot fluorescence image a similar method was used, except the fibre was filled with a 1 µM Qdot 800 in decane solution. A 560 nm long pass filter was then placed in front of the output of the fibre to ensure that any residual 532 nm pump was completely blocked. This was checked using an optical spectrum analyser, and demonstrated that the Qdot signal fluorescence was more than 1000 times larger than the residual green pump light. Again the fibre output was attenuated to avoid saturation of the detector, and then focussed on the CCD camera.

This result shows that the modal properties of the pump light and Qdot light is markedly different, even though the waveguide actually supports more modes at the shorter pump wavelength. At 532 nm Figure 57 shows the fibre is effectively single mode, while the mode from the captured fluorescence shows strong evidence of numerous higher order modes. From this result we make the reasonable assumption that the higher order modes can be ignored for the excitation of the fluorophore, however they clearly must be (and will be!) considered for the fluorescence recapture as they have a significant involvement in the way in which the fluorescence is captured within the fibre.

It has been shown in Ref [102] that for a uniform distribution of emitters with random orientation located in the area surrounding the

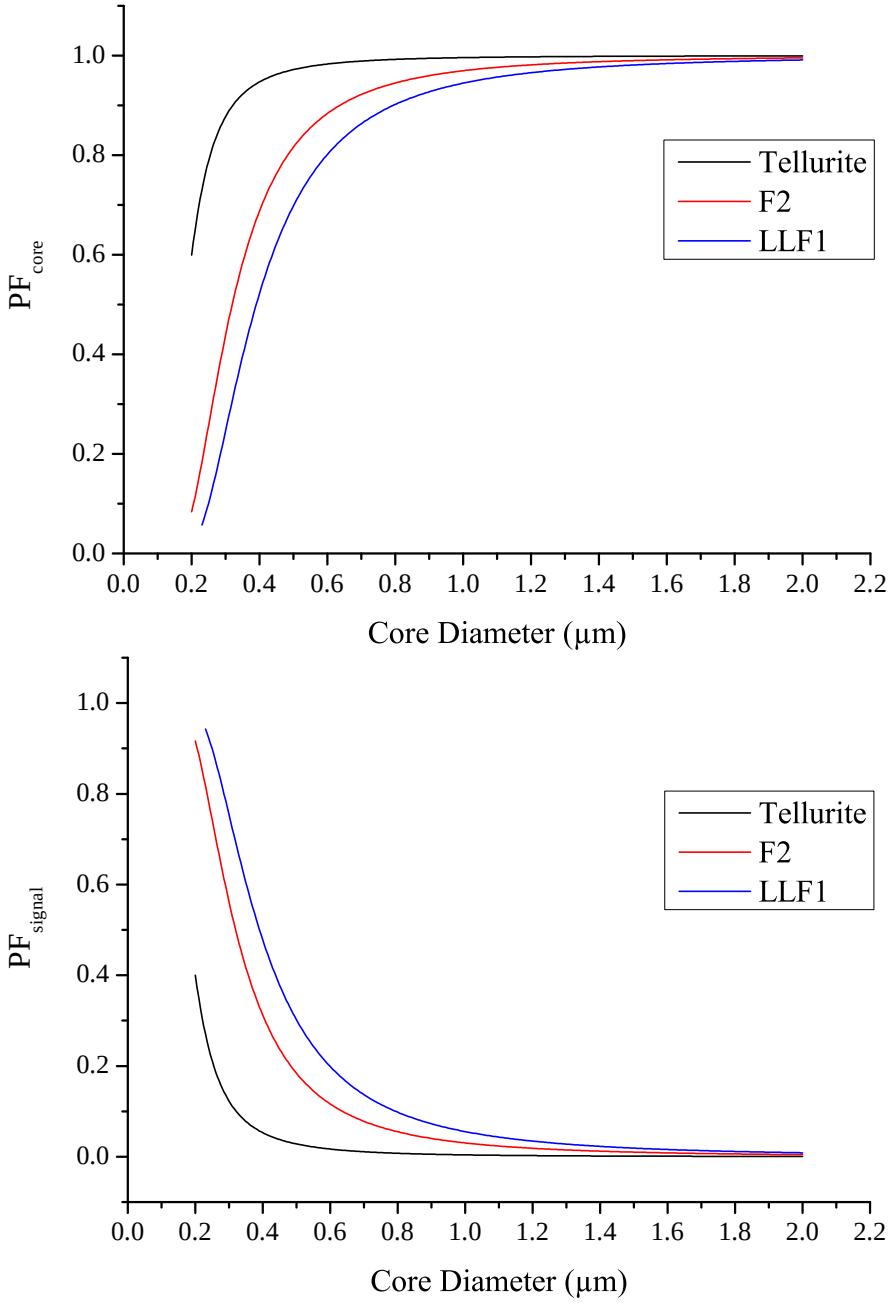

Figure 56: Power fraction in the core (top) and cladding (bottom) for tellurite, F2 and LLF1 glasses. Excitation wavelength is 532 nm, emission 790 nm. Cladding index is that of Decane (1.41).

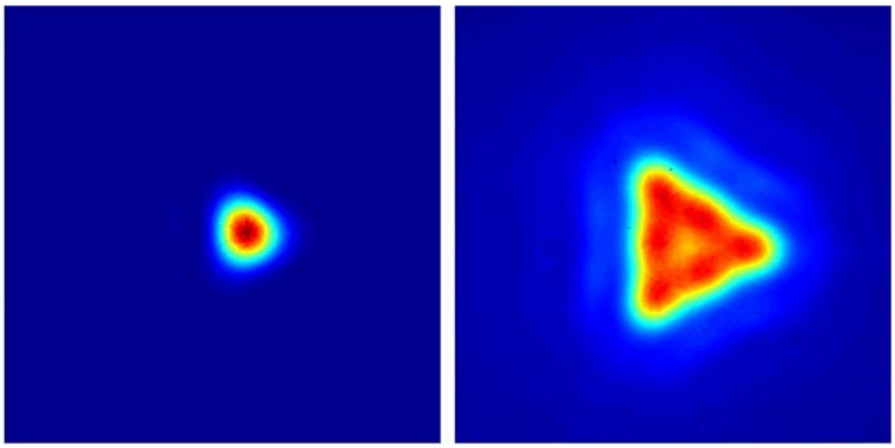

Figure 57: Experimentally measured far field mode images in 1.7 µm core size F2 wagon-wheel fibre. Left - excitation (532 nm) mode image. Right - Qdot fluorescence at approximately 790 nm. The distance between the fibre and CCD as well as the lens remained constant between measurements, and as such the scales between the two images are directly comparable.

core that the fluorescence capture into the modes v of a nanowire excited by mode j is given by Equation 2.7 [102]:

$$FCF_j = \frac{\xi\lambda^2}{16\pi n_F^{H2}} \sum_v \frac{NOI_{jv}}{A_{eff,v}} \frac{\gamma_j^H e^{-\gamma_v L}}{\gamma_v - \gamma_j} \left[e^{(\gamma_v - \gamma_j)L} - 1 \right] \tag{2.7}$$

$$NOI_{jv} = n_F^H \left(\frac{\epsilon_0}{\mu_0} \right)^{\frac{1}{2}} \left[\frac{\int_{A_\infty} s_v(\vec{r}) dA}{\int_H s_j(\vec{r}) dA} \right] \left[\frac{\int_H |e_v|^2 s_j(\vec{r}) dA}{\int_{A_\infty} |s_v(\vec{r})|^2 dA} \right]$$

$$A_{eff,v} = \frac{|\int_{A_\infty} s_v(\vec{r}) dA|^2}{\int_{A_\infty} |s_v(\vec{r})|^2 dA}$$

A similar expression can likewise be obtained for emitters located within the core of the fibre by altering the integration region. The results of simulations using different soft glasses with a varied core size are shown in Figure 58.

These results demonstrated a marked change from those obtained considering just the fundamental mode, as the *FCF* is seen to be relatively constant at core sizes beyond 500 nm for F2 glass. In contrast considering just the fundamental mode shows a clear peak at 500 nm then a steady decrease with increasing core size similar to the behaviour seen in Figure 31. From these results we can also observe that although the *FCF* for the Qdot signal fluorescence will increase with

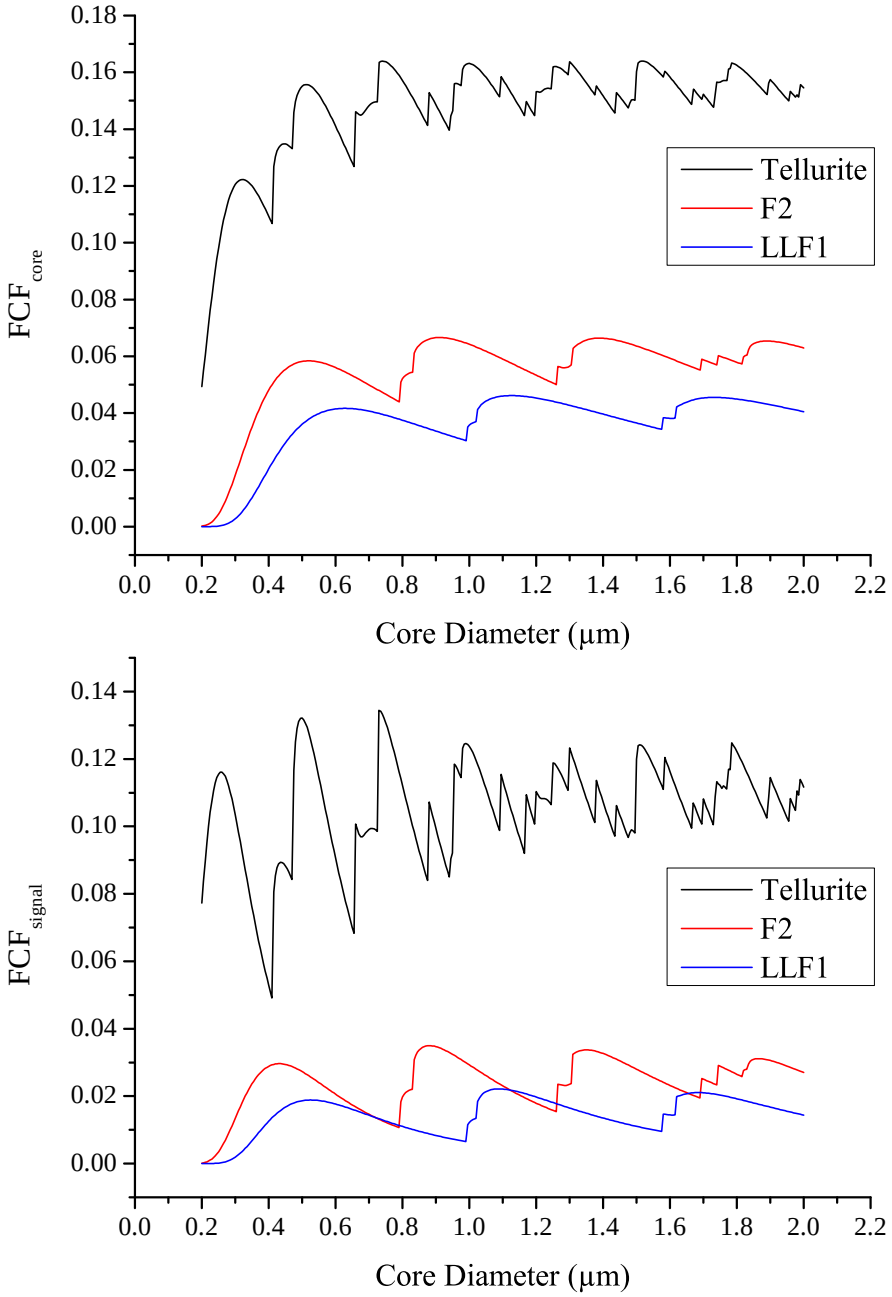

Figure 58: Fluorescence capture fraction (FCF) for fluorescence emitted within the cladding of the fibre (bottom) and core of the fibre (top) for tellurite, F2 and LLF1 glasses. Excitation wavelength is 532 nm, emission 790 nm. Again the cladding index is taken to be decane, making the assumption that the Qdot concentration is low and has minimal effect on the refractive index of the liquid.

higher refractive index glasses, the FCF for the glass fluorescence will also increase.

To better understand the practical signals that will be observed from the outputs of the fibre, we must consider more then just either of these parameters alone. It is logical that the observed fluorescence must be a function of the amount of fluorescence that is generated from the fluorophores. This is a product of the concentration of the fluorophore, its quantum efficiency and the amount of power available (PF) to excite the emission. Of these parameters only the PF needs to be considered here, since the other two are a property of the fluorophore and remain constant (ignoring surface effects) with varied core size and glass index.

We then define a figure of merit (FOM) that encompasses both the amount of fluorescence that is generated ($\propto PF$) and recaptured (FCF) into all guided modes as the product of these two, shown in Equation 2.8 for fluorescence generated within the core of the fibre. Again the same expression is obtained for fluorescence generated from the cladding, the Qdot signal fluorescence FOM_{signal}.

$$FOM_{core} = PF_{core} \times FCF_{core} \tag{2.8}$$

The results of simulations using different soft glasses with a varied core size are shown in Figure 59.

Interestingly the change in FOM_{core} with changing index contrast can be directly observed through measurements. When the fibre is filled with a decane solution the index contrast changes from 1.62 : 1 to 1.62 : 1.41. This change in refractive index contrast is similar to changing the glass itself. FOM_{core} for an unfilled 600 nm F2 fibre is approximately 0.16. When the cladding index is changed from 1 to 1.41 (corresponding to filling with decane) FOM_{core} drops to approximately 0.05. From this we would expect the observed glass fluorescence to decrease by almost 70%, since this FOM should be proportional to the amount of fluorescence that is observed. The decane itself generates no significant fluorescent signal so the only parameter being changed here is the refractive index contrast.

Observe Figure 38a, which corresponds to a fibre with decane. The core size of this fibre was approximately 0.6 µm, and it can be seen that the measured fluorescence decreases as the fibre is filled. This decrease in fluorescence is approximately 5-6×, which although larger than is expected from the theory is within the same order as predicted. The additional decrease in fluorescence could be partially explained by the model not considering confinement loss, or alternatively some drift in coupling or degradation of the fibre during the experiment.

Earlier results demonstrated that the main limitation to the total sensitivity of fluorescence based modal overlap sensing with soft glasses was the background fluorescence observed from the glass.

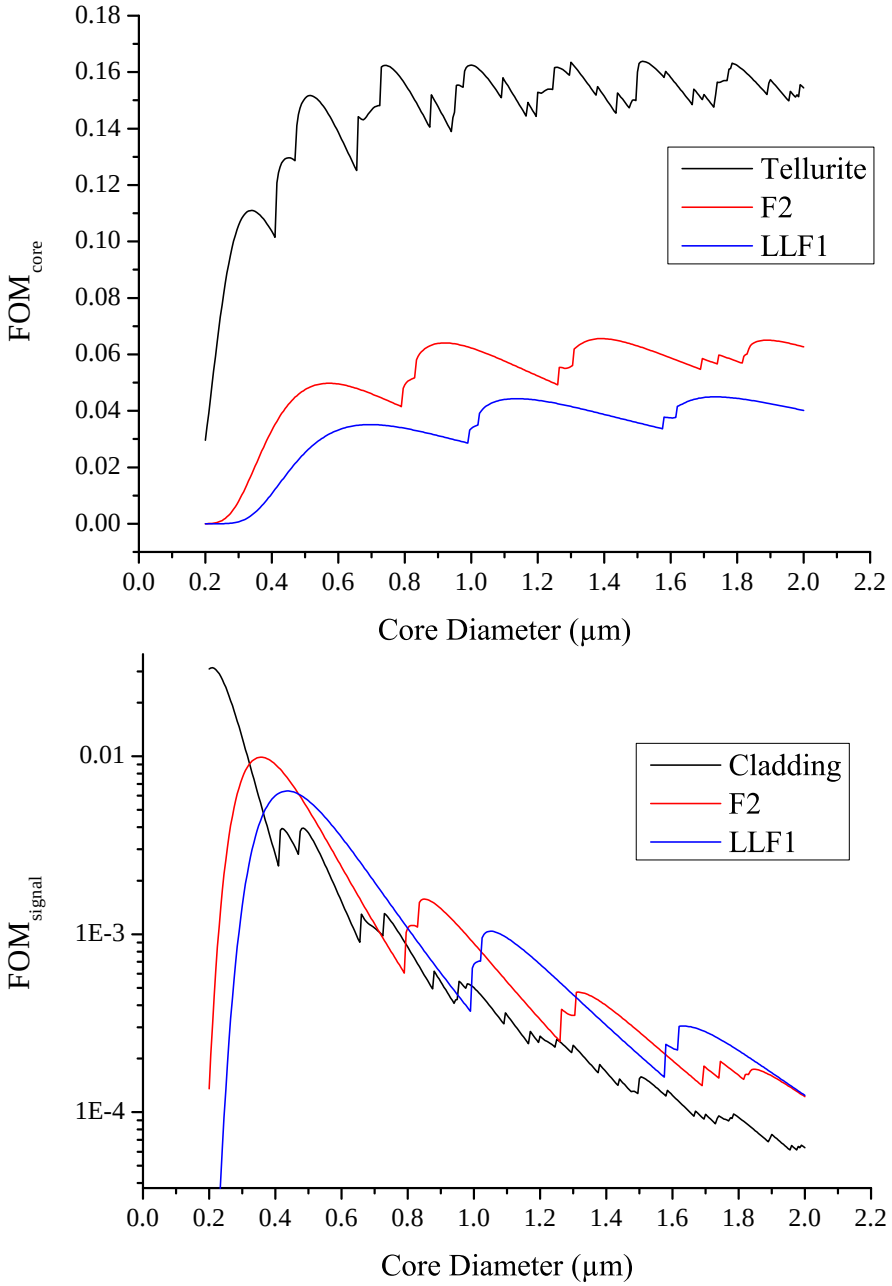

Figure 59: Figures of merit (Equation 2.8) for fluorescence emitted within the cladding of the fibre (bottom) and core of the fibre (top) for tellurite, F2 and LLF1 glasses. Excitation wavelength is 532 nm, emission 790 nm. Again the cladding index is taken to be decane, making the assumption that the Qdot concentration is low and has minimal effect on the refractive index of the liquid.

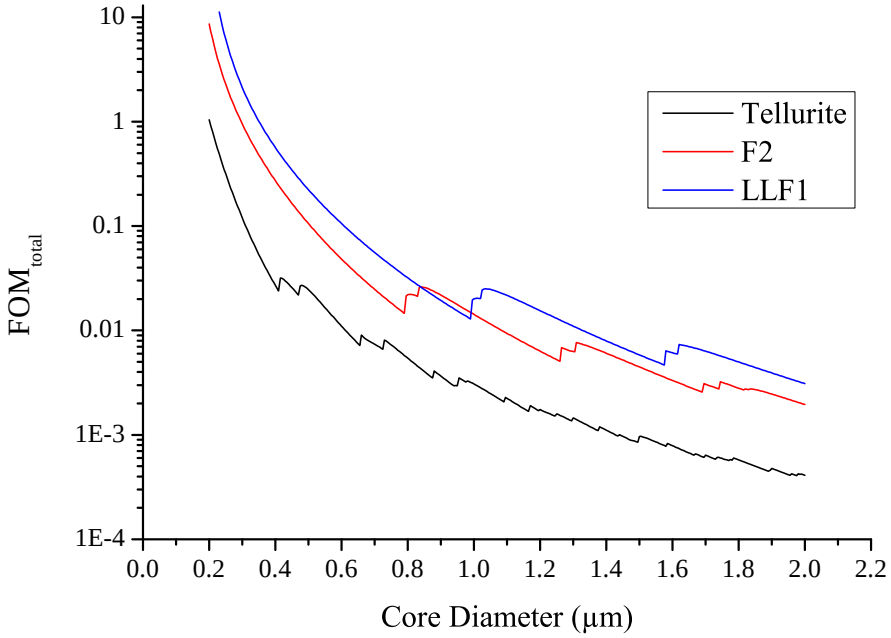

Figure 60: Figure of merit (Equation 2.9) for preferential fluorescence capture from the cladding compared to that originating from the core for tellurite, F2 and LLF1 glasses. Excitation wavelength is 532 nm, emission 790 nm. Again the cladding index is taken to be decane, making the assumption that the Qdot concentration is low and has minimal effect on the refractive index of the liquid.

As such the most important parameter to obtain from this theoretical modelling is the ratio of the detected Qdot signal fluorescence ($\propto FOM_{signal}$) to the background glass fluorescence ($\propto FOM_{core}$). So we define a third FOM, FOM_{total} in Equation 2.9.

$$FOM_{total} = \frac{FOM_{signal}}{FOM_{core}} \tag{2.9}$$

Again, this is plotted for different glasses with varied core size in Figure 60. This shows that decreasing glass index results in an increase in the FOM, and likewise with decreasing core size. Once the fibre starts to support higher order modes this behaviour flattens out considerably.

As mentioned earlier this model does not consider the effect of confinement loss on the modes. When higher order modes cut in they are extremely spread out, and as such confinement loss will be high and these modes will not be experimentally observed. The net effect of including confinement loss in the model would be a reduction in the 'sharpness' of the features where the modes cut in. Confinement loss would also be more significant for the lower index glasses.

The main conclusion from these results is that smaller core sizes should lead to an improvement in the sensitivity. The theoretical model here suggests that if a new small-core (500 nm) wagon-wheel

fibre were fabricated from F2HT that the detection limit could likely be reduced by another order of magnitude over what was demonstrated earlier in Section 2.10. Further investigations as to new choices of glasses, or alternatively the use of silica glass could also result in a reduction of the detectable concentration.

The initial measurements in Section 2.5.1 using the OSA and time resolved detection in Section 2.7 both utilised small core fibres (500 nm-900 nm) while the later work in Section 2.10 utilising a monochromator and cooled CCD arrary for detection used much larger cores (1.4 µm-1.8 µm). This was chosen even though the theory here shows that smaller cores should lead to a reduction in the detectable concentration. Two main reasons led to this decision -

1) The loss of nanowires has been shown to be highly dependent on the size of the structure [26, 98] as the surface roughness dominates over material loss at small diameters. As such when the size decreases the loss increases rapidly, making detection more difficult due to the reduced observed. Since it was shown that the excitation power has a strong effect on the ratio of Qdot emission: Glass emission this is an important consideration.

2) Practical uses. The small core sizes are difficult to couple into, and the power stability once coupled is significantly worse than is the case with larger core wagon wheel fibres. As such for extensive systematic measurements, or when a higher level of precision is required relatively larger cores compared to those used in Sections 2.5.1 & 2.7 invariably make this a great deal simpler.

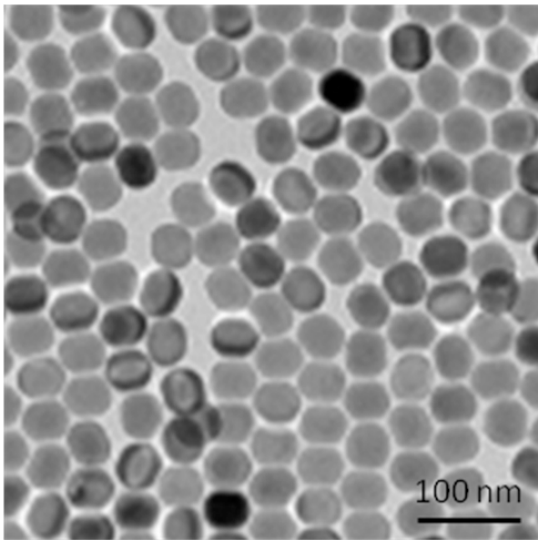

Figure 61: TEM image of Yb:Er nanoparticles.

2.12 LANTHANIDES & POSSIBLE APPLICATIONS TO SENSING

2.12.1 *Introduction*

The background fluorescence arising from the glass is a relatively fundamental limitation for this sensing approach - however it may be possible to reduce the detection limit further by reducing the core size and further improving the sensitivity of the detector. Even so, this will not enable the sensitivity to approach single molecule levels. The work in the previous section has reduced the background associated with the glass host itself (Section 2.9), but further improvements would be possible if alternative labelling molecules could be used to circumvent this autofluorescence emission. As an alternative to Qdots, rare-earth doped nanoparticles were investigated [146].

For initial experiments hexagonal-phase $NaY_{0.8}F_4$: $Yb_{0.18}/Er_{0.02}$ nanocrystals were acquired, as shown in Figure 61. These will hereafter be referred to as Yb:Er nanoparticles.

Lanthanide doped upconversion nanoparticles such as the Yb:Er nanocrystals used here are powerful tools for biological imaging and sensing [147–149]. These nanocrystals do not photobleach or blink, exhibit low toxicity, and offer comparatively bright, visible multicolour emissions when excited in the NIR wavelength, typically at ~ 976 nm. These nanoparticles can be surface functionalised by either amphiphilic carboxyl-polymer [127] or amino-silica [129] to become biocompatible [127] such that they can be used directly as fluorescent labels for biological detection.

They can be conjugated to specific antibodies or DNA strands as fluorescent tags to probe targeted analytes. In particular, the upconversion luminescence feature can provide autofluorescence-background-

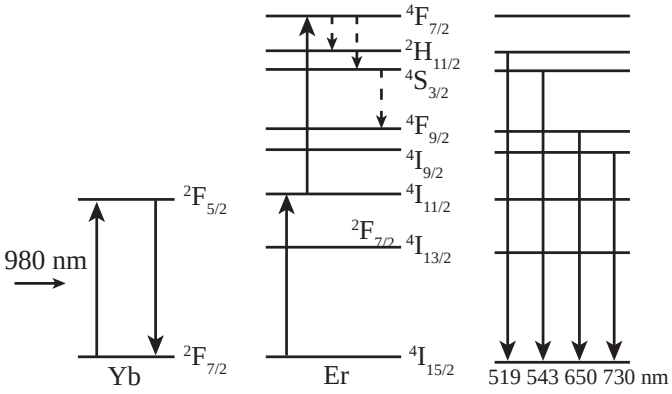

Figure 62: Er:Yb electronic energy level diagram [152].

free conditions for sensitive biosensing applications [148, 150], since the NIR excitation does not stimulate the intrinsic visible autofluorescence from the surrounding biosample. Moreover, since this anti-stokes luminescence absorbs sequential secondary photons involving metastable-excited states, the upconversion efficiency can be up to $10^5\times$ more efficient than most organic fluorescent dyes that utilise a 2-photon emission pathway [147]. Furthermore, these nanoparticles exhibit long luminescence lifetimes that range from tens to several hundreds of microseconds achieved through control of the crystal growth and surface conditions . This feature can be used for the time-resolved discrimination of multiple analytes at a single test [151]. In the following section the performance of hexagonal-phase Yb:Er nanocrystals (44 nm in diameter) are characterised when filled into the holes of a wagon-wheel fibre.

Nanoparticles were prepared by A/Prof. Yadong Yin's group at University of California, Riverside, USA, using a modified user-friendly synthesis method via the solvothermal route [147, 148] and diluted in cyclohexane or toluene. The characteristic emission peaks are attributed to the $^2H_{11/2}$, $^4S_{3/2}$ $^4I_{15/2}$ transition in the green spectral region with another red emission arising from $^4F_{9/2}$ $^4I_{15/2}$. The energy level diagram for these nanoparticles is shown in Figure 62 [152].

2.12.2 *Particle characterisation*

For the nanoparticles the green emission arises from a two-photon excitation pathway, however, the red emission also involves non-radiative decays between meta-stable states, as a mixed multi-photon process. At higher excitation power density, the efficiency for red is higher, because there are more non-radiative energy relaxations from $^2H_{11/2}$, $^4S_{3/2}$ $^4F_{9/2}$, and $^4I_{11/2}$ $^4I_{13/2}$, which compromises the green emission increase ratio but relatively accelerate red increase ratio , in spite of emission saturations at high power as shown by the reduction in slopes [153]. The power dependence feature of upconversion nano-

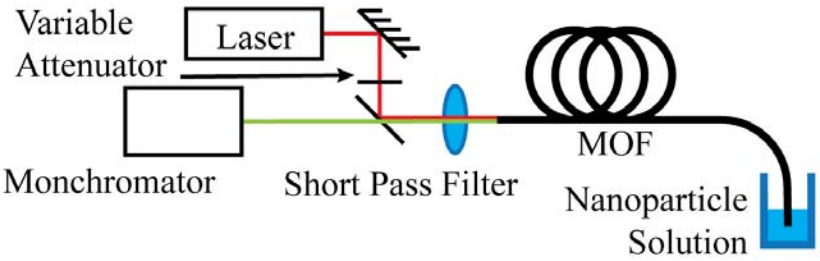

Figure 63: Experimental configuration used for fibre-based measurements on nanoparticle solutions.

crystals reflects the rich multi-photon process within single nanocrystals. A comprehensive characterization at large dynamic excitation range may allow detailed assessment for an upconversion nanocrystal.

The fibre used for these experiments was again a relatively large core F2HT wagon-wheel fibre, similar to that shown in Figure 51. This fibre had a core diameter of ~1.7 µm and an outer diameter 130 µm with a hole size of ~7 µm. For fibre-based fluorescence measurements the experimental configuration is shown in Figure 63.

Capillary action was used to fill the fibres with the solutions, with a filling time of approximately 15 minutes for 19 cm of fibre with the nanoparticles dispersed in cyclohexane. The 980 nm laser was operated in CW mode for these measurements at incident power levels from 1 mW – 300 mW. The coupling efficiency into the fibre ranges from 10-20 % depending on the core size and coupling optics used. An example of the upconversion spectra obtained is shown in Figure 64.

The tops of the vials were sealed before filling the fibres using paraffin tape, with the fibre tip able to pierce the thin layer when starting the experiment. This was required as toluene evaporates quickly - a test addind 450 µL of toluene to the same type of vial used here for filling demonstrated that an evaporation rate of 0.11 µL/min was occurring. Since sample sizes here were between 50 µL-500 µL over the 15 minutes the fibre fills this could act to change the actual concentration inside the vial by up to 3%.

Once it was established that a spectra in fibre could be obtained, characterisation was performed. The result shown in Figure 65 shows an interesting property, in that as the laser power increases the ratio between the green fluorescence and the red fluorescent peaks in the spectra decreases.

At relatively low fibre output powers of 3-4 mW the spectra shifts from being green dominant to red dominant, and this increases further as the laser power is increased. This can be understood by considering that the green and red emission channels compete for excitation energy due to the relative rates of the nonradiative decays

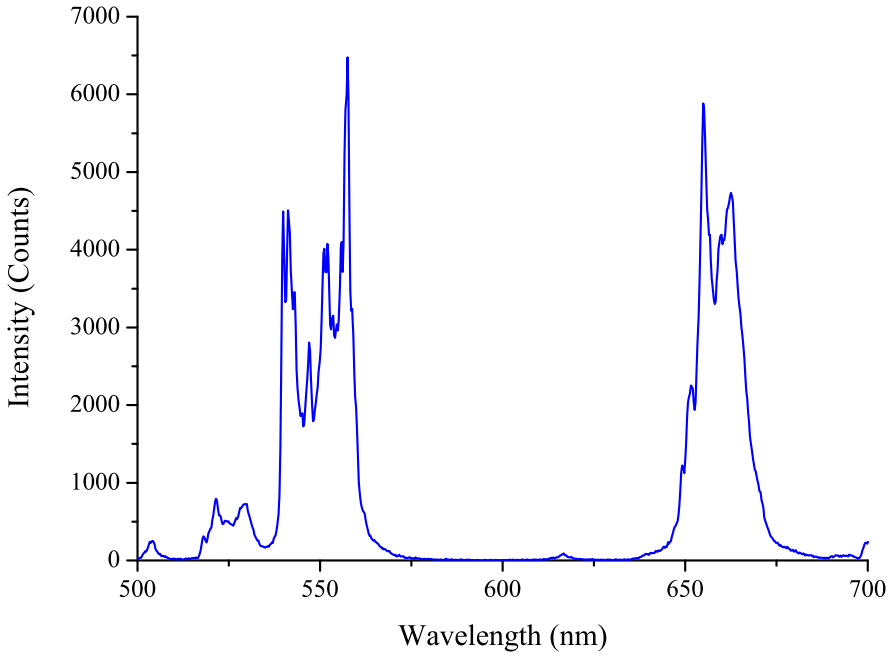

Figure 64: Typical Er:Yb spectra obtained in fibre using high-resolution gratings.

between ${}^4I_{11/2}$ and ${}^4I_{13/2}$ and between ${}^4S_{3/2}$ and ${}^4F_{9/2}$ compared with the radiative decays.

The slope of the curves in Figure 66 provide valuable information on the energy transfer, saturation and quenching between Yb and Er, and between Er and Er. The precise reasoning behind this power dependence of the red:green emission ratio could not be determined from a review of the current literature, however it is suggested that this could be due to an intermediate level possessing efficient non-radiative relaxation paths [154]. It has been reported that the red channel should have slope value from 2.4 to 0.5 and green channel should have slope value from 2.0 to 0.5 [155]. A comprehensive characterization at large dynamic excitation range may allow detailed assessment for an upconversion nanocrystal. For example, a typical rapid slope ratio for red means easier non-radiative energy relaxation, which may reflect more phonons-induced quenching in a low quality crystal structure or surface. Another example, a rapid saturation of the upconversion emission may reflect either a low quantum efficiency or higher quenching factors affecting on the Yb to Er energy transfer.

It has been reported the green band emission is higher than red emission at low power laser density achieved by bulk cuvette measurement in a spectrometer, the emission measurement at high power laser density (10^7 W/cm^2) was achieved by a careful design of a confocal setup on single nanoparticles [155]. Here similar behaviour is observed using only an optical fibre, covering the excitation power

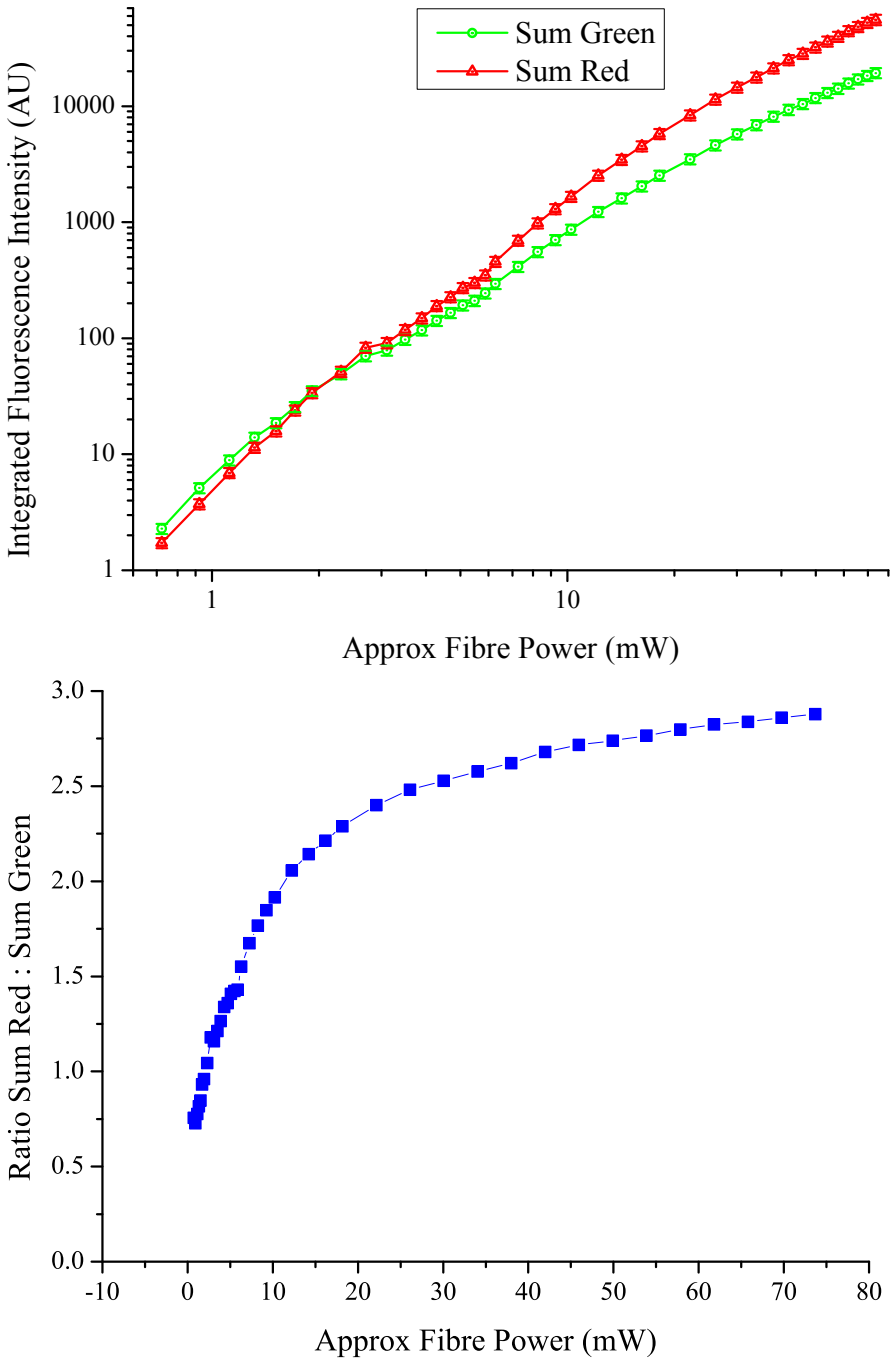

Figure 65: Integrated fluorescence intensities for green (525-575 nm) and red (625-675 nm).

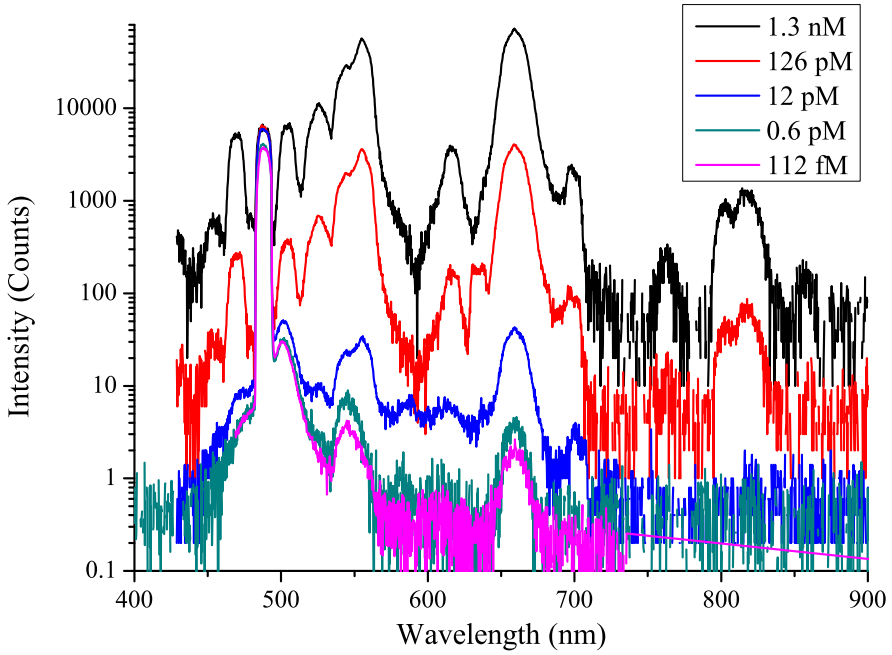

Figure 66: Upconversion emission spectra obtained for different nanoparticle dilutions in fibre.

range required to transfer from a signal showing a higher green intensity to one showing a higher red intensity.

2.12.3 *Low concentration testing*

Building on this work characterising the emission of the nanocrystals within the suspended core fibres which showed that no issues with blocking or photobleaching were observed measurements were performed on nanoparticles dispersed in toluene with a known concentration. Serial dilutions ranging between 66 nM and 66 fM (10 × steps) were performed, and spectra obtained at different input powers. An example of one of these spectra compared to that of an unfilled fibre is shown in Figure 6 below. The experimental configuration was the same as that used for the red:green power measurements, and is shown in Figure 63. To improve the signal to noise ratio the resolution of the spectrometer was dropped for these measurements, and thus the spectrum do not show the same narrow peaks as seen in Figure 64. An example of the fluorescence spectra obtained at different dilutions is shown in Figure 66.

Here it can be observed that at lower concentrations only the emissions at 550 nm and 650 nm are visible above the background level. The lowest concentration levels from this plot presented some interesting results; it was clear that even though the concentration decreased by 5×, the reduction in the fluorescence intensity was significantly less than this amount.

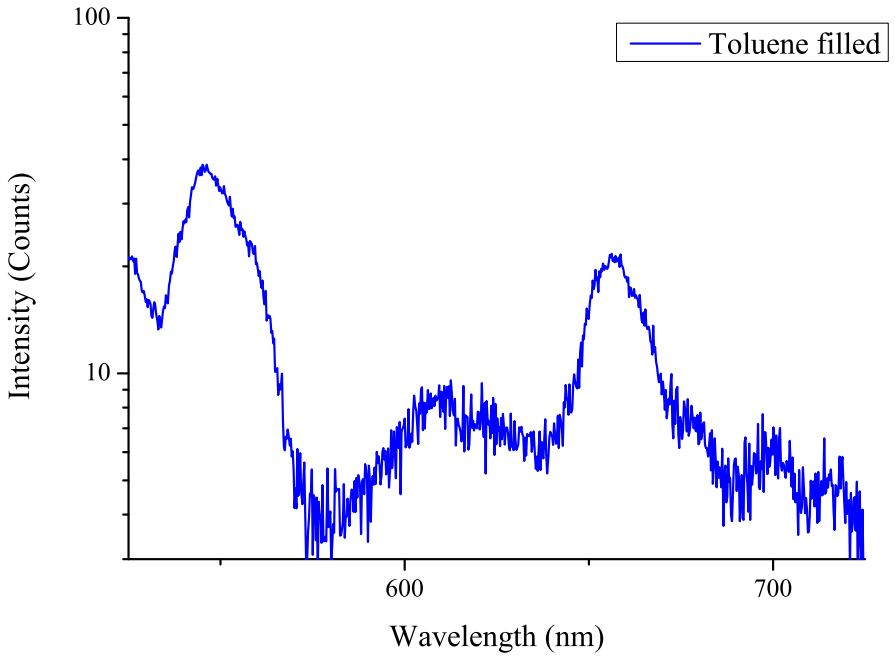

Figure 67: Glass fluorescence spectra obtained from 1 m length of toluene filled F2HT wagon-wheel fibre.

This suggests that the initial assumption that this upconversion fluorophore should present an almost background-free result is not entirely correct. To examine this in more detail a longer 1 m length of fibre was filled with toluene, and the fluorescence spectra observed. The result of this trial is shown in Figure 67.

This result shows a clear signal at both 550 nm and 650 nm, so it can be concluded that the lowest fluorescence levels in Figure 66 arise from background sources rather than the nanoparticles themselves. The location of the fluorescence emission matches with Erbium, so it can be concluded with reasonable certainty that the emission here is from Erbium impurities in the glass.

Recording the fluorescence signal when the fibre is filled with only the solvent is necessary to ensure that the only possible sources of fluorescence are either the nanoparticles themselves, or the glass itself. Indeed when the fibre is filled with toluene the recorded signal in both the red and the green drops as the mode spreads out into the holes, and the fraction of the fluorescence that is recaptured in to the guided modes drops as the index contrast decreases.

To test the minimum detectable concentration, a range of samples were tested, and compared to fibres filled with only toluene. The lowest concentration confidently detected above the background signal is shown in Figure 68.

This result demonstrates that the nanoparticles are still detectable even at relatively low concentrations of 660 fM, which corresponds to approximately 11000 particles in a 19 cm length of fibre with a total

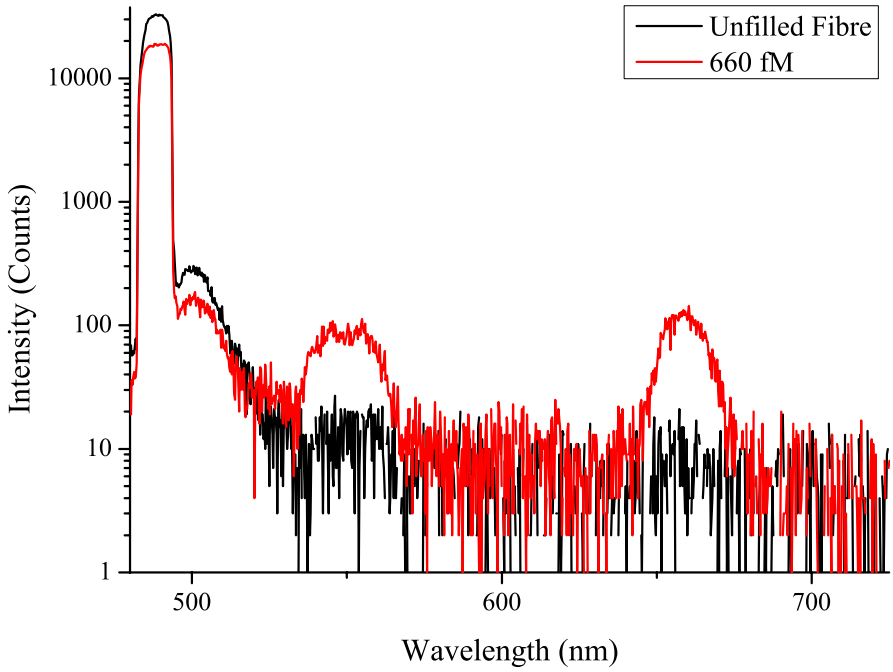

Figure 68: Lowest detectable concentration of Er:Yb nanoparticles in a F2HT wagon-wheel fibre.

volume of 29 nL. This is limited again by background fluorescence from the glass

However it is possible to differentiate between these signals and the signal from the nanoparticles as even at high powers the signal from the glass has a higher intensity in the green than in the red. This is in contrast to the signal from the nanoparticles, wherein at high laser powers the red signal is stronger. This enables determination of the source of the emission, be it from the glass or from the nanoparticles simply by examining the ratio of the red : green fluorescence.

We have demonstrated that suspended-core optical fibres make a good platform both for characterizing and utilizing erbium nanoparticles. In addition, the use of these nanocrystals within the fibre holes form the basis of an improved sensing architecture; by directly pumping the nanocrystals in the near-IR rather than at visible wavelength, the detection limit has been reduced to here of 660 fM is a significant improvement over the 10 pM that had previously been demonstrated using quantum dots and a visible laser in a similar fibre, showing that these particles have strong prospects for highly sensitive detection.

Additionally by examining the ratio between the red and green fluorescence signals the origin of the observed fluorescence signal can be observed. If it is seen to have a higher ratio of red:green fluorescence at relatively high input powers the deduction can be made that the signal originates from the nanoparticles and likewise if the green is dominant the signal is likely just background from the glass. This

feature has potential applications in biosensing, where it is possible to discriminate between the two using the differing ratios of red:green between the Erbium in the glass and Erbium in the nanoparticles.

By functionalising the particles with antibodies and utilising standard techniques the nanoparticles can be used as fluorescent labels. Using these selective techniques detecting the presence of the nanoparticle implies the detection of the target biomolecule. As such the use of nanoparticles as fluorescent labels in suspended core fibres should enable improved detection, both in order of the minimum detectable concentration compared to what has previously been demonstrated in fibre, as well as a direct method for discriminating between the signal from the nanoparticle-labelled biomolecule and the background signal from the glass.

These experiments demonstrate that this upconversion fluorescence can be characterised using relatively low laser powers from a solid-state 980 nm laser diode over a large power dynamic range, which is important for consistent power-dependent characterization of this advanced functional nanomaterial. The time-resolved luminescence can be detected by a compact semiconductor photomultiplier tube (PMT), which suggests possibilities for a portable low-cost biosensor platform. Moreover, it has been shown that due to the reduced background fluorescence from the glass at this pump wavelength compared to that observed previously using a visible laser; the detectable concentration relative to the work of the previous section based on quantum dots in similar fibres using visible 532 nm excitation has been reduced significantly.

2.12.4 *Lifetime measurements*

As a further characterisation tool, the lifetime of the nanoparticles was recorded in fibre, and compared to the results obtained with bulk measurements. The experimental configuration for these measurements is shown in Figure 69.

Due to the unavailability of a true pulsed source, the laser was operated in CW mode using an optical chopper to time gate the beam. The diode was tested using a function generator to check if it could be directly pulsed, however it was found that the rise and fall times were too long to be practical for measurements. To ensure the shortest fall time the laser was first collimated using a 10 $\times$ microscope objective, and then re-focussed with a 20 $\times$ objective. The outer edge of the chopper blade was placed at this focal point, with fine adjustment performed by mounting the chopper on a linear translation stage with differential drive adjustment. The optimised location of the chopper blade was found by observing the shape of the pulsed emission using a photodiode and oscilloscope.

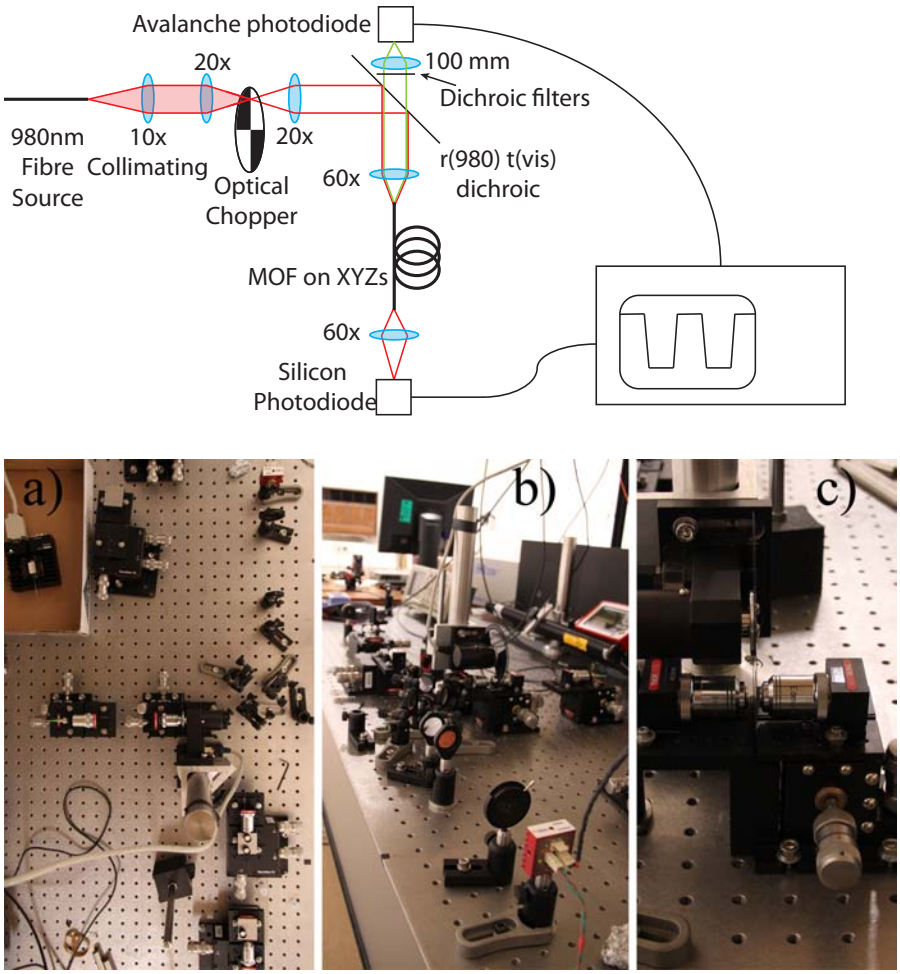

Figure 69: (top) Experimental schematic for lifetime measurements of Er:Yb nanoparticles in fibre (bottom) Actual experimental setup, showing layout (a), detection scheme and filters (b) and optical chopper configuration to minimise rise & fall times (c).

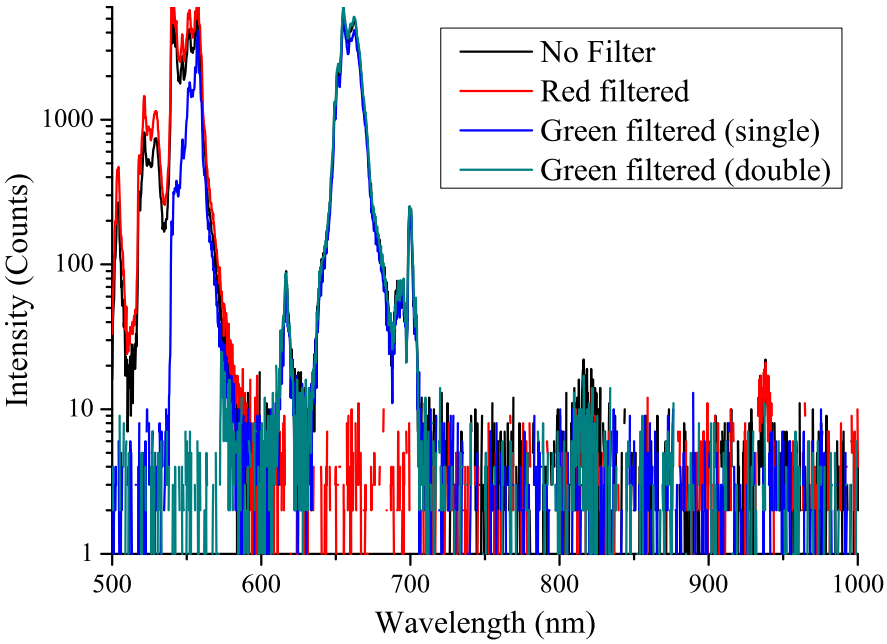

Figure 70: Spectra obtained from Er:Yb nanoparticles in fibre with various filters. "Red filtered" implies that filters were chosen to remove the red emission band, and likewise for the green.

	Red (µs)	Green (µs)
Fibre	170	250-300
Bulk	360	450

Table 3: Comparison of obtained lifetime values in fibre and in bulk for both the red and green emission bands

To ensure that only the red or green emission band was being measured, and there was no contamination of the observed signals from either the opposite band or from the pump itself short and long pass filters were used between the fibre and the detector. The emission was checked spectrally using the monochromator (Figure 70), and it was noted that when the correct filters were used there was no undesirable emission above the background levels.

The emission from the nanoparticles could not be observed temporally using the monochromator as its minimum shutter open time is 1.5 ms, so the fibre couple was replaced with a SensL-Mini silicon photomultiplier, coupled directly to the 50 Ω input of a 1 GHz oscilloscope. An example of the response obtained is shown in Figure 71. As can be seen from this plot the laser edge is not abrupt, however the fall time is significantly shorter than that which is expected from the nanoparticles so this configuration suffices for quantitative measurements.

The lifetimes measured in fibre, which are shown in Table 3 are considerably shorter than those obtained with bulk cuvette measure-

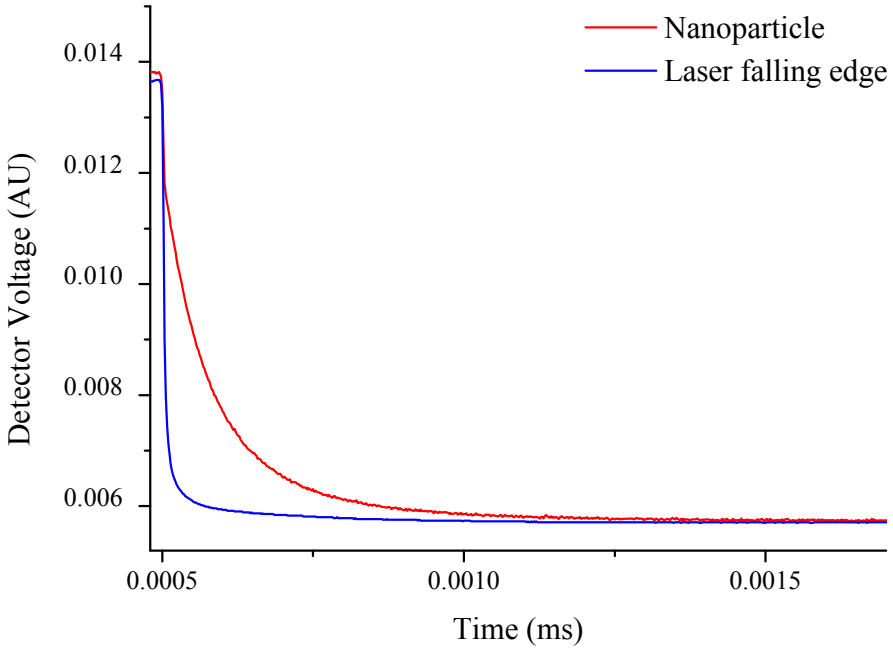

Figure 71: Typical nanoparticle lifetime measurement result in fibre. The blue curve is the signal directly from the laser itself, with the non-abrupt edge arising from the finite time it takes the beam to pass through the chopper blade. The red is a typical decay curve, in this case for the red emission band.

ments. This somewhat reduces the effectiveness of using these nanoparticles to reduce the background through time-gating [156], but should also result in a higher overall fluorescence signal directly from the reduction in the lifetime of the emission bands.

2.12.5 *Energy transfer*

Initially the goal of the measurements in this section was not to sense the nanoparticles themselves, but rather to explore the possibility of using them as an energy transfer medium to pump other fluorophores such as quantum dots [147]. The general theory behind this is that although some autofluorescence will be excited by the red and green emission bands, this fluorescence should be generated at a much lower efficiency than that from the fluorophores. If the fluorophores are in close proximity (15-100 Å [147]) to the nanoparticles they should be excited by an efficient energy transfer process, rather than relying on the absorption and subsequent re-emission of photons. Literature [147, 157] has shown that this process can occur with high efficiency and can find applications for biosensing [158, 159].

To test this the same experimental configuration used in the previous section, shown in Figure 63 was employed. A solution was mixed with Silica coated nanoparticles, as well as Qdots and Rhodamine B

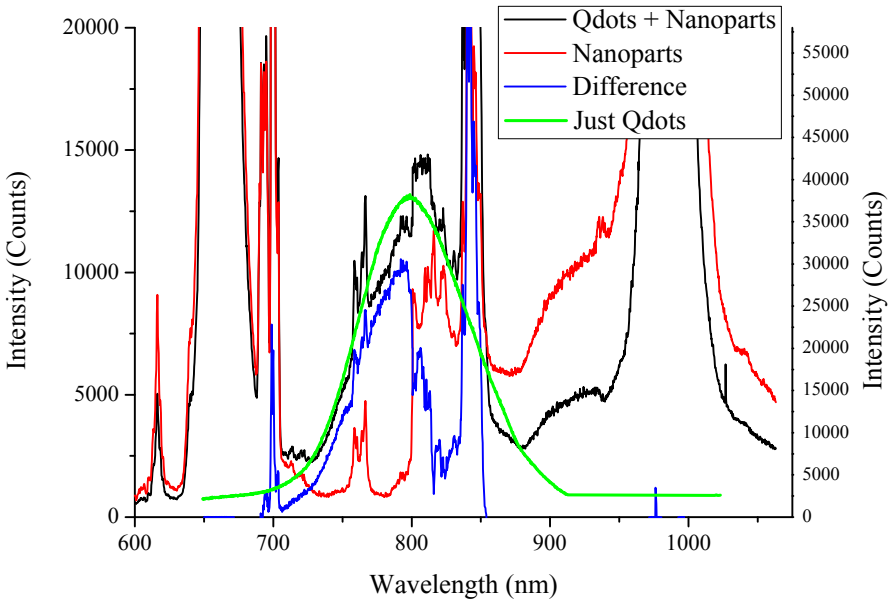

Figure 72: Qdots energy transfer.

in concentrations of approximately 100 nM all in Ethanol. The solution was filled in the fibre, and the spectra obtained. The results of this trial are shown in Figure 72.

Figure 72 shows that some Qdot emission could be observed, however the intensity was low and it was difficult to resolve this signal above that of the nanoparticles themselves. This sample was tested with up to 300 mW of incident pump power, but the signal remained low, and likewise no improvement was observed when both the fluorophore and nanoparticle concentrations were increased.

For comparison the Qdot signals obtained in Section 2.10 used significantly less than 1 mW for all measurements, and the fluorescent counts was orders of magnitude higher than obtained here. This suggests that the energy transfer is not actually occurring, rather the Qdots are absorbing the nanoparticle photons and re-emitting as usual. This potentially still reduces the intrinsic glass fluorescence signal since the Qdots are in much closer proximity to the nanoparticles, and thus will absorb with greater efficiency.

2.12.6 *Thulium nanoparticles*

With the discovery that erbium was one of the impurities present within the glass alternative nanoparticles were examined. One possible candidate was Tm:Yb nanoparticles, which utilise a similar upconversion process to produce visible light but have a completely different emission spectra to the Er:Yb particles used earlier. Since this spectra is also different from that of the glass, it should be possible to differentiate between these particles and the background signal

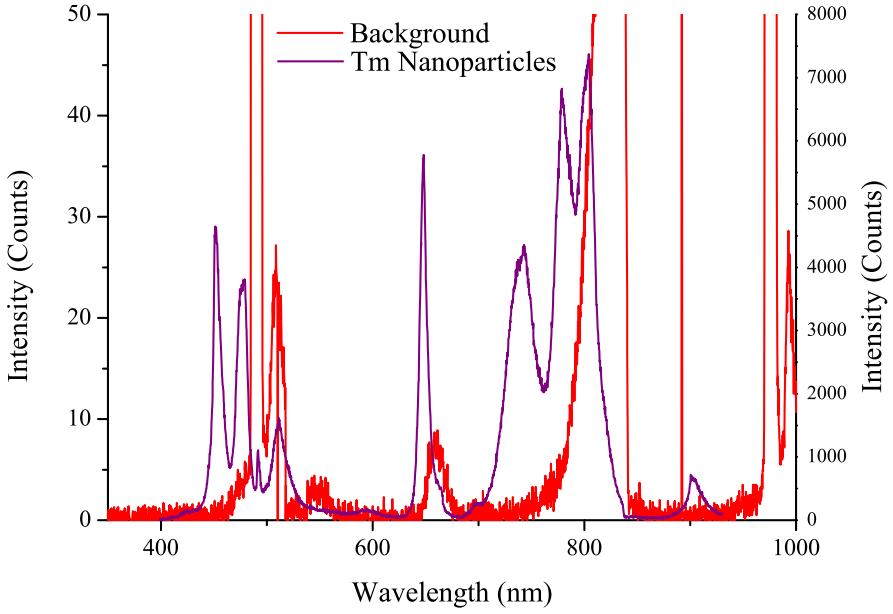

Figure 73: Example emission spectra of Tm nanoparticles, input power 300 mW compared to the emission spectra obtained from an unfilled wagon-wheel fibre.

at even lower concentrations than was previously recorded. Conveniently these nanoparticles require the same excitation source as the Er:Yb particles, so the only required change apart from the nanoparticles themselves was short pass filters with a longer wavelength transmission than earlier used for the Erbium doped particles. The experimental configuration is again shown in Figure 63, with an example of the emission spectra at an input power of 300 mW shown in Figure 73 using a 1.8 µm F2HT wagon-wheel fibre.

When this is compared to the emission spectra from just the glass it can be seen that the two can easily be visually differentiated between by the locations of the spectral features.

Next the power dependence on the emission spectra was examined to determine if there was an optimum power level to distinguish between the nanoparticles and the erbium emission from the glass. The excitation source was varied from 5 mW-300 mW, and the spectra recorded at each of these power levels. The results of this trial are shown in Figure 74.

This result shows that the 800 nm band is both the first to reach saturation, and the band which displays the highest overall emission in the fibre. This suggests that the highest sensitivity should be obtained by examining this band, and that at relatively high nanoparticle concentrations the emission begins to saturate well before the maximum possible laser power. Limitations however were found with this approach in that at low concentrations the signal began to approach

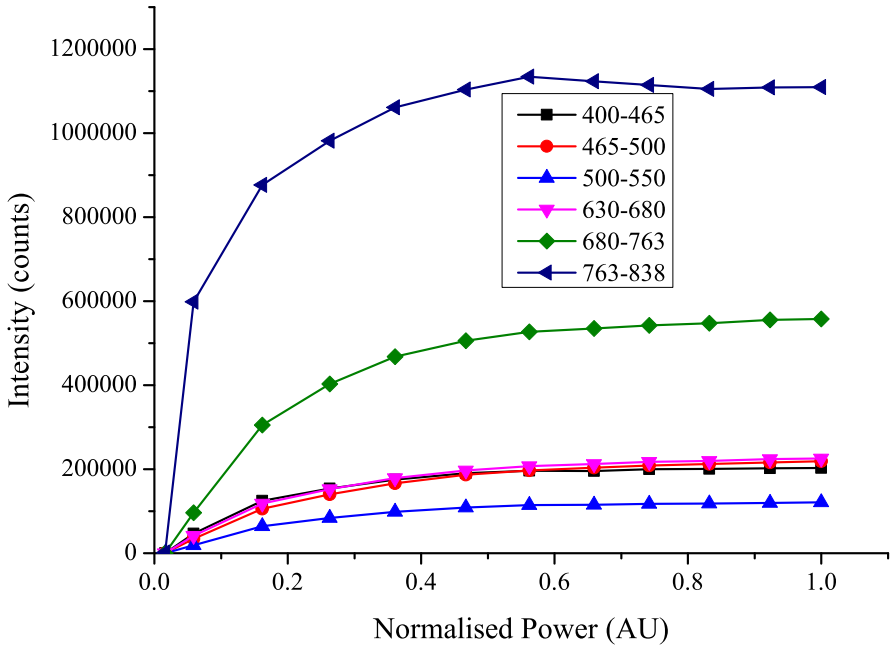

(a) Integrated intensity for each of the main emission bands, plotted versus the relative excitation power in to the fibre.

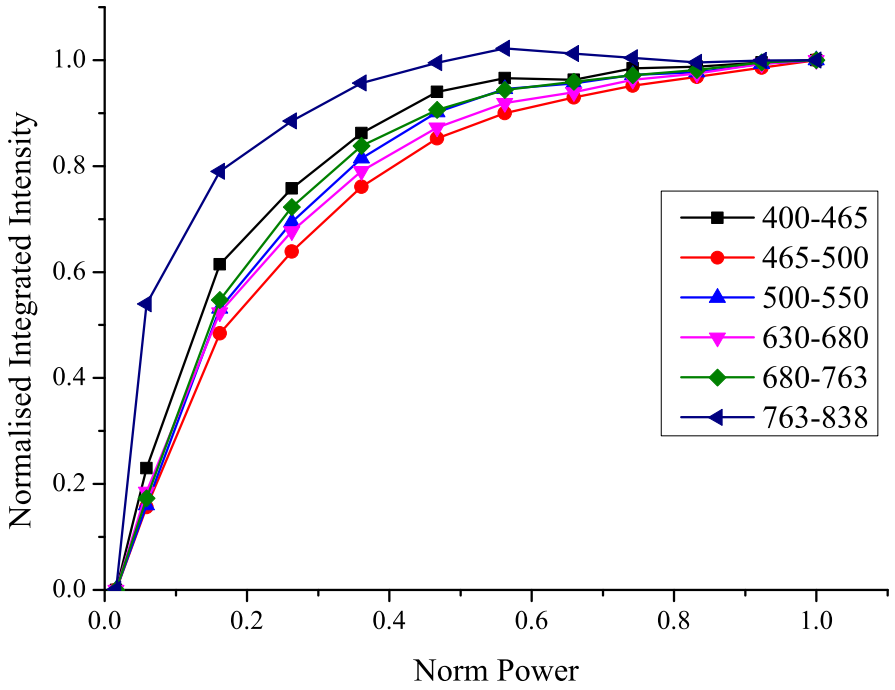

(b) (a) normalised to the emission at 100% power. This shows the saturation characteristics as the energy levels fill.

Figure 74: Tm:Yb nanoparticle emission in F2HT wagon-wheel fibres.

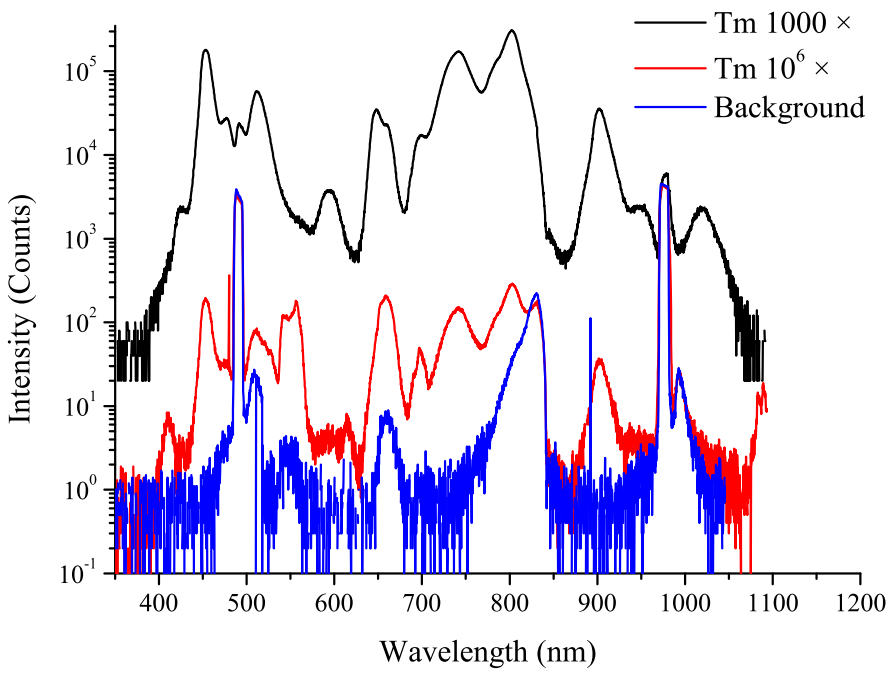

Figure 75: Tm:Yb nanoparticles in F2HT wagon-wheel fibre. The legend refers to the dilution relative to the initial concentration of approximately 0.04 nM for a 5mg/mL sample.

the noise level of the detector. This made quantitative measurements difficult, so in some cases higher powers had to be used.

A number of nanoparticles with differing Thulium and Ytterbium concentrations were analysed, and it was found that the highest signal was obtained with the $NaYF_4$:$Yb_{20}Tm_4$ sample. This sample was diluted in two serial dilutions of 1000× each in hexane, and filled in to the wagon-wheel fibres using the standard techniques. The results of this trial are shown in Figure 75.

Here the initial nanoparticle amount was 5 mg/mL, which equates to a concentration of approximately 40 pM. This implies that the 1000× sample has a concentration of 40 fM, and the 10^6 sample a concentration of 40 aM. A further concentration at 10 × this solution was tested at a later date, but could not be distinguished above the background level.

With these results a significant reduction in the minimum detectable concentration has been obtained. Using Thulium rather than the Erbium as the nanoparticle dopant has allowed the background signal to be circumvented, as there are clear features in the Thulium nanoparticles that have no detectable competing background signal from the glass. This is an important step towards increasing the possible sensitivity of fibre-based dip sensors. Further work could involve surface functionalisation of these nanoparticles for use as fluorescent labels to be able to demonstrate extremely sensitive bio detection using these microstructured optical fibres.

Part II

PRACTICAL DEVELOPMENTS TO FLUORESCENCE SENSING

3

DIP SENSORS - SPLICING

This chapter covers work on the splicing and tapering of optical fibres for sensing applications. The splicing work in this section was performed primarily in collaboration with Dr Dominic Murphy, as well as with Dr Florian Englich. This work forms the basis of a conference paper (ACOFT 2010). In addition to the experimental work reported here, modelling was also performed by the author, building on code written by Mr Matt Henderson to solve the modes of an arbitrary step index fibre. All fluorescence-based measurements were completed by the author, with Section 3.4 assisted by discussions with Dr Murphy.

3.1 MOTIVATION

One of the issues with using wagon-wheel fibres for sensing is that the presently used method requires bulky free-space optics for coupling into the fibres. This has the effect both of increasing the complexity/cost of the system, as well as increasing the skill required to operate it. Being able to consistently maximise the coupling into the fibres in a relatively short duration requires the operator to be reasonably experienced with the fibres. Ideally this type of system will find use as a laboratory or field tool, and thus being able to simplify its operation is desirable.

In addition in increasing the easy of use, splicing the fibres also provides a stable, permanent coupling amount [160]. Using free space optics, alignment can drift over time due to thermal expansion of the optical components, or instability in the pointing direction of the laser. Splicing reduces the effect of poor pointing stability by minimising the distance between the laser and the fibre compared to the standard experimental configurations such as that shown in Figure 30 which require a dichroic mirror to be placed in between the laser and fibre to allow for detection in the backwards direction. It virtually eliminates the effects of thermal expansion, as all components are in contact with each other.

One can attempt to solve both the free space optics and coupling problems through the use of splicing. The general idea of this is to splice the novel wagon-wheel fibres to conventional core-clad silica fibres. By connectorising these silica fibres direct "plug and play" operation of the sensor can be obtained. The proposed experimental configuration for sensing using a completely fiberised system is shown in Figure 76.

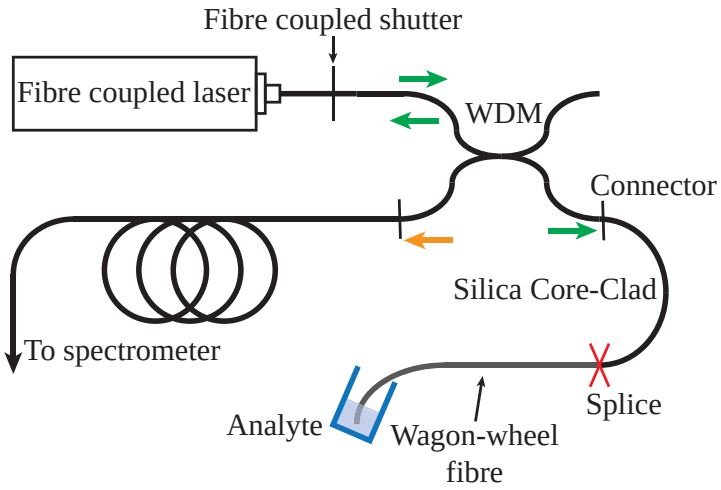

Figure 76: Proposed schematic for fully fiberised dip-sensing method.

This scheme uses a wavelength division multiplex (WDM) component to provide the same functionality as the dichroic mirrors and long pass filters used in Section 2.5.1, Figure 30. This component consists of two fibres twisted together, and then tapered carefully such that the desired transmission is obtained. This component could be fabricated using the fusion splicing system shown in Figure 81, however in this case it was purchased from Gooch & Housego specified to split 532 nm/582 nm. This was chosen to suit Amplex Ultrared (See Chapter 7) using a 532 nm laser for excitation and a fluorescence peak at 582 nm. This, together with a fibre-coupled laser source and shutter allows bulk optics to be completely removed from the experimental configuration.

3.1.1 *Modelling*

To try and gain some understanding of the coupling losses that are expected between the silica fibres and the wagon wheel fibres a simple model looking at the overlap between the guided modes was used.

This model utilised a step-index analytic code, similar to that used in Section 2.11. By Examining the modal overlaps between the silca and soft glass fibres we can estimate the loss that will be observed through the splice, given by Equation 3.1 [160] where E_1^{left} and E_j^{right} represent the fundamental mode of the silica fibre and all modes of the wagon-wheel fibre respectively.

$$S_{a1,bj} = \frac{\int_{\phi=0}^{\phi=2\pi} \int_{r=0}^{r=\infty} (E_1^{left} E_j^{right})^2 dr d\phi}{|E_1^{left}||E_j^{right}|} \tag{3.1}$$

The integration range is determined by looking at the radius required for the electric field to fall below a predetermined level. This

approach makes the approximation that there is negligible power in the z direction in the fibre, which is reasonable for larger core sizes [102]. The coupling efficiency (CE) and loss are related by $Loss = -10log(CE)$ to give the loss as a positive number by convention.

In addition to the modal overlap the Fresnel losses across the interface also need to be included. Here we consider the light incident on the interface to be a plane wave, giving the Fresnel losses across the interface by Equation 3.2 [160].

$$R < \frac{(n_1 - n_2)^2}{(n_1 + n_2)^2} \tag{3.2}$$

Since the wagon-wheel fibre here is smaller for all modelled cases than the silica fibre this parameter only gives an estimate of the loss induced here, as this equation assumes an incident plane wave and does not consider scattering.

Two silica fibres were modelled - Nufern 460HP and Corning SMF28E. The Nufern fibre is single moded from 460 nm with a core size of approximately 3.2 µm. The Corning fibre however is multimode across the whole visible spectra. The first parameter modelled was the coupling efficiency from the silica fibre to the wagon-wheel fibre, from E_1^{left} to E_j^{right} . Here this simulates the amount of excitation light that will be coupled into the wagon-wheel fibre. The assumption is made that the majority of the light is coupled into the fundamental mode of the fibre, and that the amount of excitation light guided in the higher order modes is negligible. The results of this are shown in Figure 77.

This result shows the expected behaviour, with the coupling efficiency improving as the core size of the wagon-wheel fibre increases. Large spikes are seen when new modes cut in. When the number of modes is also shown in the plot, it becomes apparent that only a small fraction of the modes in the wagon-wheel fibre have an impact on the coupling efficiency. Examining the coupling into each mode (Figure 78) shows that for both cases only the HE 1,i modes show any significant power coupling, with effectively no coupling into higher HEs or TE/TM modes. This is logical as the HE1,1 mode is the only mode considered in the silica fibre, and as such these modes will be orthogonal and thus the overlap between them will be virtually nil. Indeed coupling from the LP_{lm} modes in the left fibre will only occur into $LP_{l'm'}$ modes when $l = l'$ [160]. The high coupling into the HE1,7 mode compared to the other HE1,i modes is likely due to increased overlap between the relatively spread out HE1,7 mode and the modes in the SMF fibre. If confinement loss is considered, as will be included in future work it is likely that this HE1,7 mode will experience a high loss, somewhat reducing the coupled power measured in an actual splice.

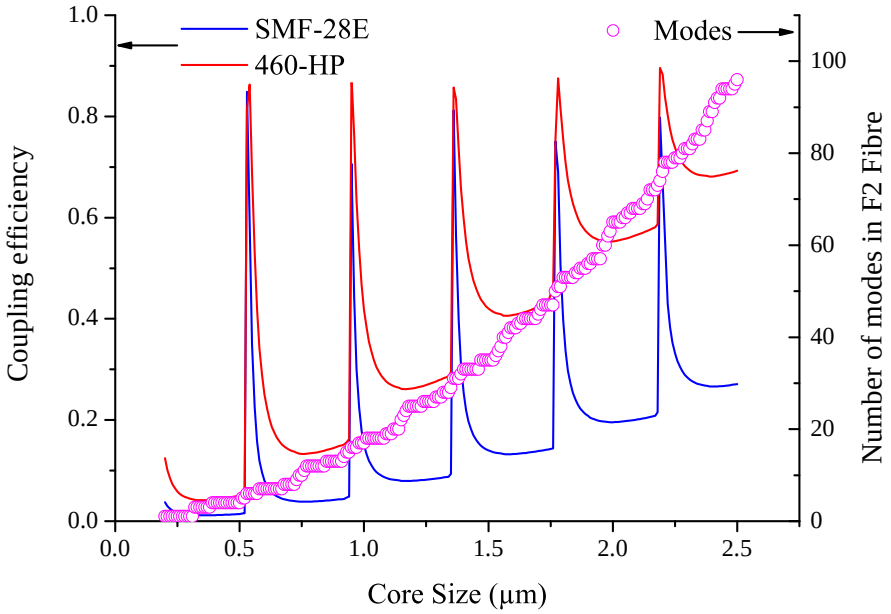

Figure 77: Predicted fractional coupling efficiency from silica core-clad fibre to wagon-wheel with varied wagon-wheel diameter at 532 nm. The core sizes of the 'small' (red) and 'big' (blue) fibres are 3.2 μm and 8 μm respectively. The number of modes guided within the wagon-wheel fibre is shown with circles.

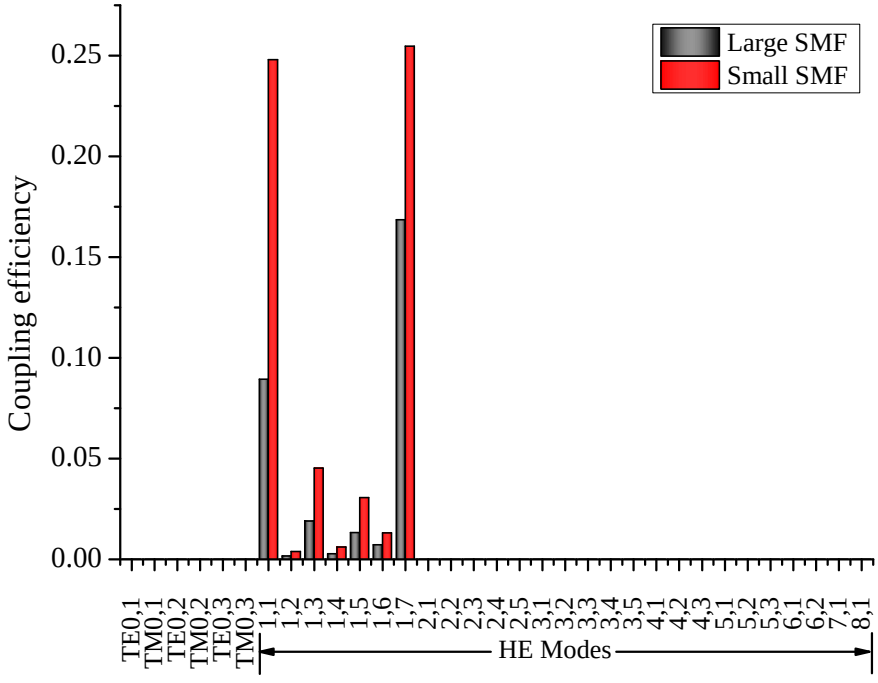

Figure 78: Modal decomposition coupling from silica core-clad to wagon-wheel with a core diameter = 1.75 μm. All modes supported by the wagon-wheel fibre at 532 nm are shown along the x-axis.

The sharpness of the peaks in Figure 77 is again due to the new modes starting to be guided. The confinement of these modes close to cutoff will be low, and their loss will be high. Thus a measurement obtained on an actual fibre will be somewhat lower than that which is shown here. Heating of the fibres causing deformation of the core and the cores of the two fibres not being perfectly concentric will likely cause additional loss above these values calculated here [160].

The coupling from the silica fibre to the wagon-wheel fibre is only one part of what needs to be considered to determine the best silica fibre to use. The coupling from the silica fibre affects the amount of light which is available to excite the fluorophores within the holes, and thus will change the amount of fluorescence that is generated. For the measurements in Sections 2.10 and 7.3 the laser was heavily attenuated; in the former case to reduce the amount of glass fluorescence, in the latter case to reduce the photobleaching rate. So although the coupling efficiency from the small core silica fibre is higher than that from the large core silica fibre, this will have much less impact on the practicality of this system than the recapture from the wagon-wheel back to the small silica fibre. Since the wagon-wheel fibre is only single-mode at 532 nm for core sizes up to approximately 310 nm and single mode at the fluorescence wavelength of 800 nm until 480 nm the capture to and from the wagon-wheel will not be symmetric.

Assume that the fluorescence emitted by the fluorophores is recaptured equally into all guided modes of the wagon-wheel fibre [103]. As we have already shown, coupling between modes in the left and right fibres only occurs for $l = l'$ so hence one expects the CE to be a fundamentally different result that decreases with increasing core size compared to that shown earlier in Figure 77 which considered only the fundamental mode in the SMF. The main point to be examined here was whether the increase in coupling between the higher order modes that will occur with the large SMF compensates for the decrease in modal overlap arising from the more dissimilar core sizes. Consider a generalised form of Equation 3.1 that examines coupling between all guided modes in both fibres. This is given by Equation 3.3 where i represents all modes in the silica fibre.

$$S_{ai,bj} = \frac{\int_{\phi=0}^{\phi=2\pi} \int_{r=0}^{r=\infty} (E_i^{left} E_j^{right})^2 dr d\phi}{|E_i^{left}||E_j^{right}|} \tag{3.3}$$

The coupling into individual modes was examined to determine if the correct behaviour with coupling into the $l = l'$ modes was being observed. An example for a 1.3 µm core F2 wagon-wheel and 8 µm core SMF is shown in Table 4. Here the efficiencies greater than 0.01% have been shaded green, 10^{-4}-10^{-10} yellow with the remainder red.

It can be seen from this result that the behaviour is as expected in the fibre, with effectively zero coupling between the $l \neq l'$ modes.

	TE0,1	TM0,1	HE1,1	HE2,1
TE0,1	2.62E-04	0	1.09E-35	1.85E-37
TM0,1	0	2.17E-04	1.60E-13	1.74E-24
TE0,2	4.55E-04	0	3.87E-36	7.58E-38
TM0,2	0	1.07E-03	1.74E-13	1.92E-11
HE1,1	7.39E-37	3.15E-15	4.25E-03	2.80E-23
HE1,2	1.27E-37	5.47E-15	1.60E-04	1.51E-19
HE1,3	3.88E-38	1.53E-14	1.66E-03	1.50E-14
HE2,1	8.12E-38	1.11E-24	9.60E-23	2.27E-04
HE2,2	2.77E-37	3.04E-24	3.06E-18	8.23E-06
HE2,3	7.07E-37	2.04E-16	4.72E-11	9.09E-04
HE3,1	2.79E-36	9.70E-20	3.51E-18	6.54E-18
HE3,2	2.47E-36	6.56E-19	9.70E-19	1.45E-13
HE4,1	6.90E-35	5.77E-15	8.47E-14	1.05E-15

Table 4: Coupling between modes in 8 µm silica core clad fibre and 1.3 µm F2 wagon-wheel fibre. The cells have been shaded red to demonstrate modes which have negligible coupling between them, yellow low coupling and green relatively strong coupling.

The code was then run for the small 3.2 µm core nufern 460-HP and a large 8 µm core corning SMF28E fibre, with the results shown in Figure 79 for varied wagon-wheel core size.

From these results we can see that the coupling efficiency from the wagon-wheel to the silica core-clad fibres is relatively low for all core sizes above 500 nm. The small and large silica fibre correlate remarkably well, and here it is apparent how much effect the higher order modes are having on the fluorescence recapture from the wagon wheel to the silica fibre. This was run again for an emission wavelength of 580 nm, with the results shown in Figure 80.

From these two results it is clear that the coupling of the fluorescence mode from the wagon-wheel to the SMF is dominated by the size of the wagon-wheel core, rather than the size of the SMF. Increasing the number of modes from 1 (both cases 460-HP) to 5 or 9 (580 nm and 800 nm respectively in SMF28-E) does introduce some extra features to Figures 79 & 80, but the overall trend is still the same. At λ =800 nm the coupling appears to asymptote towards approximately 1.5%, while at λ=580 nm the coupling drops below 1% at higher powers. This arises since as at higher powers the fluorescent light is split between more modes, and due to the limited number of available modes in the SMF fibre only a small fraction of these can couple into the silica fibre.

Since the theoretical modelling suggests that there should be minimal observable difference between the two fibres, it was decided to focus the majority of the practical splicing work on splicing wagon-

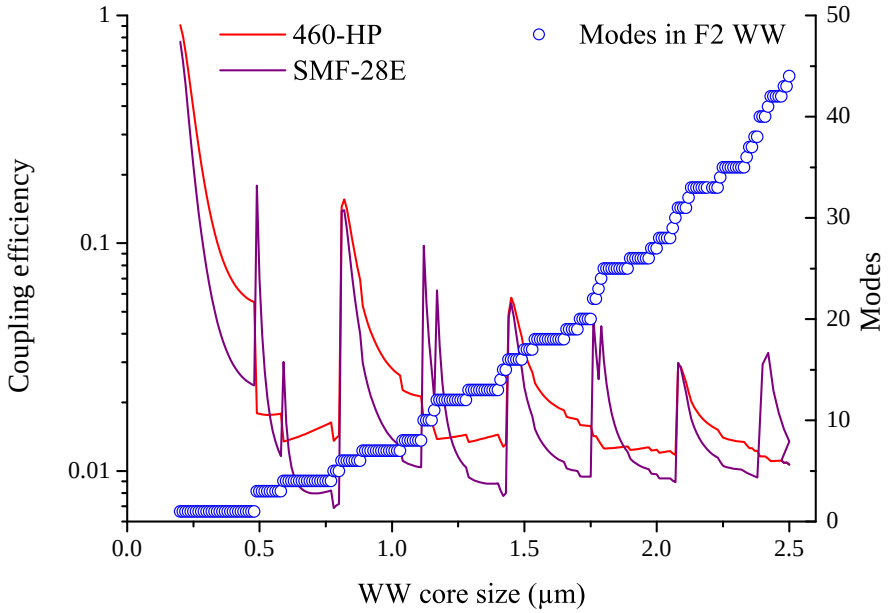

Figure 79: Coupling fraction from all modes in F2 wagon-wheel fibre to all modes in silica core-clad fibres. $\lambda = 800nm$.

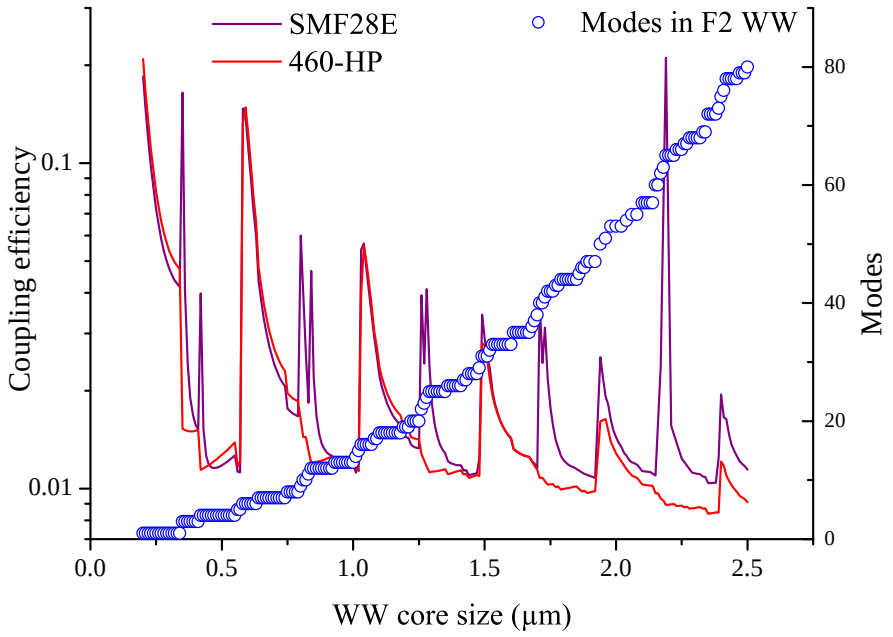

Figure 80: Coupling fraction from all modes in F2 wagon-wheel fibre to all modes in silica core-clad fibres. $\lambda = 580nm$.

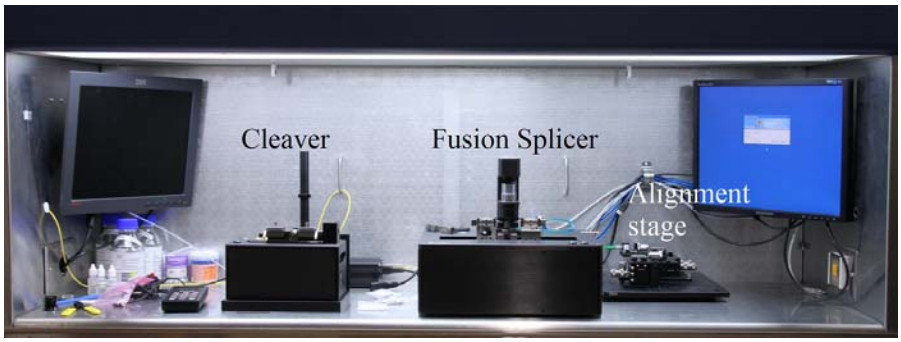

Figure 81: Vytran splicer.

wheel fibres to the smaller 460-HP fibre. This decision was made as it was observed that it is significantly easier to repeatably couple similar amounts of power from the single-mode SMF to the wagon-wheel fibre. This occurs because the SMF-28E is multi-mode, and as such it is possible to obtain a similar amount of coupled power, but actually have coupled into different modes in the fibre. Since the coupling to the wagon-wheel fibre is strongly dependent on the modal structure in the SMF fibre this resulted in a significant change in the coupled power, making any sort of quantitative measurements more difficult than with the smaller silica fibre.

3.2 INITIAL WORK

Splicing was performed using a commercial Vytran GPX-3400 splicing system, shown in Figure 81.

The splicing system consists of three primary components, a cleaver (left), fusion splicer/taperer (middle) and recoater (not shown). In addition to this a small optical setup was added to allow the power transmitted through the fibre to be monitored before, during, and after the splice. This allows the splice to be aligned with higher precision than is possible by just visually aligning the fibres. Typically fibres are aligned by matching the locations of the outer edges of the two fibres in the X & Y planes, however since the core size of the wagon-wheel fibre is so small any eccentricities in the location of the core can lead to large increases in the loss of the splice. The configuration used for splicing of silica SMF fibres to wagon-wheel fibres is shown in Figure 82. Here the splicing filament is offset by 30 µm from the splice to minimise the amount of heating and damage at the interface.

Fusion splicing of microstructured fibres also induces additional challenges in the process [161, 162], as care must be taken not to collapse the structure. This difficulty is further compounded in this case due to the markedly different softening points of the two glasses, with F2 having a softening point of 594 °C [1] compared to silica at

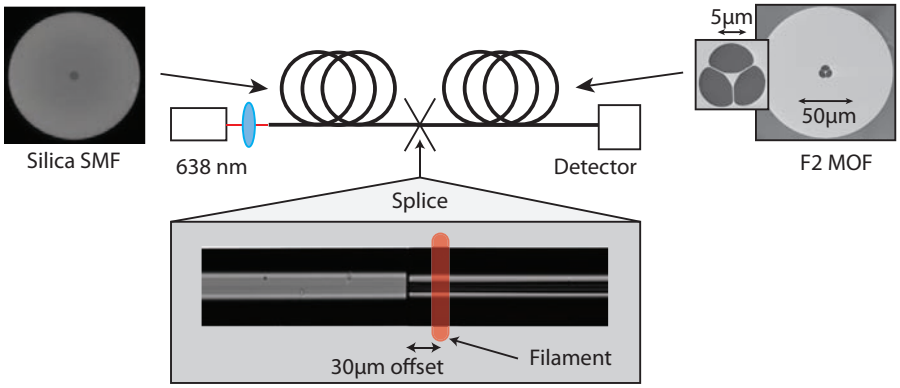

Figure 82: Schematic for splicing soft glass wagon-wheel fibre to conventional silica single mode fibre using a fusion arc splicer.

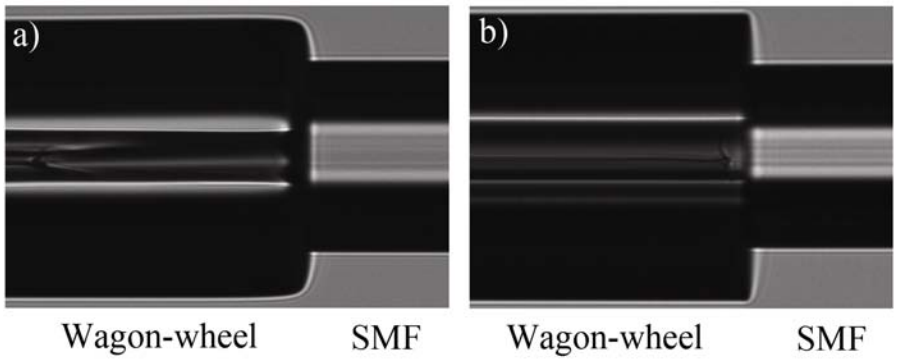

Figure 83: Comparison between fusion splices for 160 µm F2 wagon-wheel to silica SMF-28E for (a) Graphite filament at 5W and (b) Iridium filament at 2W.

1600 °C. This means that if the solid silica fibre is heated up enough to soften, the viscosity of the F2 fibre would have reduced so much that the glass would have softened and the fibre dropped away before splicing.

The Vytran system used here utilises an arc filament for splicing rather than the flame or CO_2 lasers found in alternative systems [160]. This allows the temperature of the splice to be precisely controlled, but provides limited control over the width of the hot zone. For these trials a low-power iridium filament to allow for improved control over the heating at the lower temperatures required for splicing of soft glass fibres. This machine is normally used with graphite filaments using 5-60 W of power, while the iridium filament allows the power to be reduced to below 1 W with greatly improved precision. An example of the improvement in splice quality obtained using an iridium filament is shown in Figure 83.

Closely examining Figure 83a shows that there is a significant amount of deformation of both the internal structure, and the outer surfaces of the F2 fibre when using a graphite filament even at minimum power. The structure appears to have been destroyed close to the in-

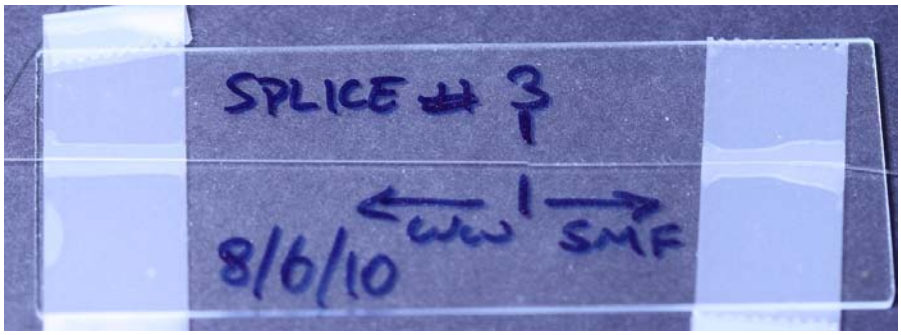

Figure 84: Mounted fibre splice.

terface, with a large (>10 µm) void observed between the two fibres. Changing to an iridium filament (Figure 83b) shows a significant improvement in the structure of the wagon-wheel fibre, with minimal heat-induced damage observed.

To improve the robustness of the splices, the fibres were mounted on a microscope slide after splicing. An example of this is shown in Figure 84. Mounting the splice like this enabled it to be handled without damage, as the splice itself was not strong enough to withstand bending which would typically result in a breakage at the splice interface.

For sensing applications a number of splices were fabricated, spliced both to SMF28E fibres and to the smaller Nufern 460-HP fibres. Four of these trials, numbered 2-5 are shown in Figure 85. Here the wagon-wheel fibres used had an outer diameter of 130 µm, and a core size of 1.7 µm. Fibre was specially fabricated to this diameter for splicing applications to make it easier to match the wagon-wheel to the 125 µm SMF fibres. The majority of wagon-wheel fibres fabricated at Adelaide to this point had an outer diameter of 160 µm, chosen as a diameter which gives good mechanical strength. The fibres used here were of good enough quality that no issues were seen with the smaller outer diameter, and breakages during handling were minimal.

The splicing procedure here involved first cleaving the F2 fibres with a tension of 130 g using the Vytran cleaver, and the SMF fibres using the standard silica 125 µm cleaving routine on the same cleaver. The fibres were then transferred to the splicer on their mounting blocks, and moved to their loading positions. Course alignment was performed using the auto-alignment procedure in the Vytran software, which leaves the fibres centred with a small gap between them. Laser illumination is then used on the SMF fibre, and the power through the wagon-wheel fibre monitored using a power meter and integrating sphere head. The coupling between the two is optimised by manually moving the stage positions in small increments until the ideal position is located. At this point the two fibres are effectively in contact, with the junction located directly above the splicing filament.

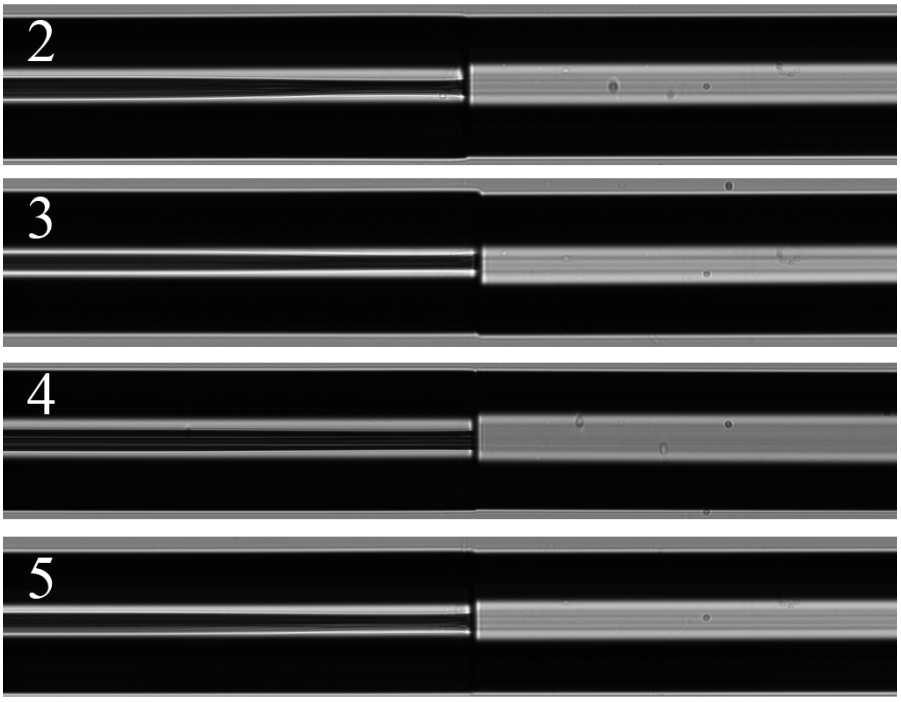

Figure 85: Splice trials, from top to bottom of 125 µm outer diameter wagon-wheel fibres spliced to 460-HP silica core-clad fibres. Numbered 2-5 sequentially from top to bottom.

The two blocks are then moved 30 µm, such that the wagon-wheel fibre is located entirely above the filament.

The heating procedure involves pulsing the filament power to ensure a more even heat profile across the fibre, before the two fibres are pushed 1 µm into each other while the heating process continues. At the conclusion of this the splice is visibly inspected using the camera, and the power coupled through the splice recorded. For these trials the splice power was varied between 1.9 W and 2.2 W, with a total heating duration of approximately 2.5 s.

Through these trials it was demonstrated that it was indeed possible to splice soft glass wagon-wheel fibres to solid silica fibres, with a loss as low as 9 dB splicing to an 8 µm core silica SMF28E fibre, and 6 dB splicing to a smaller 460-HP fibre at 638 nm. The amount of additional loss induced by the splicing process was found to be minimal, with the butt-coupled loss through the 460-HP fibre recorded before the splice at 5.6 dB. This agrees well with past work in the literature splicing silica MOFs to conventional core clad fibres [163]. Using the theoretical model described above gives an estimate for the loss of 5.2 dB for the SMF28E, and 2.2 dB for the 460-HP. As previously mentioned this loss will likely be a lower limit, since this particular model does not consider the effects of confinement loss of the higher order modes of the fibre.

3.3 FILLING & FLUORESCENCE RECAPTURE

One of the possible issues that was initially discussed was whether the fibre will fill after one end is sealed when it is spliced to a solid fibre. Various solutions were proposed, including micromachining small holes in the side walls of the wagon-wheel fibre such that the air can escape and thus let the fibre fill. A simple trial was devised, in which two wagon-wheel fibres of differing lengths were sealed at one end using a flame. The opposite end of the fibre was then dipped in a vial of water, and the location of the meniscus monitored using a microscope. The results of this trial are shown in Figure 86.

This trial demonstrates that for both fibre lengths approximately one third of the fibre fills, before the internal pressure build up in the fibre balanced the capillary forces. Two splices were then trialled to observe the amount of fluorescence signal that could be measured through the splice. One spliced fibre (Figure 87a) was filled with a 1 µM solution of Rhodamine B, the second (Figure 87b) filled with a 90 nM solution of Qdot 800 in decane. The experimental configuration for this measurement is the same as that shown in Figure 89 only with the removal of the water bath.

Both of these measurements demonstrate that it is possible to measure a fluorescence signal through a splice, even though the theoretical model suggests that the coupling from the wagon-wheel to the SMF fibres will likely be in the order of 1.5% due to the capture of the majority of the fluorescent light into modes that will not couple into the SMF fibre. This is a substantial reduction over what can be measured using bulk optics (estimated >>10%) however with the high fluorophore concentrations present in both of these cases it is still possible to observe fluorescent signals.

3.4 STUDIES OF A TEMPERATURE DEPENDENT SPLICE

During preliminary glass fluorescence measurements it was noted that two of the splices - splice #2 and splice #5 displayed a spectra that did not match with what was expected. The result of this trial using splice #5 is shown in Figure 88.

When compared to the regular glass fluorescence spectra, shown in Figure 88 in red it is clear that an interference pattern is being observed around 715 nm. It was surmised that this pattern was due to an incomplete splice, where the outer cladding regions of the F2 and silica fibres had fused while the core regions were not only unfused, but also had an air gap between the two glass regions. This air gap is acting as a Fabry-Pérot interferometer, creating the fringes [164]. To test this, the experimental configuration shown in Figure 89 was used.

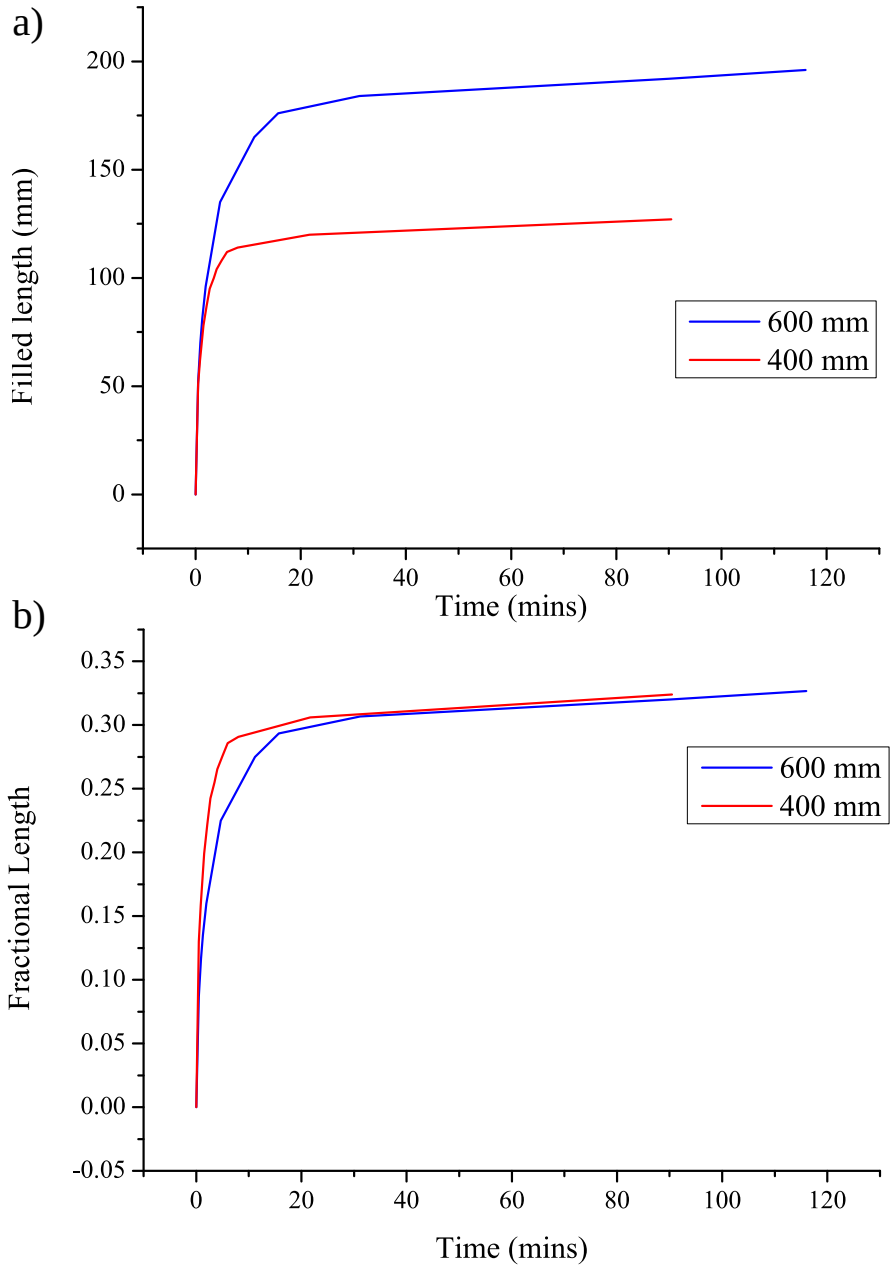

Figure 86: Filling fibre with sealed ends (a) Absolute measurement of filled length for two fibre with hole size 5 µm, using both 400 mm and 600 mm lengths. (b) Fractional filled length for the two trials.

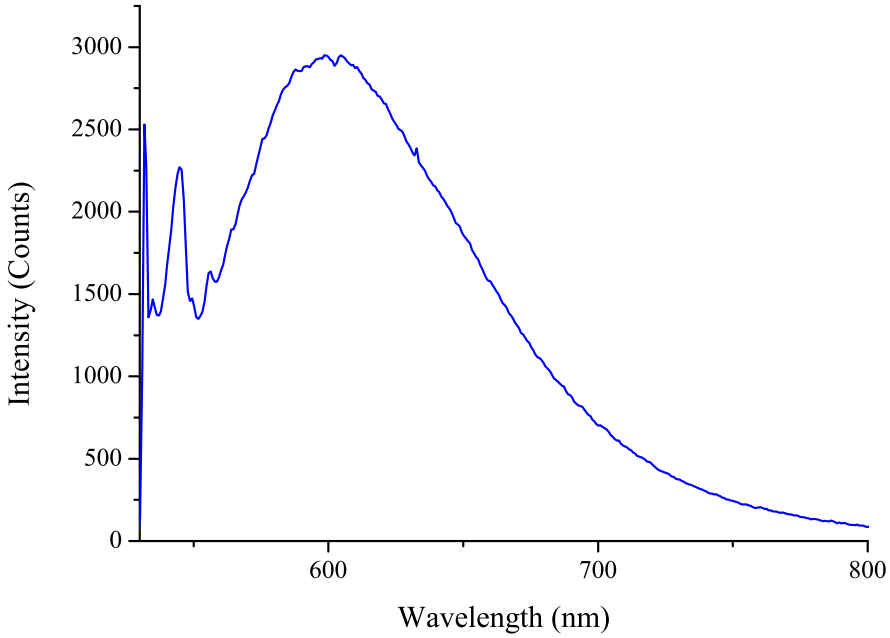

(a) Splice #1 filled 1 µM Rhodamine B.

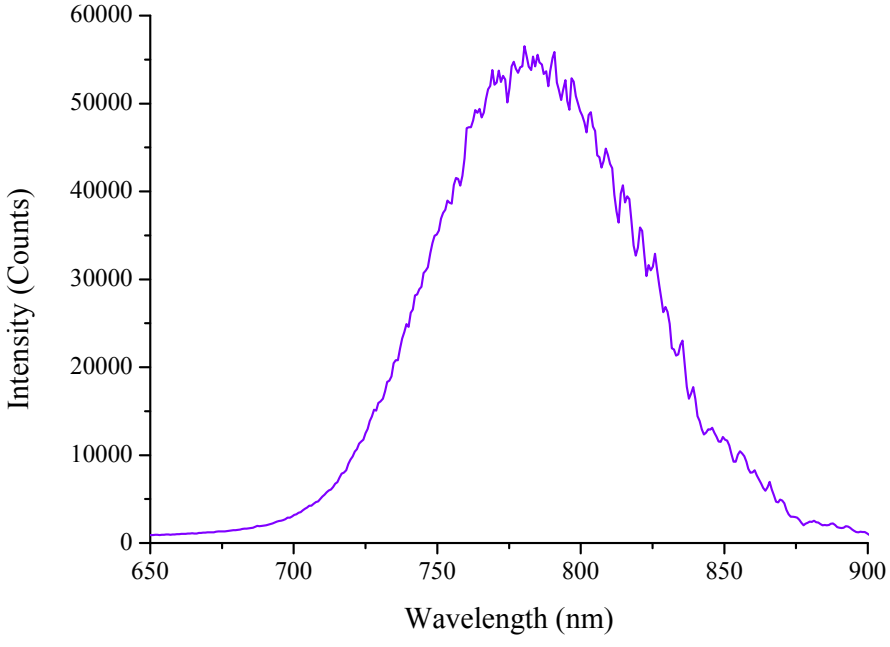

(b) Splice #3 filled 90 nM Qdot 800.

Figure 87: Example fluorescence spectra through splices #1 and #3.

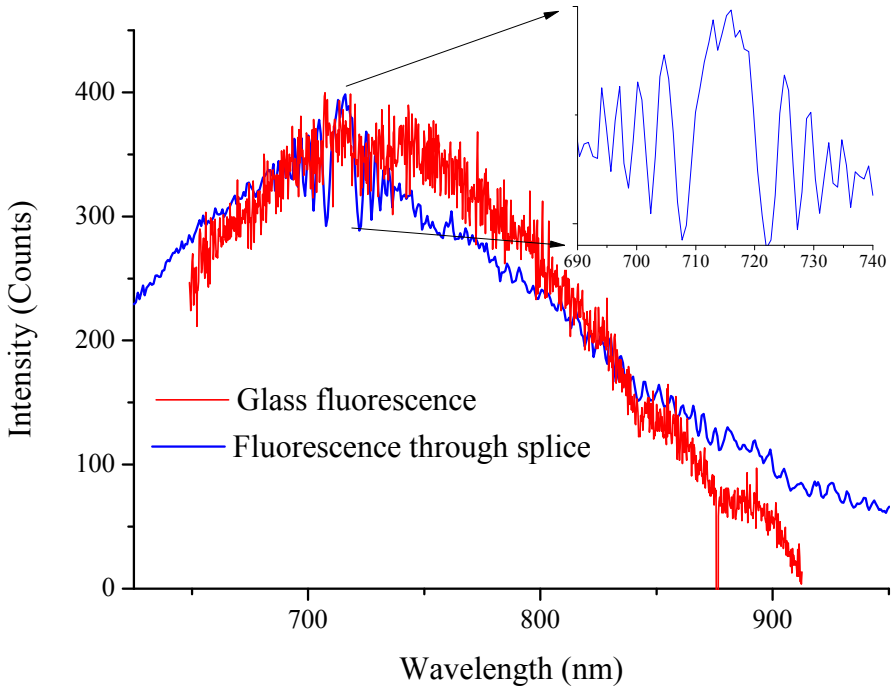

Figure 88: Fringe pattern through splice #5, compared with the fluorescence spectra obtained from just a wagon-wheel fibre.

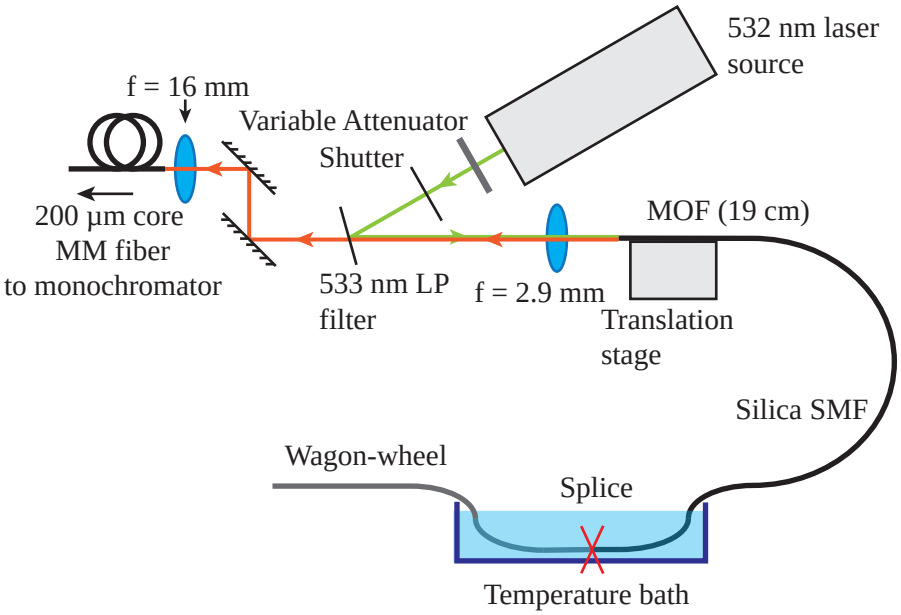

Figure 89: Temperature setup.

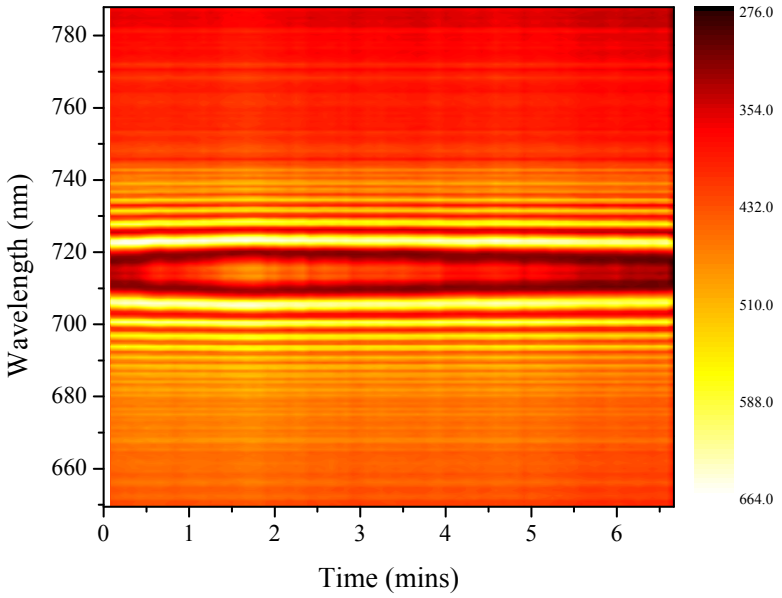

Figure 90: Splice #2 - variation in the fluorescence spectra as the spliced region is heated and allowed to cool. The colorbar shows the number of counts per pixel, which in this case corresponds to 0.8 nm.

Here the standard configuration was used for the fluorescence detection as used previously in Sections 2.10 & 7.3, with the silica fibre placed on the alignment stage in place of the wagon-wheel fibre. The spliced region was then immersed in a water bath with a total volume of 3 L which was then placed on a hotplate. The splice had been mounted on a microscope slide as shown in Figure 84 which was then placed on two small beakers such that the splice was located in the middle of the liquid. This was done to ensure that the splice only received gradual heat from the water, rather than being located on the bottom of the container where a large temperature gradient was likely to be present. The hotplate was turned on for one minute, then allowed to cool and the change in the spectra observed. The results of this trial using splice # 2 are shown in Figure 90.

This spectra showed a change in the fluorescence spectra when the bath was heated. Unfortunately in this case when resetting the experiment to include a thermocouple the splice was broken, and thus quantitative measurements could not be performed. As mentioned earlier a second splice (#5) also showed fringes, so this was used in place of splice #2. A comparison between the initial fringe patterns of the two splices is shown in Figure 91.

It can be seen from this result that the location of the fringe patterns coincide remarkably well, however the quality of the fringes from #2 is much better than those from #5. This is likely due to some deforma-

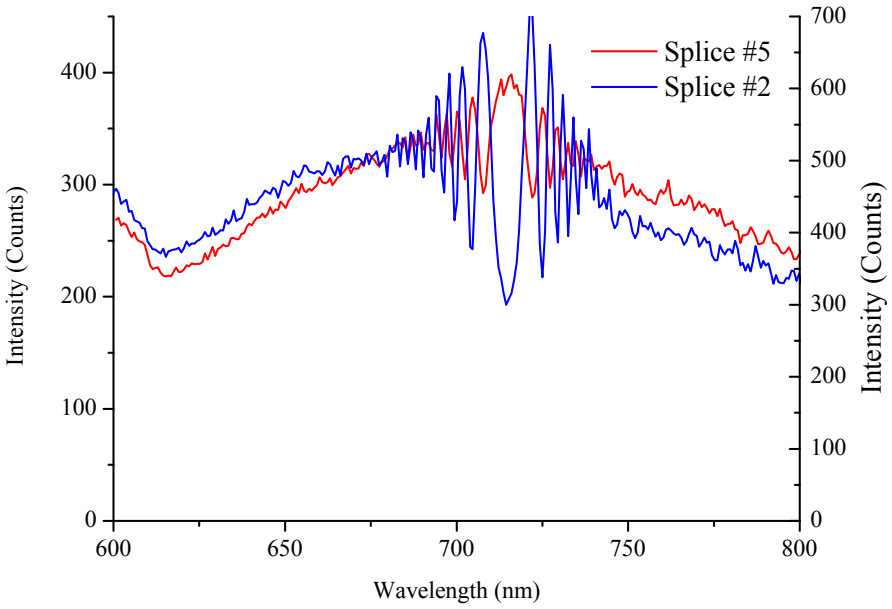

Figure 91: Comparison between fringe patterns in splices 2 & 5.

tion of the fibre face reducing the quality factor of the cavity between the two fibres.

A thermocouple was attached to the bottom surface of the slide directly below the location of the splice, and the temperature recorded at 30 second intervals. The water was then heated to boiling point, and allowed to cool back to room temperature while both the fluorescence spectra through the silica fibre and the temperature were simultaneously monitored. The results of this trial are shown in Figure 92.

A clear correlation can be observed between the fringe pattern and the temperature of the bath. A rapid change is noted in the fringe pattern as the splice is heated up, with a gradual return almost to its initial spectra over the duration of the measurement. A magnified view of the central fringe region is shown in Figure 93.

Again it can be seen that the location of this fringe depends strongly on the temperature of the spliced region. To examine exactly how good the correlation between the fringes and the temperature were, two parameters were examined. The first was the wavelength of this peak, the second the intensity. The results are shown in Figure 94.

These results demonstrates that there is a good correlation between both parameters, with the intensity of the central peak reaching a maxima and beginning to decrease as the fringe pattern expands. The location of this first peak also has a good correlation with the temperature. This result shows that it would be possible to multiplex both fluorescence and temperature sensing, by integrating a splice region with a small gap in the sensing fibre. The fluorescence signal is still able to be measured even with this gap in place, as this gap will likely

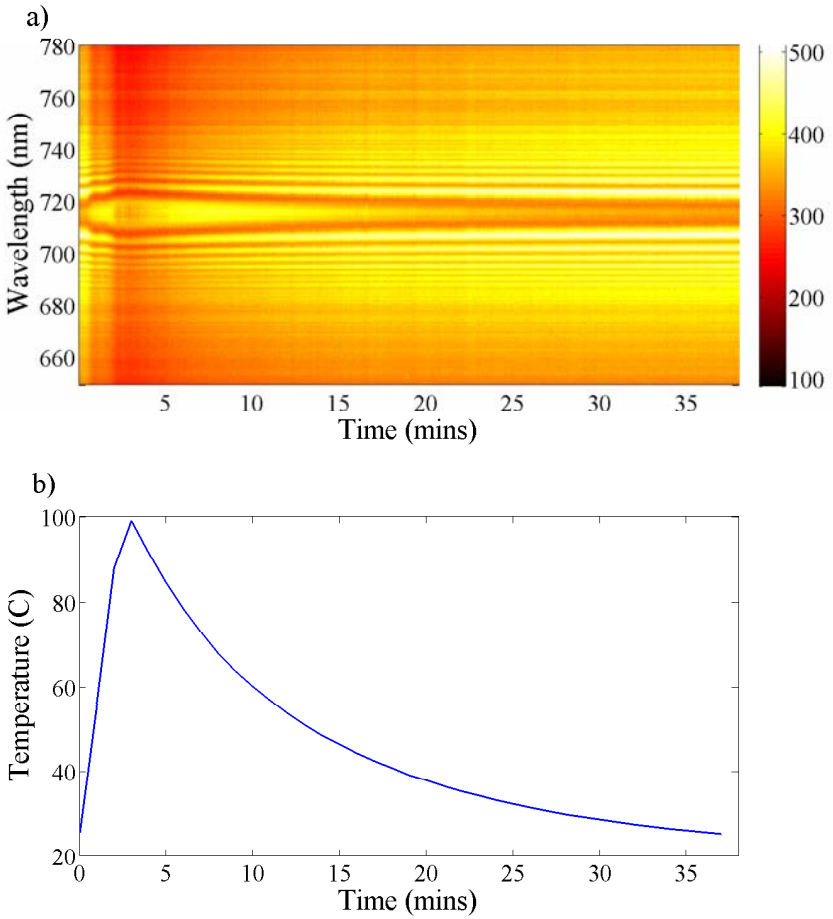

Figure 92: Results of spliced temperature sensor trial, using splice #5. (a) Change in the fringe pattern over time. The colorbar shows the number of counts per pixel, which in this case corresponds to 0.8 nm (b) Temperature vs time plot.

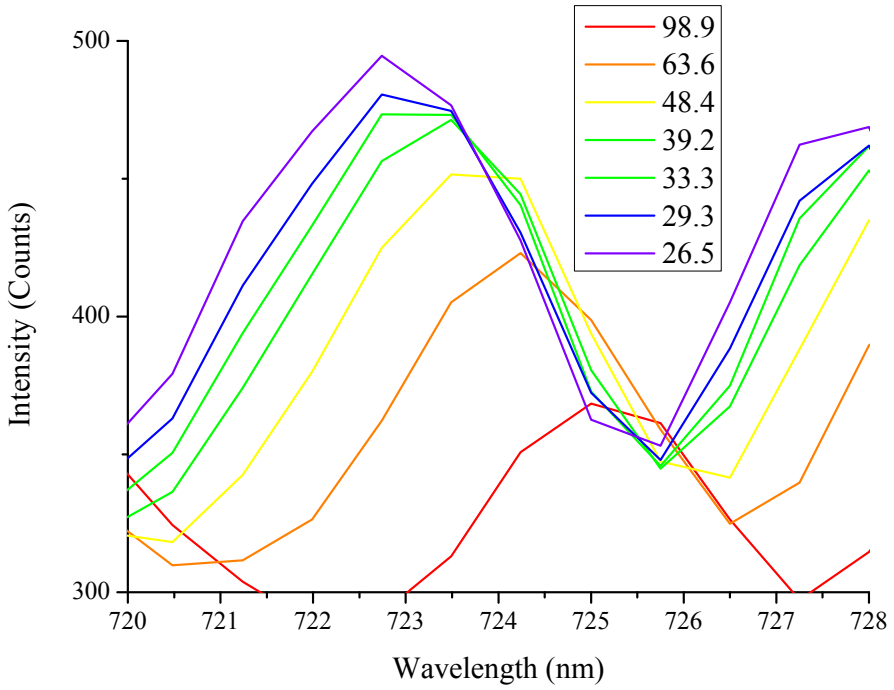

Figure 93: Location and intensity of the first fringe maxima to the right of the central region of the fringes. One spectra every 5 minutes is shown, with the corresponding temperature displayed in the legend.

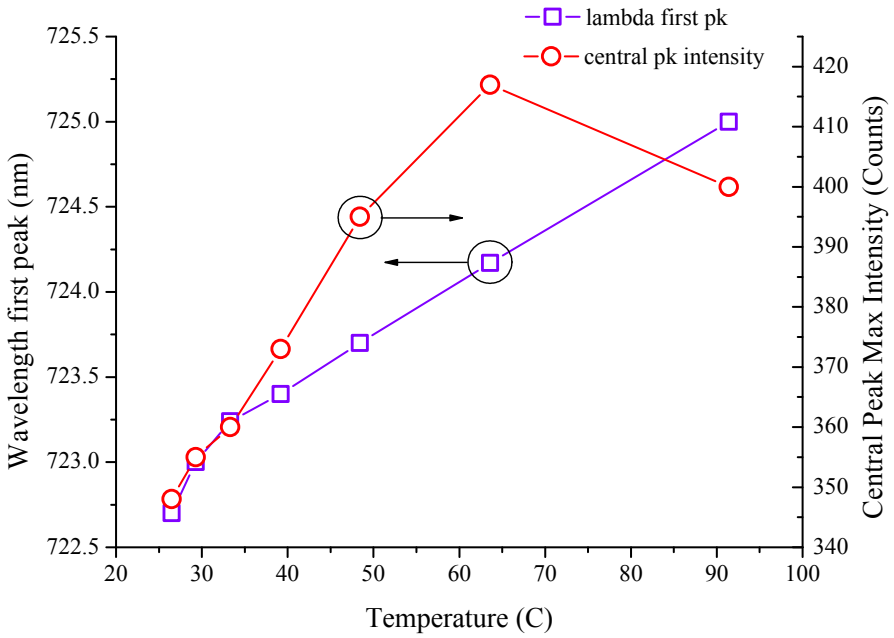

Figure 94: Relation between the two measured parameters and the temperature of the spliced region.

increase the loss through the splice. It is theoretically possibly at least to use this air gap to actually improve the coupling from the wagon-wheel fibre to the SMF fibre. This would likely require individual calibration of each splice unless a more repeatable method could be developed to ensure the gap between the fibres is of consistent width and angle. Allowing the light from the wagon-wheel to propagate in free space for a short length will increase the mode field diameter, possibly improving the coupling as the overlap between this now free space wagon-wheel mode and the mode of the SMF fibre improves.

Additionally, the location of the fringes in both of the splices matches up well with the location of the emission from quantum dots. Since the fringe pattern can be measured simply using the glass fluorescence spectra the temperature can be measured before a fluorophore is introduced, and as mentioned since this should also work when the fibre is filled with Qdots the temperature can also be measured during or after filling. This provides the capability for multiplexing with this spliced fibre, without requiring the use of separate sources to detect either the temperature or the Qdot fluorescence.

3.5 TAPERED DIP SENSOR TIP

One of the desirable characteristics of a dip sensor to sample low volumes is the ability to be able to determine spatially where the sample originates from. This is not entirely feasible using just a fibre tip, as the diameter of these fibres is typically in the order of 125-160 µm, and since samples such as those used for embryo cultures (see Section 7) are of the order of 20 µL the tip is too large to be able to determine the spatial position of the sample with any precision. When dipping the tip of the untapered fibre in a solution it is difficult to accurately place the holes relative to the desired sampling position, and removing the fibre from the solution results in a bubble of fluid forming on the tip of the fibre from surface tension. One of the possible solutions to this issue was to use the same Vytran splicing system used for the splices in the earlier section to instead perform a taper on a capillary to reduce the diameter of the sampling tip, and increase the spatial precision with which measurments can be taken. A capillary was used to simplify initial characterisation, as tapering wagon-wheel fibres introduces additional complexity as care must be taken not to damage the internal structure. Again the iridium filament was used with the Vytran to give better control over the amount of heat that was applied.

The down taper was set to 2 mm, the waist 5 mm and the up taper 1 mm. The taper speed used here was 0.5 mm/s with a filament power of 4 W. This speed is high enough such that the taper occurs rapidly, and on 4 out of 5 trials the taper broke before the splice was complete. This is actually ideal for this application, as if intact the

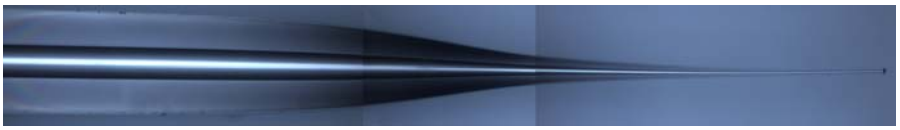

Figure 95: Composite microscope image of tapered capillary. Initial OD 160 µm, inner diameter 40 µm. Waist OD 7.6 µm, inner diameter 2.4 µm.

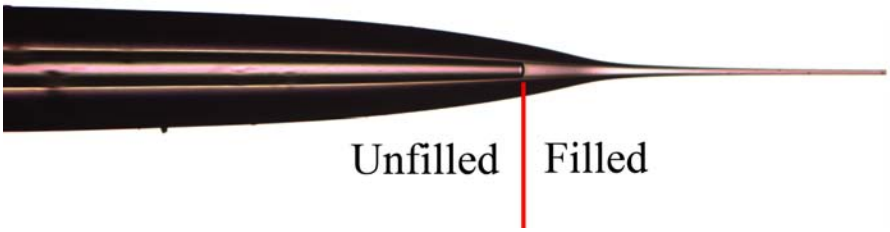

Figure 96: Partially filled tapered capillary. The meniscus has been marked with a red line.

taper needs to be broken at the end of the procedure to expose the tip. Tapering down rapidly enough to break the capillary results in the shortest possible down-taper length increasing the strength and usability of the taper.

The capillary had a small pressure applied to one end, such that when heated the internal hole remained open as the outer diameter reduced. When this process was performed without a pressure applied the internal hole was found to have collapsed before the waist of the taper. Figure 95 shows an example of this type of taper, using a 160 µm outer diameter F2 capillary with an internal diameter of 40 µm. Approximately 60 cm of fibre was cut for this trial, with nitrogen applied to one end to keep the hole open.

This result shows that the hole did indeed remain open over the tapered region. The external diameter of the tip of the taped is 7.6 µm with a total taper length of approximately 800 µm. Here the ratio of the internal:outer diameters has actually increased from 1:4 to 1:2.7 showing that applying a pressure has resulted not only in the hole staying open, but actually increasing its relative diameter. Another trial with a lower filament power (3.5 W) resulted in a taper waist of 30 µm, and an internal diameter of 18 µm which is a ratio of 3:5. This was trialed again using a higher pressure, with the result shown in Figure 96.

In addition to the increased pressure, the tapering speed was also increased for this trial from 0.5 mm/s to 1 mm/s. This resulted in a more rapid neck-down region. For both of these trials the taper was manually cleaved using a scalpel blade. To demonstrate that the hole was open and this tapered region could be used as a sensor probe the top of the taper shown in Figure 96 was immersed in liquid and the taper observed under the microscope. After only 15 seconds liquid

was observed to be filling up the fibre from the tip, and this image shows the meniscus as it travels up the fibre.

By splicing this tapered region, or alternatively even by directly tapering the tip of the wagon-wheel fibre the diameter of the sensing tip can be reduced from 125-160 µm to at least 7 µm. This is of a similar order to the total diameter of all three holes of the fibre shown in Figure 51. By controlling the pressure and tapering parameters it is likely that the internal diameter of the capillary can be maintained while the outer diameter reduces resulting in a small diameter sensing tip that does not impede the filling rate of the fibre. Alternatively the diameter of the hole at the tip of the fibre could be reduced compared to what is demonstrated here by altering the pressure used for the tapering, as while this would reduce the filling rate it should allow measurements to be taken from samples with improved spatial resolution compared to those taken with a larger diameter hole.

4

DIP SENSORS - MICROFLUIDICS

This chapter covers the development of microfluidic techniques for the mixing of small volumes of liquids for sensing applications. This work was performed initially in collaboration with Dr Dominic Murphy, and later with the technical assistance of Ms Mai-Chi Nguyen.

4.1 MOTIVATION

As an alternative to the surface functionalisation techniques investigated in Section 7.5, microfluidic methods were also investigated. While surface functionalisation should provide the absolute minimum required sample volume, other methods that do not require pre-coating of the fibre could also find applications in low-volume sensing. This should allow more rapid development of sensors, as the use of microfluidic mixing does not require specific modification of the fluorophores to allow them to be attached to the surface of the fibre. The general concept behind this is that the sample is drawn and mixed with a fluorophore in a known ratio. Again by using a fluorophore that reacts with the species of interest to generate an increase or decrease in the fluorescent signal a calibration curve can be obtained and measurements performed. This is similar in principle to the low-volume mixing approach in Figure 169, but should allow even smaller volumes to be mixed with good precision. A schematic of a proposed sensing scheme using a microfluidic chip is shown in Figure 97.

The use of a microfluidic chip means that the fluorophore does not have to be especially developed with an attachable tether, so commercially available molecules can be used.

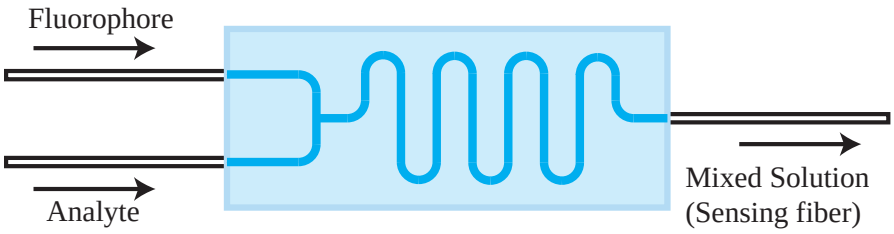

Figure 97: Generalised schematic of a typical microfluidic chip.

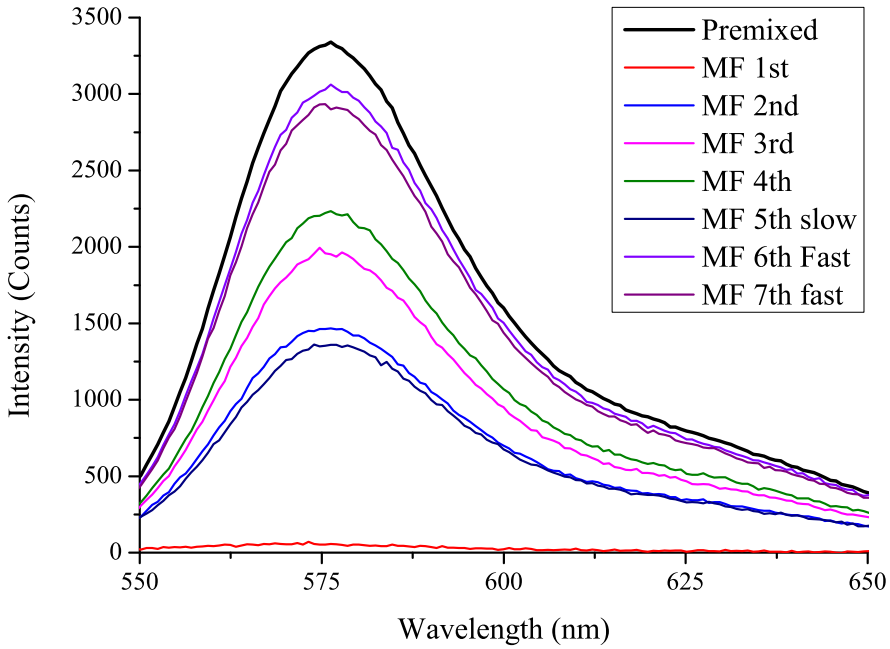

Figure 98: Fluorescence spectra obtained for 100 µM Rhodamine B mixed in a 1:1 ratio with water. The chip was flushed with water between samples 4 & 5. Samples 1-4 are at the same flow rate (50 µL/min), 5 at 25 µL/min, 6 & 7 at 100 µL/min.

4.2 PRELIMINARY WORK - LARGE VOLUME MICROFLUIDIC MIXING

A large volume (>100 µL) microfluidic chip was acquired. To test the initial performance of the chip, rhodamine B was mixed with water. The fluorescence was observed by filling ependorff uvettes with 100-250 µL of sample to be tested in a standard cuvette holder. If the chip was mixing in the correct ratio, then the fluorescence signal obtained in each of these samples should be constant between samples and equal to the amount of fluorescence that is observed when the fluorophore is pre-mixed with water in a 1:1 ratio. To flush the fluids through syringes were loaded with both a 1 µM solution of Rhodamine B and water. A syringe pump was used such that the flow rate could be carefully controlled to ensure that the volumes of the two fluids entering the chip was the same. The results of this trial are shown in Figure 98.

This trial showed that the fluorescence spectra varied significantly between samples. When the fluorescence signal of samples 1-4 is integrated and compared to the pre-mixed sample, the results shown in Figure 99 are obtained.

This shows a clear trend, with increasing quantities of fluorophore passing through the chip leading to a higher signal in the final cuvette measurement. Subsequent trials showed that this initial value could be 'reset' by cleaning the microfluidic chip with ethanol and

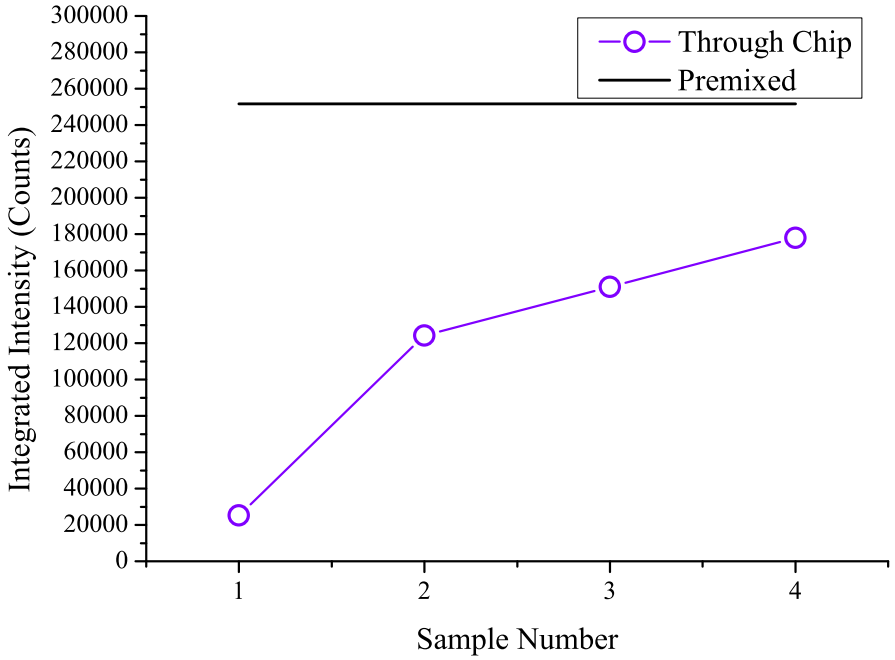

Figure 99: Integrated fluorescence intensities for sequential samples of Rhodamine B mixed with water through MF chip.

acetone. This result strongly suggests that the Rhodamine is sticking, either to the chip itself or to the plastic capillaries used for the input and output of liquid to and from the chip. Since Rhodamine was only intended as a characterisation tool, and not the actual target molecule for this chip approaches to resolving this problem were not investigated in detail.

The trial was repeated using the same procedures, but with Rhodamine replaced by a 20 µM solution of Amplex Ultrared (AUR) (see Section 7.3) and water replaced by a 10 µM solution of hydrogen peroxide. As per the previous trial two control samples were also mixed in a 1:1 ratio from the same stock solutions using a volumetric pipette. The samples were flushed through the chip, and the fluorescence spectra recorded with the results shown in Figure 100.

This result demonstrates that the two fluids are being mixed in a 1:1 ratio, as the results from the chip-mixed samples agrees with the pre-mixed samples within error. However due to the large internal volume of this chip no improvement over the minimum sample size could be obtained with this chip, so while a new chip was being fabricated alternative methods were investigated.

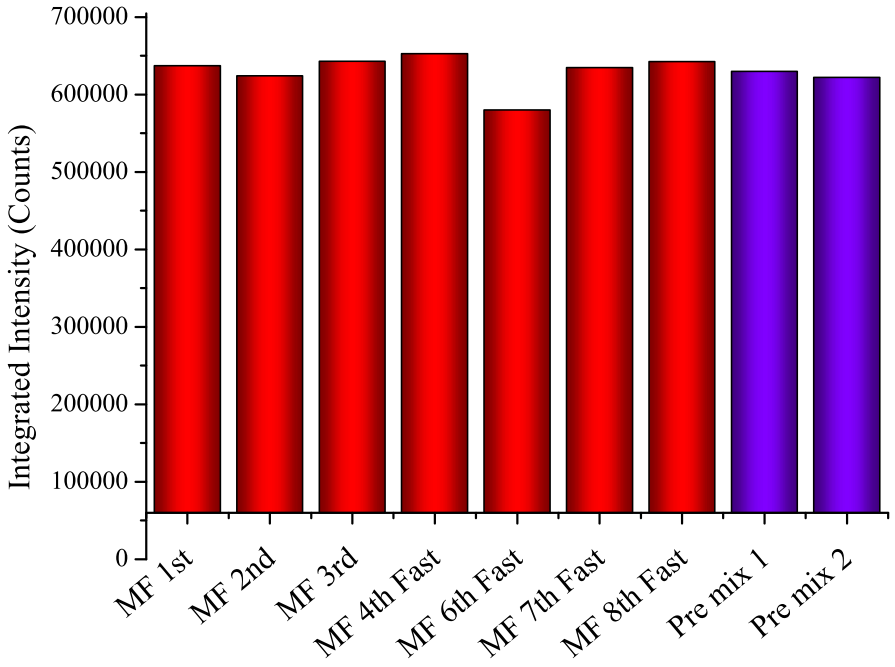

Figure 100: Integrated fluorescence intensities of 20 µM AUR + 10 µM H_2O_2 mixed in a 1:1 ratio for both microfluidic mixing trials (MF) and pre-mixed (Pre mix) trials.

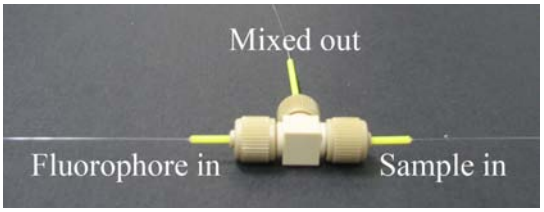

Figure 101: Micro-tee with attached capillaries.

4.3 T-MIXING CONCEPTS

4.3.1 *Concepts*

One of the possibilities that was examined was to use a micro-Tee (µTee) for mixing, with capillaries to provide the channel lengths required for diffusion to occur. The µTee is effectively a small diameter T-junction, with threaded connectors. An example of a µTee is shown in Figure 101.

In this case the µTee is being used with F2 capillaries, with an outer diameter of 160 µm. The yellow PTFE tubes are used to clamp the fibre in place, and by ensuring that the ends of these tubes are cut straight the µTee can be used with zero dead volume. Possible examples of how this µTee could find use are shown in Figure 102. Figure 102a shows the simplest possible system for T-mixing, drawing directly from two reservoirs mixing into a third fibre. This scheme

however requires the fibre to be removed for measurements, as it applies a vacuum from the distal end of the fibre to draw liquids through. The scheme shown in Figure 102b should allow measurements to be performed online as the fibre is filled, but this comes at the cost of increased complexity for the measurements. To allow the basic concept of µTee mixing to be examined only the first case will be considered here.

Figure 102a gives the simplest possible configuration for sensing using this µTee, using two capillaries to directly fill a wagon-wheel fibre. The capillaries could either be immersed in the solutions as shown, or alternatively could be pre-filled with a total volume larger than that of the µTee and fibre combined. Pressure would then be used to fill the wagon-wheel fibre, either through a vacuum on the end of the wagon-wheel fibre or an equal positive pressure on each of the capillaries. This configuration would require the fibre to be removed from the µTee before filling, as the end of the fibre would likely become contaminated affecting the coupling in to the fibre.

Figure 102b shows an alternative scheme, integrating both the µTee with a spliced fibre such as that which was fabricated in the previous section. The general theory behind this concept is to again pre-fill two capillaries, one with a fluorophore one with the analyte to be sampled. A vacuum is then applied to the output on the second µTee, drawing both liquids through to the output. Potentially this would result in a small vacuum also being applied to the wagon-wheel fibre. Once the liquids had been drawn through enough to be certain that equal volumes of each were present within the capillary the vacuum would be turned off, which should result in the partial filling of the wagon-wheel fibre. The extent of this filling depends on the balance of the capillary forces inside the mixing regions, and whether or not the wagon-wheel fibre actually experiences a vacuum.

4.3.2 *Initial trials*

Initial trials using this µTee mixing scheme used the configuration shown in Figure 102a, with a vacuum pump to pull the liquids through the system. The logic behind this is that because both sides of the µTee are being filled with either water+fluorophore or water+peroxide they should have similar surface tension/contact angles/viscosities and as such should flow through the µTee at the same rate. This was tested externally to the pressure setup, simply by observing the fill rate of the two fluids through capillaries. It was found in these trials that the filling rates agreed within experimental error.

Two sets of samples were set up: one mixed in vials using volumetric pipettes, and a second using the µTee mixing system. The capillaries were filled, and allowed to react in the dark for an identical length

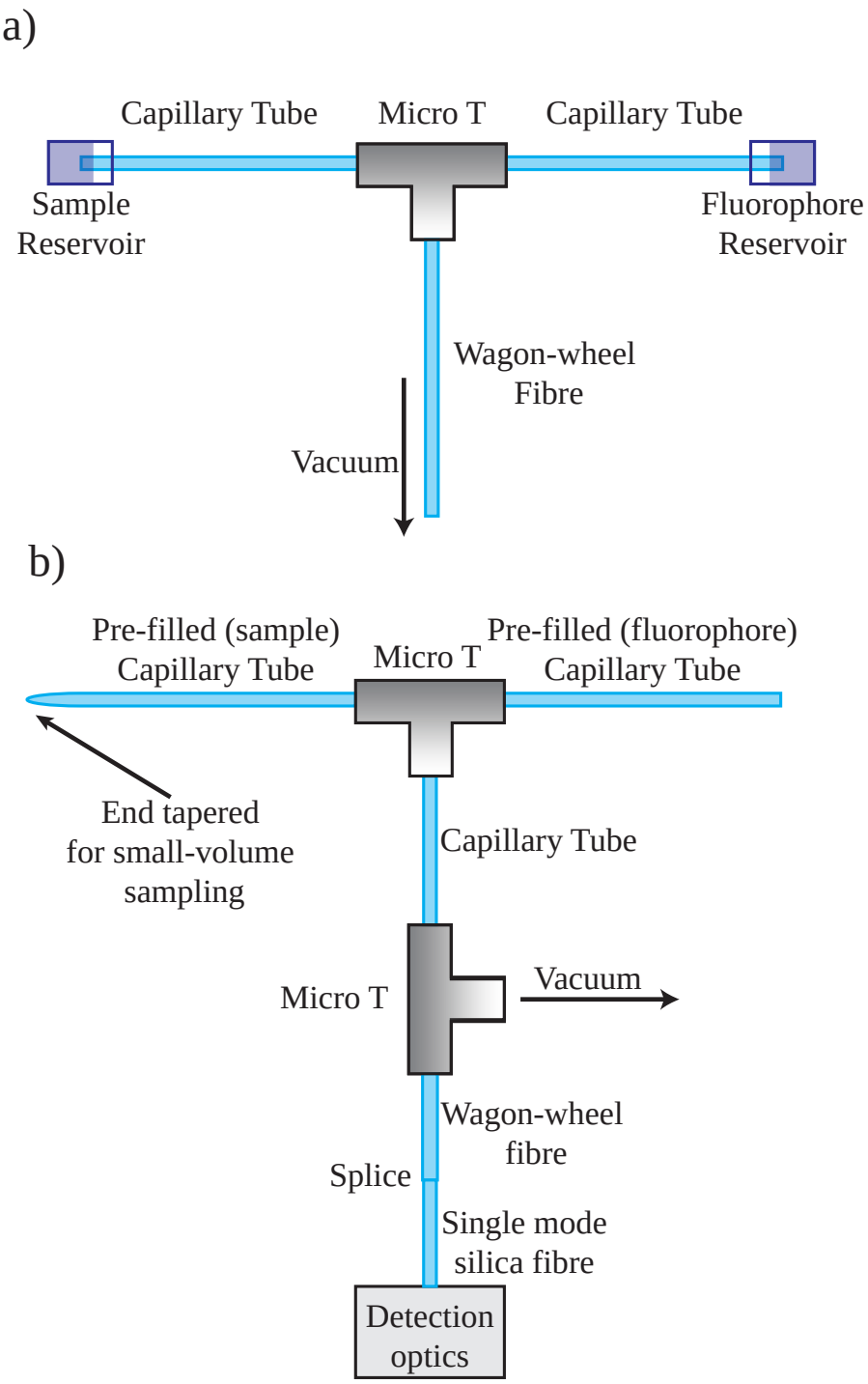

Figure 102: Possible sensing schemes using Micro-T for mixing.

of time. They were then placed on the screen of a Typhoon imager (as used in Section 7.6.8) and scans performed.

The data was analysed by integrating the number of counts observed over a set area that included a section of the capillary, and the background counts subtracted from this data. Analysis suggested that the variation in the number of counts depending on exactly where the box is positioned is somewhat subjective, with variations of up to 20% observed over what visually appears to be a relatively uniform section.

This was repeated several times with different peroxide concentrations (Figure 103) with limited success. All µTee mixed trials showed a consistently lower fluorescence than the samples that had been premixed. This was also tested with varied peroxide concentration and is shown in Figure 104.

Both the initial trials and the trial with varied hydrogen peroxide showed that the obtained signals after being mixed through the µTee were consistently lower for the initial trials, and displayed no variation in signal for the hydrogen peroxide trials.

This was also tested in fibre using the same experimental method, but replacing the output capillary with a 160 µm outer diameter wagon-wheel fibre. This showed similar results to the capillary trials, with µTee mixed samples consistently showing lower counts and limited response to hydrogen peroxide.

Multiple trials showed a typical difference in the fluorescence between the T-mixed and premixed samples with the same AUR and H_2O_2 concentrations of 4-6×. To try and minimise adhesion inside the µTee the assembly was coated with OTS using a similar method to that used for the capillaries earlier. A 5% solution was mixed, several millilitres flushed through the T using plastic tubing and then allowed to incubate overnight. The tee was then flushed with toluene and nitrogen, and checked under the microscope to ensure that the holes through the µTee had not been blocked. Testing using this coated µTee yielded similar results to the uncoated µTees, with a difference between the µTee mixed and premixed samples of 6×.

The most likely hypothesis is that the horseradish peroxidase is not being passed through the µTee or input capillaries, so the reaction between the AUR and H_2O_2 concentrations are unable to occur. Saturation trials flushing through large volumes of solution as was demonstrated with the Rhodamine B in the microfluidic chip earlier demonstrated that even after flushing for in excess of one hour showed no increase in the observed fluorescence signal. This suggests that the fluorophore is not being adsorbed to the surface, as flushing high concentrations (100 µM) through for this length of time would presumably result in at least partial saturation of the surface. Additionally the capillaries show counts above the level observed from an unfilled fibre, further suggesting that there is at least some fluoro-

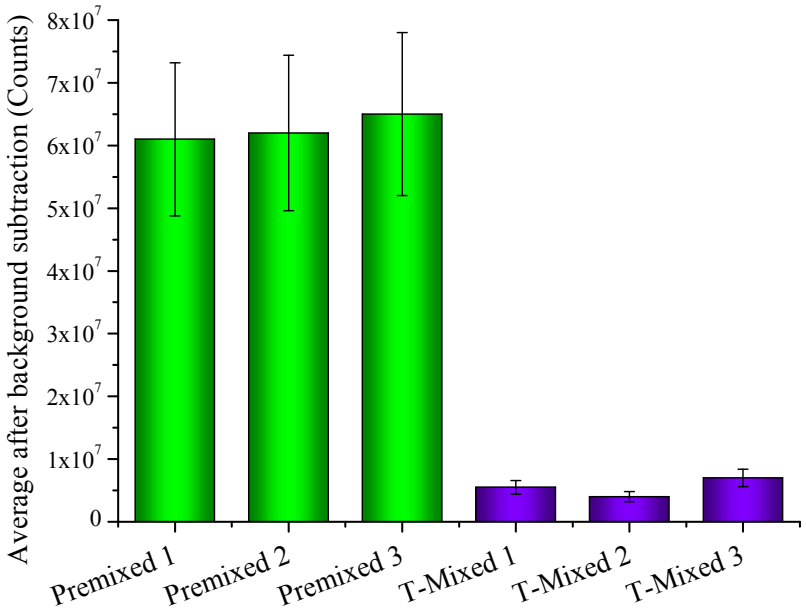

(a) First trial.

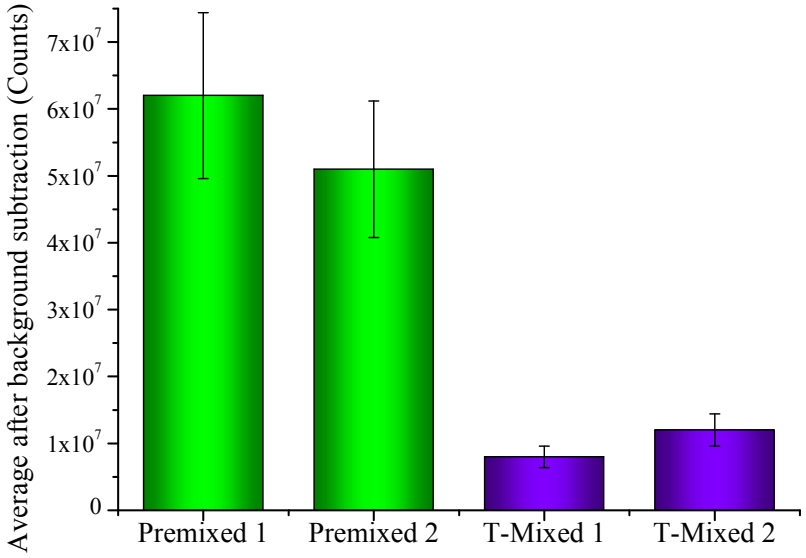

(b) Second trial.

Figure 103: Filled F2 capillaries, with both premixed and µTee mixed fluorophore + peroxide solutions. Error bars show the estimated uncertainty in measurements on capillaries using the typhoon imager.

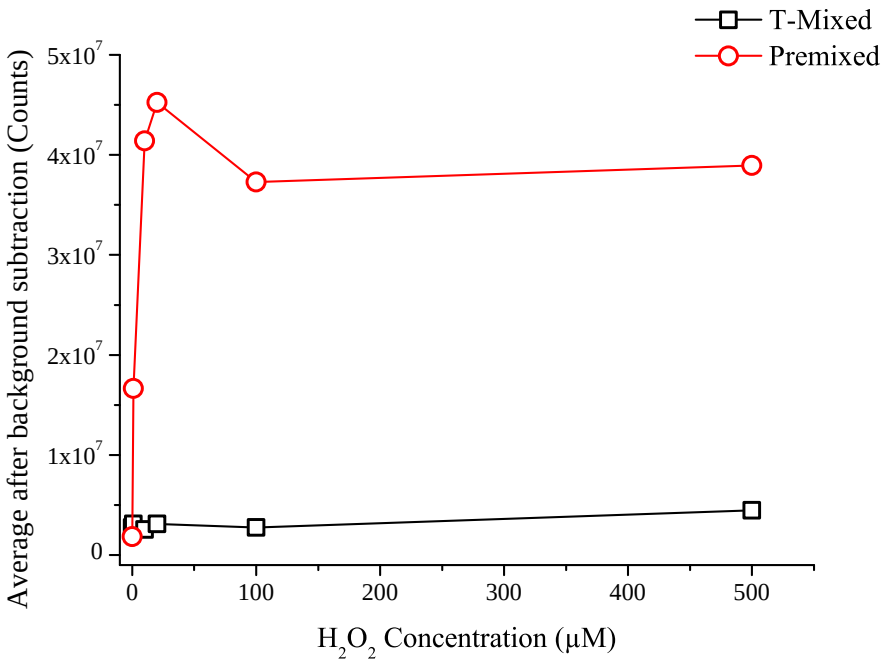

Figure 104: Typhoon imager results with varied hydrogen peroxide concentration for both µTee mixed and premixed solutions.

phore present in the capillary. If the hydrogen peroxide would be depleted again it would be expected that the saturation trial would show an increasing signal over time. Also, the trial varying the hydrogen peroxide concentration tested a concentration 100× the concentration which gave a signal 40% of the peak in the prefilled capillary. A test was performed with 10× the horseradish peroxidase concentration, but again this was unable to ascertain any response to hydrogen peroxide.

These trials demonstrate that in its present form at least this method is not suitable for microfluidic mixing of amplex ultrared and hydrogen peroxide. Extensive characterisation of the cause of this was not performed, as the focus of the hydrogen peroxide sensing work shifted towards surface functionalisation of the Amplex Red Derivative. This however does not preclude the use of this µTee system for mixing of other fluorescent molecules At the time of writing work is progressing on the use of a microfluidic chip as an alternative to the µTee for mixing.

5

ALTERNATIVE GLASSES FOR EXTRUSION AND NEW MATERIALS FOR DIES

This chapter covers work on the development of microstructured optical fibres from soft glasses, with improved short-wavelength transmission compared to previously used materials. This work was done with Prof Heike Ebendorff-Heidepriem, with technical assistance from Mr Alastair Dowler and Mr Roger Moore for fibre fabrication. Annealing trials in a controlled atmosphere in Sections 5.2.6 & 5.3.1 were completed with Prof Ebendorff-Heidepriem and Mr Kenton Knight.

5.1 MOTIVATION - PHOTODARKENING AND SHORT WAVELENGTH EMITTING FLUOROPHORES

As previously discussed one of the primary advantages of using soft glasses for fibres other than their high refractive index is their improved IR transmission compared to standard silica fibres as shown in Figure 105. However this generally comes with the drawback that the transmission of these soft glasses at shorter wavelengths is poorer than their silica counterparts. Typically there is a trend between the refractive index of the glass and its UV transmission, with lower refractive index glasses showing better transmission properties [165]. Since the refractive index of commonly used soft glasses is typically much higher than silica (see Table 2) we expect that the higher index glasses to have a correspondingly poorer UV transmission.

It was discovered during the initial literature survey that fluorophores emitting at shorter wavelengths are better studied and generally easier to acquire as well as being more stable than alternative fluorophores that emit in the visible region. As such to open up more choices for fluorophores it is desirable to have glasses that transmit light further in to the blue and ideally even the UV.

In addition to the practical issues of dealing with increased loss and thus a reduced signal from the fluorophores, it was noted during initial studies using the first synthesised fluorophore that when 458 nm blue light was coupled in to even a relatively large core F2 wagon wheel fibre that the transmission through the fibre decreased rapidly over time. Initially it was assumed that this was due to changes in the coupling, since the laser being used was an air-cooled argon ion laser with relatively poor pointing stability, however further measurements suggested this was instead due to photodarkening.

Photodarkening (or photodegradation) is a process in which defect centres are formed in the glass from incident light, generally at

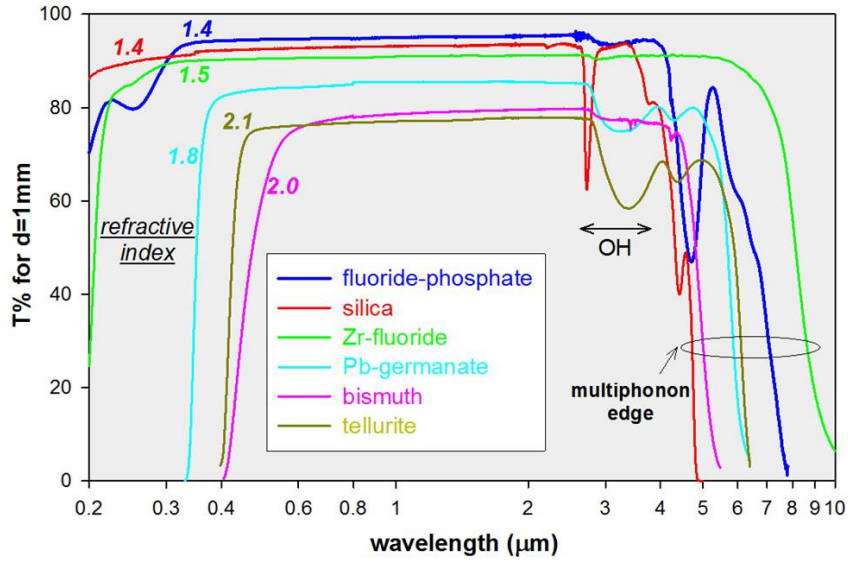

Figure 105: Bulk absorption spectras of various glasses (Courtesy of A/Prof. Ebendorff-Heidepriem).

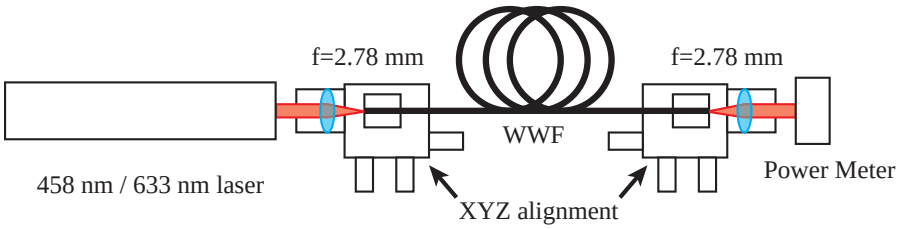

Figure 106: Experimental configuration for measuring photodarkening in wagon-wheel fibres using either a 633 nm He-Ne or 458 nm argon ion laser.

a wavelength close to the UV edge of the glass [166, 167]. It is often seen in both [167] applications especially using upconversion to generate shorter wavelength emission [168], or alternatively in glasses such as chalcogenides [169, 170] where the term "UV edge" typically refers to any visible wavelengths. It has been shown to be power and wavelength dependent [168], with higher powers and shorter wavelengths generally leading to a faster rate.

The experimental configuration was altered such that the distance between the laser and the fibre was reduced to the absolute minimum possible (<50 mm), removing all mirrors and other optics as shown in Figure 106. After altering the experimental configuration the same effects were observed, and it was also noted that the power could not be recovered to its initial level when the fibre was realigned once the measurement was completed.

Previous experience has shown that these fibres can be susceptible to degradation over time that is caused by water vapour entering

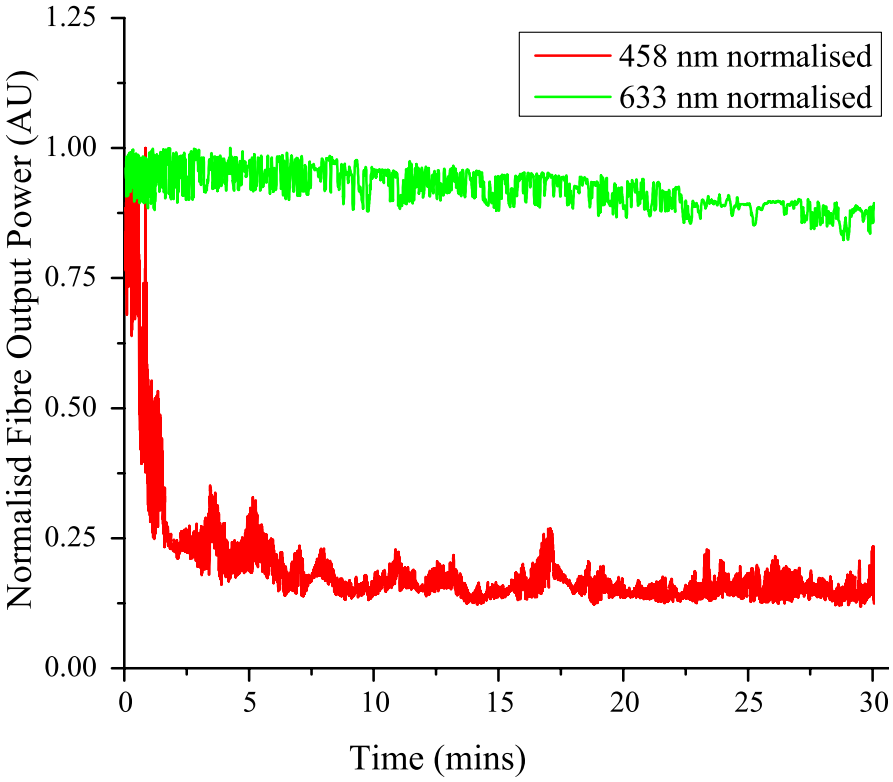

Figure 107: Wagon wheel fibre output power over time, when illuminated with both 458 nm and 633 nm lasers.

the holes of the wagon-wheel fibre. This in turn causes cracking on the surface of the glass, significantly increasing the recorded loss of the fibre. However the reduction in power observed in Figure 107 was also occurring on a much faster time scale than typical degradation of the fibres due to water absorption, with water degradation generally occurring over hours to days rather than minutes. Additionally, the reduction in power was not observed to the same extent when using a longer wavelength 633 nm He-Ne laser, thus suggesting that the shorter wavelength of the argon ion laser was inducing a change in the glass itself.

As can be seen in Figure 107 the transmitted power through a 50 cm length of wagon wheel fibre reduces rapidly when a 458 nm laser is coupled into the fibre, before approaching a steady state level after only a few minutes. Comparing this to the 633 nm sample it is observed that the higher wavelength laser light does not induce additional loss in the fibre, instead the power remains relatively constant over the duration of the measurement. There is some reduction in the power, however this is most likely due to alignment drift. The high frequency fluctuations shown in these plots are due to variations in the coupling into the fibre arising from the previously mentioned poor coupling stability. It is noted that the power for the 458 nm sample

could be recovered slightly after the measurement, but it still only improved to approximately 40% of its initial power level.

These issues make quantitative measurements coupling this laser into a small-core fibre difficult, however the trend can still be clearly observed where the power decreases immediately after the fibre is exposed to the laser radiation. Care was taken when aligning the fibre to minimise the exposure to the laser light before the recording was started, both by performing the alignment rapidly as well as using a neutral density filter to reduce the amount of incident laser light to the bare minimum required for alignment.

It should be noted at this point that although the power reduces significantly when this particular fibre is exposed to 458 nm laser light, the loss of the fibre at this wavelength is not actually that high, with a measured loss of only 2.5 ± 0.5 dB/m compared to the 1.5 ± 0.25 dB/m at 633 nm. This suggests that photodarkening [166, 167, 171] (also known as solarisation [172]) effects can arise in the fibres even relatively early in the UV edge of the transmission spectra. This will be explored in more detail using various bare fibres and a shorter wavelength laser later in Section 5.4.

It has previously been shown in the literature that lead silicate glasses are especially susceptible to photodarkening or photoinduced refractive index changes [173], with the photoinduced changes correlating well with the PbO composition of the glass [174, 175].

As such several commercially available glasses were examined with better UV transmission than the glasses that have previously been used for extrusion with the primary goal of opening up a range of additional choices of fluorophores with shorter wavelength requirements for excitation.

5.2 FABRICATION

5.2.1 *Introduction*

A glass type was chosen from the Schott glass catalogue that possessed the two required attributes - firstly an improved UV transmission compared to other soft-glasses that have previously been used for extrusion, and secondly physical characteristics enabling the glass to be extruded at temperatures suitable for use within the present extrusion furnace. Figure 108 shows the bulk material loss in dB/m, converted from the Schott data for transmittance through 25 mm samples [1]. The glasses in this plot were chosen because they either had been used in the past for extrusions (F2, SF57, LLF1) or showed suitable characteristics such that they should be able to be extruded (N-FK5, N-FK51A). The glass with the best transmission (excluding silica) from the Schott catalogue was N-FK5, so this was chosen for the initial trials. Several samples such as that shown in Figure 109

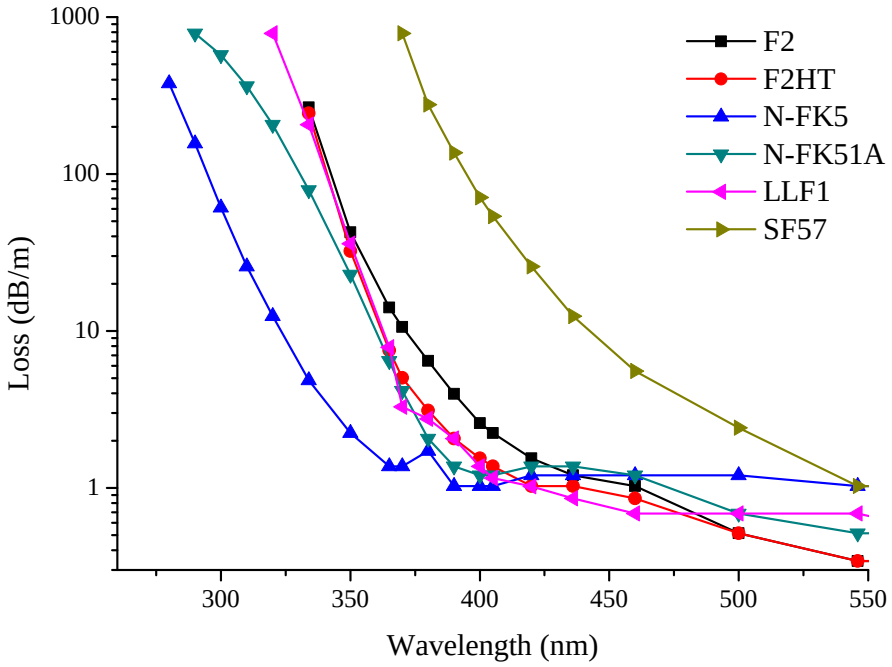

Figure 108: Short wavelength transmission for various soft glasses suitable for extrusion [1].

were acquired and manually polished for extrusion trials, an example of which is shown in Figure 109.

5.2.2 *Stainless steel die*

Although the desired fibres from this glass are microstructured wagon-wheel fibres similar to those used earlier, it was decided that initial trials would involve the simplest possible rod geometry to fabricate an unstructured bare fibre. This fabrication process results in a fibre with no higher index core or microstructured region such that the light is guided using total internal reflection on the outer surfaces of the fibre. When testing a new glass this is typically the first fibre type that is tried, as it is the least sensitive to fibre drawing conditions and enables one to determine the transmission losses of the fabricated fibre. The bare fibre suffers no additional losses induced by the fibre geometry, and allows any excess losses induced by the extrusion process to be inferred.

For this trial a 10 mm hole diameter stainless steel rod die was used, with a billet length of 30 mm. Steel is the most common material used for extrusions, and has been used with success for a number of different soft glasses. The preform was extruded at 650 °C, with a maximum force of 13 kN. The fabricated preform is shown in Figure 110a below.

This preform showed an extremely poor surface quality along its length, with deep scratches running along the preform in addition

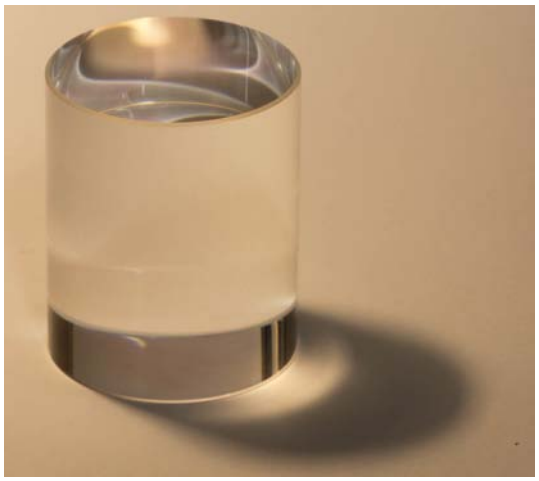

Figure 109: Polished N-FK5 Glass Billet.

Figure 110: a) N-FK5 extrusion trial one. The surface has been significantly degraded, showing what appears to be rust along the length of the preform. b) N-FK5 extrusion trial one after the preform was cut, and the surface manually polished along its length.

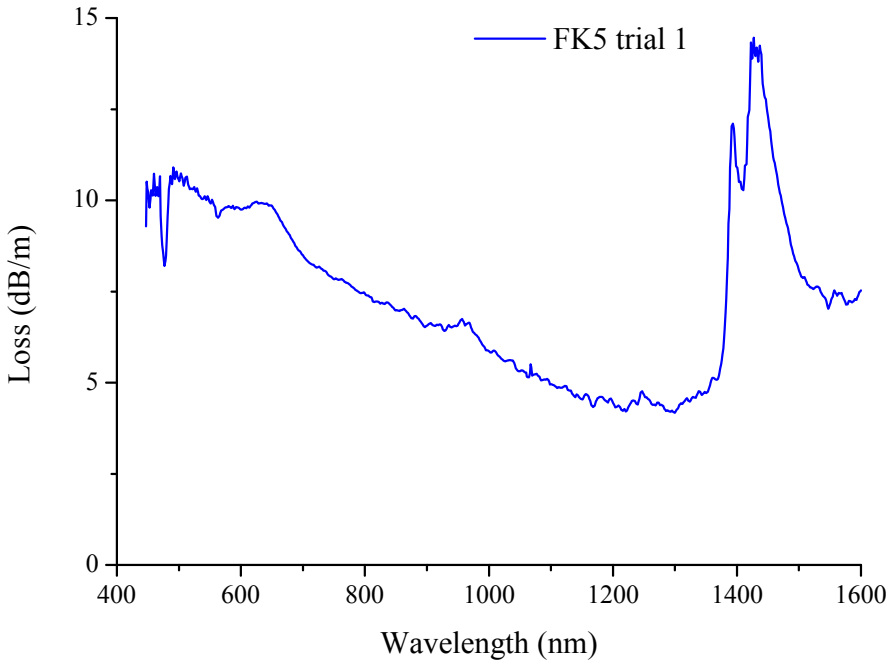

Figure 111: N-FK5 trial 1 loss spectra. Points below 440 nm have been removed due to excessive noise in the measurement.

to the obvious reddish brown rust coating the middle section of the preform. The surface of the extrusion die also showed significantly more degradation than is typically seen, with large amounts of rust seen on the exit face of the die.

Although the fibre would likely be of questionable quality, it was decided to attempt to pull this preform in to a fibre to determine approximate drawing parameters. The preform was cut along the straightest section, and manually polished to remove the surface layer. The final outcome of this polishing is shown in Figure 110b. It should be noted that a perfect surface quality was not achieved using this manual polishing method, as some fine scratches could still be observed on the preform. However this was still a significant improvement over the initial quality of the surface.

The loss spectra of the fabricated fibre is shown in Figure 111. Although this loss is high compared to that of fibres previously fabricated from glasses such as F2, it was a promising result for two main reasons. Firstly, the fibre loss, even with the questionable surface quality was already within acceptable limits for fabricating a sensing fibre. As only short lengths of around 20 cm are required to make a practical fluorescence sensor, a loss of 10 dB/m has a minimal effect on the observed fluorescence signal.

Secondly, it was possible to handle and cleave the fibre. One of the drawbacks of soft-glass fibres compared to silica fibres is that they are typically weaker than conventional fibres and there were concerns with this previously unknown glass that the fibre could be weak and

fragile. Finding that this fibre was practical to handle was a promising discovery, especially considering the prospects for improvements to the quality of the fibre if the initial surface quality of the preforms could be enhanced beyond what has already been demonstrated in this section.

5.2.3 *Unstructured MACOR*

Since the surface quality of the first N-FK5 preform was poor, a different extrusion die material was needed. Previous to this work, only two materials had found common use as extrusion dies at the University of Adelaide. The most used material is stainless steel, which is used for all oxide glass extrusions for glasses including F2, LLF1, SF57, bismuth and various tellurite glass compositions. The second material used is graphite. Graphite has previously found use as an extrusion material, both internally [76] and elsewhere [97]. Previous work has found that using graphite materials in place of steel gives better quality surfaces for ZBLAN fluoride glass extrusions. It has been shown [76] that since graphite is not wetted by glass the required force for the extrusion drops, allowing the extrusion temperature to be dropped leading to less crystallisation (and thus loss).

Although graphite would seem to be the obvious choice for fabricating an extrusion die, it has several drawbacks. Firstly, it is relatively brittle, leading to limitations on the extrusion force to prevent die die from breaking. Secondly material from the die can be removed by the glass during the extrusion, leading to graphite particles being embedded in the glass itself. When drawn in to fibre these then potentially lead to a greatly increased fibre loss. Past work has mitigated the effect of this by cleaning the graphite multiple times using methanol and an ultrasonic bath, significantly reducing the effect of this shedding process.

The main drawback however is that it oxidises at higher temperatures such as those required for N-FK5 extrusions possibly degrading the surface of the die and thus reducing the quality of the fabricated preform. The machine used for extrusions can be flushed with nitrogen, however this is a simple system, in which only the bottom of the machine has a gas-tight seal and the quality of the nitrogen atmosphere relies on the constant flow of gas from the bottom of the machine to flush out oxygen. Additionally it is not possible to purge the furnace, and it was considered to be cost-prohibitive to perform this upgrade. As such a different material for extrusion needed to be considered.

MACOR was chosen as a possible die material, as it is both easy to machine with good surface quality and should survive the high temperatures of the extrusion process with no detrimental effects. It comprises of 55% fluorophlogopite mica and 45% borosilicate glass [176]

Figure 112: Rod die and sleeve fabricated from MACOR, with FK5 billet shown inside the sleeve.

and has a maximum working temperature of 800 °C with good shear strength making it ideal for use as an extrusion die. Interestingly the composition of MACOR is similar to that of the N-FK5 glass itself, however the MACOR possesses a much higher working temperature than the glass due to its crystalline structure.

A die, sleeve and top plate were fabricated from MACOR. The design used was identical to that used with stainless steel, and the die was inserted in the same stainless steel outer body in which other extrusions are performed. Extrusion parameters were identical to that used in the initial trial with the stainless-steel die. It was decided to do an initial trial using LLF1 glass, since this has been characterised previously using a stainless steel die and bare fibre. As such this should provide a good baseline to demonstrate whether the MACOR affects the surface quality of the glass enough to impair either the strength or transmission properties of the glass. It is also the glass with the closest extrusion temperature to N-FK5, thus giving the best comparison with the closest parameters.

As can be seen in Figure 113 the measured spectra are similar in shape and magnitude to that previously obtained when extruding through a stainless-steel die, differing by only 0.05 dB/m at 633 nm. Additionally, the fibre still maintained good physical strength, which as previously mentioned is an important characteristic for fabricating useful fibres.

Drawing clear conclusions from these measurements is difficult due to the inherent uncertainties in loss measurements, which makes comparisons between measurements that are very close to each other difficult. Due to the destructive nature of these measurements, it is typically not possible to obtain a second spectra, as each loss measurement requires in the order of 5-10 m of fibre depending on the loss. The main conclusion from this trial was that the MACOR does not significantly alter the loss or physical strength of LLF1 bare fibres,

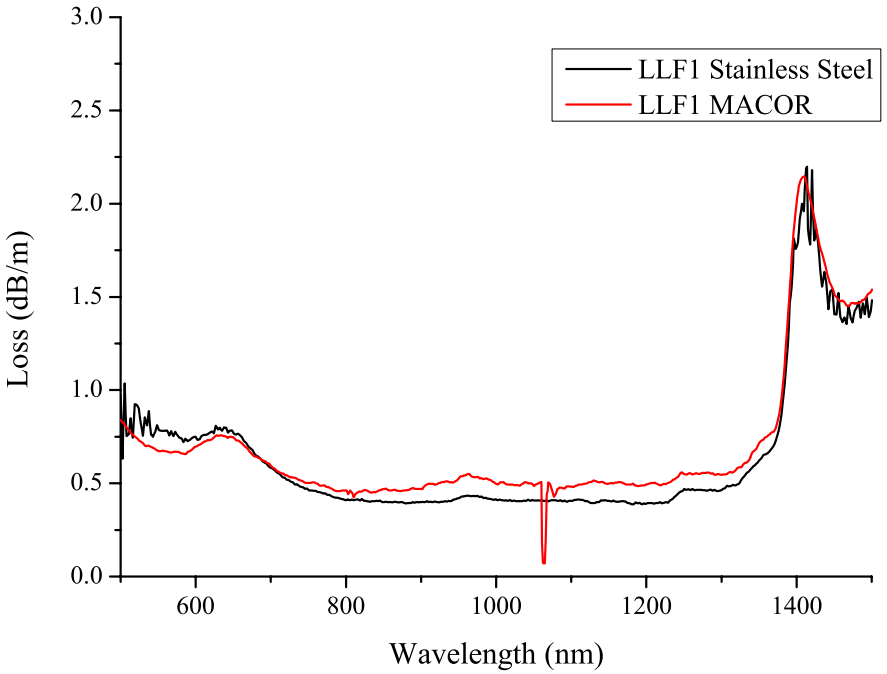

Figure 113: Loss spectra measured for fibres with preforms extruded through both MACOR and stainless-steel dies. Drawing parameters were similar between the two, with a final fibre outer diameter of 160 μm. The dip at 1060 nm in the LLF1 MACOR spectra is due to sharp features in the excitation source used for the loss measurement. This is not present in the stainless-steel spectra as a standard bulb was used for this measurement.

(a) N-FK5 extrusion trial 2.

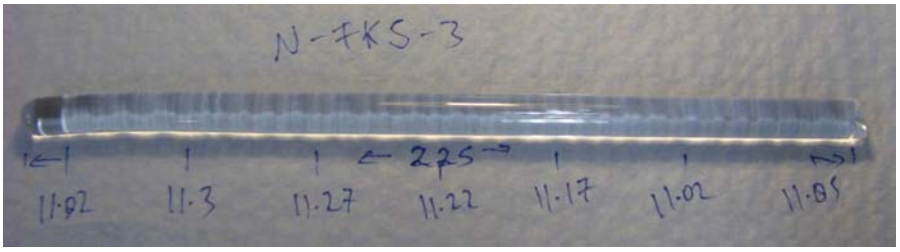

(b) N-FK5 extrusion trial 3.

Figure 114: N-FK5 Extrusions through MACOR.

with results being obtained that are comparable to the best previously seen using stainless-steel dies.

Following the successful extrusion and subsequent drawing of an LLF1 fibre through MACOR, two trials were performed using N-FK5 through MACOR dies: one with an air atmosphere (FK5-2) and one with nitrogen (FK5-3) to examine the possible difference to fibre quality that the atmosphere could make.

The preforms are shown in Figure 114. Both show significantly improved surface quality over that seen with the previous extrusion, although some light marks are observed along the lengths of the preforms. These are possibly due to imperfections in the surface of the die itself, as some fine chips could be seen on the inside rim of the extrusion die.

The two fibres fabricated from these two preforms showed considerably improved characteristics, both in their optical transmission properties and mechanical strength. Figure 115 strongly suggests that the higher measured loss of the first trial was due to scattering, as the loss increases with decreasing wavelength compared to the relatively flat spectra of the second two trials.

So by changing to MACOR as a die material we have successfully reduced the measured fibre loss (Figure 115) at 458 nm from the ~10 dB/m of the initial trial, to 2-3 dB/m which is a significant improvement. The bulk loss of this glass is ~1.3 dB/m at this wavelength so some loss is still being induced in the fabrication process, however the measured loss here would be at an acceptable level for use as a sensing fibre.

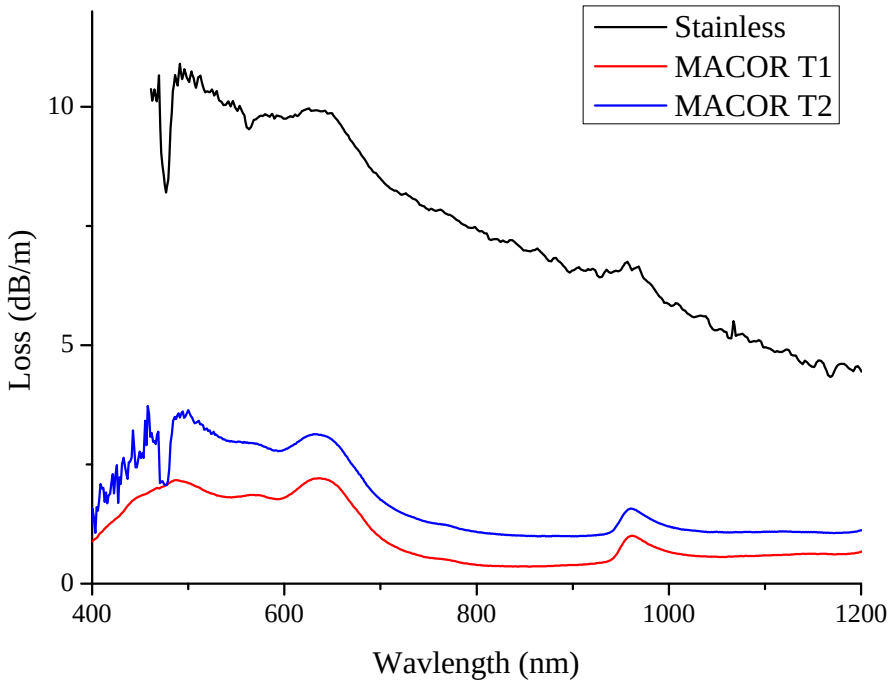

Figure 115: Measured loss spectra of FK5 trials 1 (stainless steel), 2 (MACOR, air atmosphere) and 3 (MACOR, nitrogen atmosphere).

5.2.4 *Structured extrusions through MACOR*

5.2.4.1 *FK5*

With the successful fabrication of two bare fibres from N-FK5, the next obvious step was to move towards fabricating a microstructured fibre suitable for sensing applications. Two dies were fabricated from MACOR for the purpose of creating a structured preform using a MACOR die: a 10 mm outer diameter, 1 mm inner diameter rod die (Figure 116b) and a standard wagon-wheel die (Figure 116a). It was planned to use a standard two-step extrusion process to fabricate an FK5 wagon-wheel fibre, first drawing the wagon-wheel cane down to approximately 1 mm then inserting this into the tube and pulling the whole assembly down to approximately 160 µm.

It was decided to first extrude the outer jacket, as this is the simpler structure with less critical features. The results of the first trial are shown in Figure 117a. In this trial the end face of the tube die, which can be seen in Figure 116b sheared from the end of the extrusion die. The final outcome of this was a tube with approximately 17 mm outer diameter, and 5 mm inner diameter which formed due to the shape of the spigot inside the die. This extrusion also showed an extremely poor internal surface quality, which will be discussed in more detail in Section 5.2.5.

(a) MACOR wagon-wheel die.

(b) MACOR tube die outer assembly, iteration 1. A standard tube-die inner was also fabricated from MACOR, however this is not shown here.

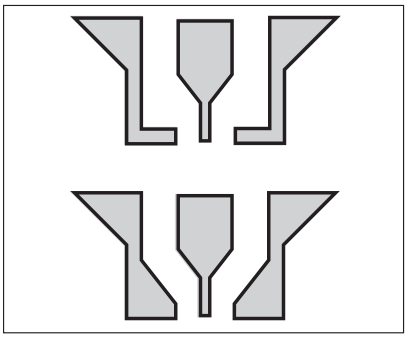

(c) Schematic of modifications to tuber die outer assembly for improved strength.

(d) Cross-type die for 10 mm outer 1 mm inner diameter tube extrusion. This die design as been shown in the past to reduce the required force with identical extrusion parameters.

Figure 116: MACOR Dies used for extrusions.

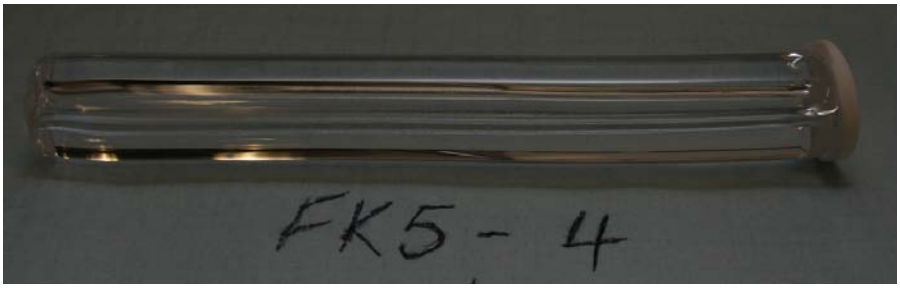

(a) First FK5 tube extrusion trial through MACOR die. The die failed almost immediately at the end face.

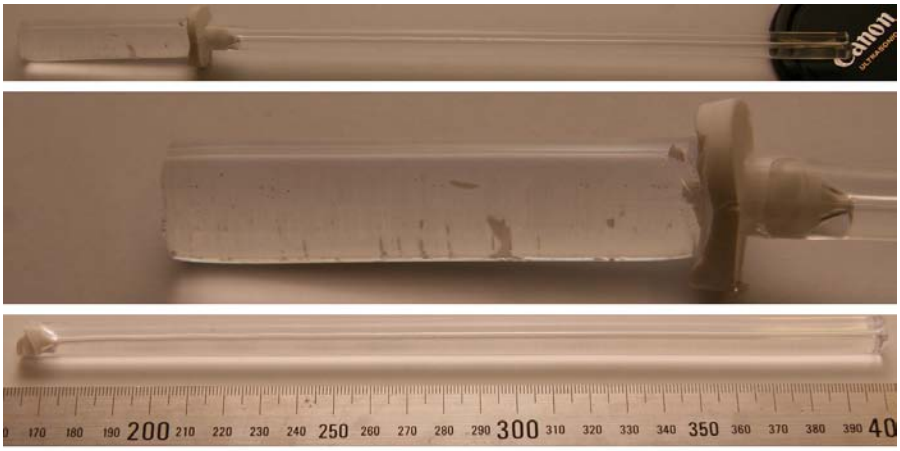

(b) Second trial with modified die design as shown in Figure 116c. Top - total extrusion length. Middle - close up of end of extrusion, and broken die. The failure point on this extrusion was the internal spigot, and it can be seen here embedded inside the outer tube. This die component caused the end face to fracture from the rest of the die, resulting in the large diameter rod. Remnants of the die can be seen in the surface of the glass beyond this point.

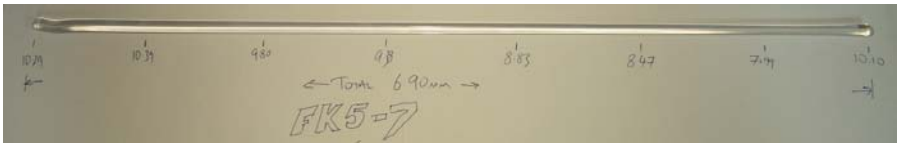

(c) Third FK5 tube extrusion through MACOR, using modified cross-type design shown in Figure 116d. The preform shows good external surface quality, however the internal surface is extremely poor.

Figure 117: Microstructured tube extrusions using N-FK5 glass with MACOR dies.

The design of the extrusion die was subsequently modified to that shown in Figure 116c. Two primary motivations lead to this design - firstly to increase the amount of die material at the point of highest stress (the end face) as well as to replace the sharp corners and perpendicular end-face with a constant slope thus reducing both the total force required for the extrusion as well as the stress on the die.

The result of this extrusion is shown in Figure 117b. The modifications to the outer structure of the die were shown to be successful, as the failure point shifted from the outer structure of the die to the inner spigot. On close inspection, it was concluded that the inner spigot sheared from the die approximately half-way through the extrusion. As the spigot was larger than the size of the hole on the end face the extrusion forced the broken spigot through the outer die, breaking the structure and resulting in a preform consisting of approximately 60% 10 mm tube and 40% 17 mm rod.

Although the tube was of the correct dimensions, it was again noticed that the internal surface quality inside the tube was extremely poor. It was hypothesised that the high shear forces on the glass as it hits the internal spigot in the tube die were inducing crystallisation in the preform. Previous extrusion trials had demonstrated that an alternative geometry for the tube extrusion die showed a lower total force, making it likely that the localised force on the glass at the spigot would also be lower.

This die design is shown in Figure 116d. The additional modifications to the die design, in the altered sleeve design and addition of a lip to the extrusion die come about for a separate reason. This is shown in detail in Figure 118. Early extrusion trials with FK5 had demonstrated that even at a relatively low extrusion force, the die and sleeve assembly were extremely difficult to remove from the outer stainless steel body. Frequently the removal of the die from the body would result in failure of the die, leaving the sleeve inside the body. It was discovered that this issue arose from the leakage of glass between the extrusion die and sleeve into the body itself.

This glass moved into the gap between the die and sleeve at high temperature and force effectively acted as a glue when the extrusion was halted and the furnace cooled. The proposed solution to this was to modify the die design, enlarging the die and adding an outer lip. By slotting the sleeve inside this lip, a seal is created effectively preventing glass from penetrating the seal between the die and sleeve removing the issue of glass gluing the sleeve to the body. This also has the additional effect of preventing contamination of the glass, as it is always contained within the clean extrusion sleeve.

A trial was attempted using this die design, and is shown in Figure 117c. This extrusion, performed at a relatively high temperature to minimise the force the glass experiences resulted in a complete preform with no die breakage with a total length of 690 mm. The

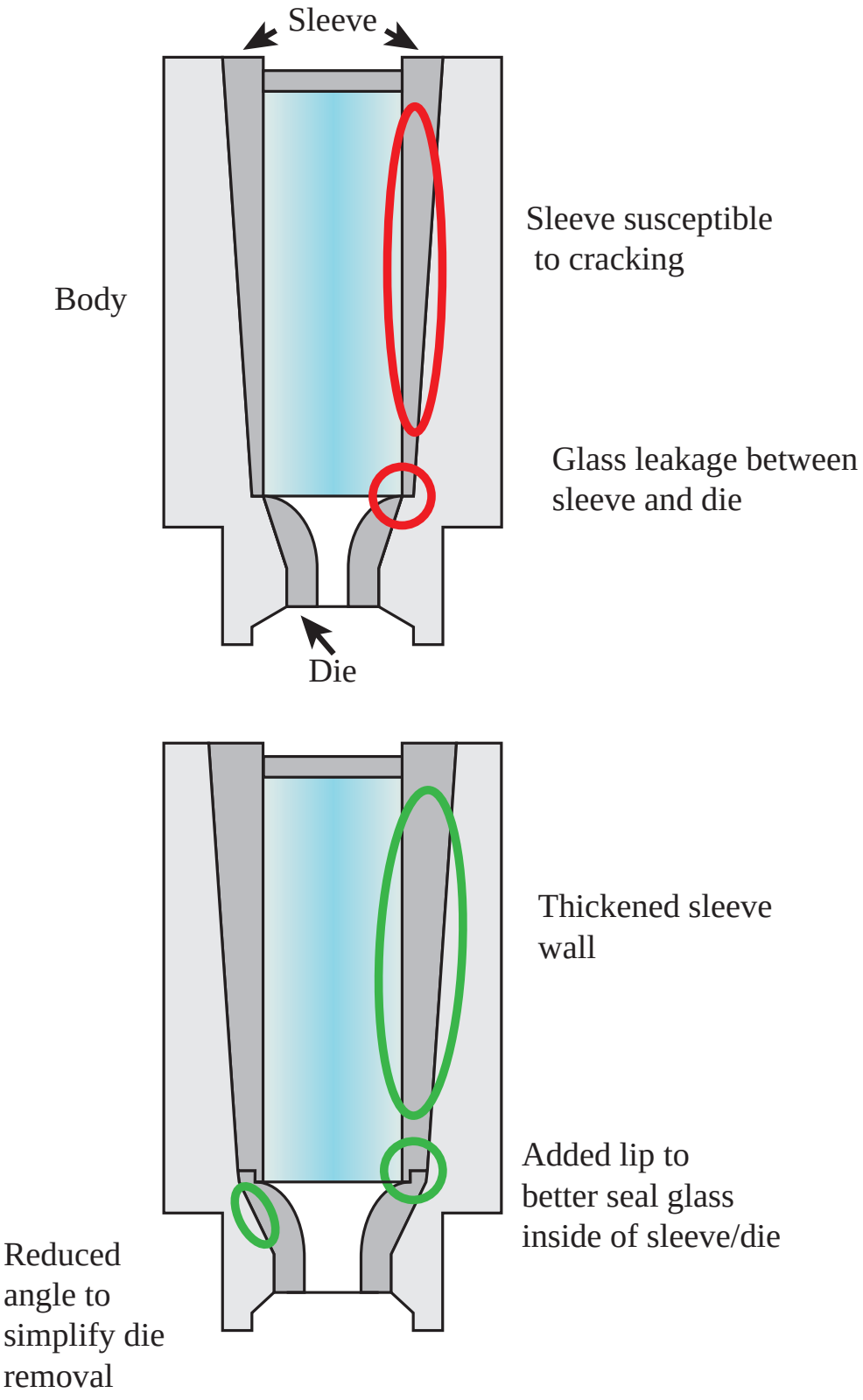

Figure 118: Modified die and sleeve design to more effectively seal the glass inside the sleeve, showing comparison between the old die design (top) and the modified design (bottom). Failure points are circled in red, modifications to the design are circled in green.

Figure 119: (top) Extruded FK5 wagon-wheel preform. The location of the preform where the die failed can be seen where the outer section of the struts rapidly expands. (bottom left) MACOR wagon-wheel die before extrusion. Note the gap between the struts. (bottom right) MACOR wagon-wheel die after extrusion. The die has failed part way through the extrusion, pushing the die parts out and creating a "Y" shape."

outer surface quality of the preform was again quite good, however the internal surfaces showed extensive defects. Due to the poor surface quality experienced on all microstructured fibres it was decided to temporarily suspend work on N-FK5 extrusions through MACOR and systematically examine other possibilities for extrusion die materials.

As a final trial a wagon-wheel die was also fabricated from MACOR, and a trial using FK5 performed. For this trial the speed of the extrusion was reduced significantly compared to a standard wagon-wheel extrusion, with only 0.05 mm/min used for this trial compared to the 0.2 mm/min of an extrusion through steel. The results of this trial are shown in Figure 119.

This trial was unsuccessful, for two reasons. The first and most obvious was the failure of the die. Only a short section of the preform had been extruded before the die failed, pushing the die outwards and blocking the ring around the struts. This resulted in a wagon-wheel preform with thick struts, no obvious core and deformed regions at the end of the struts. The second and more concerning part

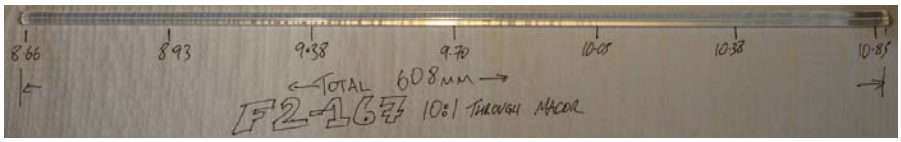

Figure 120: F2 Tube extruded through cross-type MACOR die.

of this extrusion was again the surface quality of the preform. Even before the failure of the die the preform is noted to have a "misted" appearance, possibly caused by crystals forming in the glass. The surface quality degrades further as the extrusion progresses, with the same types of large pits and scratches observed on this preform as was seen on the earlier tube extrusions.

So in conclusion to date we have been unable to successfully fabricate a structured FK5 preform, due to a combination of die failures and preforms with poor surface qualities. However the viability of MACOR as an extrusion die has been proven, at least in regards to its ability to stand up to the forces of the extrusion. The successful tube die extrusion shows that with some modification of the die design compared to the original versions from steel that this can find use as a die material. However more testing is required to determine whether or not the poor surface quality of the above preforms arises from the MACOR itself, or if it is unique to the glass that was used here.

5.2.4.2 *F2*

Following both the successful extrusions and subsequent fibre drawing of the N-FK5 bare fibres an extrusion was performed using an F2 billet in the same cross-type tube extrusion die previously used (Figure 116d) with MACOR. The aim of this trial was to determine if the defects seen on the inner surfaces of the N-FK5 extrusions were caused by the removal of the MACOR from the surface of the die, or if alternatively it was simply due to a process occurring within the glass itself.

The results of this trial are shown in Figure 120. This preform showed good internal and external surface quality, strongly suggesting that the defects do not arise directly from MACOR particles being removed from the surface, but instead involve some complex interaction between the glass and the die under pressure. Again the internal surface quality will be examined in more detail in Section 5.2.5 below. The force for this trial was similar to that used in the earlier FK5 extrusions.

The reason for the differing behaviour of F2 and N-FK5 through identical dies (and materials) is not known, but it is likely due to the pressure inside the die inducing crystallisation inside the glass. It seems probably from these trials that the F2 glass is more resistant to

(a) N-FK5-1 extruded through stainless-steel die.

(b) N-FK5-2 extruded through MACOR die.

(c) N-FK5-3 extruded through MACOR die, nitrogen atmosphere.

Figure 121: Rod extrusion surfaces. Glass was ultrasonically cleaned in detergent and methanol to remove any loose particulate matter such that any remaining defects were either firmly affixed to or embedded within the glass.

crystallisation, so the additional force does not induce defects in the glass.

5.2.5 *A closer inspection of surface quality*

As previously mentioned in Section 5.2.4, poorer surface qualities were observed on the internal surfaces of FK5 tube extrusions through MACOR. To examine these in more detail, a small length of preform was removed. This length was then cut again along its length close to the central hole, and then manually polished to expose the internal surfaces. The internals of these preforms could then be imaged used a microscope to attempt to determine the cause or origins of these imperfections. The preforms were thoroughly cleaned using an ultrasonic bath after cutting to remove any residual debris from this process.

Images were obtained for both the internal surfaces of the microstructured extrusions, as well as the external surfaces of rod extrusions.

The results in Figure 121 agree with the expectations from macroscopic examinations of the preforms. The stainless-steel die showns the most defects, which mirrors the overall preform quality shown in Figure 110.

Figure 121b shows a reduced amount of defects compared to the stainless-steel extrusion, further showing that MACOR improves the surface quality of the extrusions. The composition of the defects was not studied, they are likely composed of either abraded MACOR particles or small crystals formed within the glass. Only the surface layer of this extrusion shows these defects, small samples that were polished did not show the same quantity of defects.

The final rod extrusion of N-FK5 through MACOR in a nitrogen atmosphere and is shown in Figure 121c. The defects in this sample are more numerous than those of the sample in an air atmosphere (Figure 121b) however they are significantly smaller in size than either of the previous extrusions.

It can be quite clearly seen from the images in Figure 122 that the surfaces of the structured FK5 preforms show significantly poorer surface quality than either the F2 MACOR extrusion in Figure 120 or the earlier unstructured FK5 extrusions through MACOR. Large crystal centres can be observed in the majority of the trials, and even in locations where these large defects are not observed the surface quality appears poor, such as the wagon-wheel preform shown in Figure 123. Further trials (see next section) demonstrated that raising the temperature of the extrusions was not feasible, and indeed it is unlikely that the temperature of the extrusion could be lowered further than was used for the FK5 wagon-wheel trial (645 °C). Reducing the speed of the extrusion drastically could possibly reduce the force such that the temperature can be lowered, but has the side effect that the glass spends longer in the hot-zone of the furnace and as such the probability of crystallisation is increased.

5.2.6 *Temperature dependence*

Since all structured FK5 extrusions had showed a poor surface quality an examination of exactly how the glass responds to temperature was required to determine if the poor surface quality was solely due to the temperature of the extrusions, or if it was indeed a product of a reaction with the die material. To test this, glass samples were cut to thin disks, and mechanically polished on one side. These were cleaned using the standard technique, and placed in a nitrogen atmosphere inside a controlled atmosphere furnace. Each sample was sequentially placed in the furnace at a set temperature on a platinum plate and left for a period of one hour. The top (polished) surfaces of the samples were examined using a 50 × objective on the microscope as shown in Figure 124.

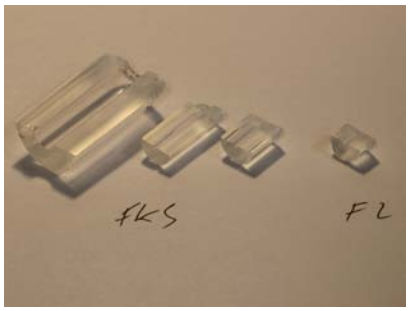

(a) Sections of tube extrusions used for surface quality measurements.

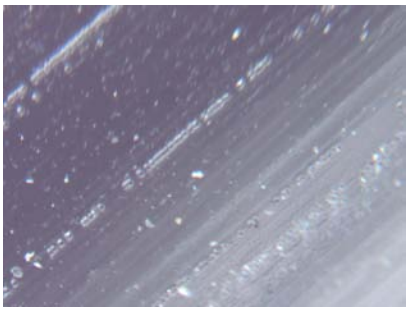

(b) Internal Surface of large N-FK5 tube shown in the Figure 117a).

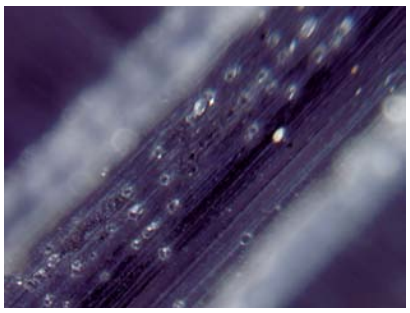

(c) Internal surface of N-FK5 tube shown in Figure 117b).

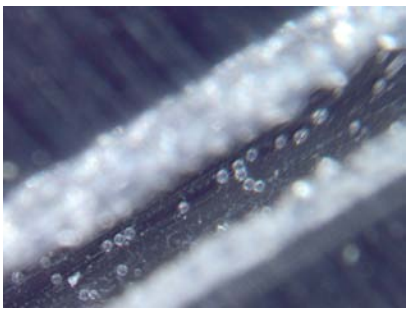

(d) Internal surface of N-FK5 tube shown in Figure 117c).

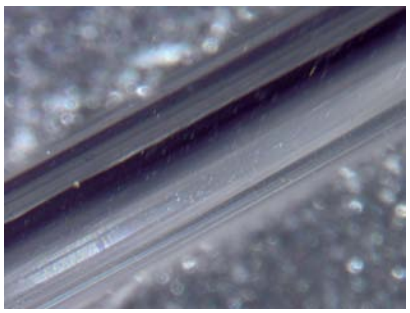

(e) Internal surface of F2 tube shown in Figure 120.

Figure 122: Microscope images of internal surfaces of both N-FK5 and F2 extrusions through MACOR tube dies. The tubes were cut using a diamond saw just outside of the inner tube, then manually polished to expose the internals of the tube. It should be noted that the large tube in b) was formed by the die breaking, rather than a different die design. The cut tube sections in a) are shown in the microscope images of b) to e), going from left to right.

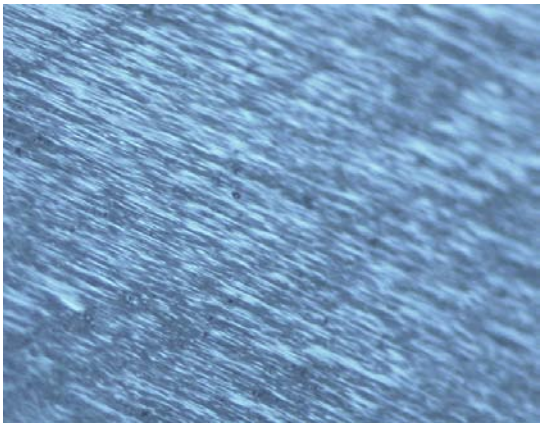

Figure 123: Top section of wagon-wheel preform extruded through MACOR die as shown in Figure 119

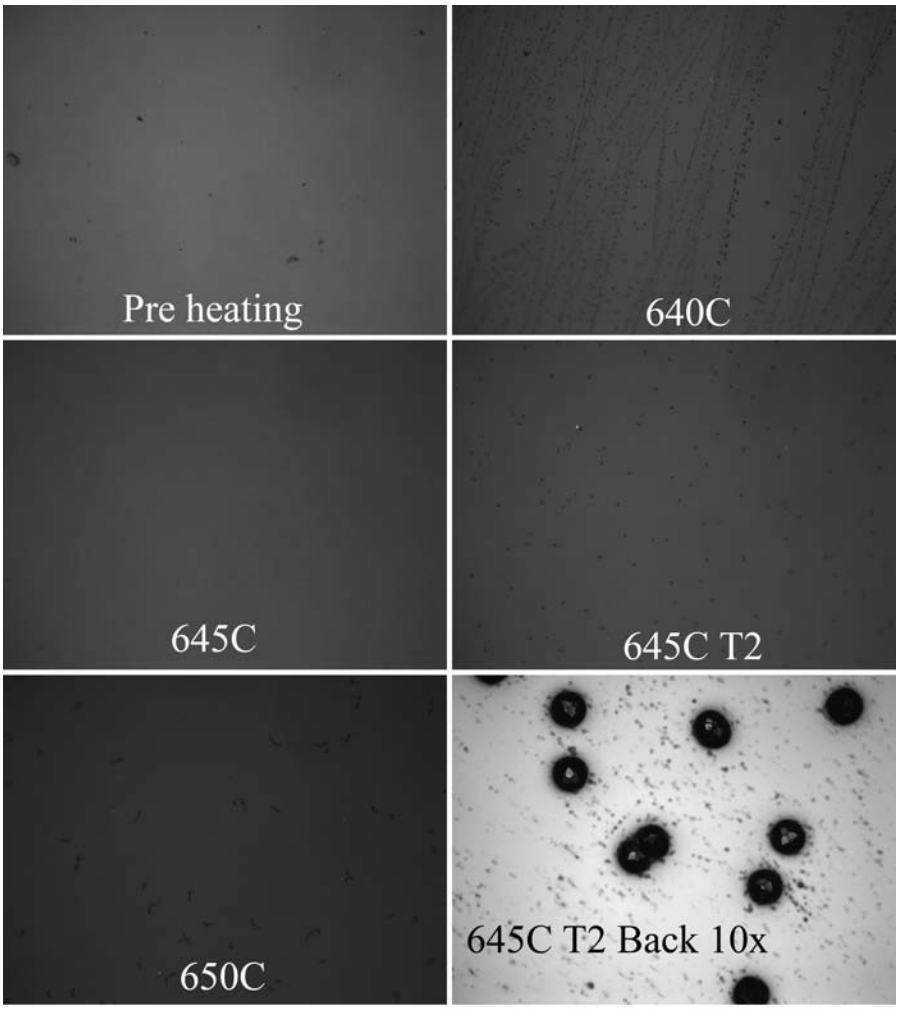

Figure 124: Controlled atmosphere crystallisation test with varied temperature.

Figure 125: Die materials trial on platinum plate, with polished FK5 wedge on each disk. From top, clockwise - MACOR, graphite, Inconel, stainless-steel.

It is clear from these results that there is a significant amount of variability between the samples, as the 640 °C sample shows more defects than either of the 645 °C samples. This is likely partially due to overshoot of the furnace temperature, although the defect rate could also be highly dependent on the initial surface quality. If this is indeed the case this is somewhat concerning, as the samples were polished to the same specifications as that used for billets in extrusions, and before heating showed no visible differences between the samples. The second 645 °C sample shows the formation of defect centres, with the 650 °C sample showing larger but less numerous centres. Especially concerning was the back of the second 645 °C sample, which showed very large crystals even though this surface was only in contact with the clean platinum plate. This was also the sample that was least likely to have suffered from overshoot, since the furnace heating parameters were adjusted for this trial to attempt to minimise any observed overshoot.

This experiment also utilises a much higher quality nitrogen atmosphere than is possible using the current configuration of the extrusion machine. At the present time the extrusion machine remains in an air atmosphere, with only the lower section (below the die exit) being flushed with nitrogen before the extrusion, so the above trial presents a somewhat ideal scenario for the oxygen concentration present.

5.3 GRAPHITE AS AN EXTRUSION MATERIAL

5.3.1 *Motivation*

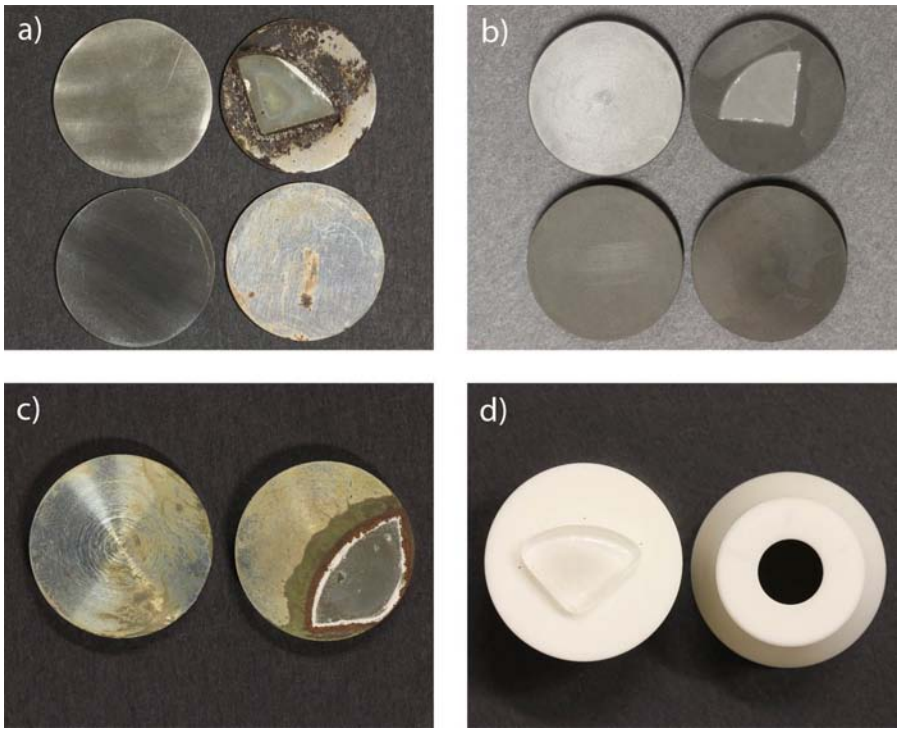

Figure 126: Various die materials temperature stability and materials compatibility trials. Listed from top left clockwise. a) Stainless steel - no heating; thermally cycled with glass (sample removed); thermally cycled; thermally cycled (repeat) b) Graphite - no heating; thermally cycled with glass (sample removed); thermally cycled; thermally cycled (repeat) c) Inconel - thermally cycled; thermally cycled with glass (sample removed) d) MACOR - thermally cycled with glass (sample adhered to surface); thermally cycled. A rod die outer was used in place of a disk for this trial.

As a significant number of defects were observed with MACOR structured extrusions, these were temporarily put on hold. More fundamental analysis of how the glass interacts with other potential die materials was required. This involved two separate tests, with the trials being performed inside a separate melting furnace in a controlled nitrogen atmosphere to minimise both variations between the trials and the possible effects of oxygen or water on the die materials. The first trial, shown in Figure 125 before heating examined the interaction of the glass and the die materials, both of the effects of the glass on the die material and vice versa. The second trial (not shown) consisted of identically machined and cleaned die materials, however omitting the glass to examine the performance of the materials themselves at higher temperatures in the controlled atmosphere. Inconel was added to the previously mentioned die materials (Stainless-steel, graphite, MACOR) as it has the potential to be an excellent die material, as it is both oxidation and corrosion resistant at high temperatures [177].

As can be seen in Figure 126 visible effects could be seen on all materials except MACOR for both the trials with and without the presence of FK5 glass. Stainless-steel (Figure 126a) and Inconel (Figure 126c) showed the most profound effects of the glass on the die material, with extensive corrosion or deposits formed on the surface of the die surrounding the location of the glass. This strongly suggests that something is being outgassed from the glass at high temperature . No visible change was observed for the FK5 on MACOR trial, however since the glass could not be removed from the MACOR disk it was not possible to observe the MACOR:glass interface under the microscope. Unfortunately at the time of writing this hypothesis could not be tested due to restrictions on the use of glasses containing fluoride in the equipment in the chemistry department. Additional planned experiments examining the composition of the deposits left on the surfaces of the metals in 126 was restricted due to the breakdown of the TOF-SIMS equipment.

Additionally, degradation was observed, especially on the surface of the graphite even without any glass present. Since graphite should be unreactive in a nitrogen atmosphere, this suggests that the trace amounts of oxygen present in the controlled atmosphere environment inside the glovebox. From the results of these trials it would appear that these trace amounts are significant enough to visibly degrade the surface quality.

As a comparison, this experiment was repeated using the extrusion furnace in a virtually identical configuration to that used for a standard extrusion using nitrogen. The extrusion body was replaced with a large graphite plate, which was cleaned using methanol as per the standard preparation methodology. Similar results to that shown in Figure 126b were obtained, with small amounts of degradation being observed after 5 hours (approximately equivalent to the time of an extrusion) on the lower surface in the nitrogen atmosphere. The upper surface in open air experienced extensive degradation, with large amounts of black powder seen on the surface. This trial was repeated, with very similar results.

The results of these trials were not entirely conclusive, although it can be concluded that neither stainless-steel or Inconel are suitable for FK5 extrusions. Due to the difficulties experienced with the MACOR microstructured fabrication discussed previously, it was decided to explore explore graphite as a possible candidate for extrusion.

5.3.2 *Graphite at higher temperatures*

Although graphite has previously found application as an extrusion die for ZBLAN fluoride glass, these extrusions are performed at a significantly lower temperature than what is required for FK5 extru-

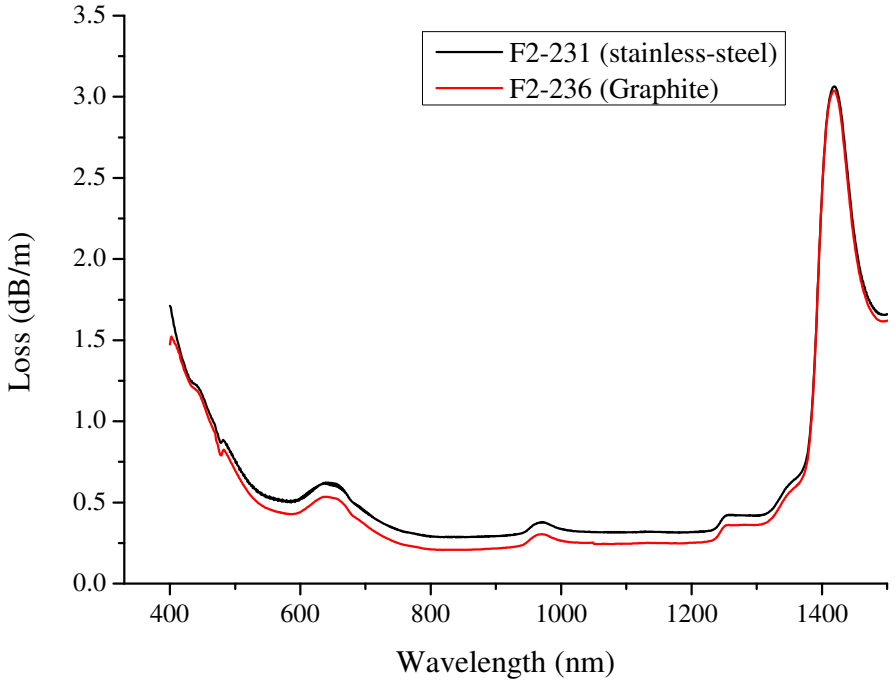

Figure 127: Loss spectra of F2 bare fibre extruded through stainless-steel (black) and graphite (red)

sions. As such, there is a strong risk of the graphite oxidising during the extrusion process, resulting in a poor quality preform.

An initial trial of a standard rod extrusion through a graphite die was performed using F2 to obtain an estimate of the loss that should be expected from a graphite extrusion at a relatively high temperature. The extrusion was performed in a nitrogen atmosphere to reduce potential degradation of the die surface.

It can be concluded from this trial that extruding F2 through graphite does not induce any significant loss. Due to the uncertainties in the loss measurement it cannot be concluded that graphite produces a fibre with lower loss than steel, only that graphite extrusions produce a fibre which has a statistically identical loss compared to one produced using a steel die.

With this promising result, work proceeded on extruding two FK5 samples through graphite dies. The parameters of the two extrusions were identical with the exception of the nitrogen flow, with the second trial being performed with a higher flow rate (2L/min) than the first trial (1L/min). As can be seen in Figure 128 the surface quality of these preforms was very poor, with scratches seen along the length. However, it was theorised that these defects could potentially be 'healed' by the fire polishing that occurs in the fibre drawing process.

The loss spectras of these fibres compared to the earlier fabricated FK5 fibres is shown in Figure 129. It is clear from these results that the poor surface quality of the fibres is inducing a large increase in

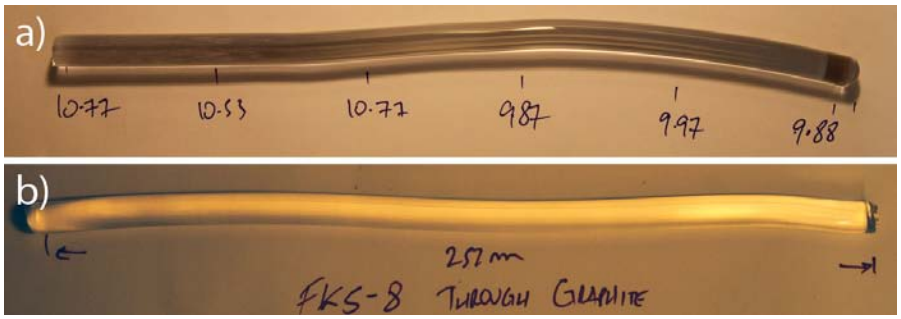

Figure 128: a) FK5 extrusion through graphite,N_2flow 1L/min b) FK5 extrusion through graphite,N_2flow 2L/min.

the loss of the fibres regardless of the nitrogen flow in the extrusion machine. The loss of both fibres is more than an order of magnitude higher than previous fibres, showing that graphite is not a suitable material for extruding FK5. The precise reason for this incompatibility is unknown at this time, however it is likely that it is either due to the glass reacting with and degrading the surface, or issues arising from using the graphite at higher temperatures than desired in an imperfect nitrogen atmosphere. EDX measurements demonstrated that fluoride is present in the glass, so it is possible that the molecules are outgassing [178] from the glass at temperature and reacting with the surface.

5.4 PHOTODARKENING IN BARE FIBRES

To further characterise the bare fibres fabricated from FK5, some quantitative measurements of the photodarkening rate compared to F2 were required. The reason that this parameter was examined is demonstrated best in Figure 107, where the 458 nm light induces additional loss in the fibre over time in the F2 WW fibre.

For the FK5 fibres used earlier the rate of photodarkening at 458 nm was observed to be too slow to accurately observe, as the pointing instability of the argon-ion laser leads to temporal changes in power through the power. This presents a significant challenge here, as the reduced power density in the fibre arising from the greatly expanded mode area compared to the F2 wagon wheel fibre used in Figure 107 leads to a significantly longer photodarkening time than is observed with a wagon-wheel fibre.

To enable characterisation to be performed a shorter wavelength 405 nm laser was used. This laser both increases the rate of photodarkening in the glasses compared to that which is observed at 458 nm as well as increasing the reliability of the measurements as the laser is significantly more stable than the argon-ion used earlier. To improve the precision of the results the experimental configuration used in Figure 130 was used. The experimental configuration used here is greatly

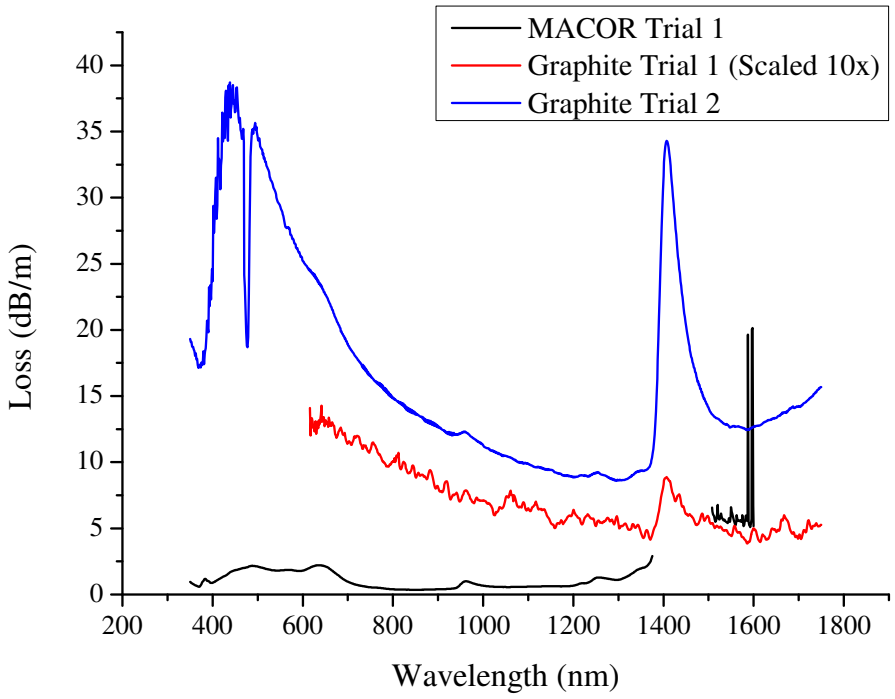

Figure 129: Loss spectras of FK5 extruded through graphite compared to MACOR. Note that "Graphite trial 1" has been scaled down by 10×to fit on the scale shown here. Some segments of the "MACOR Trial 1" and "Graphite Trial 1" were removed due to excessive noise.

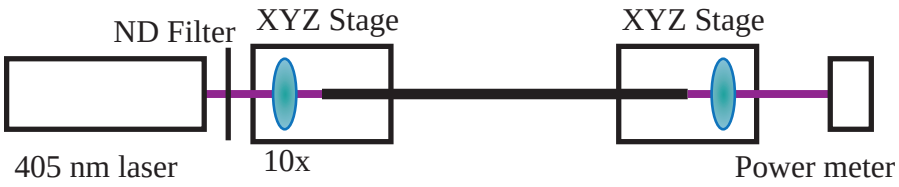

Figure 130: Experimental configuration for photodarkening measurements. The distance between the laser and the stage was minimised to reduced power variations due laser instabilities. The fibre was kept as flat as possible to minimise bend loss.

Glass type	Loss (dB/m)	Manufacturer's Data
F2	1.81	2.23
FK5	1.76	1.03
LLF1	2.4	1.15
FK51A	7-13.4	1.2

Table 5: Loss measurements in various bare fibres at 405 nm, with manufacturer's data for bulk glass loss [1].

simplified, with no optical elements used between the laser and the focusing lens with the exception of a neutral density filter which is removed before starting measurements. This is done to minimise both the distance between the laser and the fibre to reduce errors arising from pointing stability fluctuations and to remove any drift arising from thermal expansion in optical mounts. The same setup was used for the loss measurements described later in this section.

The loss of a number of fibres was measured using the experimental configuration used in Figure 130, and is shown in Table 5. It was noticed that for the lower-index glasses significant amounts of bend loss of up to 3 dB/m was observed using even a relatively large bend radius of approximately 0.5 m. Care was taken to minimise any bending of the fibre, with a long straight length being used with intermediate supports to keep the fibre at approximately the same height on the table.

Conveniently, both F2 and FK5 display similar losses at 405 nm, making direct comparisons between the two glass types possible. The measurements agree reasonably well with the stated bulk glass losses provided by Schott [1] which list a loss for F2 at 405 nm of 2.2dB/m and 1.02 dB/m fpr FK5. Again, the setup used in Figure 130 was used. A highly attenuating neutral density filter (OD4) was used during alignment to minimise the effects of any possible photodarkening that may occur before the experiment commences. The discrepancy between these values and the values listed in the table above most likely arise from additional defects being created during the fibre drawing process.

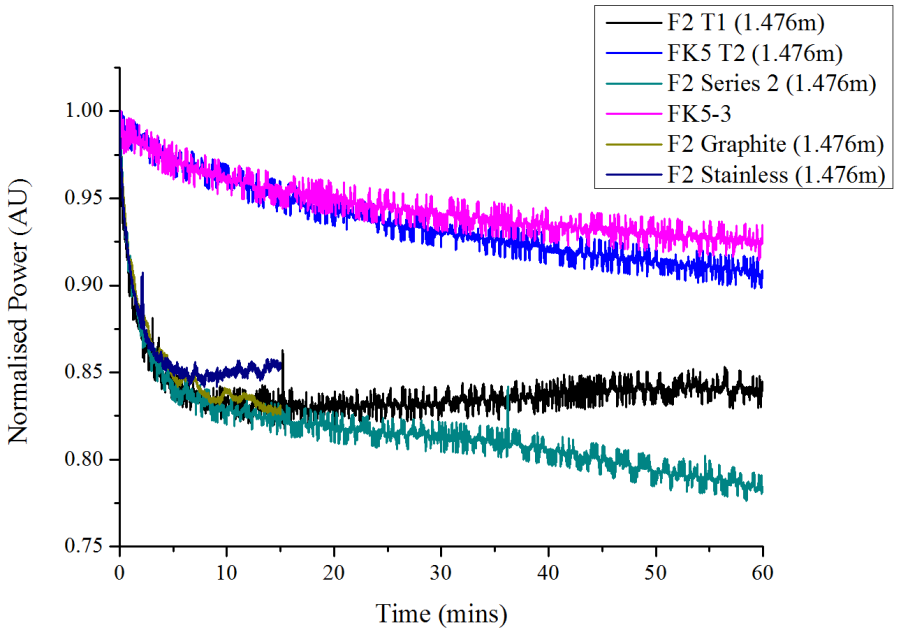

Figure 131: Bare fibre photodarkening results with 405 nm laser. Multiple samples are shown here, consisting of the two best FK5 fibre draws (FK5-3 & FK5-T2) and two F2 draws using preforms extruded through both graphite and stainless steel.

As can be observed from Figure 131 significantly different behaviour is noted comparing F2 bare fibres to FK5 fibres. The F2 experiences a very rapid decay before plateauing, while the FK5 fibre follows a more conventional [168, 179] exponential decay with a much longer decay constant. From this we can imply that fibres made from FK5 glass should find easier use as sensing fibres at short wavelengths since the exposure time required for them to decay to the same transmission levels as the F2 glass should be much longer. The two curves of each glass in this plot split after approximately 20 minutes, this is likely due to variations in the coupled power rather than a physical effect in the glass.

This reduced photodarkening rate has demonstrated an excellent application for this type of glass, enabling shorter wavelength excitation sources to be used to open up new possibilities for fluorophores for detection of various chemicals or biological species. The expected rate of photodarkening of FK5 at 405 nm with a small-core wagon-wheel fibre is difficult to ascertain, however it is likely that if care was taken to minimise exposure of the glass to the laser radiation that measurements could be performed with minimal impact observed from photodarkening.

Two new methods for the extrusion of preforms have been explored, covering the use of MACOR dies as well as using graphite dies at higher temperatures than had previously been demonstrated for extrusions. This opens up new possibilities for glasses that can

be extruded, with the ultimate goal of possibly being able to extrude silica glass to fabricate novel structures that would be difficult or impossible to realise using conventional stacking or drilling techniques. Work towards this goal is currently progressing, however this requires a number of current issues to be resolved before it can successfully be demonstrated.

Part III

PEROXIDE SENSING APPLICATIONS

6

FUEL DEGRADATION SENSING

This chapter covers work on the development and characterisation of fluorescent molecules for the detection of hydroperoxides or hydrogen peroxide. None of the chemical synthesis work was performed by the author, with the initial development work performed by Dr Markus Pietsch with Prof Andrew Abell, and later by Dr Sabrina Heng and finally Dr Ondrej Zvarec. All measurements in this section were performed by the author, with the exception of the absorption measurement shown in Section 7.6.7 which was performed by Rachel Moore, and any NMR or mass spectrometer results which were performed by the synthesising chemist or Mr Tze Foo. TLC measurements were performed under the supervision of Dr Markus Pietsch. The author acknowledges the assistance of Mr Tze Foo and Mr Kevin Kuan in remedying some of the chemistry related knowledge gaps that existed at the start of this project. The work on surface functionalisation was performed with Dr Alexandre Francois, who developed some of the initial methods on coating soft-glass fibres with polyelectrolytes as well as further developing silane coatings on the same glasses. All coating trials were performed by the author with some assistance from Dr Francois when due to the extremely time consuming nature of these trials it became impractical to perform all steps in two of the trials. The author would also like to acknowledge the assistance of Dr Beniamino Sciacca in developing the protocol for the biotin/avidin trials and PEG linker test.

The applications side of this chapter has been driven firstly by a grant from the Defence Science and Technology Organisation (DSTO), with Dr Claire Davis and Dr Chris Hulston who provided funding support as well as initial technical advice regarding the concentration range of interest and the shortfalls of the presently used methods. A degraded and undegraded jet fuel sample, as well as some chemicals were also provided. The work on wine sensing was primarily driven by discussions with Prof Dennis Taylor, and Dr George Skouroumounis from the Waite Institute at the University of Adelaide. Again, desired characteristics of the sensor as well as concentration ranges of interest were provided. The final section of this work looking at embryo sensing was driven by discussions with Prof Jeremy Thompson from the Robinson Institute, who assisted greatly by demonstrating currently used sampling methods as well as giving an overview of what is needed for this project to be successful. The initial phase of these discussions also included Dr Dominic Murphy, with whom

work in an earlier chapter was also performed. Samples of IVF buffers were provided by Dr Deanne Feil.

6.1 BACKGROUND

6.1.1 *Aviation fuels*

As jet fuel is the primary heat sink for modern gas turbine military aircraft, the detection of fuel degradation has become an increasingly important field. The use of jet fuel as a coolant acts to thermally stress the fuel that may form gums and deposits capable of disrupting flow in fuel nozzles and fouling fuel heat exchangers [180].

Although considerable effort has been invested in developing oxidation inhibitors, a quick and simple method for the early detection of degradation is desirable to prevent the formation of deposits that can block narrow tubes and inhibit the flow of both fuel and the heat that it is required to transfer [7].

At present, tests for fuel degradation require samples to be taken from the aircraft, before being transported to a lab with results typically returning in several days. Here we propose the use of microstructured optical fibres as an alternative method for in-situ degradation detection.

The proposed method is to fabricate a "dip" sensor, in that the distal end of the fibre can be immersed in the fuel solution that then fills up the holes in the fibre via capillary forces or by applying an external vacuum. A fluorescent dye will be used for the detection of the degradation products. The detection of the degradation process is enabled via the use of a fluorescent dye that changes its fluorescent response.

6.2 MECHANISMS

The mechanisms of fuel degradation have been extensively studied over the past few decades. Due especially to the practice of using jet fuel as an aid to cooling in aircraft, this process is accelerated significantly with fuel inside the aircraft compared to fuel being stored in normal conditions. The fuel is used to cool various subsystems of the aircraft, both incidentally and through the use of heat exchangers specifically designed to remove heat from components in the aircraft and transfer it to the fuel [181, 182].

However it is difficult to view the species directly as there is a great deal of variability between the exact types and quantities of chemical species present in fuel samples, even if the fuel is of the same type but from a different batch [183].

There are a number of different molecules present that may contribute to degradation eg polar species, which generally increase the rate

of surface deposits forming in the fuel [184]. In addition molecules such as thiols and phenols can have a large effect on the degradation rate of fuels [185]. Some types of fuel also contain active hydrocarbon molecules such as olefins and active aromatic compounds such as Tetralin that can autoxidise to hydroperoxides [185].

Due to the complexity of the fuel compounds, and the difficulty in modelling the complete degradation chain, there is some debate about the exact effect that some of these molecules have. Phenols in particular have been shown by Kuprowicz et al. to greatly decrease both the oxidation and deposition rate [182], however Beaver et al. state that phenols can be a nucleophilic species in the coupling reactions, and thus greatly increase the rate of deposition formation [186].

Hydroperoxides are the first stage in the autoxidation chain of the fuels at temperatures less than ~140°C. Once the temperature of the fuel increases beyond this point, the hydroperoxides begin to react with trace amounts of oxygen dissolved in the fuel via the reaction chain shown below [181, 187]. This has the effect of rapidly increasing the oxidation rate of the fuel. If allowed to continue this autoxidation chain eventually results in the formation of both surface deposits and insoluble solids in the fuel. These are clearly undesirable if the fuel is to be used as a coolant in sensitive systems, as a blockage could result in either poorer than required fuel flow, or excess heat build-up and possible damage to the system [182]. Equations showing the involvement of hydroperoxides in the fuel degradation process are shown below.

Production of hydroperoxides -

Hydrocarbon radical + oxygen forms peroxy radical

$R + O_2 \rightarrow RO_2$

Peroxy radical 'abstracts' hydrogen from fuel species, forming hydroperoxides and hydrocarbon.

$RO_2 + RH \rightarrow ROOH + R$ [187]

This reaction occurs at higher temperatures, and shows the decomposition of the hydroperoxides molecules to form radicals.

$2ROOH \rightarrow RO_2\bullet + RO\bullet + H_2O$

The main issue with preventing fuel degradation is that extremely limited quantities of hydroperoxides (<<1%) greatly accelerate the decomposition rate of the fuel. It is widely believed that even these trace levels of hydroperoxides are not only the primary initiator of the autoxidation process in fuels, but when reacting with other elements in the fuel such as sulphides or disulphides they can also initiate reaction chains that lead to deposits forming in the fuel.

Studies have been done into adding hydroperoxide decomposing species to the fuels may decrease the rate of oxidation, as long as phenyls that generally occur naturally in jet fuels are present [188]. Sulfides and disulphides can also act in this manner, as they can react

with hydroperoxides to form products that do not continue the autoxidation chain, effectively removing the chance that these hydroperoxides could react with other products to initiate degradation.

6.3 ESTABLISHED METHODS

6.3.1 *Methods for detection - fluorescent techniques*

6.3.1.1 *Triphenylphosphine*

Numerous methods for detection of oil degradation have been demonstrated. Each possesses various intrinsic advantages and disadvantages when compared to other methods, and there is no clear cut "best" method for detection.

As the first step in the degradation chain of fuel oils is generally the production of hydroperoxides molecules, a sensor based on their detection can theoretically at least detect degradation of fuels at an earlier point than alternate methods such as those that look for pH changes in the fuel [181, 183].

One of the possible flaws with a method utilising hydroperoxide detection is that while the hydroperoxide level initially increases steadily with time as the fuel degrades, it in fact saturates at a point before dropping off. If no other tests are performed on the fuel it would be difficult at best to determine whether a given sample of fuel with a relatively low hydroperoxides concentration is still of high quality, or if it has already passed the hydroperoxides peak and has started to become acidic and dangerous to the aircraft.

Since the hydroperoxides show no useful absorption features (especially at low concentrations) a compound such as Tri-phenylphosphine (TPP) can be used. When hydroxyl groups such as those in hydroperoxides are present with TPP the free electron pair bonds with an oxygen atom from the HP, forming Tri-phenylphosphine oxide (TPPO) and an alcohol corresponding to the type of hydroperoxides involved in the reaction.

This is summarized using the equation below, where ROOH represents a generic hydroperoxide species [183] –

$$ROOH + TPP_{excess} \rightarrow ROH + TPPO$$

Due to the structure of the molecule this has the effect of altering both the absorption and emission spectras of the dye, and depending on the dye used generally results in an increase in the magnitude of both quantities. This provides a possible method of measuring the hydroperoxide content. There are several different methods that can then be used to quantify the amount of hydroperoxides present in solution. The residual concentration can be directly measured using gas chromatography, which will display a separate result for TPP and TPPO [183, 189]. An assay can then be performed to determine the amount of residual TPP. From analysing the results and comparing it

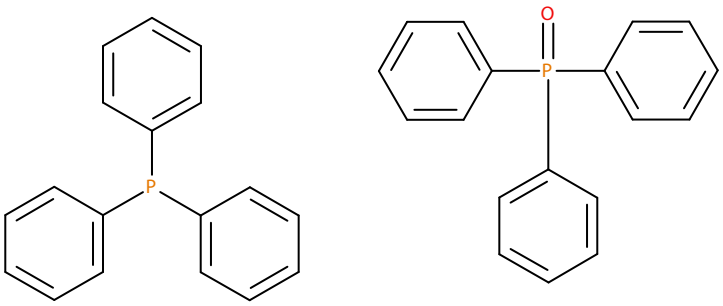

Figure 132: a) Triphenylphosphine (TPP) b) Triphenylphosphine Oxide (TPPO).

to the expected values of the TPP molecules an approximate quantity of hydroperoxides can be determined.

One possible issue with this type of assay is that the TPP can also react with species such as aldehydes, ketones or carboxylic acids, and oxidise to TPPO with identical properties as when the reaction occurs with hydroperoxide molecules [189]. Reactions with sulphide to form Tri-phenylphosphine sulfide (TPPS) are also possible with TPP [183] which again can produce spurious results. When the quantity of TPP is less than that of the hydroperoxides, TPPO is formed in preference to TPPS. However, when the amount of TPP is greater than the amount of hydroperoxides, quantities of TPPS can also be formed.

Another issue with TPP is that both its absorption and emission features are located within the UV spectrum, and depending on the analyte being used these features could overlap some of the natural absorption/emission features of the material. There has been a great deal of interest in developing a fluorescent molecule that displays the same type of increase in absorption/emission when exposed to hydroperoxide molecules, but instead possesses spectral features further in to the visible than standard TPP molecules. This presents additional problems when looking to use soft glass optical fibres (see Section 2.3.1) for detection, as the transmission window for this fibre does not cover the UV.

6.3.1.2 *Diphenyl-1-pyrenylphosphine*

Akasaka et al. [190] demonstrated the usage of diphenyl-1- pyrenylphosphine (DPPP) as a fluorescent reagent for hydroperoxide molecules. It acts in a similar fashion to TPP, in that once oxidised to diphenyl-1-pyrenylphosphine (DPPP=O) by the hydroperoxide the fluorescence output of the DPPP=O molecules is far higher than the original DPPP molecules [191, 192]. However unlike TPP, which has extremely short absorption/emission peaks at around 250 nm, the absorption/emission peaks of DPPP are 352 nm and 380 nm respectively. Using high pressure liquid chromatography (HPLC, method described below) Akasaka was able to show that DPPP demonstrated a much higher se-

lectivity for hydroperoxides than TPP showed as well as being able to be used for more hydroperoxide types with different polarities than previous methods. DPPP has also been used by Okimoto et al. to detect hydroperoxides during lipid peroxidation in cell membranes [191, 193].

A number of other fluorescent probes for hydroperoxides have also been developed, such as 3-perylene diphenylphosphine by Ref. [194] with Absorption/Emission features at 440 nm/470 nm [195]. This fluorophore was used in a later paper to image lipid hydroperoxides located within the muscle cells of fish [195] and again to record hydroperoxide production within mouse liver and heart cells .

Soh et al. [196] have also developed several different perylent derivative fluorophores, including several using perylene 3,4,9,10- tetracarboxyl bisimide as the fluorophore – Spy-HP [196] - Absorption/ Emission: 524 nm/ 535 nm, SPH-LHP [197] - Absorption/ Emission: 535 nm/ 574 nm.

Onoda et al. [198] developed 4-(2-diphenylphosphinoethylamino)-7-nitro-2,1,3-benzoxadiazole. (Absorption/ Emission: 458 nm/ 520 nm) This type of fluorophore does not use the same Intramolecular charge mechanism fluorescence process as TPP, instead the fluorescence is controlled by the photoinduced electron transfer (PET) process. This type of fluorophore should be much more controllable in its characteristics than fluorophores relying on ICM [199]. A second set of fluorophores also based on this fluorescence mechanism was also developed, by Ref. [191] with absorption ranging from 364 nm to 425 nm, and emission from 471 nm to 521 nm depending on the solvent & compounds used and the oxidation state of the molecules.

6.3.2 *Chromatography methods*

Yamamoto et al. [200] demonstrated an effective sensor for lipid hydroperoxides. Hydroperoxides are first reacted with microperoxidase, then the product of this reaction is again reacted with luminol. One of the results from this reaction is a semiquinone radical that reacts with oxygen to form oxygen radicals. These then can react with further semiquinone radicals resulting in the formation of isoluminol endoperoxide, that produces light in a HPLC column. This method was used to successfully determine the hydroperoxide content in a human blood sample.

A similar luminol based HPLC method was used by Baj et al. [201] and again showed that chemiluminescence could reliably be used for detection of organic hydroperoxides using some minor modifications to the standard technique to improve the sensitivity of the assay.

Marquette et al. [202] also considered the application of a luminol-based chemiluminescence assay for various oxidising species. They comment on the possibility of using this assay directly with a CCD

photodetector in place of the HPLC column to enable easier and more cost-effective sensing of oxidising species. However since luminol is not selective about the species that oxidises it, this method does not enable one to tell what type of molecule is causing the reaction to occur.

Another degradation detection method is possible through the use of Iodometric titration. Tian et al. [203] describes a method in which it is possible to quantify the amount of hydroperoxides in a given sample of diesel fuel. Samples were firstly weighed, and 0.5-1 g dissolved in 35ml of acetic acid. 1 ml saturated potassium iodide (KI) was added and the solution puffed with N_2 to remove oxygen. After 10 minutes the sample was diluted with H_2O and titrated by 0.1 mol/ml $Na_2S_2O_3$ and 1 ml 1% starch added when the color was about to disappear. The concentration of hydroperoxides found within the solution could then be calculated using the equation given in [203].

Gas liquid chromatography (GLC) for hydroperoxides generally has limited applications as it relies on the hydroperoxides being sufficiently stable and volatile [204]. However if the hydroperoxides are reacted with Triphenylphosphine (TPP, as described earlier) then GLC can be carried out on the sample, seeking one of a number of possible products:-

1. The alcohol derived from the hydroperoxide post-reaction with TPP by Ref. [204]. It was found that this was not possible due to dehydration of the products in the GLC column.

2. The TPPO formed from the reaction. Experimental difficulties found with this method were found by Barnard et al. [204].

3. Residual TPP – This was the primary method used in Ref. [204]. Since the quantity of TPP introduced into the solution is known, it is then simple to determine the amount of hydroperoxides present as this is just the difference between the original amount and the amount of TPP recorded through GLC. This gives accurate result consistent with other known methods, but reliant on other components such as the alcohol or its dehydration products not interfering with the observed TPP peak.

Kolthoff et al. [205] demonstrated a colorimetric method in which organic hydroperoxides are reacted with Ferrous Iron to form ferris ions. However they found that this particular method gave inaccurate results due to the presence of oxygen in solution as well as decomposition of the hydroperoxide.

This work was reexamined by Mihaljevi et al. [206] looking at lipid hydroperoxides in a deoxygenated chloroform:methanol or a dichloromethane:methanol (2:1, v/v) mixture solvent. Iodometric determination of hydroperoxide levels was performed using spectrophotometry using the standard technique. A detection limit of 170 pmol

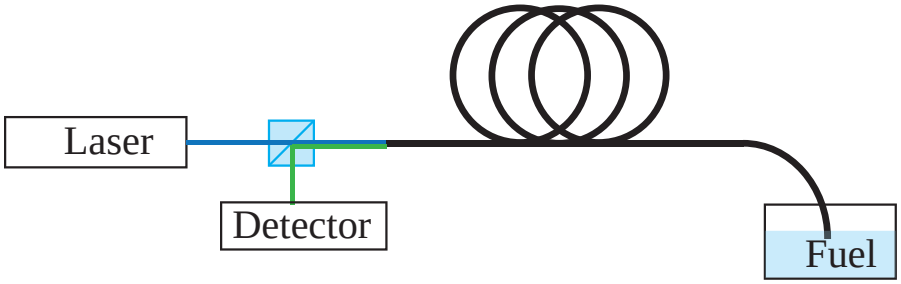

Figure 133: Schematic for dip sensor for hydroperoxide detection in fuel using fluorophores. Here "fuel" can be either a premixed fuel+fluorophore solution, or alternatively the fluorophore could be functionalised onto the internal surfaces of the fibre.

Hydroperoxide/ml in solution, corresponding to approximately 50 µmol hydroperoxides/kg lipid was recorded. This method was shown to be fast compared to other methods, although time is required for sample preparation before the measurement can be performed. This work was again looked at by Richards et al. [207] who determined the best solvent to be a chloroform:ethanol solution, or alternatively to use dichloromethane (DCM).

Alternate methods are also possible for hydroperoxide detection, such as-the tin (II) reduction procedure. These are generally more accurate but extremely cumbersome and time consuming [204].

6.4 PROPOSED METHOD

The initial aim of this work was to develop a fibre-optic based fuel degradation sensor. The proposed method was to fabricate a 'dip' sensor, in that the end of the fibre can be immersed in the fuel solution, that then fills up the holes in the fibre via capillary forces or external pressure. A fluorescent dye is then used for the detection of the degradation products. This fluorophore reacts with the hydroperoxide, producing an increase in the fluorescence signal. By monitoring the amount of observed fluorescence signal from the fibre the approximate concentration of hydroperoxide can be determined using a calibration curve. This is a measurement performed beforehand to establish the expected fluorescence levels at given concentrations of hydroperoxides.

Present methods from the sponsor of this project utilise the titration method described in Section 6.3.2. This method requires removal of the sample from the aircraft or fuel tank, which is then sent to the laboratory for analysis. The turnaround time for this process is in the order of several days, so it is desirable to develop a method which can give almost instantaneous results.

The aviation fuel examined during this project was the F-34 (US designation JP-8) which is a kerosene based aviation fuel commonly

used by military aircraft. F-34 is almost identical to the commercial jet fuel Jet A-1, but with added corrosion inhibiters, lubricity additives, antioxidants, fuel-system icing inhibitors and static dissipation additives. The fuel has a flash point of 38°C. Its optical properties were not found in literature, so these had to be determined experimentally. For modeling purposes it was initially assumed that the refractive index of the fuel is the same as that of kerosene, which is approximately 1.44 for visible wavelengths [208].

The use of F2 wagon-wheel fibres compared to silica wagon-wheel fibres shows a prospective advantage here due to the refractive indices of the liquids involved (see Section 1.3.2). As will be discussed in more detail later, some of the solvents that will be used for characterisation include benzene, toluene and o-xylene. These liquids have refractive indices of 1.501, 1.49 and 1.51 respectively [208]. The refractive index of silica is approximately 1.4584 at 589 nm (sodium 'D' line) meaning that the suspended core fibre design will no longer guide light in the glass core, as the refractive index will be higher in the holes surrounding the core than in the glass itself.

Additionally, the refractive index of fuel was close to that of the silica glass (1.4448 at 20 °C) such that using suspended core fibres with small cores will result in the light becoming extremely spread out, and possibly causing issues with confinement loss. Since there are significant batch-to-batch variations with the fuel, in addition to the natural variations in the refractive index with temperature this introduces an additional variable when taking measurements. If the index contrast were larger, as it is with soft glasses the effects of slight changes in the refractive index would be negligible since the initial difference is at least 0.1 refractive index units.

Since there are presently no commercially available fluorophores that absorb and emit in the visible spectrum, as required for use in a soft-glass fibre, this requires synthesis of fluorescent compounds that display the required properties. The fluorophore must absorb and emit in the visible as this corresponds with the transmission window of the soft-glass fibres that will be used here. The loss of these fibres is prohibitive in the UV (see Figure 108) so longer wavelength fluorophores are required.

Although significant progress has been made developing oxidation inhibitors [188], it is still desirable to create a quick and simple method of analysing the degradation state of a sample of fuel. At present the primary test for degradation of the fuel samples is a pH test, but this has several disadvantages compared to the fibre sensor proposed here. Firstly, as the pH test is looking specifically for a product produced some way down the degradation chain, the fuel may have already degraded enough by the time that the pH test gives a positive result for damage to occur to the systems on board the aircraft. The second factor is the time required for the test. The

general turn-around from the time the sample is taken to the time that the result is received is of the order of several days that again could result in damage to the aircraft before the state of the fuel is known.

The intent of this work was to develop a sensor which could be used to give virtually instantaneous measurements of the degradation state of the aviation fuel by mounting this detector in a portable system. To this end some work was done on how to splice these fibres to conventional silica index-guiding fibres. The motivation for this was to be able to remove the need for the free space optics used for measurements in this section, and fabricate a disposable, connectorised sensing "tip" which could simply be dipped in to a fuel sample to perform the measurement. For more details on this see Chapter 3.

One critical component of this system was the fluorophore, which had a number of critical requirements to be able to be successfully utilised in a practical fibre dip sensor device. This will be explored in more detail in the next section.

6.5 FLUOROPHORE REQUIREMENTS

Fluorophore selection for this project had a number of requirements

1. Significant change in the fluorescence intensity after reaction with hydroperoxides. To obtain a reasonable working range for the sensor the fluorescence must change by a significant amount from initial state before the reaction to the post reaction state. If this change in fluorescence is small, this reduces the dynamic range or the precision of the sensor.

2. Photostability. The use of microstructured optical fibres have been shown to dramatically increase the photobleaching rate in fibre compared to that which is typically seen in bulk measurements (see - Section 2.2). The fluorophore needs to have good photostability to give a relatively constant fluorescence intensity over the required duration of the laser exposure required to perform a measurement.

3. Suitable absorption/emission wavelengths. The loss of a typical F2 wagon-wheel fibre is shown in Figure 52. It can clearly be seen that the loss of the fibre increases dramatically at shorter wavelength as the glass nears the UV transmission edge. Additionally, photodarkening can occur even when a wavelength not near the UV edge is used where loss would not otherwise be a significant factor. This process adds an extra time-dependent component to the measurement, complicating the process of obtaining a quantitative measurement of the peroxide content. Therefore the fluorophore not only needs to have an emission wavelength with a relatively low loss to ensure that it can be

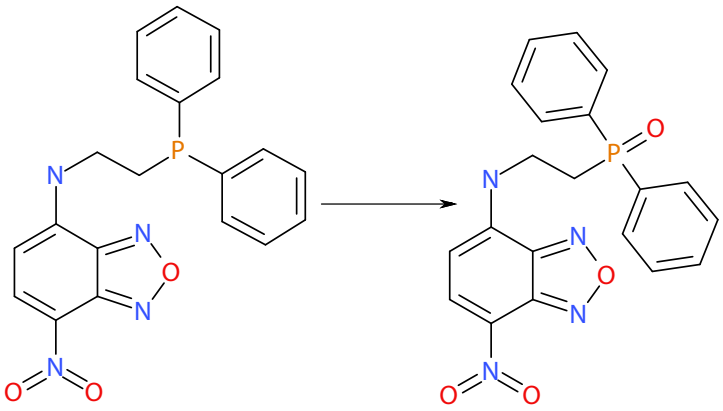

Figure 134: Initial fluorophore choice 1) 4-(2-diphenylphosphinoethylamino)-7-nitro-2,1,3-benzoxadiazole before oxidation in its 'off' state 2) The molecule is oxidised by the hydroperoxide, changing the quantum efficiency in benzene from 0.051 to 0.42 [198].

detected even at low concentrations, it also must be able to be excited by a wavelength that does not induce significant photodarkening in the fibre.

4. Selective. The fluorophore must show some selectivity to hydroperoxides (or radicals).

5. Relative ease of synthesis, or commercial availability. The synthesis must have a minimal number of steps such that it can be made in a reasonable time frame with a good yield.

6. Potential for surface functionalisation. As previously mentioned the ideal technique for a dip sensor involves attaching the fluorophore to the internal surfaces of the fibre. The analyte to be tested is then filled directly in to the fibre, and can interact with the fluorophore that is bound to the surface producing a change in fluorescence. Using this method it is possible to perform measurements in a single step, without pre-mixing of chemicals. This will be discussed in more detail in Section 7.5.1

6.6 FLUOROPHORE SELECTION

A literature survey of known fluorophores that can be used for hydroperoxide detection in fuel lead to 4-(2-diphenylphosphinoethylamino)-7-nitro-2,1,3-benzoxadiazole (DPPNBD) [198] as a possible candidate for the fluorophore. The structure of this molecule is shown in Figure 134. Literature suggested that this fluorophore fulfils most of the requirements above. Details about the photostability however were unknown. Preliminary discussions with Dr. Pietsch also gave a pos-

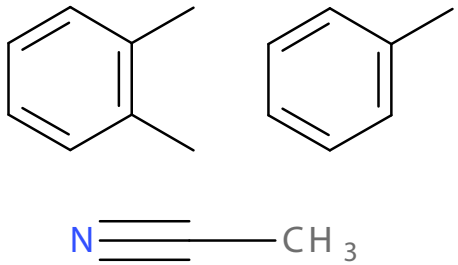

Figure 135: Solvents . Left) o-xylene Right) toluene Bottom) Acetonitrile.

sible path towards surface functionalisation, but initial trials focussed solely on characterisation of the compound in solution.

Literature reports that the quantum yield (Φ) of this fluorophore in benzene increases from Φ=0.051 to Φ=0.42 when the fluorophore is oxidised by a hydroperoxide molecule. This change in fluorescence intensity ($> 8\times$) is large enough such that the difference between the oxidised and unoxidised versions would be easily observed using a microstructured optical fibre.

The mechanism for the fluorescence quenching of this fluorophore is photoinduced electron transfer (PET) [209–212]. For this particular fluorophore the phosphine moeties donate electrons to the fluorophore effectively quenching the fluorescence signal. Once the phosphine is oxidised however the methyldiphenylphosphine HOMO energy changes from -9.029 eV to -9.910 eV, and the K value drops from 67.1 to a negligible value. This implies that the unoxidised methyldiphenylphosphine should quench the fluorescence with good efficiency, while the oxidised derivative should show a high fluorescence signal [198].

6.7 INITIAL TRIALS

The fluorophore was synthesised in house by Dr. Pietsch, following the protocol described by [198] for reagent 1. Initial trials were performed with the compound dissolved in toluene (Figure 135 (right)). This was chosen to closely mimic the chemical characteristics of aviation fuel [183], however toluene has the advantage that it can be purchased without impurities thus greatly simplifying quantitative measurements of the hydroperoxide concentrations.

A sample fluorescence spectra of a 100 µM sample dissolved in toluene is shown in Figure 136. This spectra was recorded in cuvette using an ANDO AQ6315E OSA.

This was then changed to o-xylene which due to its lower vapour pressure has a higher boiling point and a lower evaporation rate than toluene. This makes measurements safer, as well as making them more quantitative since the concentrations should be more accurately known.

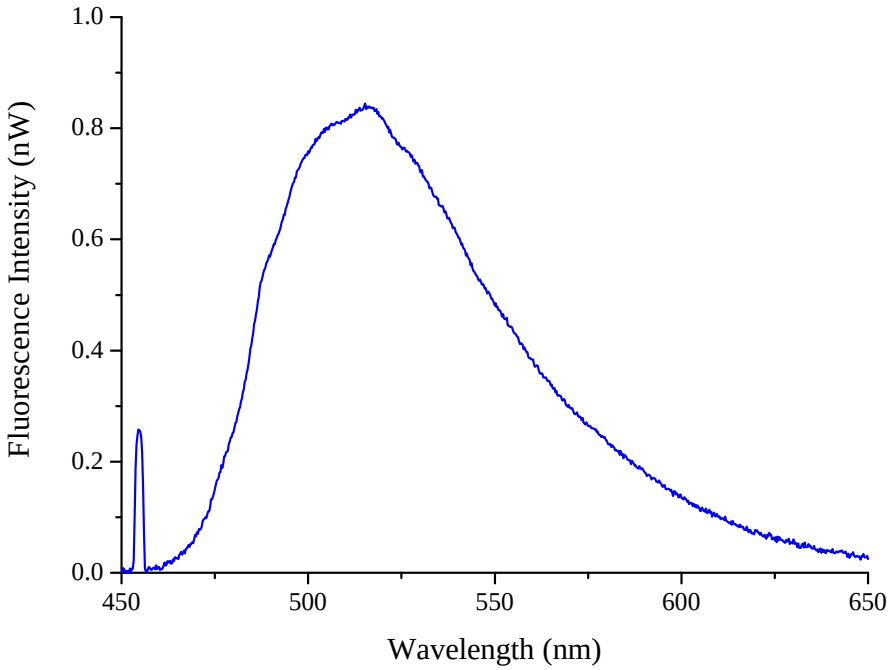

Figure 136: Example cuvette DPPNBD fluorescence spectra for 100 µM sample, 458 nm excitation. Recorded using optical spectrum analyser (OSA).

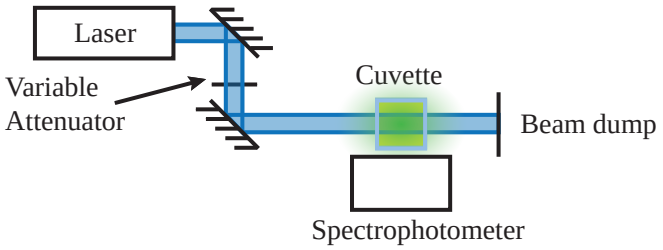

Figure 137: Experimental configuration for photobleaching & characterisation measurements.

6.8 PHOTOBLEACHING & SELF OXIDATION

To be feasible as a chemical to be used in fibre, this compound has to both react with hydroperoxides and produce a large ($\gtrsim 2\times$) increase in its fluorescence signal as well as being photostable. This choice of the required increase in the fluorescence intensity is based on typical variations in the observed fluorescent signal in fibre, which at this time was approximately 20%. To conclusively determine not only the presence of hydroperoxides, but also to estimate the concentration a relatively large increase in the fluorescence signal is required after oxidation. Initial measurements were performed on bulk solutions in cuvettes with the compound dissolved in o-xylene.

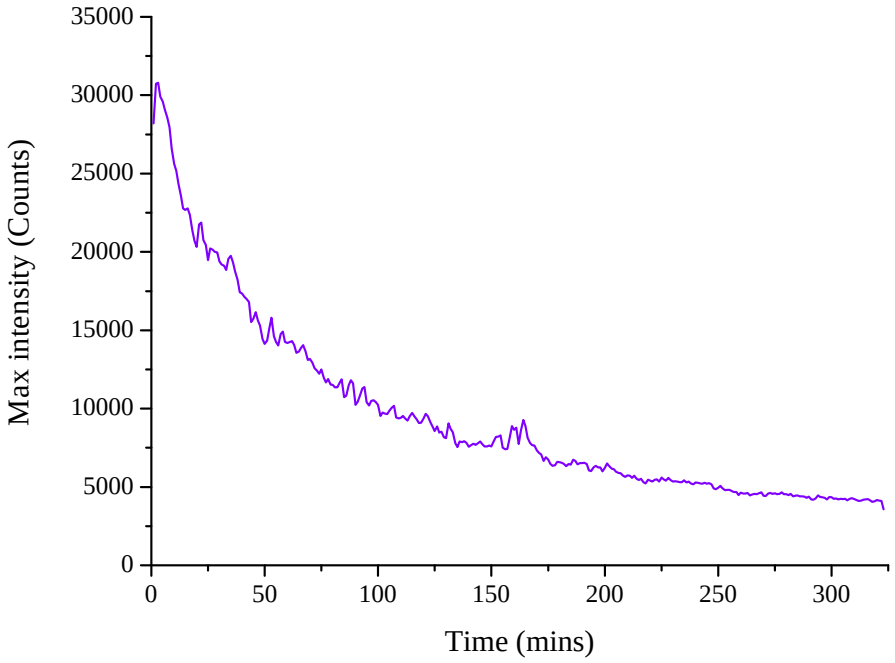

Figure 138: Cuvette based photobleaching measurement. 10 µM DPPNBD fluorophore concentration in o-xylene, 10 mW 458 nm excitation. The fluorescence was recorded using an ocean optics QE65000 spectrometer. No hydroperoxides were added to this sample. For comparison Rhodamine B at the same concentration and power level shows no measurable photobleaching over the same time period.

To test the photostability of the fluorophore, 2 mL of 10 µM solution was exposed to 10 mW of 458 nm laser excitation, using the experimental configuration shown in Figure 137.

The results of this measurement are shown in Figure 138. This plot shows the variation in the peak of the fluorescence signal observed from the fluorophore over time. One scan is recorded every minute even though the sample is constantly illuminated. The fluorescence intensity drops from its initial peak of approximately 30000 counts and follows an approximately exponential trend down to its final value of approximately 4000 counts after 320 minutes of illumination.

Previously it had been noted that the photostability of the fluorophore is orders of magnitude worse in fibre. This stems from two main components, being the limited volume inside the fibre and the increased light intensity. Photobleaching effects in bulk solutions are mitigated by constant diffusion of the molecules in and out of the excitation field. Since not all avenues of photobleaching are irreversible, this acts to allow molecules time to recover from the photobleaching before they again drift in to the excitation light.

Finite element modelling of a generic wagon-wheel structure demonstrated that the peak intensity inside the holes of a wagon-wheel fibre is approximately 5×10^5 W/cm^2 when 10 mW of light is guided

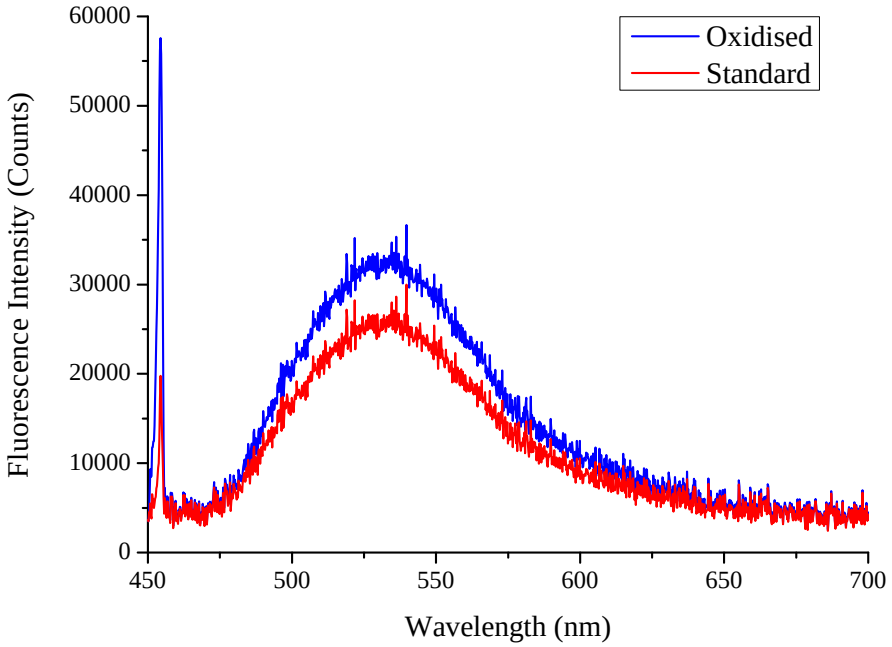

Figure 139: Fluorescence spectra for 1 µM fluorophore in o-xylene. The red curve is just the fluorophore, blue is an identical concentration of fluorophore and 100 µM hydroperoxide added.

within a 700 nm F2 wagon-wheel fibre with the holes filled with o-xylene. This peak intensity naturally lies at the interface between the glass and liquid, and decreases exponentially away from the interface. This is significantly higher than that which is seen here in cuvette, with a peak intensity of approximately 0.22 W/cm^2 at an identical power assuming a gaussian beam distribution with a full width half maximum (FWHM) of 2 mm.

For comparison a similar volume of Rhodamine B (Figure 20) was exposed to 25 mW of 532 excitation. The higher power was used as the spot size of this laser is larger than that of the 458 nm argon-ion source. This sample showed no significant photobleaching over the course of 5 hours in stark contrast to the results in Figure 138.

Even though the photobleaching rate seen here is mitigated somewhat by the recovery processes that were just discussed, the rate is still substantial enough to create concerns for fibre-based measurements.

Figure 139 shows the results of the initial characterisation of a 1 µM solution of fluorophore with and without the addition of hydroperoxides. The experimental configuration was the same as that used for the photobleaching measurements, and is shown in Figure 137. For this trial hydroperoxides were added in a large excess to show the maximum potential increase in fluorescence. The reaction consumes the peroxy radical, so adding hydroperoxides in a 100:1 excess ensures that all available unoxidised fluorophores will react.

Literature [198] suggests that this fluorophore should show approximately a 8.2 × increase in fluorescence when oxidised, however Figure 139 clearly does not show this same change. The increase recorded here is only approximately 20%, which is not sufficient for quantitative measurements to be performed in fibre. Since this fluorophore has been previously characterised in literature, investigation is needed to determine why the behaviour observed here differs from what has earlier been reported. It appears that the case here is more that the unoxidised compound is displaying a fluorescence emission higher than expected, although this requires more work to fully examine this.

6.8.1 *Increased background*

These high background levels (Figure 139) are in contrast to what has previously been shown in the literature, so experiments were performed to attempt to determine the source of this high background level.

Thin layer chromatography (TLC) [213] is a measurement technique that separates out compounds with different retardation factors (R_f). This factor can be affected by several properties, including the polarity of the molecule and its solubility in the solvent. TLC is typically performed by spotting the compound at the bottom of a plate, then immersing the lower section of the plate in a chosen solvent. Spotting involves filling a small capillary with the fluorophore solution, and repeatedly placing a dot of solution on the plate and allowing the liquid to evaporate. The solvent is picked depending on the exact properties that one wishes to discriminate between. The solvent is then allowed to travel up the plate via capillary action until it reaches a set point, when the plate is removed from the solvent and dried. In the case shown below the compound is coloured and can be directly observed, otherwise a UV lamp is typically used to measure the location of the compound.

The aim of this was to determine whether the fluorophore is in its oxidised or unoxidised states by looking at the polarity of the molecules which changes after oxidation.

Figure 140 shows the results of a TLC measurement on aluminium-backed silica gel slides using 3:1 petroleum ether (PE) :ethyl acetate (EA). The left sample in Figure 140a shows the results from a 1 mM unoxidised sample of the fluorophore, and the right a 50 µM oxidised sample. The latter was done at a lower concentration as the solubility of the oxidised version of this molecule is much lower than the initial version, and the amount of fluorophore that could be dissolved in the o-xylene was limited. It can clearly be seen from this result that the right (unoxidised) compound travels a significantly shorter distance than the left (initial) compound. We can conclude from this that

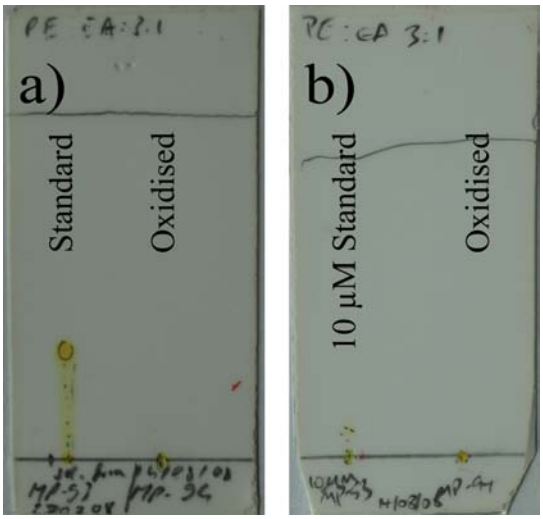

Figure 140: Thin layer chromatography for DPPNBD samples in o-xylene using 3:1 PE:EA. a) left - 1 mM unoxidised. right - 50 µM oxidised b) left - 10 µM unoxidised. right - 50 µM oxidised. The longer distance travelled up the plate demonstrates a higher mobility of the compound compared to compound which remains at the origin.

the initial compound is highly non polar, while the oxidised version is considerable more polar. This is to be expected by looking at the compound structure, and also explains the lower solubility for the oxidised compound.

Figure 140b shows the same experiment repeated, however with a much more dilute concentration of 10 µM for the initial (unoxidised) compound on the left. Again the right sample is a 50 µM oxidised compound. Comparing the results of this trial to Figure 140a it can be noted that the distance travelled by the unoxidised sample in Figure 140b is significantly shorter than the equivalent sample in Figure 140a. Care was taken to ensure that a similar amount of compound was deposited for all trials, with the lower concentration samples requiring multiple drops of sample to be added and then allowed to evaporate off their solvent.

Since the only difference between this sample and the first one was the concentration, this supports the earlier hypothesis that the fluorophore is being oxidised in o-xylene, even without the addition of hydroperoxides. This trial was repeated filtering the o-xylene through alumina powder in a column to attempt to remove any impurities, however a similar result to that shown here was obtained.

The measurements in Figure 140 were repeated with more concentrations, and the results are shown in Figure 141. This test was performed approximately 8 weeks after the initial trial, both to see how the concentration affects the measurement, as well as to see if any degradation of the fluorophore is observed over time. Comparing this trial to the two unoxidised samples in Figure 140 it can be noted

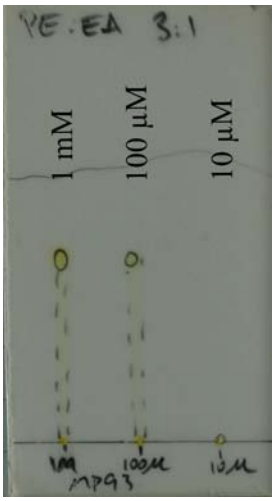

Figure 141: Thin layer chromatography for DPPNBD samples in o-xylene using 3:1 PE:EA. Left) 1 mM unoxidised. Middle) 100 µM unoxidised. Right) 10 µM unoxidised.

that the 10 µM sample remains on the line, implying that it is oxidised just as the earlier 10 µM sample was. The 100 µM sample shows more than half of the sample remaining on the line, with slightly less for the 1 mM sample. The 1 mM sample is qualitatively similar to the first trial, and due to variations in the exact amount of compound applied to the TLC card and experimental uncertainties it is difficult to reach a conclusion from this measurement.

The consistency between this measurement and the first trial still suggest however that the source of the oxidation (and thus the increased background signal) is from the solvent.

As a final trial the solvent was degassed by bubbling nitrogen through it for 72 hours to attempt to remove any oxygen radicals or other oxidising products that may be present within the solvent. For this trial the solvent was changed from 3:1 PE:EA to 25:1 EA:Methanol. For this solvent, the more polar oxidised compound moves a shorter distance than the unoxidised version. Figure 142 demonstrates that for 10 µM samples even with degassed solvent the same behaviour as seen earlier is noted. Likewise Figure 142b shows similar behaviour to earlier, with the 1 mM sample remaining mostly unoxidised while the 100 µM sample is almost completely oxidised.

This high level of background makes measurements at relatively low hydroperoxide concentrations extremely difficult, as the difference before and after the addition of hydroperoxide is likely not high enough to be able to be resolved in fibre-based measurements. The above results suggest that the DPPNBD molecules are being oxidised in the o-xylene before the addition of hydroperoxides, so the dynamic range of this molecule will be limited as detection of low concentrations of hydroperoxides will likely be prevented by the background oxidation from the solvent.

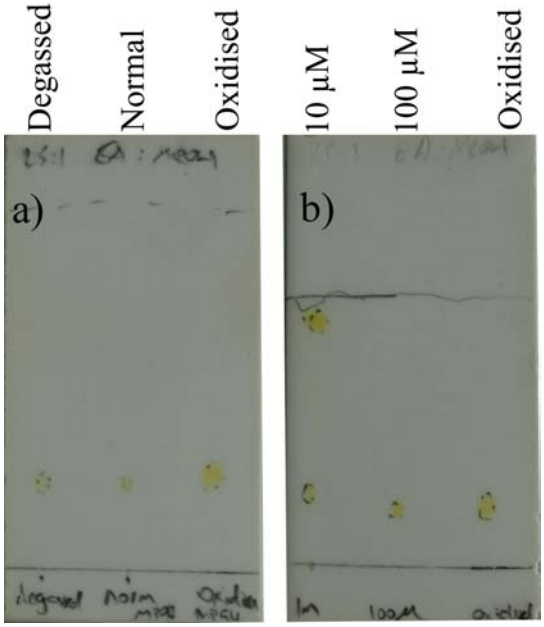

Figure 142: Thin layer chromatography for DPPNBD samples in o-xylene using 25:1 EA:MeOH. a) Left - 10 µM unoxidised in degassed o-xylene. Middle - 10 µM unoxidised in regular o-xylene. Right - 50 µM oxidised. b) Left - 1 mM unoxidised in degassed o-xylene. Middle - 100 µM unoxidised in degassed o-xylene. Right - 50 µM oxidised.

6.8.2 *Alternative solvents*

With the results from the previous section strongly suggesting that the solvent was the cause of the oxidation issues, a trial using an alternative solvent was proposed. Acetonitrile, whose structure is shown in Figure 135, was another solvent used by Ref. [198]. Literature reports that this compound should show a 31 × increase in its fluorescence emission when oxidised in this solvent. The initial trial, which is shown in Figure 143 compared the fluorescence emissions at the same concentration in both o-xylene and acetonitrile. This measurement was recorded using a commercial Cary spectrophotometer.

As can be seen from this plot the fluorescence emission from the unoxidised acetonitrile is significantly lower than the o-xylene sample without the addition of hydroperoxides. Once the sample was spiked with a high concentration of hydroperoxides the fluorescence emission from this sample rapidly increased to a level approximately 16× higher than the initial unoxidised level. This increase is in reasonable agreement with the expected literature values, and again supports the hypothesis that the solvent is the issue rather than the compound itself. The shift in the fluorescence peak that is noted between the o-xylene and acetonitrile samples is also similar to what is expected from literature, with Ref. [198] reporting that the peak in benzene is 508 nm while the peak in acetonitrile is 520 nm.

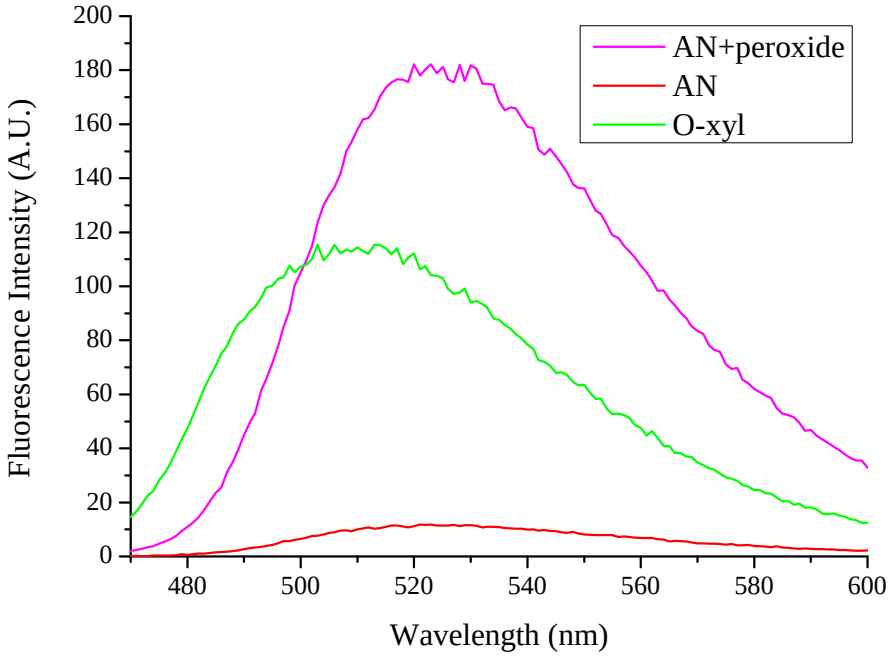

Figure 143: Fluorescence emission spectra for 10 µM samples in two solvents. Green is o-xylene, and red and magenta are acetonitrile samples before and after the addition of hydroperoxides.

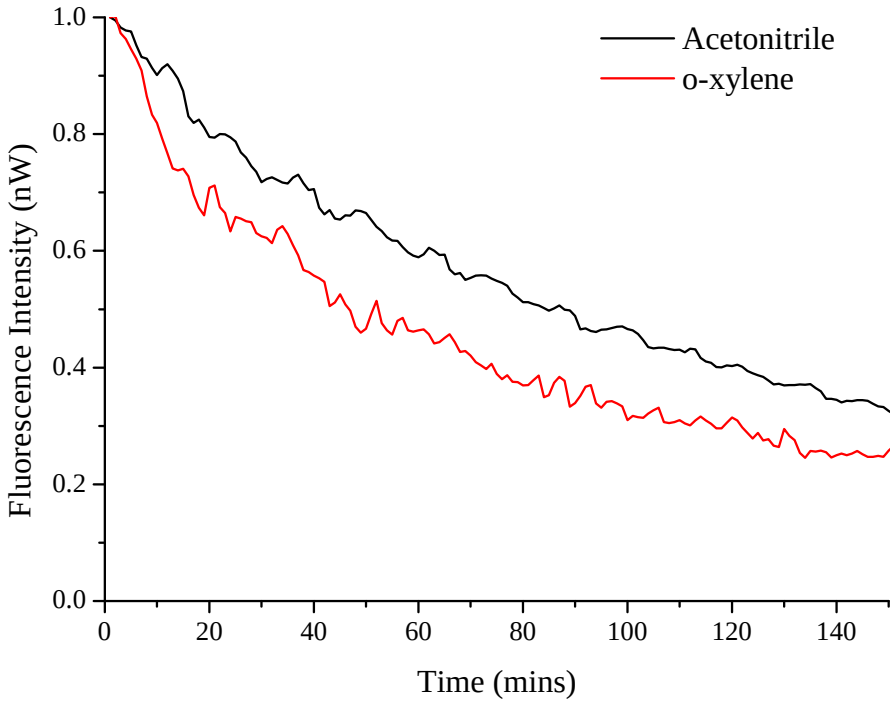

Figure 144: Photobleaching rate in acetonitrile and o-xylene.

This solution of oxidised fluorophore in acetonitrile was then exposed to intense 458 nm light using the experimental configuration shown in Figure 137. Again 10 mW of 458 nm light was used, and the fluorescence spectra recorded every minute. The results of this trial compared to the same concentration of solution in o-xylene are shown in Figure 144 normalised to the initial fluorescence intensity. The main conclusion from this experiment is that the photobleaching rates between the fluorophore in o-xylene and acetonitrile are comparable. Again since these observations are based on cuvette measurements where other fluorophores such as Rhodamine do not experience measurable photobleaching (see Figure 22) this strongly suggests that measurements in fibre will be problematic. It has previously been shown (Figure 22) that the photobleaching rate is significantly worse in fibre than in cuvette, due to a combination of the high intensities and confined volume.

6.8.3 *In fuel sensing trials*

As a final trial with DPPNBD in cuvette some actual fuel samples were measured. One of these samples was a fresh sample, the other degraded by thermally cycling. As previously mentioned thermal degradation in aircraft is the main cause that promotes early degradation of the fuel, so artificially thermally cycling the fuel creates the same conditions that generate actual degraded samples. Since hydroperoxides are a product of degradation, the degraded sample shows a higher level of hydroperoxides than the fresh sample. The goal of this measurement was to observe if there was a measurable difference in the observed fluorescence intensities, and thus if a difference in the hydroperoxide concentrations could be determined between the two samples.

Two fluorophore solutions were mixed, a 100 µM solution in acetonitrile and 1 mM in toluene. These were mixed using fresh compound, with the toluene degassed and passed through a basic alumina filter. This solution was then mixed in a 1:9 ratio with two JP-8 aviation fuel samples. This gave a final concentration of 10 µM for the toluene/aviation fuel samples, and 100 µM for the acetonitrile/aviation fuel samples. These measurements were performed with different detection methods, but using the same excitation power. The results are not directly comparable to each other, however the standard/undegraded samples are obviously comparable with the degraded samples at the same concentration. The toluene sample used an Ando AQ6315E OSA, while the acetonitrile sample used a compact ocean optics USB4000 spectrophotometer.

Figures 145 & 146 show the results with the fluorophore first dissolved in toluene and acetonitrile respectively. Figure 145 suggests that there is a slight increase in the fluorescence signal between the de-

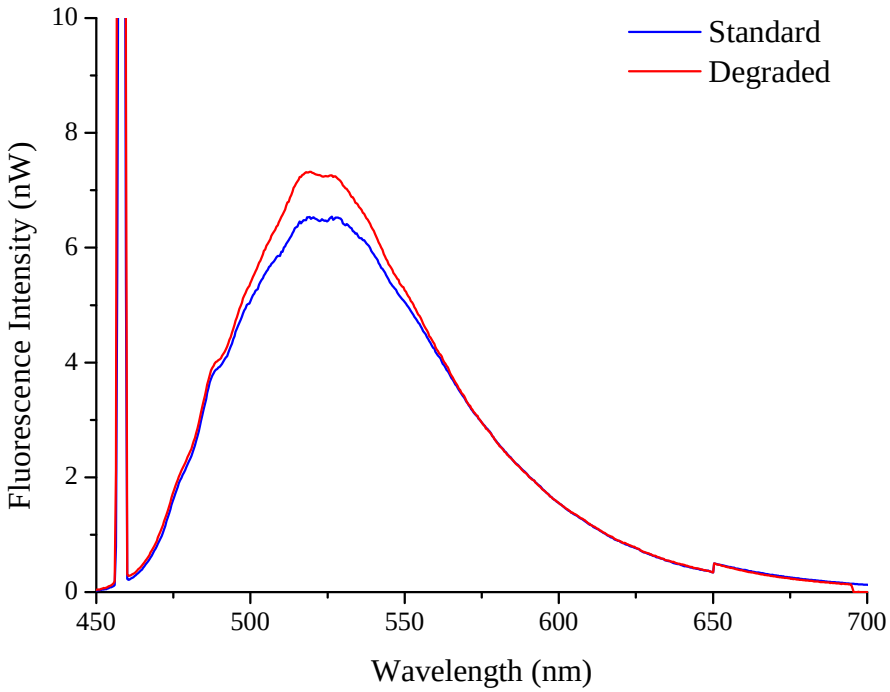

Figure 145: 100 µM fluorophore solution. Dissolved in toluene then aviation fuel (JP8/JET-A1).

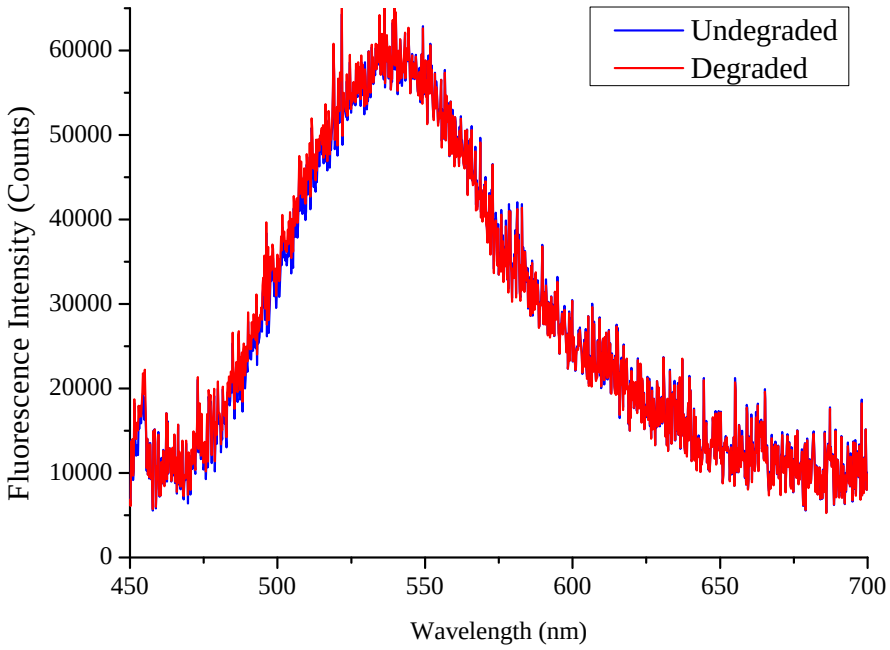

Figure 146: 10 µM fluorophore solution. Dissolved in acetonitrile then aviation fuel (JP-8/JET-A1).

graded and undegraded samples when the fluorophore is dissolved in toluene then aviation fuel. This measurement shows approximately a 12% increase in the fluorescence signal for the degraded sample. However when the measurement was repeated the reverse was seen, with the undegraded sample showing approximately 5% more fluorescence than the degraded sample. This trial failed to distinguish between the degraded and undegraded fuel samples.

There was no measurable difference between the two fuel samples in acetonitrile, as can be seen in Figure 146. It should be noted that the acetonitrile was only partially miscible in the aviation fuel, and only partial mixing was observed even after ultrasonication.

Spiking either of these samples with several drops of 80% hydroperoxide again produced no measurable increase in the fluorescence signal from the levels shown above. This suggests that the fluorophore has already been oxidised either before contact with the fuel or in the base fuel itself, and thus the quantum yield can not increase any further.

Although these results suggest that DPPNBD will not be suitable for fibre based measurements it was decided to proceed with some trials to gain data to help with the choice and development of future fluorophores. It would be ideal to gain some understanding of how the photobleaching rate of these molecules that have been demonstrated to be susceptible to photoinduced damage behave in fibre compared to the results obtained here.

6.8.4 *Fluorophore measurements in fibre*

6.8.4.1 *DPPNBD in fibre*

Initial trials had shown that the fluorescence signal from this molecule in o-xylene at low concentrations (10 µM-100 µM) could not be detected using either the ocean optics spectrophotometer or ANDO OSA. A 30 cm length of F2 wagon-wheel fibre with a 1.5 µm core size was filled with a 100 µM solution of fluorophore in 9:1 o-xylene/aviation fuel. The filling rate was measured using two separate techniques to check if there was any separation of the fluorophore (initially dissolved in toluene) and the aviation fuel.

Filling measurements for the fuel + fluorophore sample were performed using the same method described earlier in Section 2.5.2.

To measure the location of the liquid in the fibre without the fluorophore present the laser light was coupled in as per usual, although at a higher power level. Unlike the fluorophore measurements, the laser light was not blocked between measurements. Instead the fibre was carefully monitored, and the location of the meniscus at the front of the filling liquid could be measured by closely examining the fibre and looking for a location with increased scattering. Since the aviation fuel is a much higher index than the air that it displaces there

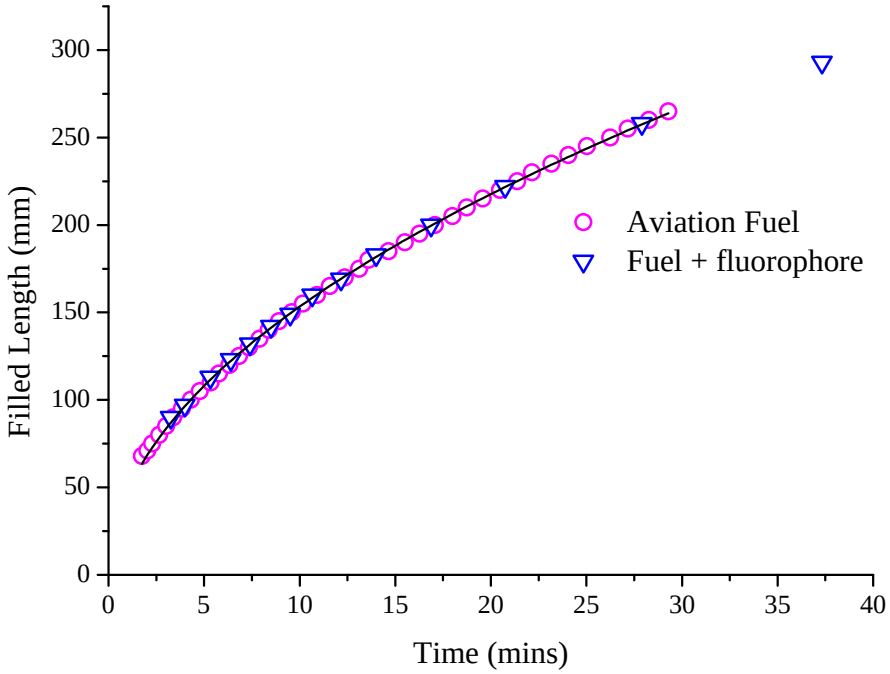

Figure 147: Aviation fuel (JP8) filling in F2 wagon-wheel fibre, hole size 7 µm. Magenta circles - filling with only fuel, blue triangles filling with fuel and fluorophore. Black line is a fit to $y = Ax^{\frac{1}{2}}$.

is a change in the mode field distribution at the interface between the air and the liquid. This interface creates a mode mismatch at this point, scattering laser light as it crosses this interface.

The fuel and fuel + fluorophore measurements, shown in figure 147, agree within experimental uncertainty and from this we can conclude that there is no separation of the liquids within the fibre. Earlier trials using isopropanol + aviation fuel did show a separation, with two clear menisci visible as the fibre fills.

A new fibre was then aligned, and filled with the aviation fuel/toluene + fluorophore mixture, the results of which are shown in Figure 148.

This trial produced ambiguous results, as the general shape of the signal appears to match that obtained in cuvette (from Figure 145) however the signal level is extremely low, and basically at the noise floor of the detector used. At the time of this measurement there were two detectors available - the first; an Ocean Optics USB4000 CCD spectrophotometer has a relatively poor signal-to-noise ratio, and could not pick up the fluorescence signal in this measurement. The second detector, an Ando AQ6315E OSA is much more sensitive than the CCD, however it has the drawback that the scan times at these high sensitivities is long. So since the signal was relatively small it is likely that the vast majority of the fluorophore had photobleached, as the results in Figures 138 and 144 suggest that this molecule is particularly prone to these effects.

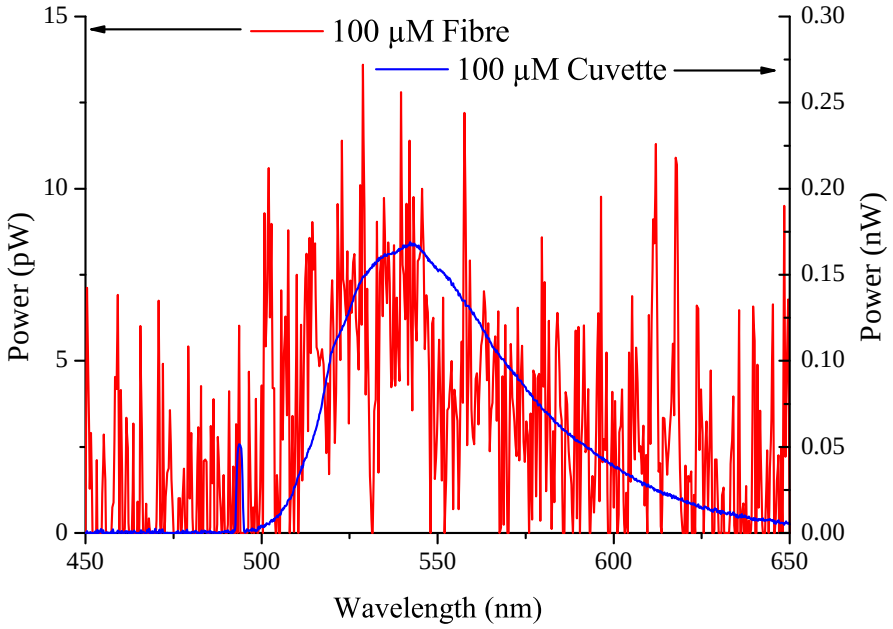

Figure 148: Fluorescence signal of a 1 mM solution of DPPNBD filled in 30 cm of F2 wagon-wheel fibre with 1.5 µM core. Input power approximately 30 mW.

This experiment was revisited at the conclusion of the project, using the optimised detection apparatus developed for the low-concentration measurements in Chapter 2. The primary change here was that the 532 nm laser used for the quantum dot measurements was obviously not suitable for use with this fluorophore, so it was changed for the 458 nm line on an argon ion laser. The laser was attenuated for these measurements down to approximately 10 µW, which is more than 3 orders of magnitude lower than that which was used for the previous in-fibre result. The fluorophore used was a 100 µM solution which had hydroperoxide added. The results of this are shown in Figure 149.

Unfortunately at the time this measurement was taken the correct filters for collection of the fluorescence in the backwards direction were not available, so a 500 nm long pass filter was used. This resulted in the peak of the fluorescence being pushed to longer wavelengths as the filter attenuated the original peak. The sharp peaks shown in the unfilled scan arise directly from the laser, and are again due to insufficient filtering of the laser output. Immediately after this initial scan the beam was blocked, and the fibre allowed to fill.

A shutter was used to block the beam between scans, and 20 scans made with a scan time of 1 second per scan. The photobleaching rate for these measurements, shown in Figure 150 is slow enough that it would be feasible to do measurements using this fluorophore in fibre with the new detection apparatus. This is a clear contrast to the

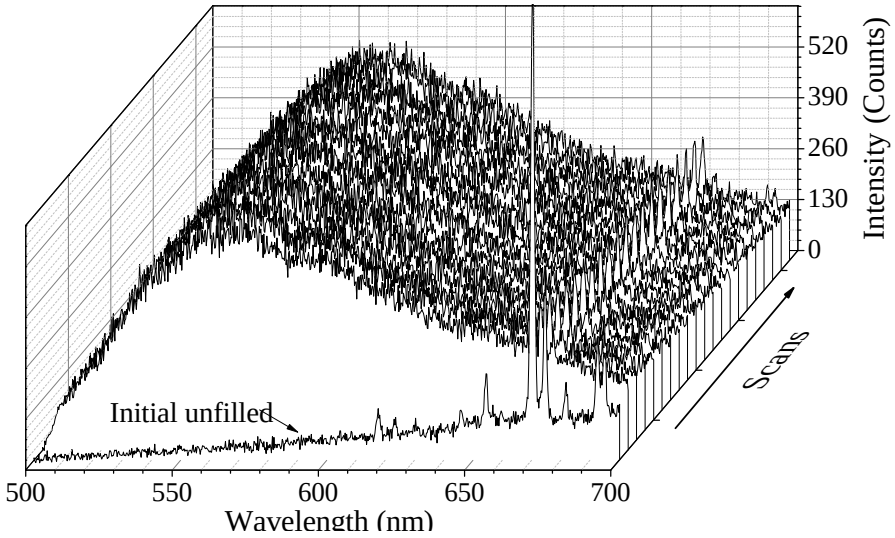

Figure 149: In fibre DPPNBD signal using optimised monochromator + Cooled CCD detection and time gating for the measurement.

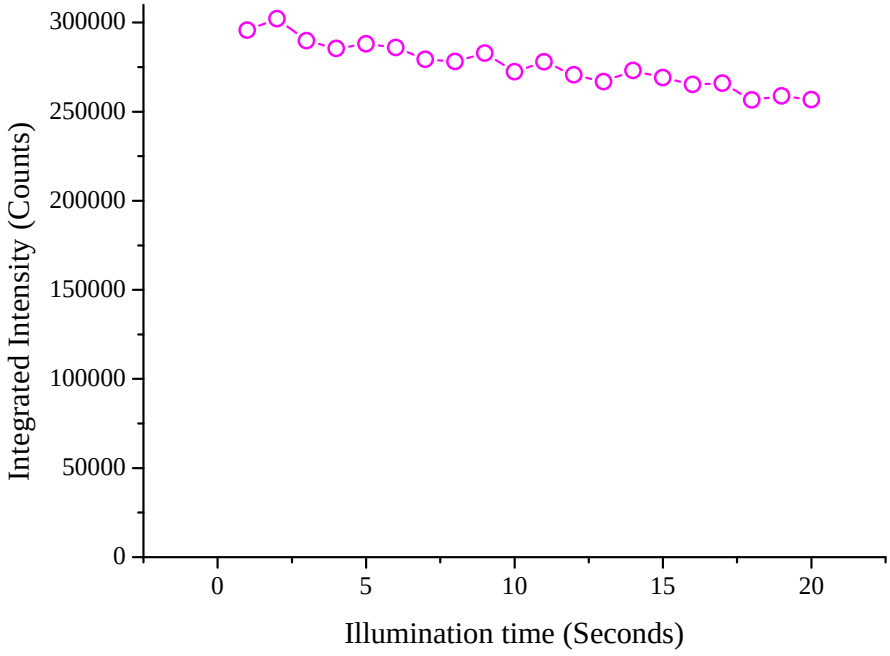

Figure 150: Integrated fluorescence intensity of Figure 149 with DPPNBD.

earlier fibre results shown in Figure 148 where the fluorescence signal is barely (if at all) distinguishable above the noise from the detector.

An attempt was made to demonstrate hydroperoxide sensing in fibre using this fluorophore and the new detection apparatus, however it was noted that all of the available fluorophore stocks appeared to be non-reactive. This is most likely due to them having already reacted to their highly fluorescent (oxidised) configurations, since the samples were more than 2 years old at the time they were measured. Due to time constraints, combined with the issues described earlier with self-oxidation in o-xylene repeating the previous work using the improved detection apparatus was not deemed possible.

From these measurements we can conclude that it is possible to do fibre-based measurements even with fluorescent molecules that show an extremely rapid photobleaching rate by using sophisticated detection apparatus. These measurements could possibly be performed in the field using a more compact detector, such as a cooled spectrophotometer such as the Ocean Optics QE65000 or alternatively using an avalanche photodiode. Both of these detection methods would likely enable measurements using this fluorophore to be performed using a much more portable experimental configuration than was demonstrated here. This was the first known demonstration of a PET molecule using a microstructured optical fibre.

6.8.4.2 *Amplex red testing in fuel*

The fluorophore that found use for aqueous hydrogen peroxide testing, Amplex Ultrared (see Section 7.2), was also trialled in fuel. It was found however that this compound was not soluble in fuel when added directly to the solution. Large particles of fluorophore were visible in the container even after extensive ultrasonication and heating.

To attempt to remedy this the sample was dissolved first in dimethyl sulfoxide (DMSO), which is the solvent recommended by the manufacturer. This DMSO + fluorophore + horseradish peroxidase (HRP) solution was found to be miscible in the fuel sample, and was prepared to a concentration of 10 µM. When concentrated (30%) hydrogen peroxide was added however the solution did not change colour as expected. Measurements showed that virtually no fluorescence could be observed from this sample. When water was added to this solution it immediately separated in to a layer of fuel (clear) and a layer of fluorophore/water. This fluorophore water layer changed to a pink colour rapidly, and was observed to show a strong fluorescence signal.

This result strongly suggests that this fluorophore is not suitable for use in fuels, so from here it was used exclusively in aqueous solutions.

6.8.4.3 *Summary*

The work covered so far in this section demonstrates that using DPPNBD measurements can be taken in fibre when using sophisticated detection apparatus. So although the fluorophore is extremely susceptible to photobleaching (See Figures 138, 144 & 150) this issue can be somewhat overcome through the reduction in the excitation power and the significantly reduced exposure time that this improved detection method allows.

7

AQUEOUS H_2O_2 SENSING

7.1 INTRODUCTION

The capacity to measure the concentration of hydrogen peroxide in aqueous solutions is critical for many disparate areas, including wine and In Vitro Fertilization (IVF) [214]. Conventional methods generally revolve around chemical-based techniques, using methods such as titrations or chemiluminescence [215] to quantify the peroxide content, however these techniques have several drawbacks.

One of these is the time involved in testing - a single titration for hydrogen peroxide takes in the order of 10 minutes, so doing multiple samples takes a significant length of time. These methods also require a relatively large sample volume of liquid. Generally a titration requires in the order of 5-50 mL depending on the expected H_2O_2 concentration. The ability to measure extremely small sample volumes has numerous possible applications, with the current focus on this work being the development of a low-volume hydrogen peroxide sensor for applications in the area of reproductive health science.

The primary aim of this work is the development of a sensor that can sample the culture medium of developing embryos to assist in monitoring the health and viability of embryos. These samples vary in size, but generally the total volume of the culture medium is less than 20 µL. Measurements of large ensembles of embryos has revealed that the hydrogen peroxide levels during the development of the embryo can be correlated to the health of the embryo, and are a good indicator of its viability and the impact of environmental stresses on the embryo [214, 216].

At present, available testing techniques generally require the removal of the embryo from the culture medium, at which point the sample medium is diluted and conventional measurement techniques employed. Although this technique is successful in determining chemical concentrations, it has the major drawback of requiring measurement of the entire culture medium thus making temporal measurements on the same embryo virtually impossible. To date measurements of the peroxide concentration over time have required the use of multiple embryos, as the measurements themselves are destructive. The method proposed here will allow temporal measurements to be performed using a single embryo, thus reducing the number of embryos required for systematic results to be recorded.

Sensing for hydrogen peroxide in aqueous solutions is a much more developed field than sensing in aviation fuels, and opens up

many more choices for fluorescent molecules. Two avenues were simultaneously explored during this project; a commercial fluorophore and internal fluorophore development. The goal of the commercial fluorophore work is to characterise the possibility of doing hydrogen peroxide sensing in fibre, with a fluorophore that is known to behave well in regards to auto-oxidation, photobleaching etc. Having a fluorophore that is known to work well enables progress to be made on development of the sensor platform itself, such that the sensor is well characterised and well understood when a useful fluorophore is synthesised.

Developing an internal fluorophore however is primarily focussed on creating a fluorophore that can be surface functionalised on the internal surfaces of the holes in the fibre. Development of a novel molecule was required as no suitable molecules could be found either in literature or from commercial sources that both reacted with hydrogen peroxide and could be surface functionalised. As previously mentioned this has two main advantages over a free-floating fluorophore. Firstly it does not require pre-mixing of the chemicals, and has the potential to be a true "one-step" sensing method, where the only action required is to dip the fibre in the desired solution then perform the measurement. This also allows the volume of the measurement to be minimised. Since the internal volume of wagon wheel fibres is in the order of 10 nL-100 nL for practical (10-50 cm) fibre this is a method that has potential to perform numerous measurements on micro-litre sized samples without disturbing the sample itself.

The objective of this research is to develop a rapid test for the hydrogen peroxide content that can be performed on low volume samples (ie sub-µL) that is relatively independent of other products within the sample. The final section comprising the majority of this work focussed on detection of hydrogen peroxide in the vicinity of embryos, while initial characterisation was performed with the intent of performing measurements on wine samples.

7.2 WINE SENSING WITH COMMERCIAL FLUOROPHORE

With the focus moving towards sensing in aqueous mediums, a fluorophore was acquired for initial measurements. The molecule chosen was Amplex Ultrared (AUR), a commercially available fluorophore from Invitrogen [118]. This molecule reacts with hydrogen peroxide in the presence of horseradish peroxidase (HRP) to produce a large increase in the fluorescence. This fluorophore is a derivative of one which has been studied previously in the literature, N-Acetyl-3,7-dihydroxyphenoxazine (Amplex Red) [217–219]. The main differences between Amplex Ultrared and the examples in literature is a higher fluorescence yield per hydrogen peroxide molecule, and a reduced sensitivity to pH.

The first application focus for this work was on sensing for hydrogen peroxide in white wine samples. Initially this was limited to white wine, to avoid issues with the strong absorption features present in red wine. Wine is a complex solution, with a pH ranging from 3.0-3.9 [220] and a typical ethanol concentration of 10-14% [221, 222]. The presence of hydrogen peroxide is important at several stages, both during the development of the grapes themselves and during the winemaking process.

Initially it was decided to test samples in water, and then slowly increase the complexity of the solution. A standard tool in wine science is to use model wine solutions, which consist of tartaric acid, ethanol and the possible addition of phenolics and other compounds to better mimic the properties of actual wine which ensuring consistency between measurements that would not be possible with real wine samples.

7.2.1 *Initial characterisation*

To ascertain some of the relevant properties of this fluorophore, characterisation was first performed on bulk samples using cuvettes. This enables a much faster throughput of samples, so that many properties can be examined quickly. Typically making a measurement in fibre requires between 5-20 minutes depending on the filling time, whereas measurements on cuvette samples can be performed in less than a minute.

The key parameters that were to be measured here were -

1. Photostability.
2. Magnitude of the increase in fluorescence intensity with hydrogen peroxide.
3. Linearity and useful working range of the fluorescence emission.
4. Sensitivity to the horseradish peroxidase content.
5. pH sensitivity.
6. Stability of the compound for long-duration measurements.

The experimental configuration for cuvette measurements is shown in Figure 151.

This fluorophore has its peak absorption significantly higher (Figure 152) than the fluorophore in the last section, allowing usage of alternative laser sources. Rather than the bulky argon ion laser used for the previous fluorophore a diode-pumped solid state 25 mW 532 nm crystal laser source was used. This wavelength is not at the peak

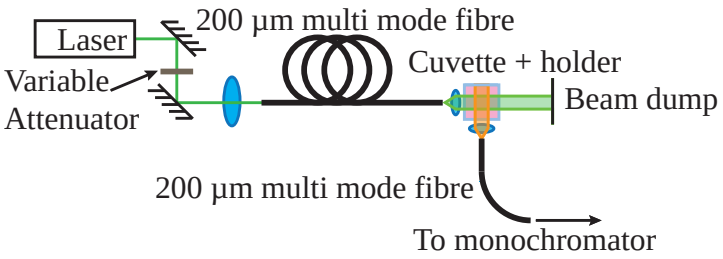

Figure 151: Experimental configuration for cuvette measurements on Amplex Ultrared. A 532 nm source was used for all experiments, and the detection apparatus varied between a compact Ocean Optics QE65000 spectrophotometer and a Horiba iHR320 monochromator.

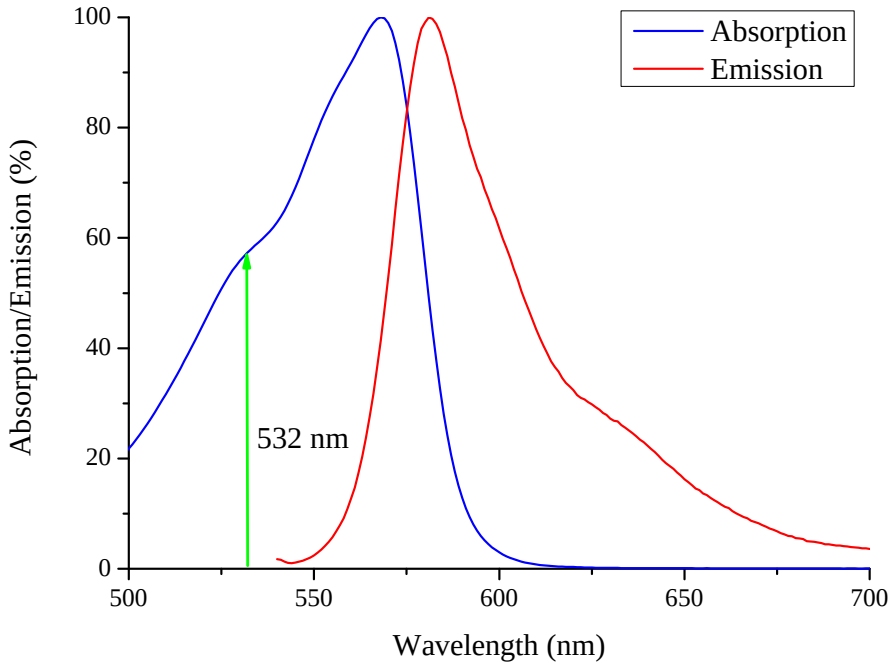

Figure 152: Amplex Ultrared relative absorption and emission [118].

absorption wavelength of 568 nm, but the absorption efficiency relative to this maximum is still 57% at this shorter wavelength. This wavelength was chosen in preference to one closer to the absorption peak as the longer distance between the pump and emission wavelengths enables the pump signal to be better filtered when performing measurements. The laser source used here also possesses other advantages over the argon-ion used in the previous section, such as its improved beam quality and pointing stability.

The first test to be performed was exploring how the fluorophore reacts with hydrogen peroxide in bulk solutions. For these measurements no buffer was used, instead all measurements were performed in water. This was done to ensure that the compounds used to stabilise the buffer solutions had no effect on the observed fluorescence

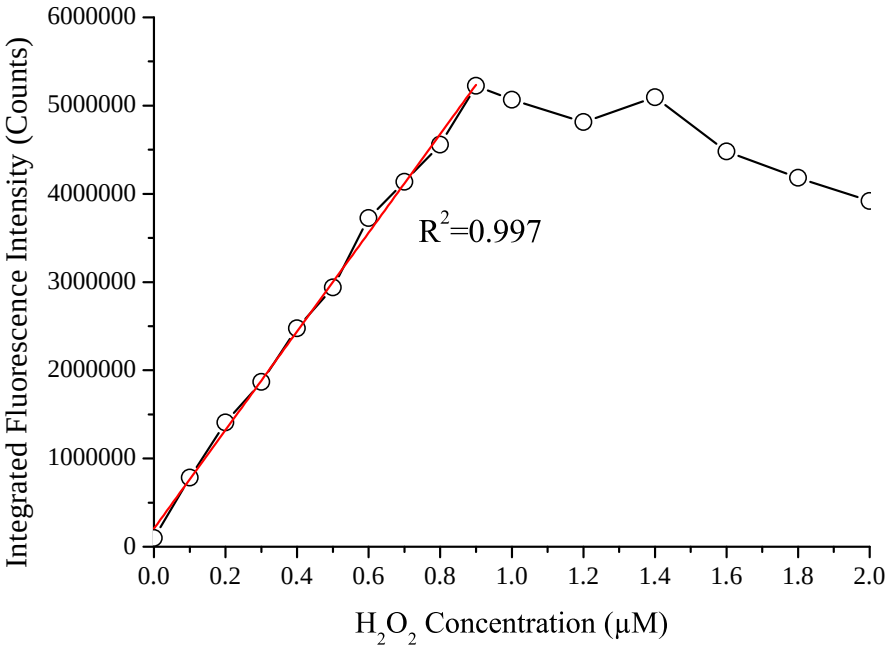

Figure 153: Cuvette measurements for 10 µM Amplex Ultrared solution with varied hydrogen peroxide concentration.

signal. The results of this trial for a 10 µM solution of Amplex Ultrared is shown in Figure 153 below. Integrated fluorescence intensity refers to the sum of the counts obtained between 550-700 nm.

A relatively linear range was demonstrated over the target hydrogen peroxide concentration of 0-1 µM (Figure 153) which was the given range of detection for wine samples [223]. Applying a linear fit to the points 0-900 nM gives an R^2 value of 0.997 which shows good linearity over this range. Importantly, the increase in fluorescence signal between the unoxidised 0 µM sample and the peak fluorescence signal at 900 nM was 26 ×. A large increase in the fluorescence signal is critical for obtaining a large dynamic range for measurements in fibre. If this ratio of unoxidised:oxidised fluorescence is too small then changes in the fluorescence signal occurring due to changes in the peroxide concentration may be masked by changes in the coupling of the fibre. Likewise, small changes in the coupling of the fibre could easily be interpreted as a large change in the peroxide concentration, possibly giving false positive or negative results.

The next parameter to measure was the speed of reaction, as well as the stability post reaction. To facilitate this another cuvette measurement was performed using the experimental configuration shown in Figure 151. To ensure that this measurement records only the natural reaction rate, and not a rate affected by photobleaching or even a photoinduced increase in the reaction rate the measurement was performed using a minimum excitation power. The laser was attenuated to 2.5 µW, with approximately 2 µW incident on the cuvette sample.

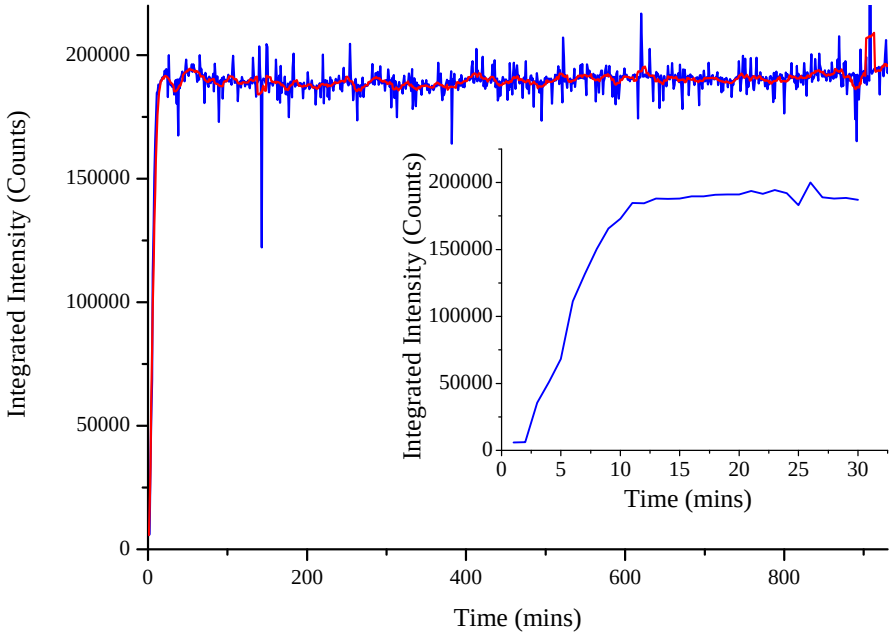

Figure 154: Reaction rate of 1 µM Amplex Ultrared solution, when H_2O_2 is added such to bring the peroxide concentration to 1 µM. The measurement was performed at low input power and blocked between scans to ensure that photobleaching (or any sort of photoreaction) occurred. The inset shows the same data over the initial 30 minutes of the trial.

This had the undesirable consequence that the noise increased in the measurement, but since it was desirable to create a scenario that closely mimics the actual reaction conditions (i.e. in the dark) the exposure to light needed to be minimised. For comparison a second sample was mixed to the same concentration at the beginning of the measurement, and stored in the dark for the duration of the measurement. This sample showed the same final fluorescence signal within experimental error, suggesting that exposing the fluorophore to this low intensity laser light even for prolonged periods had minimal effects on the fluorescent properties of the solution. The results of this measurement using a 1 µM AUR concentration are shown in Figure 154. Hydrogen peroxide was added to the cuvette immediately after the first scan to make a final concentration of 1 µM.

This result shows that the fluorescence signal initially increases rapidly, before plateauing and remaining relatively constant. The important observation from this measurement is that the reaction rate is relatively fast, so multiple measurements can be performed using this fluorophore in a short duration. The fluorescence reaches to within 5% of its peak value 10 minutes after the addition of the hydrogen peroxide. This is of a similar order to the actual filling time of the fibre, which is typically between 5-15 minutes depending on the length of fibre to be filled and the solvent being used. This implies that the rate

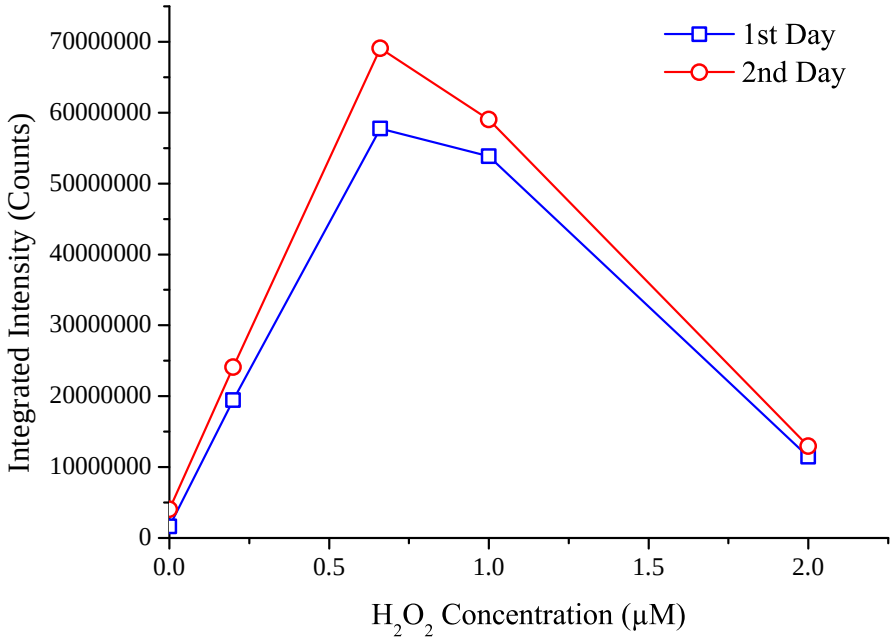

Figure 155: Stability of fluorescence signal at various peroxide concentrations over 36 hours using 10 µM AUR sample in cuvette.

of reaction seen here should not significantly increase the amount of time that is required to perform a measurement.

For any practical sensor, the results need to be able to be recorded after a reasonable length of time. Any system where the fluorescence spectra changes constantly induces an extra unwanted variable. To test how AUR reacts over time, cuvette samples were prepared using the same concentrations of AUR and HRP used in Figure 153. Hydrogen peroxide was added to these solutions in various concentrations, and allowed to react for one hour. Once this time had elapsed the samples were pipetted into cuvettes, and sealed using paraffin tape to minimise evaporation. The fluorescence signal was then recorded using the experimental configuration shown in Figure 151.

Following this measurement the cuvettes were placed in a dark location for 36 hours. The temperature in the laboratory varied between 15-20 °C over this time. The samples were then measured again using the same input power and collection parameters. The results of this measurement are shown in Figure 155.

The fluorescence signal obtained after 36 hours was consistently ~20% higher at all peroxide concentrations than the signals obtained after one hour (Figure 155). This suggests that a portion of the AUR molecules had not yet reacted with the hydrogen peroxide. The initial sample with no added hydrogen peroxide also increased in magnitude, suggesting that some self-oxidisation is also occurring. This agrees with observations during other measurements, where samples left at room temperature for several days gradually increased their fluorescence signal. The fluorescence signal in Figure 154 after 15

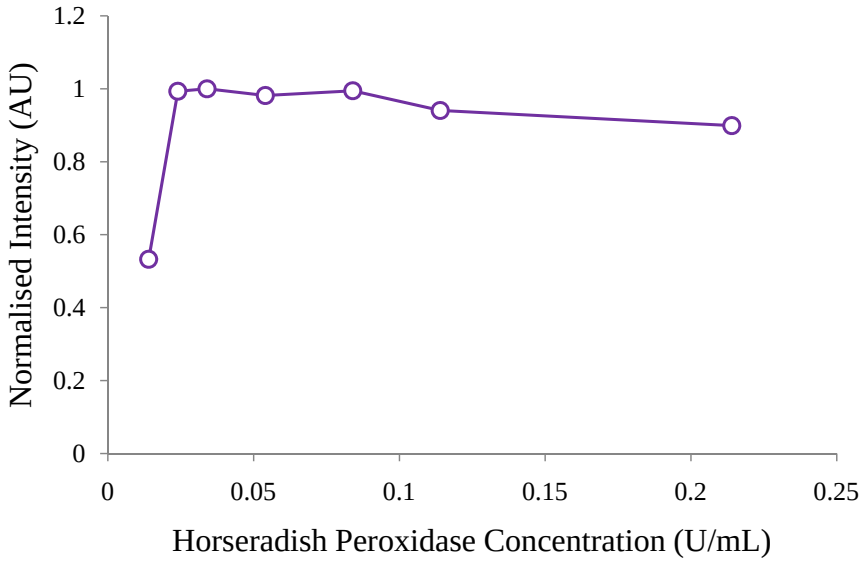

Figure 156: Variation in AUR fluorescence intensity with HRP concentration for 1 µM AUR, 666 nM H_2O_2.

hours is approximately 5% higher than the measurement after 1 hour. It should be noted that the 2 µM hydrogen peroxide signal in Figure 155 was significantly lower than expected, the exact reason for this was not explored.

The increase is relatively slow, so this increase in fluorescence over time can be compensated for. This can be done either by keeping samples at 4°C, where there was no measurable change in the fluorescence signal after 36 hours. Alternatively a calibration curve could be created. This would however increase the minimum detectable concentration due to the self-oxidation that seems to be occurring.

Next the effect of changing the concentration of the horseradish peroxidase (HRP) was examined. Since AUR can also be used as a quantitative test for HRP by using an excess of hydrogen peroxide, it is obviously desirable to choose a HRP concentration such that small changes in this concentration have the smallest possible changes to be fluorescence signal. To determine the required level a 1 µM AUR/666 nM H_2O_2 solution was used, with the HRP concentration varied from ~0.01-0.22 U/mL. The results of this measurement are shown in Figure 156. A unit of HRP is defined by pyrogallol units. One pyrogallol unit will form 1.0 mg purpurogallin from pyrogallol in 20 sec at pH 6.0 at 20°C [136].

For concentrations over 20 mU/mL, the observed fluorescence signal is relatively constant, with small reductions seen at high concentrations (Figure 156). From this it was decided that the concentration of HRP to be used for all measurements with 1 µM AUR solution was 100 mU/mL.

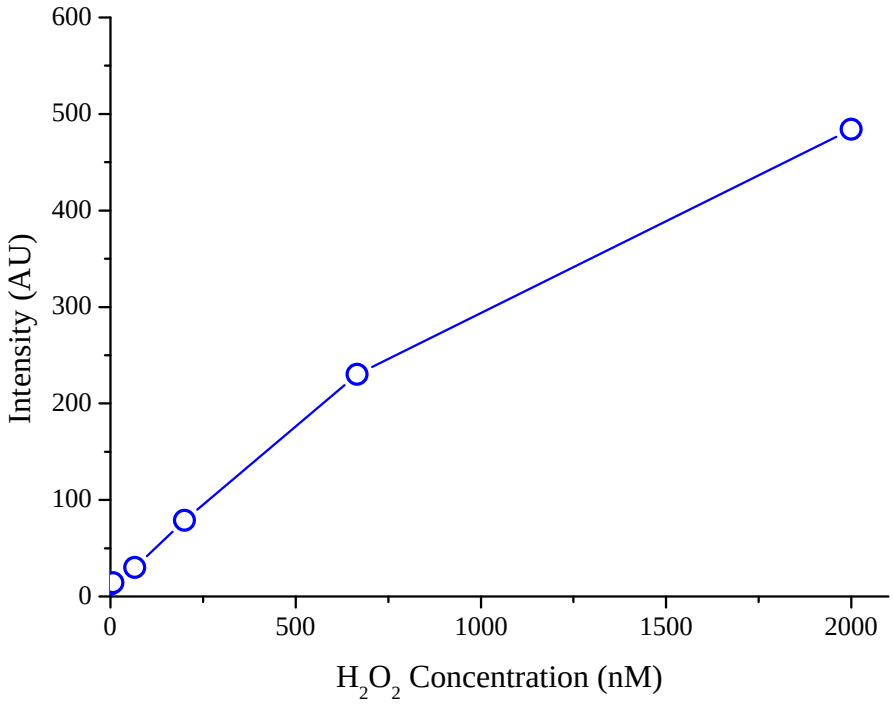

Figure 157: Peak fluorescence response in a 12% ethanol solution with varied hydrogen peroxide concentration for a 1 µM AUR concentration. Performing a linear fit on the first 5 points of this plot gives an R^2 of 0.99978.

7.2.2 *Wine applications*

With the initial characterisation completed, the next step was to gradually increase the complexity of the solution in which the measurements are performed, with the final goal of performing measurements in actual wine solutions.

Firstly ethanol was added to the solutions. The concentration of ethanol in wine typically varies from 10-14% for dry white wines. Two different ethanol concentrations were used, 5% and 12% in addition to a reference water sample. The solutions were made up with identical concentrations of fluorophore 1 µM and allowed to react for 15 minutes. Intensity vs concentration curves were obtained using a Cary Eclipse fluorometer, an example of which is shown in Figure 157 for the 12% ethanol solution.

This plot shows a similar response to Figure 153, with a linear response at lower concentrations and the fluorescence intensity rolling off at high concentrations. This measurement can not be compared directly with the earlier results shown in Figure 153 due to the different detection methods used. The spectra comparing the fluorescence spectra obtained from this 12% sample to the 5% and water samples is shown for a single concentration in Figure 158.

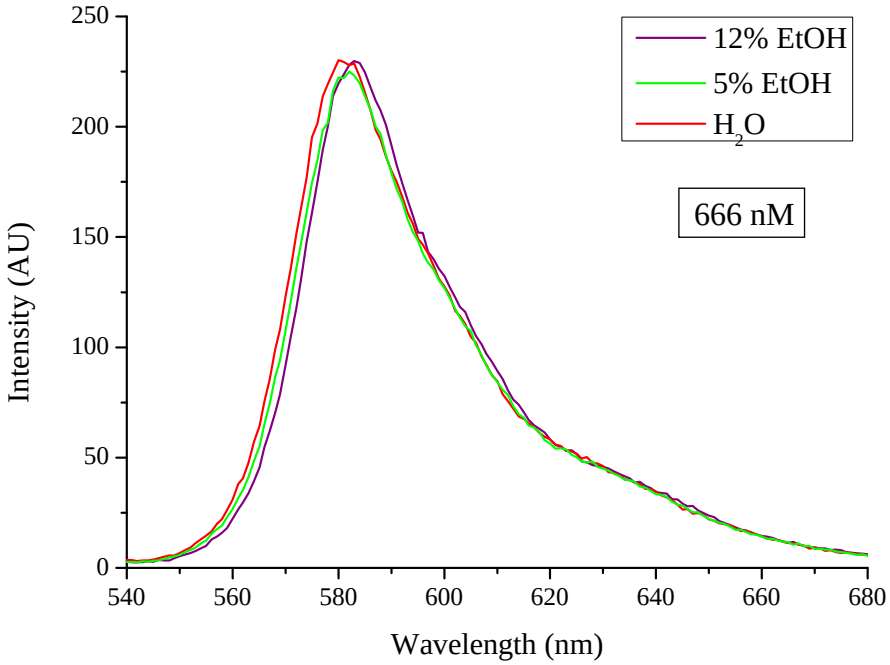

Figure 158: Fluorescence spectra for 1 µM AUR solution with 666 nM H_2O_2 concentration. The ethanol concentration is varied from 0-12%.

This result shows that the ethanol concentration has no effect on the obtained fluorescence response. When the fluorescence signal is integrated across the spectra the results for each of the samples agrees within 2%.

The next parameter varied was the pH, which in white wine is generally between 3-3.9. For this measurement hydrochloric acid (HCl) was used to alter the pH, between the level of the water being used (approximately 5.25) and 2.5. A calibrated pH meter was used to check the exact pH of each of the samples after the addition of the acid. The results of this measurement are shown in Figure 159 for a 1 µM AUR concentration and 666 nM hydrogen peroxide concentration.

As expected from the manufacturer's data [118], the fluorescence signal decreased at low pH levels (Figure 159). At the expected wine pH values of 3-4 there is a substantial change in the fluorescence signal from ~0.12 →0.53. This implies that for quantitative results simultaneous measurements of both the fluorescence signal and the pH of the wine solution will be required. Alternatively it may be feasible to dilute the wine sample in a buffer solution to increase the pH above 5, where the fluorescence response is seen not to change significantly with the pH.

With the effects of changing the pH and the ethanol concentration characterised, it was decided to attempt to use this fluorophore directly in a model wine solution. Model wine consists primarily of tartaric acid and ethanol, sometimes with some phenolic compounds to

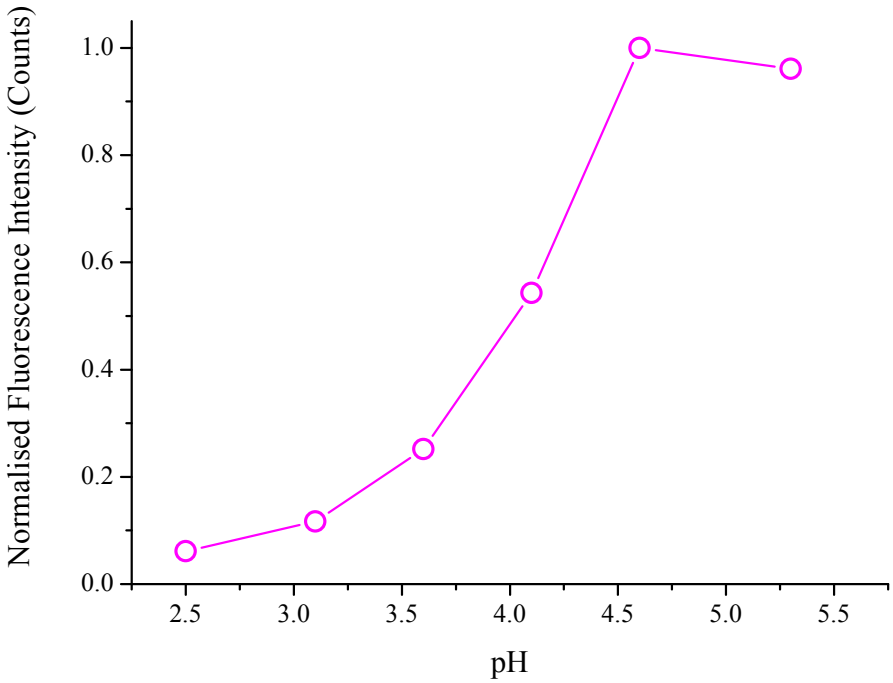

Figure 159: Variation in AUR fluorescence with changing pH. AUR concentration 1 µM, H_2O_2 concentration 666 nM.

more closely replicate the conditions in actual wine. The results of this measurement are shown in Figure 160, compared to a control sample in just water.

As can be seen the model wine samples all show negligible fluorescence signal, regardless of the concentration of hydrogen peroxide. While the control samples show a good response to hydrogen peroxide (see Figures 160 & 161) the model wine solutions at similar hydrogen peroxide concentrations is significantly lower. Note the different scales for the two measurements in Figure 160.

This result shows that the fluorescence signal obtained from the solution diluted in model wine is quenched compared to the solution diluted in water. Indeed the model wine spectra shown in Figure 160 is integrated for 10 seconds, while the corresponding spectra in water are only integrated for 250 ms. There is possibly a small increase in the fluorescence signal at higher hydrogen peroxide concentrations, though it is difficult to distinguish whether this is a real feature over the high level of noise.

As shown earlier in Figure 159 the fluorescence obtained from the Amplex Ultrared solutions is strongly dependent on the pH. The pH of the model wine was measured as 3.57. According to Figure 159 this should correspond to a a fluorescence signal approximately 24% of that of the signal with neutral pH. However this is clearly not the case, with the fluorescence intensity with a hydrogen peroxide concentration of 200 nM only 1.4% that of the control sample. It is clear from this that the reduction in the fluorescence signal is likely only

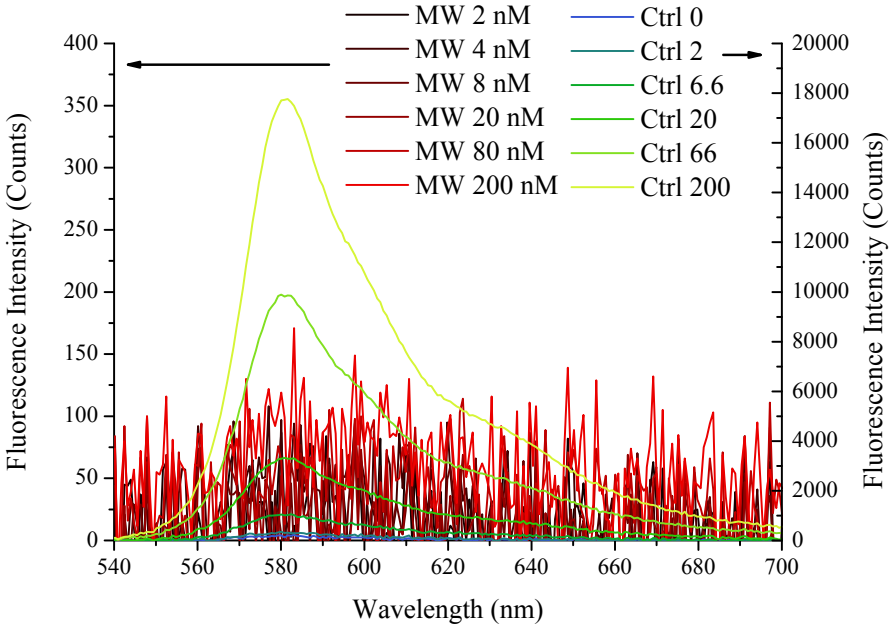

Figure 160: Comparison between fluorescence spectrum obtained with AUR in model wine (MW), and a control solution in water (Ctrl).

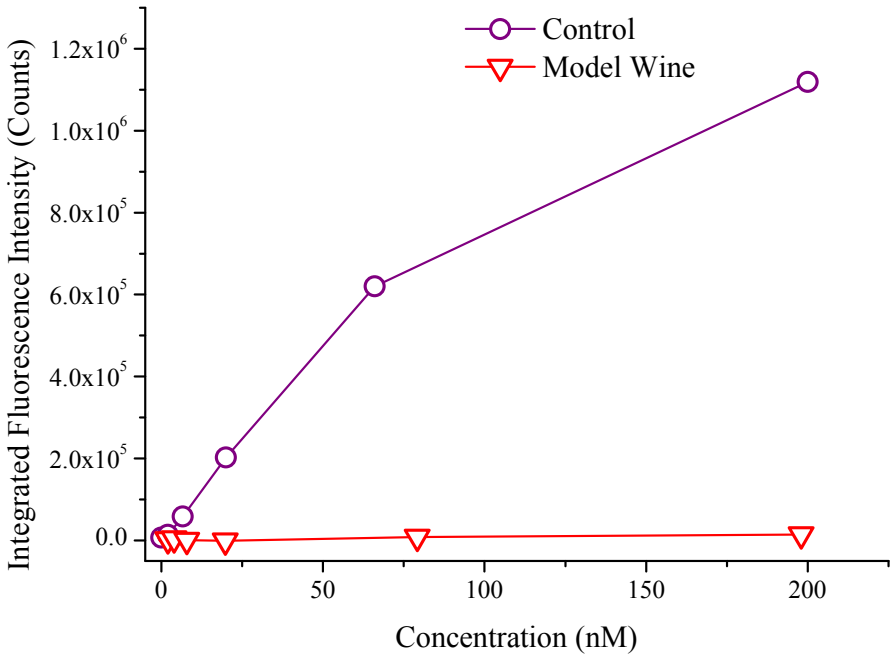

Figure 161: Comparison between identical concentrations of Amplex Ultrared diluted in model wine and deionised water with varied hydrogen peroxide concentration. The integrated intensity corresponds to the sum of the counts between 540 - 700 nm.

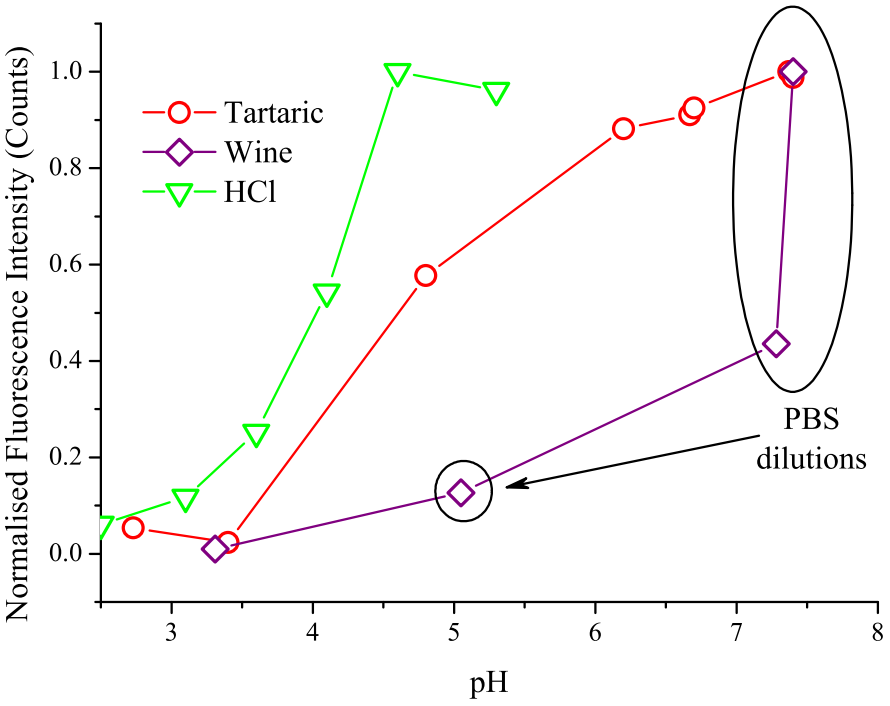

Figure 162: Variation in the fluorescence intensity with pH for solutions prepared with tartaric acid, hydrochloric acid and in model wine.

partly from the pH of the solution, with some other factors further reducing the intensity.

To examine this further, two separate trials similar to the one used earlier with hydrochloric acid were performed. The first consisted of a series of 1:10 dilutions of tartaric acid with deionised water. The initial solution (no dilutions) was recorded to have a pH of 2.80, with the pH of each subsequent solution being measured with a pH meter. In addition to this, two further solutions were diluted with a 0.01 M solution of Phosphate Buffered Saline (PBS) in both a 1:9 ratio and 1:99 ratio. This gave two solutions with relatively high concentrations of tartaric acid, but through the use of the buffer solution they still possessed a neutral pH. Amplex Ultrared and hydrogen peroxide were added to these solutions to bring the concentrations to 1 µM and 660 nM respectively. The solutions were allowed to react for 1 hour, and the fluorescence spectra recorded using a spectrophotometer. The results of this trial are shown in Figure 162.

The same general trend as the HCl measurements were visible in these results, however the curve is clearly shifted to higher pH levels than was observed with the HCl. Additionally the pH 2.8 and pH 3.4 tartaric acid solutions showed virtually a nil fluorescence signal. However when the tartaric acid is diluted with PBS the maximum fluorescence intensity is observed. The pH when the tartaric acid solutions was diluted was measured as 7.2 and 7.4 when the initial solutions were diluted by 10× and 100× respectively.

As a final trial the same measurement was repeated, but using actual white wine (Berri estate classic dry white). Four samples were prepared - wine, wine 1:9 PBS, wine 1:99 PBS, PBS. The results of this trial are shown in Figure 162, with the four samples here listed in order of increasing pH. This measurement again shows a near-negligible fluorescence result for the undiluted sample, with less than 1% of the integrated signal (and < 0.5% of the peak) of the PBS signal observed. The fluorescence signal increases to 13% for the sample diluted 10× with PBS and 44% when diluted 100×. The reduced signal at 100× dilution is clearly not due to the pH, since the measured pH of 7.37 agrees within error of the pH of the PBS solution itself (7.4).

This result suggests that this fluorophore would only be suitable for measurements in wine with a high (100 nM - 1 µM) concentration of hydrogen peroxide, since the sample needs to be diluted by a significant amount before the measurement can be successfully performed. Additionally, to make this measurement in fibre the wine solution would need to be pre-mixed with the buffer solution, making the envisioned single-step dip sensor difficult to accomplish. Regardless of this, sensing of hydrogen peroxide in wine solutions has been demonstrated in bulk using Amplex Ultrared using this fluorescent technique. However due to the added complexity required to perform measurements in wine samples the initial characterisation of this fluorophore in fibre used water as the solvent to avoid any issues with the reduced fluorescence intensity from wine (Figure 162) or crystallisation from the PBS buffer (Section 5.2.4, Figure 24).

7.3 FIBRE MEASUREMENTS

With bulk characterisation completed the next step was to determine whether this fluorophore could be used within a fibre. With the issues observed earlier with the synthesised fluorophore, photobleaching was the main concern for these measurements. If the fluorophore is not photostable then this introduces additional uncertainty to the measurements, as they will be constantly evolving over time. However no evidence of photobleaching was seen during the cuvette measurements, which implies that this fluorophore is significantly more photostable than the one used in Section 6.6. For these trials measurements were performed in water rather than buffer or model wine solutions to minimise the complexity of the system. These could introduce additional variability to the measurements, so it is desirable for initial work to be performed with the minimum number of possible variables.

Additionally the detection apparatus improved significantly between those measurements and the present ones, such that measurements can be performed in a much shorter time using orders of magnitude less input power. The combination of this significant improvement in

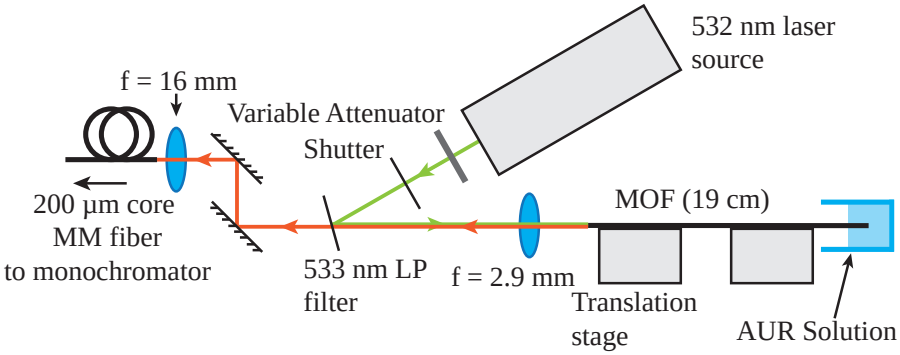

Figure 163: Experimental configuration used for fibre-based measurements with AUR.

the detection apparatus with the increase in the photostability of the fluorophore being used should mean that detection of peroxide using an optical fibre is a realistic prospect.

The experimental configuration for the fibre based measurements is shown in Figure 163. This is virtually the same configuration as used previously for the Quantum dot measurements, with the addition of a shutter to enable time-gating of the input signal. This ensures that the fluorophore is exposed to the excitation light for the absolute minimum possible duration, reducing the photobleaching rate to its lowest possible level.

Since the solvent being used here was water rather than decane (as used in Section 2.5.1) an alternative filling method could be used, in which the fibre is not removed from the stage to perform filling. Instead the initial setup leaves approximately 10-15 mm of fibre overhanging from the block on which it is mounted. Alignment is performed as per normal methods, with the output coupling lens removed upon completion of this alignment. 50-150 µL of fluorophore is then pipetted in to a small tube, and the tube mounted at the same height as the fibre tip. The tube is then gently moved towards the fibre, until the tip of the fibre is immersed in the liquid where it remains until the fibre is filled. This method is possible for AUR due to the surface tension of the water & the contact angle on the tube keeping the liquid in the horizontal tube while filling. When a similar method is attempted using decane or toluene the liquid generally runs out of the tube. The use of this method ensures that the alignment of the fibre does not change while the fibre is being filled.

For these measurements 19 cm of F2HT wagon wheel fibre (see Section 2.9) was used. The fibre tip was immersed in the sample for 10 minutes before being removed. This was sufficient to completely fill the full length of the fibre. After removal the liquid was allowed to stabilise for 1-2 minutes before the measurement was performed. This is done to allow the position of the meniscus to stabilise. When the fibre is removed from the liquid the meniscus is initially located

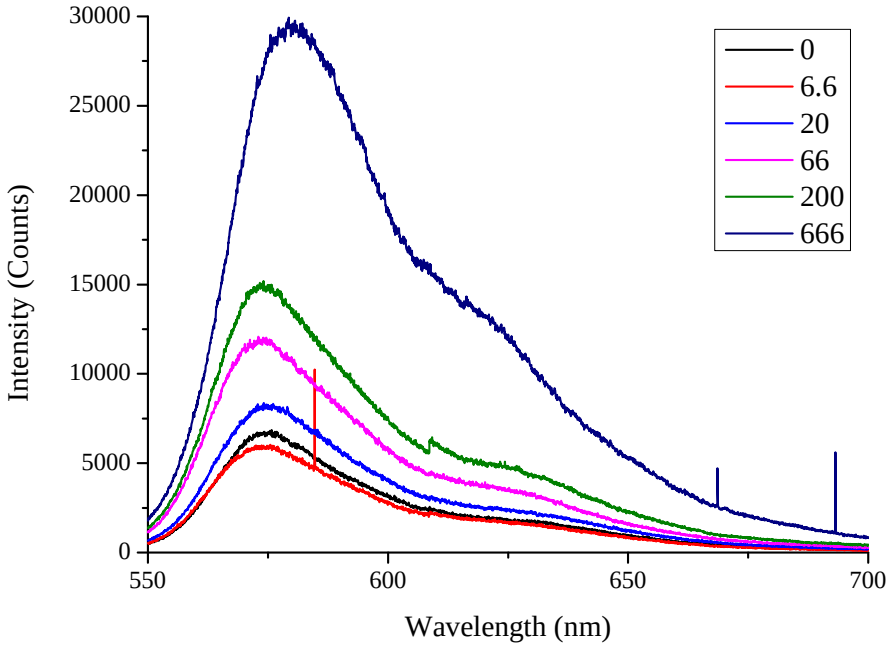

Figure 164: In fibre fluorescence measurements of Amplex Ultrared with varied hydrogen peroxide concentration. The legend shows the concentration of the hydrogen peroxide in nM. 532 nm excitation, ~1.8 µM core F2 WW fibre.

at the very end of the hole, and rapidly drops back after the fibre is removed from the solution. The results of this measurement for varied hydrogen peroxide concentration is shown in Figure 164. The concentrations of AUR used for this measurement was 1 µM.

To gain a quantitative understanding as to the linearity of these results the spectra were again integrated from 550-700 nm, with the results of this shown in Figure 165.

This measurement demonstrates that the linear range using this fluorophore in fibre is similar to that obtained earlier in cuvette. Also, using moderate input powers (2.5 µW) photobleaching had minimal impact on the measurements. This measurement showed a minimum detectable concentration of 20 nM, as the 6.6 nM measurement showed a recorded power which was lower than that of the samples with no added peroxide.

To test the repeatability of in-fibre measurements, identical samples were measured using the same technique 9 times. The aim of this was to quantify the uncertainty in the measurements arising from changes in the coupling or fibre geometry actually is. The results of this are shown in Figure 166.

Some scatter in the measurements were visible in these results, corresponding to a standard deviation of approximately 11%. This uncertainty is likely primarily from differences in the coupling, both of the laser light in to the fibre and the fluorescent light in to the spectrometer. The coupling of the laser does not show a linear relation

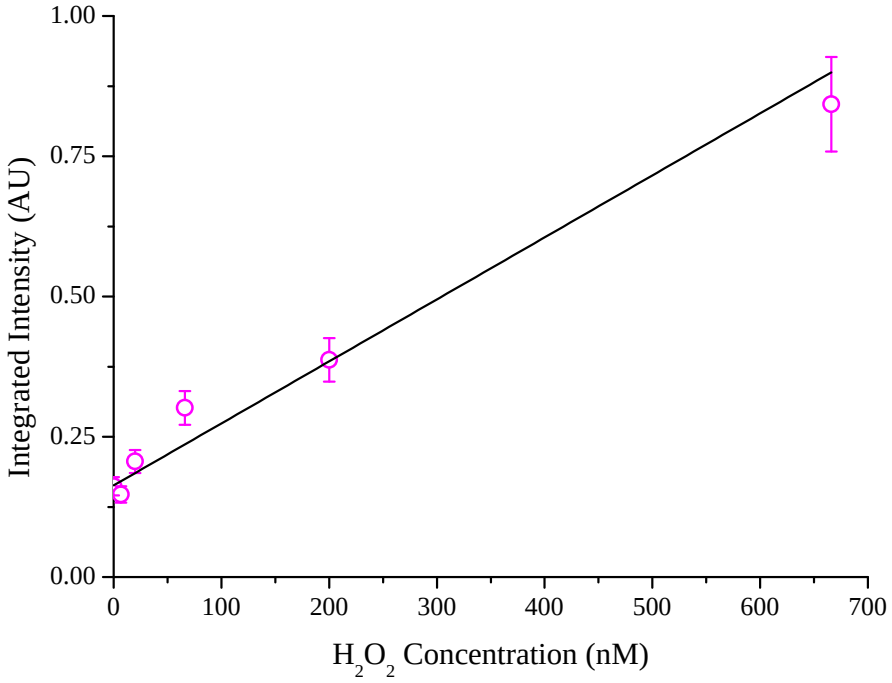

Figure 165: Fluorescence spectrum from Figure 164, integrated between 550-700 nm. This result demonstrates that the detection limit using this method is approximately 20 nM. Below this level the fluorescence signal is indistinguishable from the spectra of the reference sample. The fit shown is a linear regression over all points with an R^2 value of 0.98161.

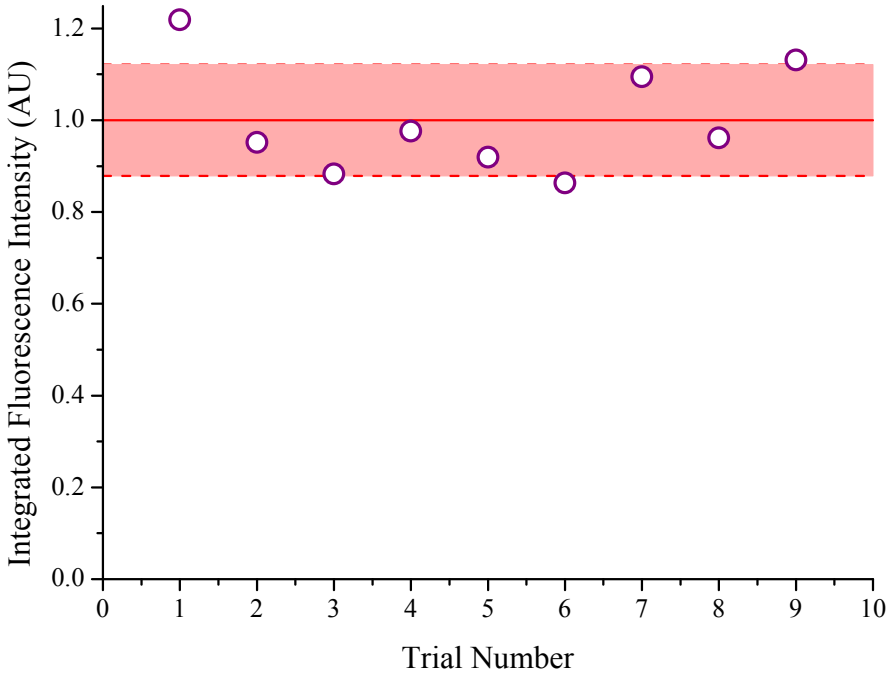

Figure 166: In-fibre repeatability trials using AUR in an F2 wagon-wheel fibre. The solid represents the average of the 9 trials, the shaded region the standard deviation. The plot has been normalised to the average value.

with the fluorescence intensity, simply because when the coupling drifts away from its optimum point higher order modes start to be excited. Each of these higher order modes will have a different overlap with the fluorophores within the holes, and thus a different amount of fluorescence will be generated. Since there are a large number of higher order modes present in a 1.8 µm waveguide with a refractive index contrast of 1.62:1.33 it is possible to obtain a similar coupled power through the fibre, but have different higher order modes excited within the waveguide.

7.4 EMBRYO CULTURE MEDIUM SENSING

7.4.1 *Amplex Ultrared*

Following on from the work with wine sensing, the application focus shifted to looking at embryo sensing applications, specifically looking at the hydrogen peroxide concentrations in In vitro fertilisation (IVF) samples. To ensure that similar issues to what was seen with the wine work and tartaric acid were not also observed in IVF environments, the fluorophore was tested in several common IVF buffers. Here the focus shifted to methods that could be used to measure low volume samples, as only small (20 µL maximum) volumes of buffer solutions are used around the embryo.

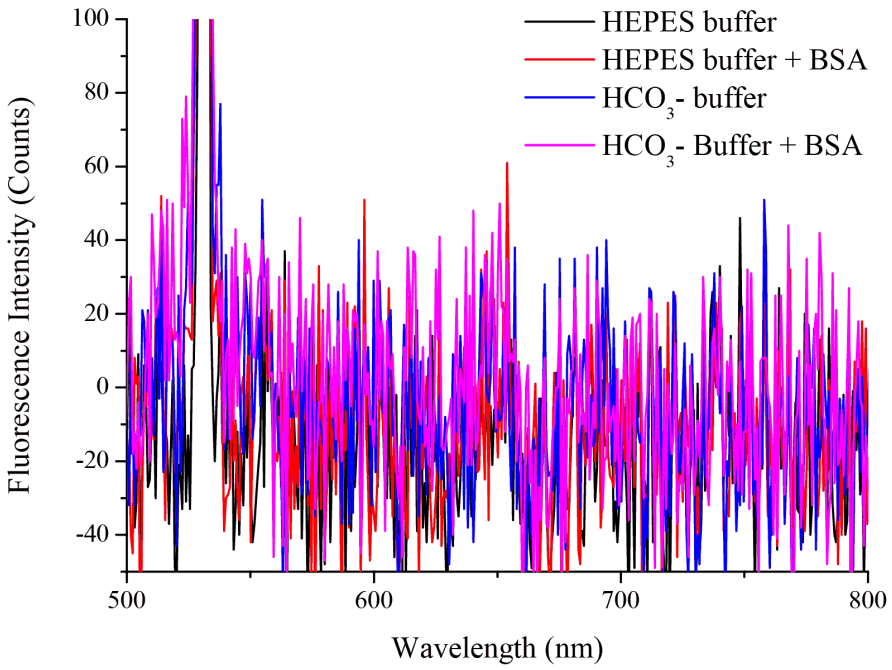

Figure 167: IVF Buffers background signal.

Four separate solutions of two different buffers were used, a 4-(2-hydroxyethyl)-1-piperazineethanesulfonic acid (HEPES) [224, 225] buffer and a HCO_3- [226] buffer. These are both standard IVF buffers, and successful demonstration of a fluorescence response to hydrogen peroxide in these buffers would be a good indicator as to the viability of this fluorophore in IVF applications. Two solutions of each buffer were used; with and without the addition of bovine serum albumin (BSA). The addition of BSA to IVF solutions is to aid in the embryo development [227], so again there is a requirement to see if the presence of BSA affects the observed fluorescence response.

The first measurement performed was to ensure that the buffers themselves showed no intrinsic fluorescence with 532 nm excitation. The results of this measurement are shown in Figure 167.

This measurement was performed at the same excitation power and integration time as the fluorescence measurements in Figure 168. This demonstrates that there is no appreciable background signal using these buffers using the same parameters as the actual experiments.

The results of cuvette measurements in these buffers is shown in Figure 168. Again this plot is the combination of a number of spectra, integrated between 550-700 nm.

The fluorescence obtained in these results changes significantly with the concentration of hydrogen peroxide that was present. This was an important result, since the same test in wine demonstrated that this fluorophore could not be directly used with the wine samples. Similarly to Figure 153 this shows a linear fluorescence response from 0-1 µM, with a roll-off at higher concentrations.

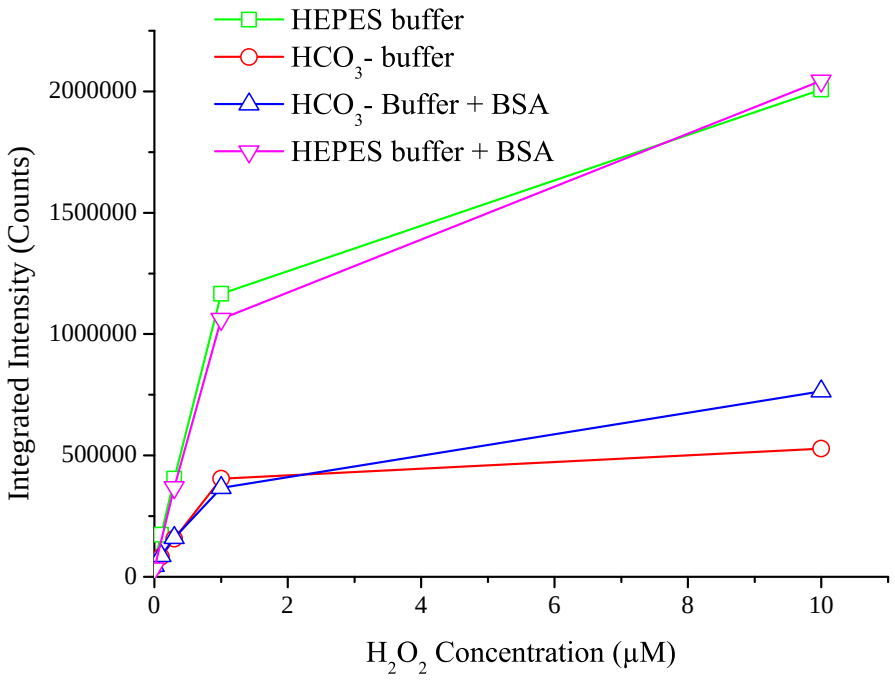

Figure 168: IVF Buffers AUR 10uM.

7.4.2 *Low volume mixing*

As a benchmark for the alternative methods that were pursued, discussed in Section 7.5 and Chapter 4, the limitations of making bulk measurements using volumetric pipettes were investigate. Trials showed that the minimum sample size required to obtain repeatable measurements using the MOFs was in the order of 10 µL. This arises solely due to the need for the tip of the fibre to be fully immersed in the liquid, without actually hitting the bottom of the vessel. Significantly below this volume it becomes difficult to know when the tip of the fibre is fully immersed in the liquid, thus reducing the reliability of individual measurements. The volume could be further reduced using the same method, but to ensure that the fibre is immersed in the liquid for the full duration of the measurement would likely require the use of a long working distance microscope to monitor the location of the tip relative to the surface of the liquid.

For a proof of concept, a 1 µM AUR solution and a 2 µM H_2O_2 solution were mixed. These were then pipetted into a small tube, and allowed to mix for an hour. 1 µL of peroxide was added to a 9 µL AUR solution, giving a total volume available to fill the fibre of 10 µL. The tubes were sealed while this mixing occurred, and to avoid issues arising from evaporation the tubes were covered with paraffin tape for filling. The tape could be easily pierced by the tip of the fibre, allowing the fibre to fill while still preserving the concentrations of the solutions.

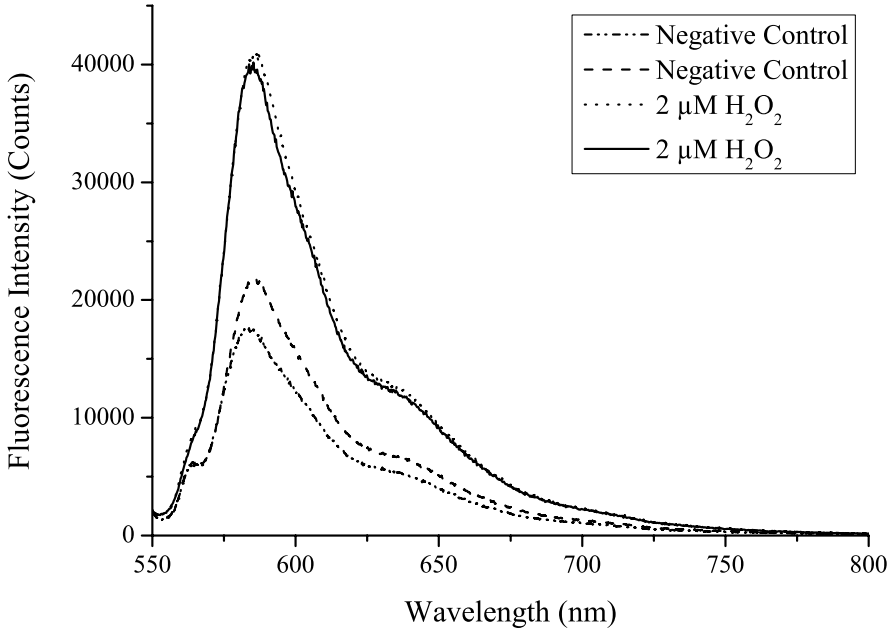

Figure 169: 'Bulk mixing,' small volume measurements. The total analyte volume for each of these trials was 1 µL, with the negative control having the same AUR concentration but with 1 µL water added instead of H2O2. Two separate trials of both the negative and 2 µM samples were performed.

Measurements were performed using the same experimental configuration as shown in Figure 163. The tip of the fibre was carefully moved in to the small amount of solution in the bottom of the container, and allowed to fill for seven minutes. The fibre was then removed from the solution, and a scan taken. This was repeated with new samples and fibres to ensure consistency between results. These results are shown in Figure 169.

This showed an approximately 2 × increase in fluorescence between the control samples with no hydrogen peroxide and the positive samples with 2 µM of peroxide. These results demonstrate that measurements can be performed using MOFs and relatively small sample volumes. However this has the obvious drawback that the sample has to be taken with a volumetric pipette, so there is little precision with choosing the exact location that the sample is taken from due to the relatively large size of the pipette tip compared to the tapered glass pipettes typically used in embryo monitoring applications. Here the tapered pipette could not be used as this measurement required the quantity of sample taken to be measured. While the tapered pipette tip offers better spatial sampling resolution, it has no accurate method of determining the volume of the liquid. It could potentially be used firstly to remove the sample from the vicinity of the embryo to another vial where a known volume can be taken with a volumetric pipette, but this would naturally increase the total solution volume

required for a measurement. As it is desirable for a final sensor to be able to sample the H_2O_2 concentration spatially as well as temporally, alternative methods were investigated.

The method described here while an improvement on the previous section, does not take full advantage of the fibre platform itself as the required sample volumes are still significantly greater than the internal volume of the fibre. As such it is desirable to be able to move towards a system in which the required fluid volumes approach that of the volume of the fibre itself.

7.5 SURFACE FUNCTIONALISATION

7.5.1 *Methods*

With the characterisation of the bulk fluorophore in fibre completed, the next step towards fabricating a one-step dip sensor was developing a functionalised surface in the fibre. By directly attaching the fluorophore to the surface of the fibre the requirement for mixing is circumvented, and detection should simply require the tip of the fibre to be dipped in the desired analyte.

Two primary methods have found previous use in surface functionalising soft-glass optical fibre in the past, with the basic concepts for functionalisation shown in Figure 170. The first method that was used for functionalising these fibre was silanisation [228, 229]. This process utilises the hydroxyl groups present on the surfaces of oxide glasses to create a covalent bond with a silane. Initially the chlorine groups on the silanes react via hydrolysis with water, forming silanols. These silanols then covalently bond to the hydroxyl groups on the surface via a condensation reaction. The density of the layer has been shown to be dependent on the initial surface density of the hydroxyl groups, and while most work on this has been done on oxide glasses successful silane coatings on non-oxide glasses such as ZBLAN has also been demonstrated.

Alternatively polyelectrolytes can be used [230, 231]. These can be broadly divided into weak and strong polyelectrolytes, each of which have positive and negative variants. Coating with polyelectrolytes typically involves multiple steps. Polyelectrolytes attach through electrostatic interaction, which requires an initial charge to be present on the surface of the glass. In the case of the oxide glasses used here this is provided by the hydroxyl groups on the surface, which give the glass surface an overall negative charge. A positively charged polyelectrolyte can then electrostatically interact with the surface, creating a monolayer. If a second polyelectrolyte with the opposite charge is introduced another layer can be built on top of the first polyelectrolyte layer. Alternating the charges of the polyelectrolytes enables the

density of the layer to be increased, until the surface is saturated and full coverage is obtained.

The primary coupling method that will be considered here are amine/carboxylic acid interactions. Attaching a fluorophore using this method requires the fluorophore to have either one of these functional groups present, in a location which does not alter the fluorescent properties of the molecule when the fluorophore is attached to the surface of the glass. For example, if the fluorophore were to have an amine group available for coupling, a carboxylic acid could be required on the glass surface to attach this molecule. This carboxylic acid is not naturally present on the surface, so it must be attached before the fluorophore can be bound. Both silanes and polyelectrolytes can possess this carboxylic acid, so this presents a natural path towards functionalisation.

The carboxylic acid will not naturally react with the the amine, so a coupling reagent to facilitate this is required. Probably the most commonly used method is to introduce 1-Ethyl-3-(3-dimethylaminopropyl)-carbodiimide hydrochloride (EDC) and *N*-hydroxysulfosuccinimide (NHS) to the reaction. The EDC reacts with the carboxylic acid group to produce an O-acylisourea intermediate which is then reactive with the amine groups [232]. If this intermediate encounters an amine group it can react to form a stable amide bond. However if this does not occur then the intermediate can be hydrolysed back to a carboxylic acid. Adding NHS to the reaction stabilises this intermediate group by converting it to an ester. Although the reaction will still occur without the presence of NHS it has been shown in literature that adding NHS greatly increases the yield of the reaction.

This is only one possible method in which carboxylic acids and amines can be bound, other alternatives will be explored in a later section.

7.5.2 *Synthesised Fluorophores*

7.5.2.1 *PFBS*

The first in-house synthesised fluorophore for sensing of hydrogen peroxide in aqueous solutions was pentafluorobenzenesulfonyl fluorescein. This molecule, whose structure is shown in Figure 171 reacts with hydrogen peroxide to produce an increase in the fluorescence emission [233]. This increase is approximately 1.5 × higher than the fluorescence obtained from the unreacted molecule [233].

The fluorophore was diluted to 25 µM in water, and hydrogen peroxide to a final concentration of 50 µM added. This solution was then placed in a cuvette, with the result shown in Figure 172.

Previous work had demonstrated that the main concern with fluorophores for fibre based sensing was the photostability of the molecules (see Figure 138), so this was recorded using the same cuvette tech-

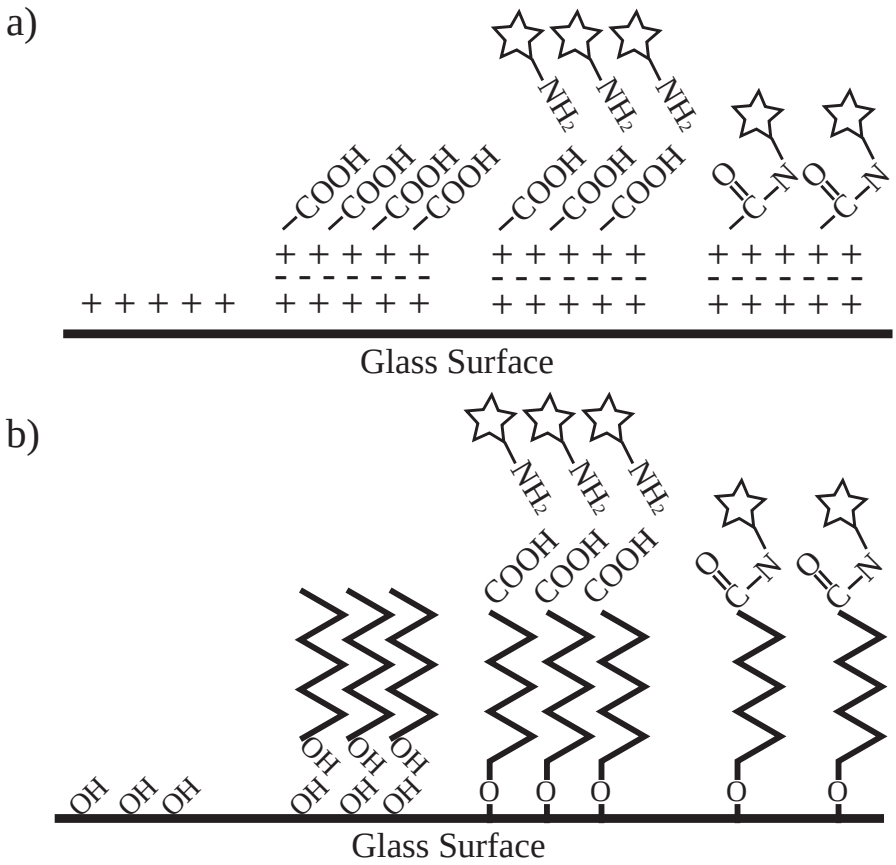

Figure 170: Alternatives for surface functionalisation a) Polyelectrolyte - Initial surface charge. Layers of polyelectrolytes with alternating charges are added until a complete later is obtained. One of the polyelectrolytes is chosen such that it possesses the desired functional group, such as a carboxylic acid as shown here. This acid then reacts with the corresponding functional group on the fluorophore, in this case an amine. A coupling reagent is used to enable this reaction, forming a covalent bond between the carboxylic and amine groups. b) Silane - The silanes react with hydroxyl groups on the surface of the glass forming a covalent bond. The same carboxylic/amine reaction is then used to attach the fluorophores to the surface of the glass.

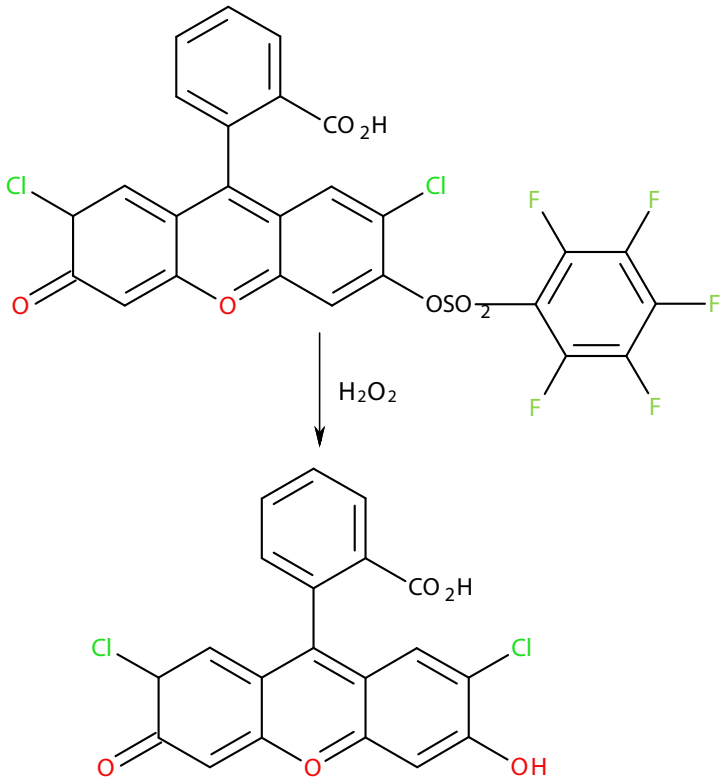

Figure 171: Pentafluorobenzenesulfonyl fluorescein (PFBS) for aqueous hydrogen peroxide sensing. Top) Initial, low fluorescence molecule. Bottom) Final, high fluorescence molecule after reaction with hydrogen peroxide. Synthesised by Dr. Sabrina Heng.

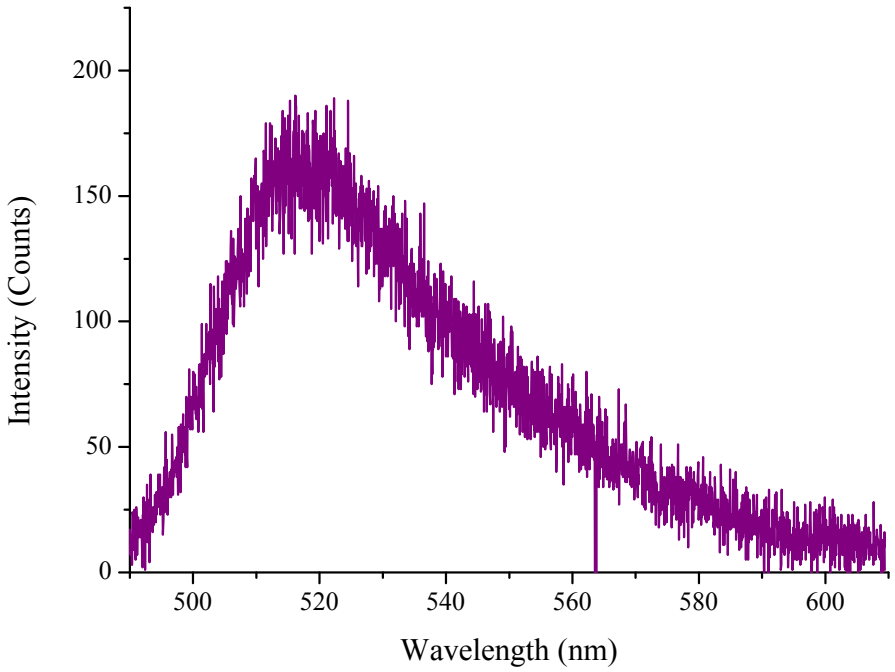

Figure 172: PFBS fluorescence spectra obtained in cuvette.

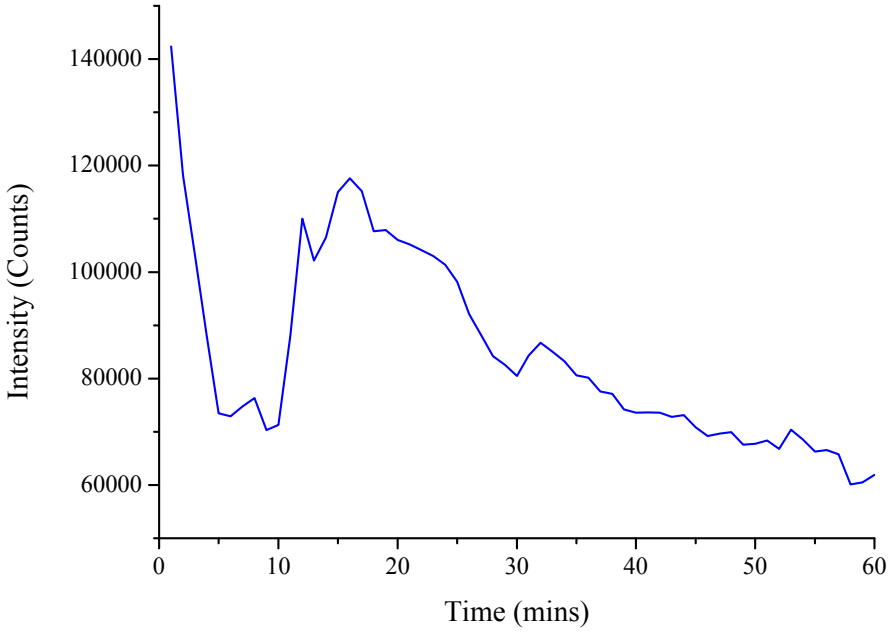

Figure 173: 50 µM PFBS with 25 µM, H_2O_2 photobleaching rate. 488 nm excitation, input power 2.5 mW.

nique as was used for Figure 172. 2.5 mW of 488 nm light was incident on the cuvette, with the results shown in Figure 173. One scan was performed per minute, with the fluorophore constantly exposed to the laser light for the duration of the measurement.

Even though the solutions were allowed to react for two hours before this measurement was performed, double the time allowed by [233], the fluorescence signal was shown to be unstable over the course of an hour. Initially the fluorescence intensity dropped rapidly from 145000 total counts to 72000 counts over the course of 4 minutes. The fluorescence intensity then increases, possibly due to a photoinduced reaction process cleaving the molecule from its low to high fluorescence state. This peaked after approximately fifteen minutes, before steadily declining again due to photobleaching. The relatively poor stability of this molecule in cuvette presents great concerns for utilising this system in fibre, as the photobleaching rate in fibre is significantly increased compared to that observed in cuvette.

7.5.2.2 *Rhodamine B derivative*

The next synthesised fluorophore was chosen to be a derivative of Rhodamine B. This was chosen as Rhodamine has been shown in the past to have good stability in fibres, while the fluorescein on which the last fluorophore is based is generally considered to have a poor photostability. The structure of the synthesised molecule is shown in Figure 174. The fluorophore initially beings in a quenched state, with

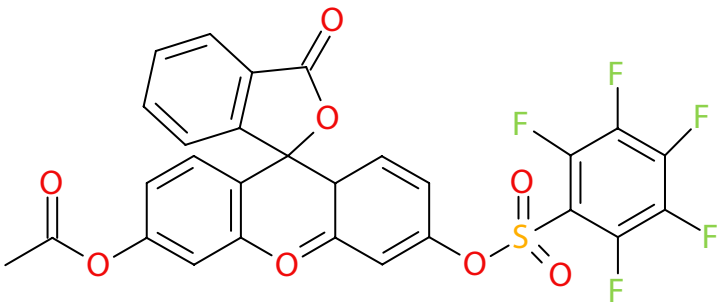

Figure 174: Rhodamine B derivative, MW 605.46 synthesised by Dr. Sabrina Heng.

the fluorescence intensity from the molecule increasing significantly when the functional group is cleaved.

The fluorophore was diluted to 10 µM in PBS, and various concentrations of peroxide added to the solutions. Again 488 nm excitation was used, with the results shown in Figure 175.

The graph shows that this fluorophore exhibits a poor sensitivity to hydrogen peroxide, with virtually no increase seen for 10 µM H_2O_2 and minimal for the 30 µM solution. Even at high concentrations of 100 µM the observed increase in fluorescence intensity is only in the order of 50%. Again the primary concern with this molecule was its photostability, so this was tested in cuvette. 2.37 mW of input power was used with one scan per minute for 27 minutes. The fluorophore was constantly exposed to the laser light for the duration of this measurement, with the results shown in Figure 176.

Again this fluorophore shows poor photostability, even though it is based on a molecule which has been shown to be relatively photostable. The fluorescence intensity decreases by greater than 70% in ten minutes, before plateauing. This stabilisation of the fluorophore is likely due to photoinduced reactions occurring, as was seen with the previous molecule.

This result shows that this fluorophore will likely not be suitable for use in fibre, as the instability in cuvette suggests that measurements in fibre would be problematic due to the aforementioned increased photobleaching rate.

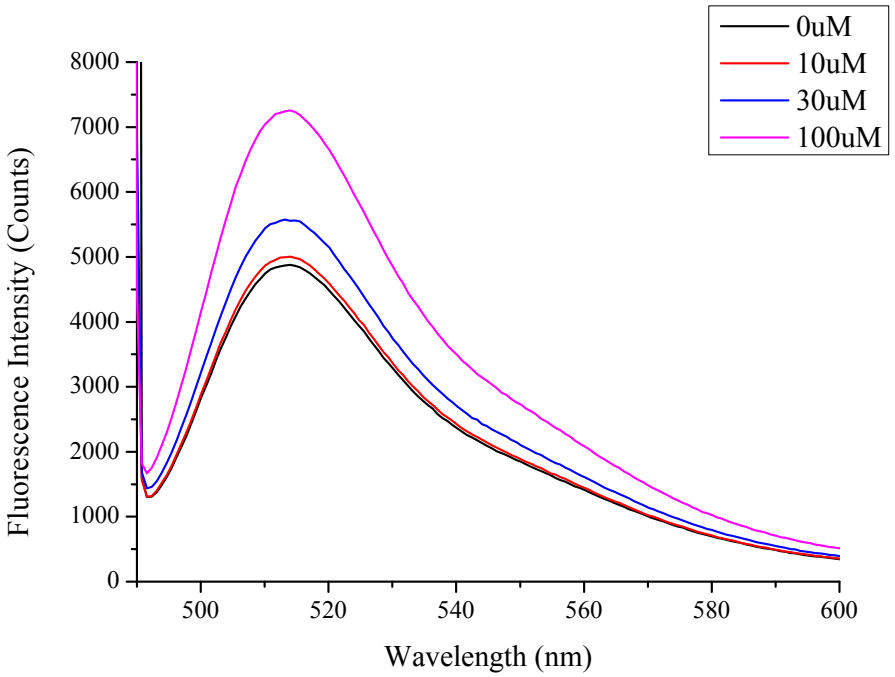

Figure 175: Rhodamine B derivative fluorescence spectra for varied hydrogen peroxide concentration. The fluorophore concentration was 10 µM, with 488 nm excitation used.

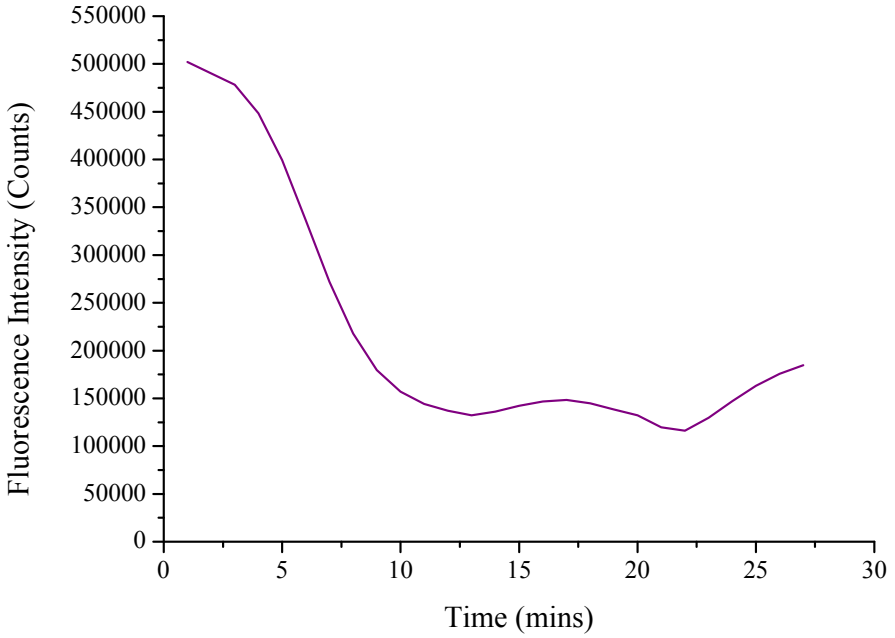

Figure 176: Rhodamine B photobleaching in cuvette. Concentration 10 µM, input power 2.37 mW.

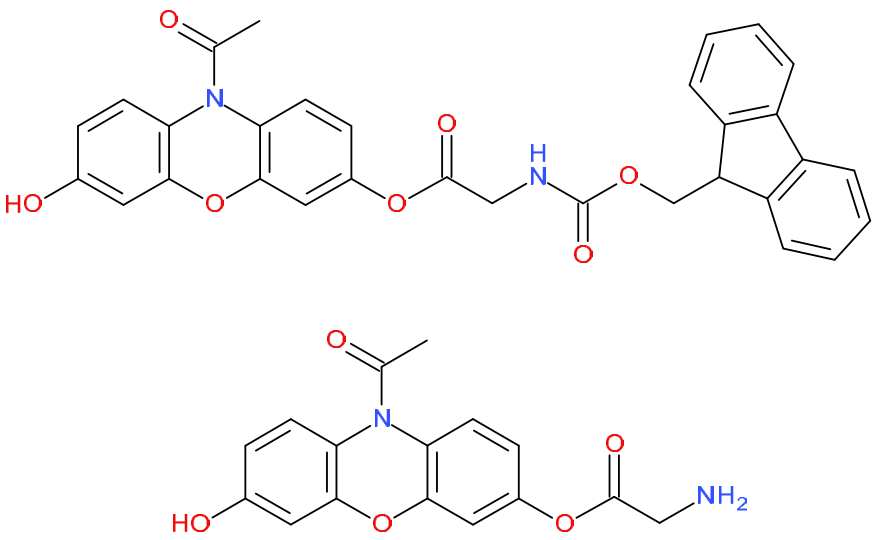

Figure 177: Amplex red derivative, before (top) and after (bottom) deprotection Synthesised by Dr. Ondrej Zvaric & Dr. Sabrina Heng.

7.6 AMPLEX RED DERIVATIVE

7.6.1 *Initial characterisation*

The next fluorophore synthesised was a derivative of Amplex Red (AR), hereafter referred to as Amplex Red Derivative (ARD). This fluorophore is based on Amplex Red, however with one of the hydroxyl groups of the molecule replaced with a short tether with an amine group available for surfance functionalisation. The fluorophore was synthesised with a protective Fluorenylmethyloxycarbonyl (FMOC) group on the amine, as concerns were raised about the stability of the compound with only the amine tether. The structure of the fluorophore before and after deprotection is shown in Figure 177. The deprotection was performed by dissolving the fluorophore in a 5% Piperidine solution, using either Dimethylformamide (DMF) or Dimethyl sulfoxide (DMSO).

Several versions of this fluorophore were synthesised. The one used for the majority of experiments is a shorter tether version as shown in Figure 177, with a longer tether version synthesised later (Figure 186). Unless specifically mentioned otherwise ARD refers to the short tether version.

The absorption spectra of the molecule was measured using a commercial spectrophotometer (Cary eclipse), and is shown in Figure 178. This spectrum is virtually identical to that of standard amplex red, suggesting that the addition of the tether does not significantly influence the fluorescence properties of the molecule.

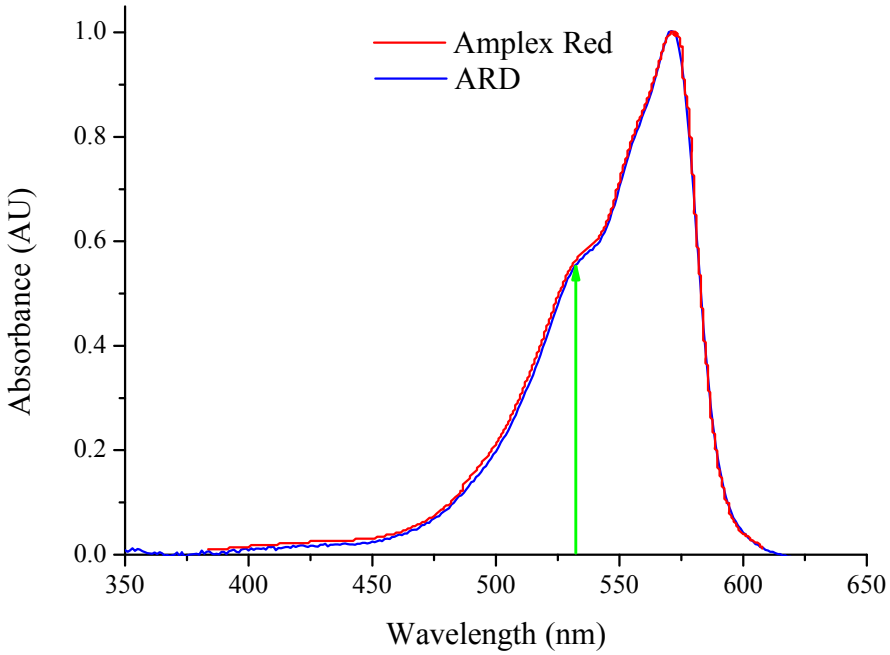

Figure 178: Measured absorption spectra of the synthesised ARD molecule (blue) compared to the absorption spectra of commercial amplex red (red).

Initial trials were performed in cuvette, and the results are shown in Figure 179. These measurements used the same experimental configuration as previously described, which is shown in Figure 153.

These measurements demonstrated that an increased fluorescence signal was observed with the addition of hydrogen peroxide to the solution, however this increase was not to the same magnitude as expected from the literature. Here we observe only a maximum of 4 × increase in the fluorescence signal. The fluorophore also appeared to show a relatively large background signal compared to what had previously been observed of both amplex red and amplex ultrared in cuvette measurements.

7.6.2 *Surface functionalisation*

With initial measurements on the fluorophore performed it was decided to immediately move to surface functionalisation of this compound due to concerns about the long term stability of the molecule. As ARD has an amine functional group, while previous work [41, 100, 234] on surface functionalisation in F2 fibres has used molecules with a carboxylic functional group a different surface functionalisation protocol was required. Here it was chosen to explore direct attachment of the molecule to the surface, as opposed to the sol-gel [235], hydrogel [236] or titanium-dioxide [237] methods that have previously been demonstrated. The procedure used here is modified from previ-

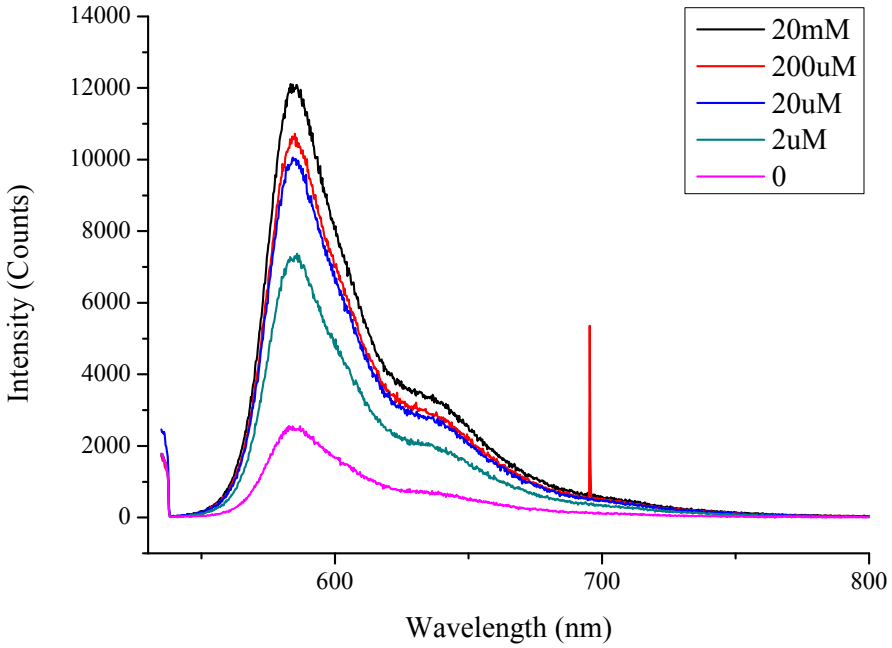

Figure 179: Cuvette fluorescence measurements for ARD, with varied hydrogen peroxide concentration. A 10 µM solution of fluorophore was used for these measurements.

ous work attaching Qdots to the glass surface by Franćois et al. [234] as well as work by Coscelli et al. attaching DNA probes to the fibre surface [238].

Two different attachment molecules with carboxylic functional groups were used for the initial trials. Here silica fibres and capillaries were also considered, both due to the availability of large-diameter silica capillaries, but also as previous work [234] has shown that higher surface densities can be obtained with silane coatings on silica due to the increased OH group availability compared to soft-glasses after appropriate surface treatment, which will be discussed later in the methods section.

1. Silane - Carboxyethylsilanetriol (CEST) sodium salt $C_3H_6Na_2O_5Si$ 25% in water was obtained from Gelest. For functionalisation it was diluted to 1-5% in RO water.

2. Polyelectrolyte - polyacrylic acid (PAA) and polyallylamine hydrochloride (PAH). PAA carries a negative charge, while PAH carries a positive charge. Although PAA is only a weak polyelectrolyte, it has been shown [230] that coatings with a high percentage of coverage can still be created using these chemicals. Both solutions were used at a concentration of 2 mg/ml.

The coating procedure for the silane was as follows.

1. For silica fibres/capillaries the surface was first cleaned using Piranha solution [228] to ensure that the maximum possible number of OH sites were available on the surface of the glass.
2. 1-5% solution of CEST filled through the fibre or capillary. This was done either using a syringe for short (< 30 cm) lengths of 70 µm internal diameter capillary, or with the pressure filling setup shown in Figure 180 for smaller capillaries or optical fibres. To ensure that the surface density was maximised this was left to incubate for 15-72 hours.
3. Nitrogen ~30 minutes.
4. RO Water ~30 minutes.
5. Nitrogen ~30 minutes.
6. Fluorophore + coupling solution ~ 2 hours. The exact details of the "coupling solution" will be described in detail later.
7. Water ~30 minutes.
8. Nitrogen ~30 minutes.

A similar procedure was used for the polyelectrolyte functionalisation. However for polyelectrolyte coatings multiply layers need to be deposited to ensure that full coverage is obtained [230, 234].

1. Piranha solution.
2. PAH 6-36 hours.
3. Nitrogen.
4. Water.
5. Repeat 2-5 with PAA/PAH.
6. Nitrogen.
7. Water.
8. Nitrogen.
9. Fluorophore + coupling solution.

To fill longer lengths of capillary/fibre, or alternatively to fill fibres with <20 µm holes it is impractical to use a syringe-based setup as the filling rates are low, and the time required to fill becomes impractical. While short lengths of capillary can be filled using the syringe method within seconds, filling lengths in the order of one metre would require tens of minutes. Since the pressure was provided manually be depressing the plunger of the syringe, this becomes impractical for lengths requiring long filling durations. Additionally it

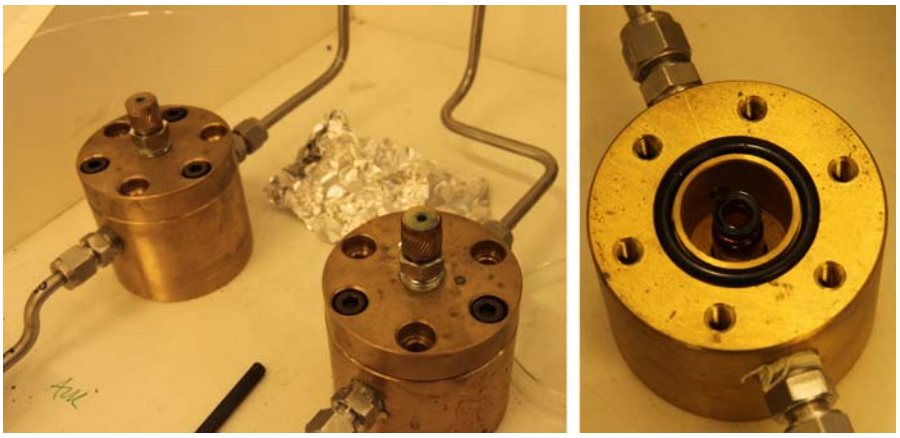

Figure 180: Filling setup used for surface functionalisation of the internal surfaces of fibres. (left) Sealed chambers, with fibres shown inserted through the rubber seal (right) Internal pressure chamber with vial used for holding reagents.

becomes increasingly difficult to ensure that adequate flushing of the previous step's solution due to the slow rate with which the liquid is pumped through the fibre. To remedy this a pressure filling setup was used, as shown in Figure 180. The pressure in the chamber could be varied from 0-300 psi. Importantly all four chambers could be linked, such that the pressure in each chamber is the same. This ensures that when coating multiple fibres simultaneously consistent conditions are used such that systematic measurements can be performed.

7.6.3 *Induced loss from silane coating*

To be able to use these fibres for measurements it is important to ascertain how much additional loss will be induced by the coating process. Here full systematics were not performed due to constraints with the number and length of the fibres that could be coated, so the loss was measured on a much shorter length than typically used than that used for a loss measurement on a standard WW fibre. Generally loss measurements on F2/F2HT wagon-wheel fibres are performed using 5-10 m of fibre, sealing the ends of each offcut such that they can be used for fluorescence measurements. Here only 1200 mm of fibre was used for coating, as lengths beyond this increased the uncertainty as to whether or not a uniform coating was being formed inside the fibre.

This length of F2HT wagon-wheel fibre was coated using the first steps of the procedure described above, with a 5% solution of CEST flushed through the fibre for several hours, and then allowed to sit for 48 hours. The fibre was then cleaved, and then placed on an XYZ alignment stage. Initially the fibre was tested with a broadband bulb source, but it was found that the transmission in certain spec-

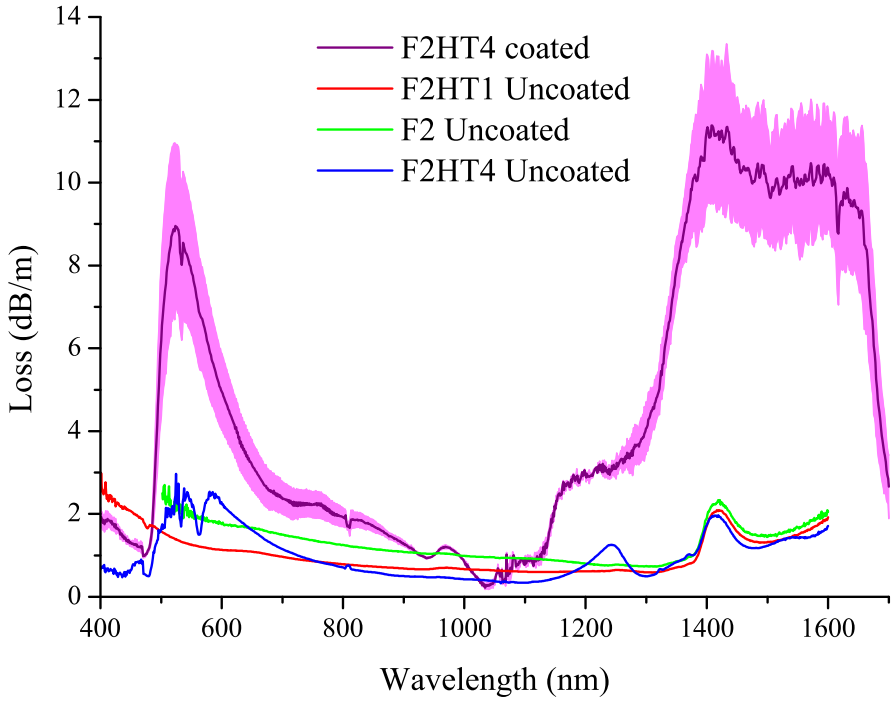

Figure 181: Comparison between measured loss for coated & uncoated F2HT, and uncoated F2 wagon-wheel fibres. The shaded region encompasses the error in the fit for the coated loss.

tral regions was below the noise floor of the detector. The source was then switched to a Koheras Super-K compact supercontinuum source which greatly increased the coupled power. The output light was free space coupled in to an ANDO AQ6315E OSA. Several cutbacks were performed, changing only the output coupling from the fibre in to the OSA. The obtained loss spectra is shown in Figure 181.

Here it can be seen that the coating process induces significant losses over the uncoated wagon-wheel fibres. The error in these measurements is quite large due to the short length and limited number of cutbacks, but clear absorption bands can be seen. Here the error shown is the error in the least squares fit used for the loss measurement. The first peak is located at 520 nm, with a loss of 9 ± 2 dB/m compared to the uncoated fibre loss of ~1.4 dB/m. This unfortunately aligns well with the intended excitation source for the fluorophore, with the loss still 8 ± 2 dB/m at 532 nm compared to 1.3 dB/m for the uncoated fibre. Another absorption band is also seen in the IR region, with a peak of 11 ± 2 dB/m at 1408 nm, which is again much higher than the uncoated loss of 2.2 dB/m.

Here it has been shown that the first step in the coating process already induces significant extra loss in the fibre. However for the application as a dip sensor, this loss is manageable due to the short lengths that are intended to be used. Initial experiments will be performed on 10-20 cm of fibre, so the induced loss at 532 nm at these

#	1st layer	Type	Coupling Reagent	Comments	Fig
1a	CEST	WW	NHS EDC	High loss	182
1b	PE	WW	N/A	Blocked	N/A
2a	CEST	WW	NHS EDC	1 fibre blocked	184
2b	CEST	WW	N/A	Control	184
3	CEST	WW	NHS EDC		N/A
4	CEST	WW	EDC	Compound cleaned	185
5	CEST	WW	EDC		N/A
6	CEST	WW	EDC	Long tether	N/A
7	CEST	F2 Cap	EDC		194

Table 6: Part 1 of overview of surface functionalisation trials.

wavelengths is only 0.9-1.8 dB for these short lengths of fibre. Assuming that the induced loss is relatively constant between samples this will have limited effect on both the number of fluorescent photons that will be observed as well as the effectiveness of the fibres as hydrogen peroxide sensors.

7.6.4 *Summary of trials*

For reference an overview of all coupling trials are shown in Tables 6 and 7. The first table shows initial trials, the second trials after the removal of piperidine from the filled solutions. Not all trials listed here are described in the text, but they are included here for completeness. Unless otherwise specified all trials were performed using the short tether derivative (Figure 177). Trials not included in the text are displayed with "N/A" as their figure reference. "WW" in all cases refers to F2HT wagon-wheel fibres, "F2 Cap" to 160 µm outer diameter/ 70 µm inner diameter F2 capillaries, "Si cap" to 300 µm outer diameter silica capillaries. All other terms will be defined in the following sections.

7.6.5 *In fibre results*

Four fibres of ~50 cm length were prepared, two each for silane and polyelectrolyte coatings. Here the first issues were noted, with the fibre coated with PAH and PAA failing to flush after the PAA was introducted. It appeared that the fibre was being completely blocked by the solution, as neither water nor nitrogen could be passed through the fibre even after cleaving several centimetres of fibre from each of the ends. The fibres filled with silane were still able to be flushed after

#	1st layer	Type	Coupling Reagent	Comments	Fig
8a	APTES	Si Cap	NHS EDC	Biotin/Avidin	195
8b	PE	Si Cap	NHS EDC	Biotin/Avidin	195
9	CEST	F2 Cap	EDC		194
10a	APTES	WW	HATU	Failure	N/A
10b	PE	WW	HATU	Failure	N/A
11a	CEST	F2 Cap	HATU		N/A
11b	CEST	F2 Cap	Control		N/A
12a	APTES	F2 Cap	NHS EDC	Biotin/Avidin	197
12b	PE	F2 Cap	NHS EDC	Biotin/Avidin	197
12c	CEST	F2 Cap	NHS EDC		197
12d	CEST	F2 Cap	SNHS EDC		197
12e	CEST	F2 Cap	HATU		197
13	CEST	WW	HATU		200
14	CEST	WW	HATU		203

Table 7: Part 2 - coating trials after removal of piperidine from bulk solution.

almost three days reacting, so initial measurements were performed on these.

The coupling solution used here consisted of EDC and NHS to promote the amine - carboxylic acid reaction. The fluorophore was dissolved in the piperidine + DMF solution to a concentration of 2 mM, then further diluted to 10 µM in the EDC/NHS solution. This solution was then filled in to the fibre and allowed to react for two hours. The fibres were kept in the dark while this reaction occurred to ensure that no photobleaching of the molecule was induced. During the reaction a slow flow rate was maintained such that fluorophores should always be present for any unreacted carboxylic acid sites on the inside of the fibre.

After two hours the solutions were removed from the chamber, and the fibres flushed with nitrogen/water/nitrogen. The fibre tip was checked under the microscope to ensure that liquid was still flowing through the fibre. To check for nitrogen flow the tip of the fibre was dipped in to a beaker of water, with bubbles showing that gas could still flow through the fibre.

To perform fluorescence measurements each fibre was cut into three segments of equal length using a mechanical cleaver. The experimental configuration was the same as used earlier for the AUR measurements, and is shown in Figure 163. The cleaved fibre segments were placed on the XYZ stage, and aligned using minimal power. Testing with uncoated fibres had demonstrated that alignment could be performed using only 250 nW of input power, which corresponds to

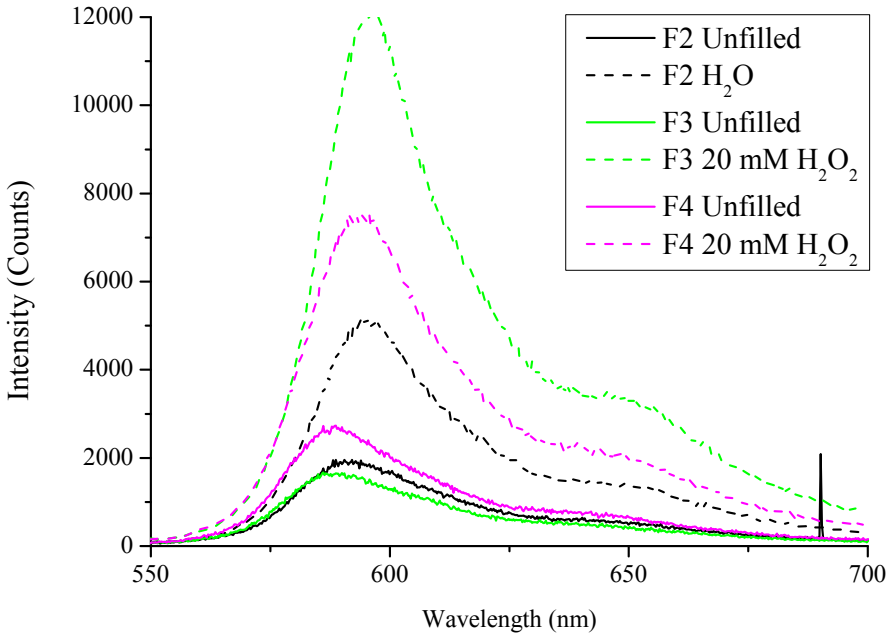

Figure 182: First coating trial of ARD in F2 wagon-wheel fibre. Solid lines show the initial (unfilled) fluorescence, dashed lines show the fluorescence signal filled with a given solution.

approximately 100 nW of power coupled in to the fibre. Trials showed that the photobleaching rate of standard AUR in the fibre at these power levels was negligible over a period of fifteen minutes, suggesting that performing alignment with this amount of power should have minimal impact on the fluorescent properties of the molecule. An unknown quantity here however is the effect that the fluorophore being bound to the surface will have on the photobleaching rate. It is logically expected that the rate will increase, as since the molecule is bound diffusion cannot move non-photobleached molecules in to the excitation field. The exact increase arising from the molecules being bound has not been studied.

The fibres were filled with the hydrogen peroxide solutions for ten minutes, using the previously mentioned technique (see Section 7.3) to allow the fibre to be filled without removing it from the stage. The fibres were then allowed to sit to react, and another scan performed.

The results of this trial are shown in Figure 182.

Two separate fibres were coated for six total pieces were prepared with a silane coating, but it was found that the second fibre showed no guidance. This figure shows the fluorescence signal obtained from each segment of fibre before and after filling. The input power used for these measurements was 2.5 µW, with a scan time of five seconds.

This measurement possibly shows sensitivity to hydrogen peroxide, but the results are somewhat inconclusive. The fibre filled with water showed a 2.7 × increase in fluorescence, the first 20 mM H_2O_2 fibre a 7.5 × increase and the second 20 mM H_2O_2 fibre a 2.8 × increase.

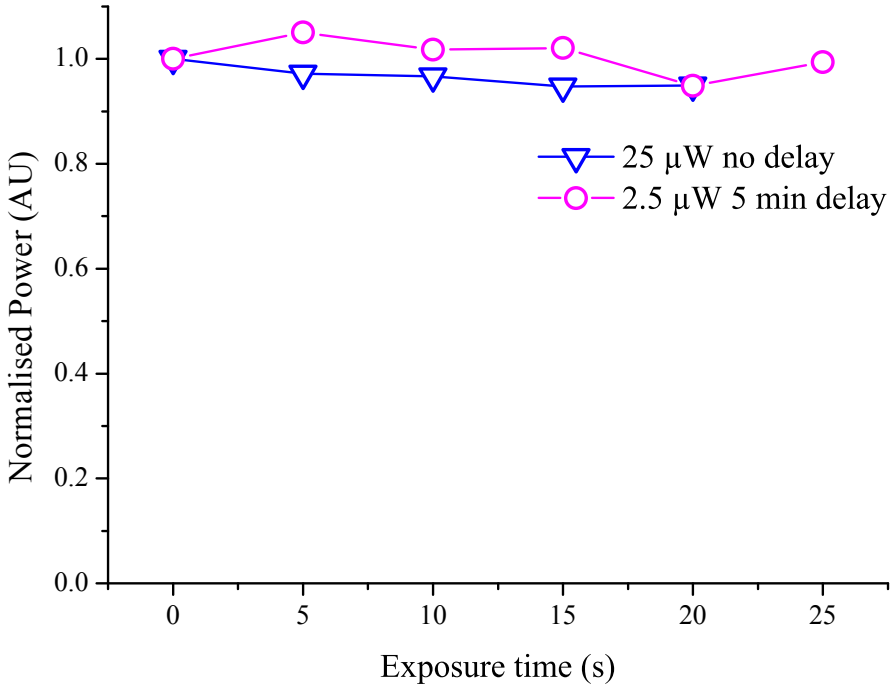

Figure 183: Photobleaching rate for surface functionalised fibre before filling, normalised to the initial fluorescence intensity. Magenta shows the integrated fluorescence intensity at 2.5 µW input power, with a 5 minute delay between each scan. Blue the integrated fluorescence intensity at 25 µW with no delay between scans.

Some increase in fluorescence with the water sample is not entirely unexpected here, as the quantum efficiency of the fluorophore is dependent on the solvent in which it is immersed. The inconsistencies in the results here make it difficult to come to a conclusion about the success of this trial.

With a possible fluorescence response after functionalisation demonstrated, one of the main open questions with this fluorophore was how this functionalisation would affect the photobleaching properties. To test this two measurements were performed, one at lower power with a high delay to test the overall stability of the fibre measurements and a second with the same fibre, but with an input power of 25 µW to test the photobleaching rate. The former is the same power level as used in the measurements above, the latter 10 × higher.

The results of this trial are shown in Figure 183. Again the fluorescence signal here is integrated from 540-800 nm, and then normalised to the initial fluorescence intensity.

This measurement shows two important results. The first is that the signal is relatively stable over a period of 30 minutes with 2.5 µW input power. Since the measurement technique proposed here involves no realignment of the fibre after filling, the fibre must be stable on the stages for the duration of both the filling as well as the reaction time

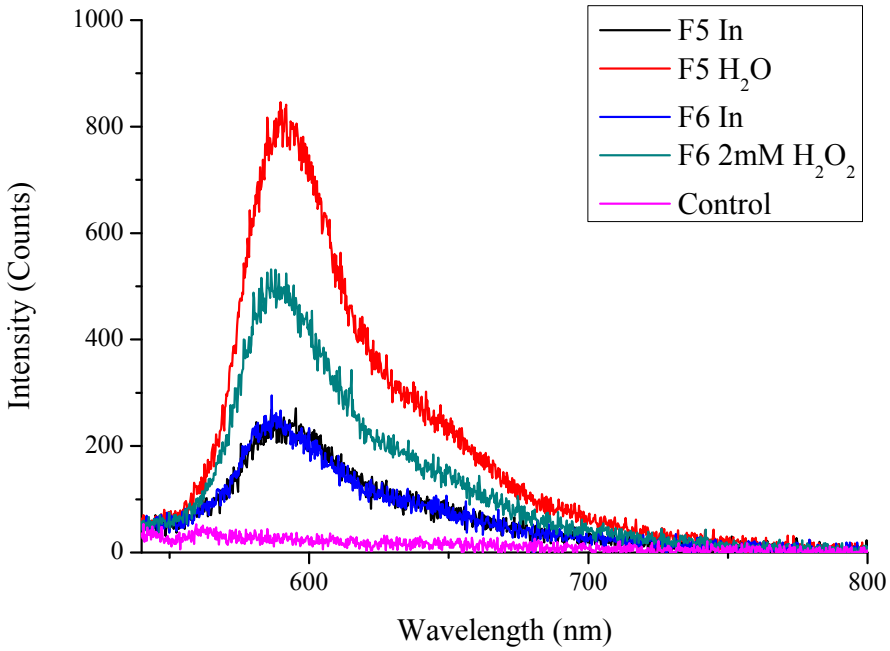

Figure 184: ARD fibre coating trial with additional flushing step.

afterwards. The average for this trial was 1.00, with a standard deviation of 3.3%. This demonstrates that the fluorescence signal does not deviate significantly over a time frame that is comparable to that required to perform a measurement.

The second plot here at 25 µW shows that with an exposure time of 25 seconds that the fluorescence intensity only decreases by 5%. Since this is at a power level 10 × higher than that used for the fluorescence scans and 100 × higher than the alignment this suggests that neither of these processes should have a significant impact on the level of photobleaching of the sample. Typically alignment of the fibre takes less than 30 seconds, so extrapolating from the results in Figure 183 this should have negligible impact on the amount of fluorescence generated by ARD in the fibre.

This measurement was repeated using a virtually identical coating procedure, with the only change being the addition of an extra rinse/-flush step at the end of the coating process. The results of this trial are shown in Figure 184.

Like the first trial two fibres were prepared, however it was found that one of fibres again displayed no guidance. The second fibre was cleaved into segments, and measurements performed. The fluorescence signal from the unfilled fibres was more consistent, but the total counts were much lower. Again filling the fibre with water was found to increase the fluorescence, although not to the same extent that filling with a high concentration of hydrogen peroxide increased the fluorescence. The reason that this trial displayed a much lower overall fluorescence signal than the first trial is not well understood.

The power transmitted through the fibre was noted to be lower than that of the first trial, although not to the same extent as the magnitude of the reduction in fluorescence. The fluorescence signal here was >10× lower than in the first trial. It is possible that the higher fluorescence from the first trial was due to non-covalently bound fluorophores on the internal surfaces of the fibre, while the more thorough flushing in this fibre resulted in these unbound fluorophores being washed away.

In addition to the two fibres with fluorophore/EDC/NHS, an additional fibre was also coated. The coating procedure used for this fibre was identical to that of the first two fibres, with the exception that no EDC was added with the fluorophore. Without the EDC present the amine/carboxylic acid can not occur, and no covalent bonds will be formed. Thus performing a coating trial with no EDC gives us a control measurement, showing the amount of fluorophore that is present in the fibres that is not covalently bound to the surface.

The result of this trial is also shown in Figure 184, labelled as "control". This measurement shows no significant fluorescence signal without the presence of EDC, suggesting that the fluorescence signals obtained for the other trials are a result of covalently bound molecules.

It was noted during this trial that the amount of both water and nitrogen that could be passed through the fibre after the ARD/NHS/EDC step was greatly reduced compared to fibres before this coating step. Indeed one of the two fibres coated above became completely blocked after this coating step, meaning that it could not be subsequently flushed and used for measurements.

The power transmitted through the fibres was also greatly decreased compared to the power through an unfilled fibre. Due to the short lengths and limited quantities of coated fibre filled making standard cutback measurements difficult, the exact loss of the fibre could not be recorded. However estimating the coupling efficiency from the laser to the core of the fibre as a low 10% and recording the total transmitted through the fibre the loss of these coated fibres was estimated to be in excess of 100 dB/m. Typically the coupling efficiency in to an F2 wagon-wheel fibre with a core size of 1.8 µm would be in the order of 20-30%, so the actual loss value would be correspondingly higher.

Further testing showed that the primary cause of this increased loss was the addition of NHS to the coating solution. The NHS appeared to be crashing out of the solution, presumably forming crystals inside the fibre due to the limited solubility of NHS in water. These crystals would greatly increase the losses due to scattering, much like was seen previously with the PBS solutions in Section 2.5.1. Removing NHS from the coating solution should alleviate both the increased loss and the fibre blockages. However literature [232] shows that without NHS the efficiency of the amine/carboxylic coupling re-

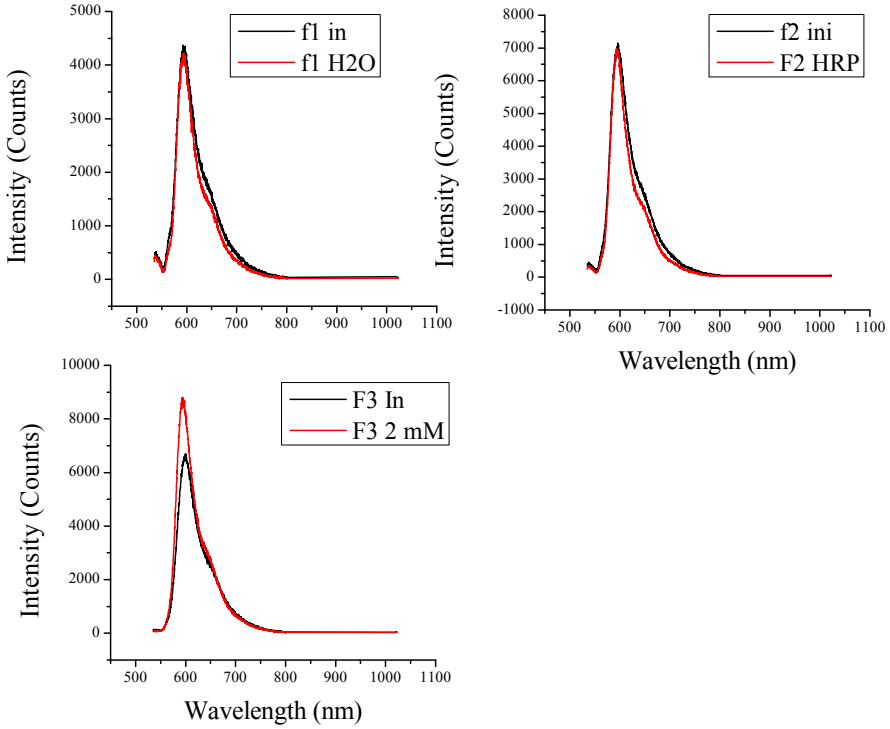

Figure 185: First trial of in-fibre coating trials for ARD with no NHS in the coupling reaction. Black shows the initial fluorescence signal obtained, red the signal after filling with water, water+ HRP and 2 mM H_2O_2 respectively. The input power for these measurements was 2.5 µW.

action drops significantly, reducing the overall surface density of the obtained layer. Based on the first trial the surface density could be reduced by at least 90%, while still having a large enough fluorescence signal to be able to perform measurements at the same power level as used for the first two trials.

To test the impact of removing NHS from the coupling solution another coating trial was performed using an identical coating procedure, but only using EDC + fluorophore in step 6. The results of this trial are shown in Figure 185.

It was found during the coating process that these fibres were able to pass through much greater volumes of both liquids and gases. The gas flow was observed by dipping the tip of the fibre in water, and examining the bubble flow. A significant improvement was also noted in the guidance properties of the fibre, with greater than an order of magnitude increase in power coupled through the fibre observed compared to the previous coating trials.

This was also reflected in a greatly increased fluorescence signal compared to the second trial. Even though the removal of NHS from the coupling solution should reduce the amount of fluorophores that are bound to the surface the significant reduction in the loss of the fibre appears to have more than counter balanced this effect.

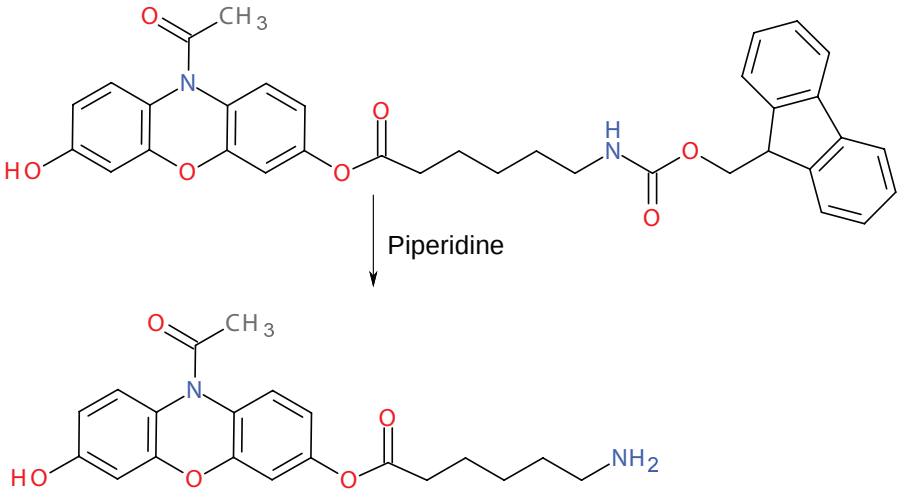

Figure 186: Longer tether ARD, before and after deprotection with piperidine. Synthesised by Dr. Ondrej Zvaric.

7.6.6 *Longer tether*

While all of these trials showed that a fluorescence signal was present after coating, none of them was able to conclusively demonstrate that there was a fluorescence response to hydrogen peroxide. One consideration here was whether the short length of the tether was causing the response of the fluorophore to diminish due to its close proximity to the glass surface. To test this a longer tether derivative was synthesised, with the structure shown in Figure 186. The concept of this was to increase the distance between the portion of the molecule responsible for fluorescence as far away from the glass surface. It was surmised that the expected increase in fluorescence after the reaction with hydrogen peroxide was being washed out.

This synthesised compound was deprotected using piperidine, and coated using the same method before. Like the last short tether trial no NHS was used. These results were inconclusive. All coated fibres showed a strong fluorescence signal, however there was no consistency as to how the fluorophore responded to hydrogen peroxide. The highest noted increase in fluorescence was from the fibre filled with water. This trial made it clear that more analysis of the fundamental behaviour of this fluorophore was required to be able to understand why the surface functionalisation measurements were so inconsistent.

7.6.7 *Cuvette measurements*

The main issue with the functionalisation measurements to this point has been the sheer number of variables involved. The coating process changes between fibres being coated, and likely changes along the length. To try and understand how both the fluorescence of the mo-

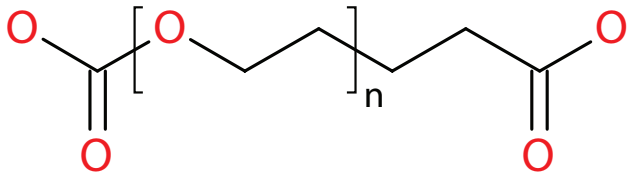

Figure 187: Carboxylic PEG linker.

lecule, as well as how it responds to hydrogen peroxide an alternative method was required.

Previously [100] this has involved coating glass slides with the fluorophore, and analysing the results using a typhoon imager. However it is clear here from the earlier results that the fluorescence of this molecule changes when it is immersed in liquid. The typhoon imager is effectively a large scanner, that uses a laser source for excitation. Since the slides must be flat on the surface of the scanner it is impractical to have the slides immersed in liquid during the scan. Past work [100] has coated the slides, reacted them with the target molecule and then dried the slides before measurement. This does not give a realistic representation of how the measurement would actually be performed in fibre, since the proposed dip sensor technique provides no possibility for flushing the fibre after filling.

The second issue involves the functionalisation process itself. The density of the silane coating is dependent on the surface of the glass. Different amounts of OH groups are available for reaction with the silane molecules depending on how the surface is prepared. The surface in the fibres should be consistent, since the fibres are fire polished during the drawing process. When coating on slides the slides are typically cut from a bulk piece of glass, and then mechanically polished. This creates a different surface to fire polishing, meaning that a different amount of OH groups are likely available and thus a different surface density of silanes will be obtained.

Here we chose to use an alternative method to examine how the fluorophore responds after being bound, without the restrictions of using the typhoon imager on slides.

Rather than binding the fluorophore to the surface, it was considered that possibly binding the fluorophore to another large molecule could give a similar effect. Additionally, if this showed a positive result it was proposed that this fluorophore + spacer could then be attached to the surface, further removing the fluorophore from the surface of the glass. The molecule chosen here was PEG7-0013 from nanocs [239]. The structure of this molecule is shown in Figure 187. This molecule is a long chain, with a molecular weight of approximately 2000 gM^{-1}. The carboxylic functional groups on the molecule should react the same way as the carboxylic groups on the silanes. However since both the PEG and the fluorophore will be in solution,

the effect of binding the fluorophore to this molecule can be examined using a bulk cuvette measurement.

The fluorophore was reacted with the PEG spacer in the same way as previous methods functionalising on the surface of the glass. A PEG solution was made up to 1 mM in 1 mg/ml EDC. Both the shorter tether and longer tether fluorophores were added to separate solutions, to a final concentration of 10 µM. A 100:1 excess of PEG was used both to ensure that all fluorophore molecules had reacted, and to make it statistically probably that a PEG molecule would only have either no fluorophore molecules or one fluorophore molecule bound. For this trial the fluorophore solution with no PEG was also diluted in EDC to ensure consistency between results.

The results shown in Figure 188 are a clear indication that neither of these fluorophores were working as intended. When compared to the initial cuvette measurement shown in Figure 179 which showed a >4×increase in fluorescence over the same range of H_2O_2 concentrations with the same fluorophore concentration the increase in fluorescence intensity is greatly diminished. This occurred for both the short and long tether derivatives with and without PEG. These results strongly suggest that either the EDC is affecting the way in which the fluorophore reacts with hydrogen peroxide, or that the compound itself has degraded.

Before this was checked, the fluorophore was re-analysed using an identical experimental protocol as the initial measurement shown in Figure 179. This measurement did not show the expected fluorescence response, rather the fluorescence was almost constant for 2 µM -200 µM H_2O_2, and only saw a statistically significant increase in the fluorescence signal at 2 mM. The measurement was repeated in both PBS solutions and solutions with NaOH added to bring the pH to ~10 to test to see if this was related to the buffer solution, but no improvement was noted. It was hypothesised that the piperidine itself could be interfering with the reaction, however the reason that this effect was not noticed in the first trial was not understood.

The short tether fluorophore was then deprotected, the residual piperidine removed and the compound purified. Qualitative tests demonstrated that when mixed in solution this fluorophore was clear until hydrogen peroxide was added, at which point the solution slowly changed to a pink colour. This is indicative that the fluorophore is reacting with the hydrogen peroxide as it would normally be expected to do. The reason that only the short tether derivative was deprotected was the limited available quantity of the longer tether version making it difficult to perform purification on this molecule.

This behaviour was then qualitatively tested by adding varied concentrations of hydrogen peroxide to the solutions. The results of this trial are shown in Figure 189.

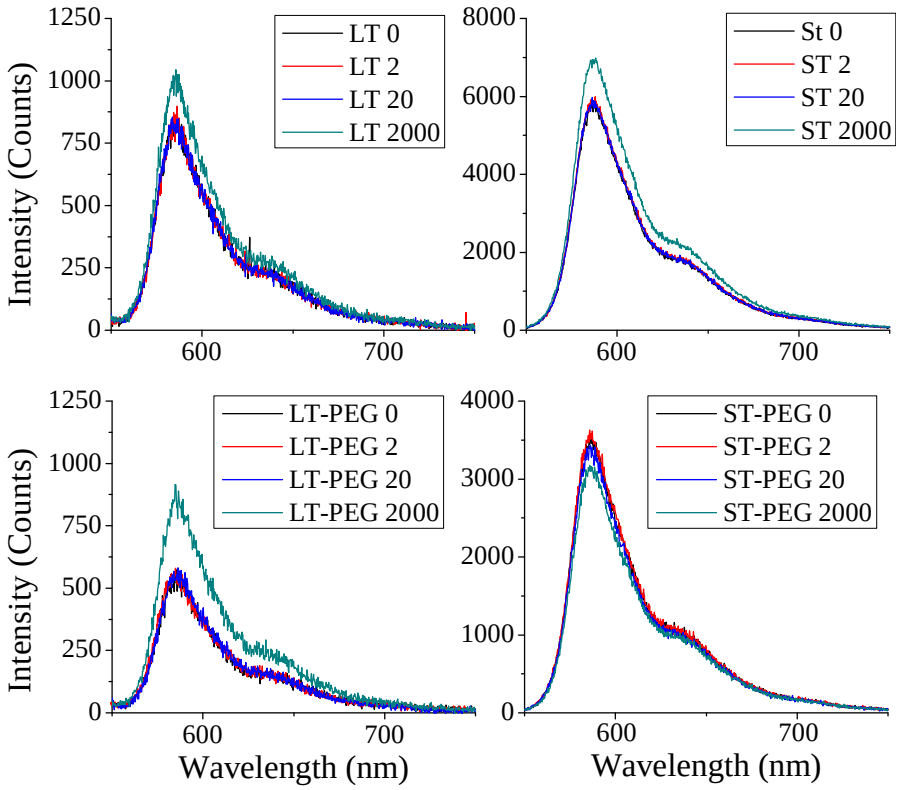

Figure 188: Cuvette measurements with original short tether ARD (ST) and long tether (LT) version, with varied hydrogen peroxide concentration. The bottom row also shows the cuvette measurements with the addition of PEG.

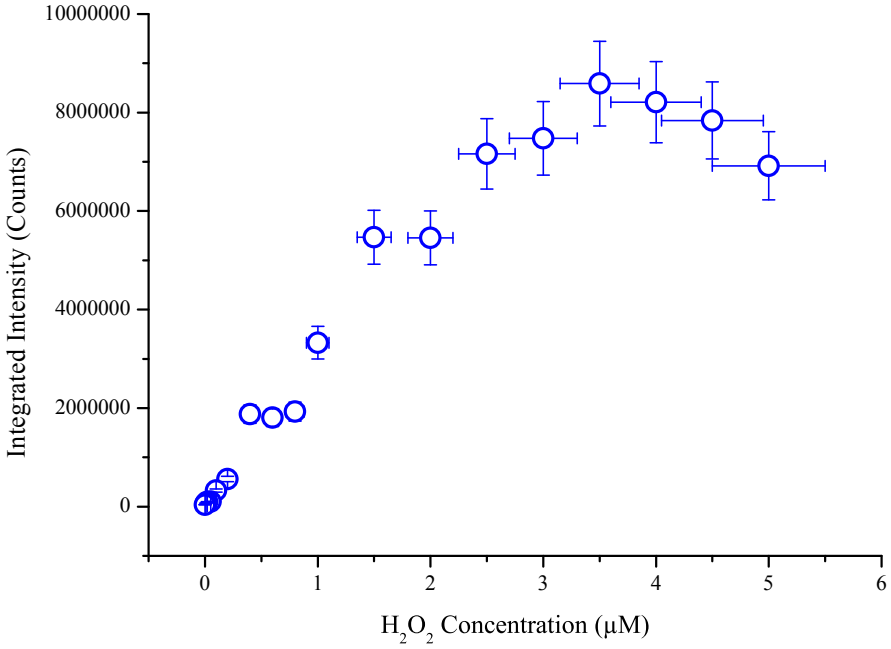

Figure 189: Cuvette measurements of short tether ARD, with varied hydrogen peroxide concentration. The fluorophore concentration is 10 µM, and the fluorescence intensity was integrated from 550-700 nm.

This result shows that with the removal of the piperidine the fluorophore now shows a linear response to hydrogen peroxide with a large dynamic range. The minimum detectable concentration in this measurement was 100 nM, with saturation not occurring until >3 µM. The effect of the peroxide concentration on the absorption of the fluorophore was also measured for the same fluorophore concentration, and is shown in Figure 190.

A significant response to hydrogen peroxide was also visible in these results as expected. Since this fluorophore does not quench via a PET mechanism we expect the absorption of the fluorophore to display the same trend as the fluorescence emission which is what we do indeed observe here. This could plausibly impact the linearity of the fluorophore, since potentially at high fluorophore concentrations the absorption from the molecules could increase the loss of the fibre, reducing the amount of fluorescence that is transmitted to be detected.

With the confidence that the fluorophore was responding correctly to hydrogen peroxide, additional solutions were then mixed added 1 mg/ml of EDC, NHS and EDC+NHS to the fluorophore. The results of this trial are shown in Figure 191.

A substantial increase in fluorescence is observed in these results when hydrogen peroxide is added, with a further increase when the concentration is doubled. It is important to note here than the NHS, EDC & NHS+EDC solutions all show fluorescence signals more than

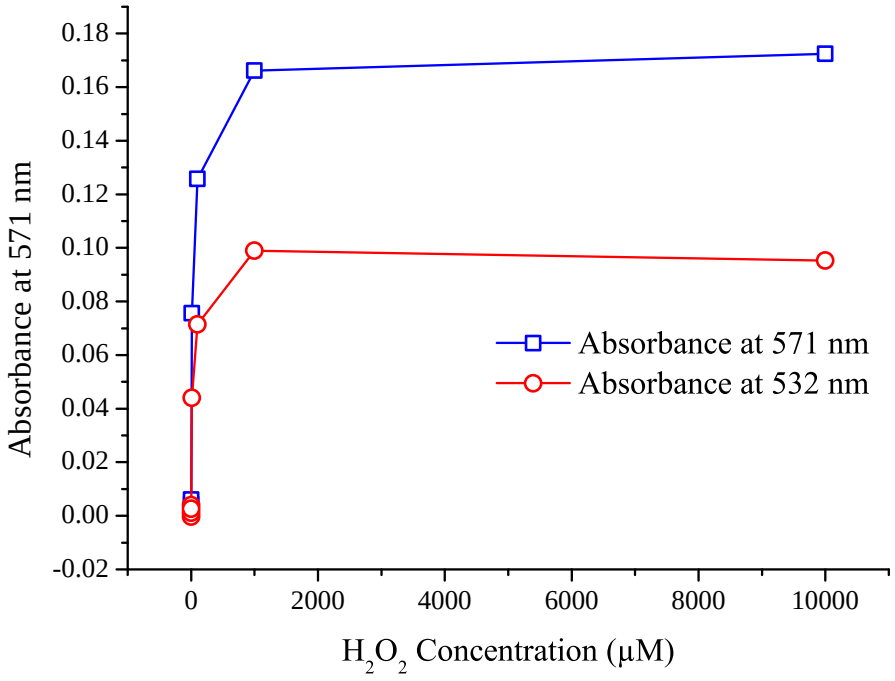

Figure 190: Bulk cuvette absorption measurements on ARD 10µM.

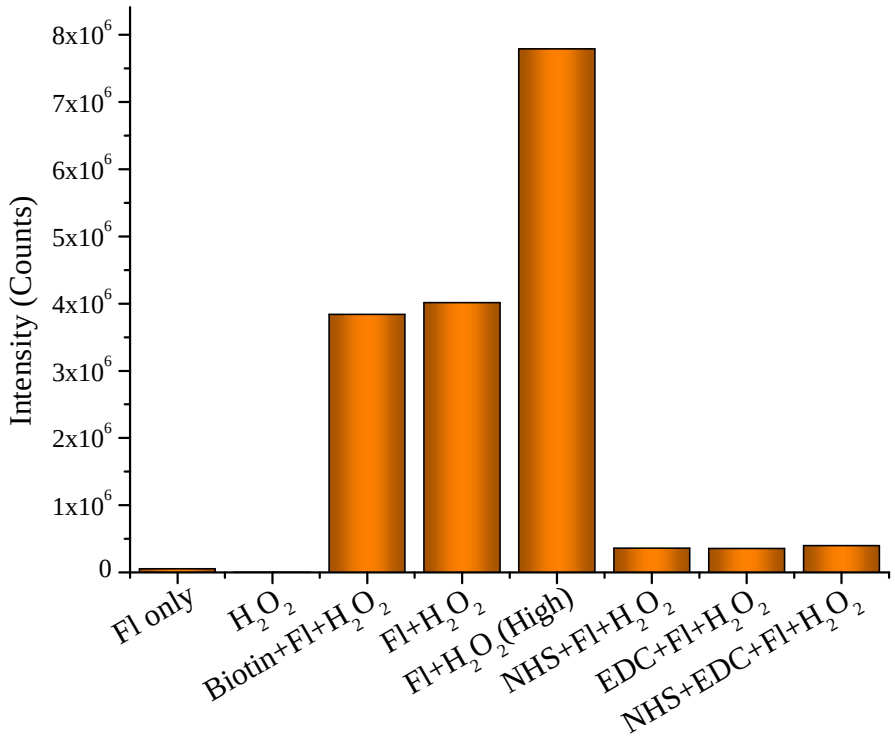

Figure 191: Cuvette trial of 10 µM short tether fluorophore. This shows the integrated fluorescence intensity from 550-700 nm.

10× lower than that of the solution in water for an identical hydrogen peroxide concentration. This suggests that both of these molecules are somehow interfering either with the fluorophore itself (quantum efficiency or absorption) or the mechanism of interaction with the hydrogen peroxide.

Although theoretically both of these molecules should be flushed from the fibre at the conclusion of the filling process, in practice it is likely that small amounts will still remain electrostatically bound inside the fibre. This could have a significant impact on the measurement results for using ARD for peroxide sensing in fibre.

This cuvette trial was also used to test another step in a possible functionalisation process. As mentioned earlier, the PAH polyelectrolyte was found to block the fibre when flushed through for coating. This polyelectrolyte was chosen as it gives a carboxylic acid for attaching the amine group on the fluorophore. Previous work [234] has successfully coated polyelectrolytes on the glass surface, however this has been with the aim of leaving an amine surface, to attach to a molecule/Qdot with a carboxylic functional group. The PEG spacer used earlier in Section 7.6.7 could possibly be attached to amines on the glass, leaving a carboxylic functional group free to be attached to the amine group on the ARD molecule. However since this spacer has two carboxylic groups, it is possible that both ends of the spacer could attach to the surface, leaving no free groups for the fluorophore to attach to and reducing the possible surface density of the fluorophore on the glass. So it is preferable to use a spacer that can only bind in one orientation.

An alternative coating process was proposed. Rather than just using the amine/carboxylic interaction of the previous process, it was proposed to use a biotin/avidin coating method, as shown in Figure 192. The polyelectrolyte coating is performed as per the previous trials, using poly(allylamine hydrochloride) (PAH) and poly(sodium styrene sulfonate) (PSS). The PSS here is the negatively charged polyelectrolyte, the PAH positive. Coating with PAH leaves free amine groups on the surface, to which biotin with a carboxylic functional group can be reacted. Avidin is then introduced, and due to its high affinity (Kd ~ 10^{-15}M) to biotin they form an extremely strong bond. To this avidin molecule an NHS-PEG-Biotin molecule [240] is attached, which can then react with the amine group on the fluorophore.

This proposed method should allow the previously successful coating process to be used with a fluorophore that has an amine functional group. The NHS-PEG-Biotin should also act as a spacer, to move the fluorophore away from the surface and reduce any surface-related effects.

The first test of this process was to react the NHS-PEG-Biotin molecule with the fluorophore in solution. The solution was made up 1:1 NHS-PEG-Biotin:fluorophore, and reacted with the same concen-

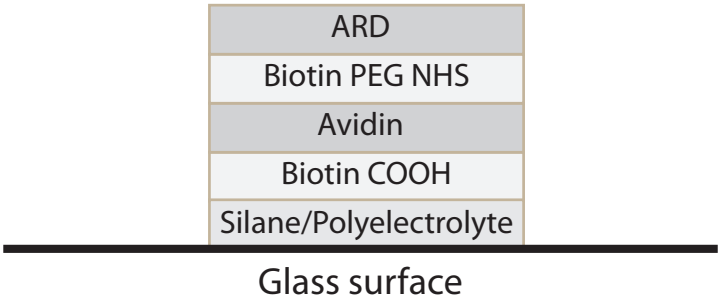

Figure 192: Biotin/avidin surface functionalisation.

tration of fluorophore for 2 hours. Peroxide was then added to this solution and the scan performed after 30 minutes. The results in Figure 191 show that the fluorescence signal obtained is the same as that for just the fluorophore + peroxide within error, demonstrating that the NHS-PEG-Biotin does not interfere with either the fluorophore:peroxide interaction, or the fluorescence generation from the fluorophore. This trial was also repeated with a 20:1 excess of NHS-PEG-Biotin, and demonstrated that there was no significant reduction in the fluorescence intensity. The large excess of NHS-PEG-Biotin ensures that virtually all fluorophore molecules in the solution should have reacted with the NHS-PEG-Biotin before the hydrogen peroxide was introduced.

The final item to be tested with bulk cuvette measurements was the reaction rate, to determine how long to wait before performing a scan. The same cuvette method as previous was used, with the spectrometer set to scan every 30 seconds for one hour. Hydrogen peroxide was added immediately after the first scan, with the results of this trial shown in Figure 193.

The trials involving the biotin/avidin interaction now give several possibilities as to the method with which the fibres can be functionalised which will be explored in the next section. Since this reaction does not require a carboxylic functional group to be available on the surface, both silanes and polyelectrolytes which have previously been successfully used for fibre coating can be trialled to attach the biotin to the surface.

7.6.8 *Testing in capillaries*

To determine the optimum coating conditions, it was decided to move away from using fibres for measurements and instead perform the coating on capillaries with large internal diameters. The motivation for this work was to enable more straightforward characterisation of the coated surfaces, as well as reducing the complexity required for fibre filling by greatly increasing the internal diameter of the holes. F2 capillary fibres with an outer diameter of 140 µm and an inner dia-

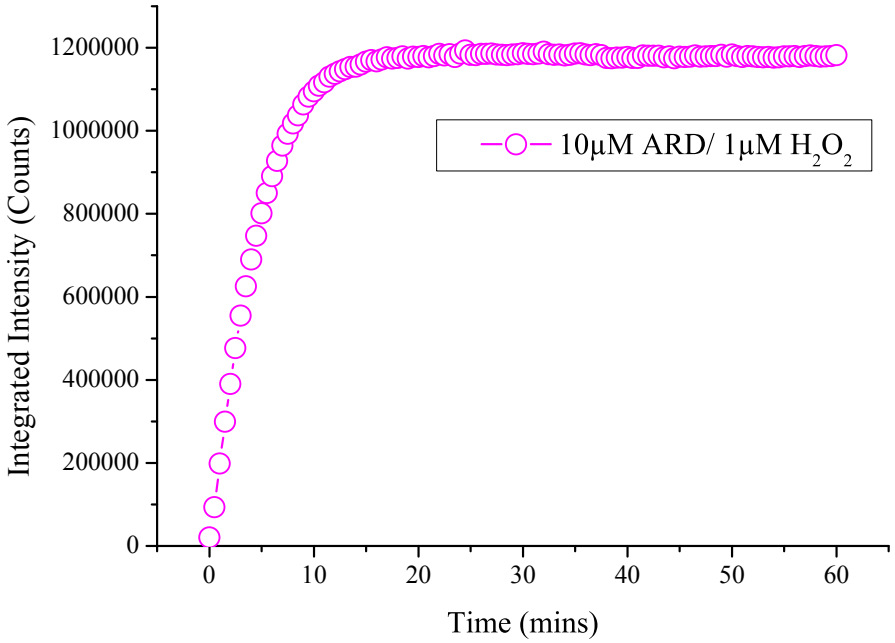

Figure 193: Kinetics of reaction in cuvette between 10 µM ARD solution, with H_2O_2 to a final concentration of 1 µM added immediately after the first scan.

meter of 70 µm were used for this section. This allowed much faster filling rates to be used, as the larger internal diameter results in less restriction on the liquid being passed through. The flow rate through these capillaries at 50-100 psi is sufficient to flush through 1-2 mL of liquid in less than an hour. One metre of capillary with a 70 µm internal diameter has an approximate volume of 3.9 µL, so we can then find that 260-520 $\times$ the total internal volume of the fibre is flushed through over an hour. Additionally the use of these large capillaries makes measurements using the typhoon imager more quantitative, as the filled volume inside the 70 µm inner diameter capillaries is significantly larger than the individual pixels of the imager. For a WW fibre the total diameter of all the holes is 10-15 µm, meaning that the fibre only sits on top of a single pixel. When the fibre is not located perfectly parallel to the pixel array this creates banding, where periodic regions of high and low intensity are observed along the length of the fibre. Using the large capillaries at 50 µm resolution this issue is almost completely resolved.

To analyse the fluorescence signal from the capillaries a typhoon imager system was employed. This system uses a laser source for excitation and a photomultiplier tube for collection of the fluorescence. The imaging technique is similar in principle to that of a photocopier, with the excitation and collection point physically traversed across the screen to perform the measurement. To perform the measurement the capillaries are first coated and filled with peroxide solutions. The external surfaces of the fibre are then cleaned using ethanol to en-

sure that contamination of the outer glass surface does not influence the measured fluorescence signal. Skin oils can also show in the final image, with numerous examples of these seen in Figure 197. To minimise the effect of contamination the capillary was only handled from one end, with measurements always being performed on the central section.

Using the typhoon imager for analysis provides a semi quantitative method to measure the fluorescence intensity and thus the density of the fluorophores. The method here involves drawing a box of fixed area in an image analysis program, and look at the counts obtained in this region after subtraction of the background signal. The box is drawn such that its length is much greater than its width, and is oriented such that the fibre is parallel to the long axis of the box. This technique is highly dependent on the uniformity of the fibre, as well as the background itself. Choosing to use large internal diameter capillaries increases the reliability of these measurements, as with smaller diameter capillaries significant amounts of "banding" are observed on the final image. This banding arises as the capillary crosses over lines in the pixels producing an image that suggests that the intensity of the fluorescence varies with the fibre length. However when the capillary is moved the location and period of these bands shifts, demonstrating that this feature is an artefact of the sensor rather than a product of non uniformity of the coating.

Additionally this method struggles to obtain reliable measurements when the fluorescence signal is low, and the total number of counts becomes comparable to the background level. Figure 195 shows a good example of the difficulties of using this method, as it shows the regions of higher intensity in the background signal. These appear even after the screen had been cleaned with ethanol and water, and it is difficult to obtain a completely clear background signal.

The first coating trial using these capillaries was performed shortly before the compound without piperidine was obtained, thus the solution flushed through the fibre still contains piperidine as per the earlier fibre coating trials. For this trial capillaries were coated with silane using the same technique and approximately the same durations as the earlier fibre coating trials.

This trial used EDC as the coupling reagent. with a fluorophore concentration of 1 µM fluorophore over a period of 1 hour. In this hour 1 mL of fluorophore was passed through the capillary. The plate on the typhoon imager was first cleaned using hydrogen peroxide, followed by ethanol and water to minimise the background counts. The capillary was cut in to short lengths, and then filled with various concentrations of hydrogen peroxide. The capillaries were then placed on the plate, using a microscope slide to hold the capillaries firmly against the plate. The results of this trial for a PMT voltage of 650 V collection using the 580 nm BP filter are shown in Figure 194.

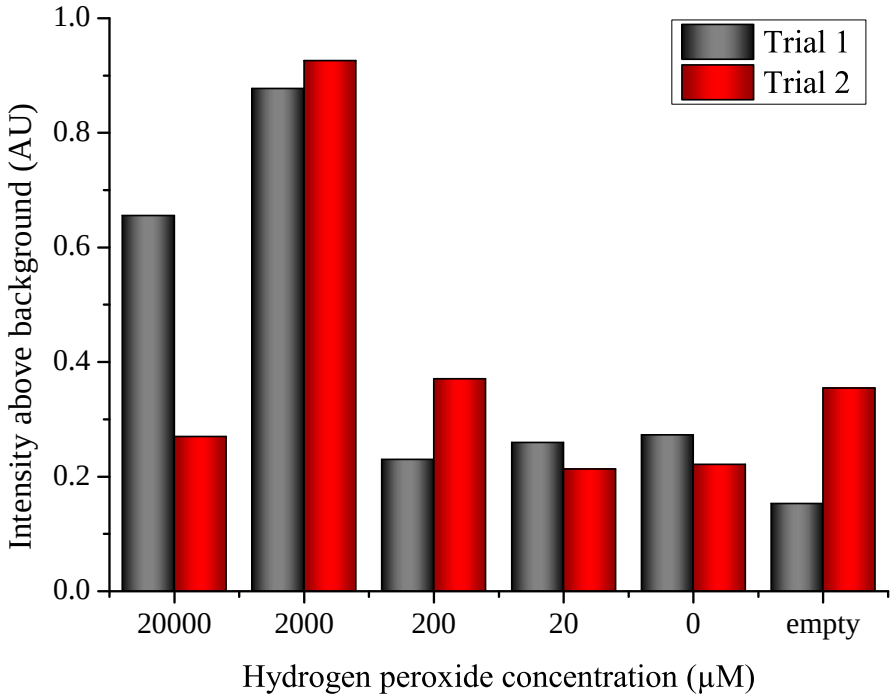

Figure 194: Large diameter F2 capillary coating trial using ARD with piperidine in the solution.

As can be seen from this figure high concentrations of hydrogen peroxide appear to show an increase in the fluorescence intensity, but as can be seen from the 20 µM case there is limited consistency between the fibres. The signal obtained is only marginally above that of the signal seen from an unfilled fibre, and it is not until 2 µM of hydrogen peroxide are filled in to the capillaries that the signal becomes statistically significant above that of the uncoated fibre. So this appears to demonstrate a sensitivity to hydrogen peroxide, however the concentration required is high and the signal:background level is not high enough to be able to utilise this as an effective sensor.

As mentioned earlier in Section 7.6.7 numerous alternative coating procedures are possible for attaching these molecules on to the surface of the glass. One that has previously been used applied to SPR sensing [231] utilises the biotin/avidin interaction, and since the protocol for performing this coating is well understood this method was chosen for the next coating trial. For this experiment silica capillaries were used, since it has been demonstrated before [234] that since the OH group count on the surface of the silica glass is higher than that with F2 glass that a higher surface density is obtained. Thus performing the trials in silica capillary should allow an increased amount of fluorophores to be bound to the surface increasing the ratio between the signal fluorescence and the background fluorescence.

Two separate coating protocols were used for this trial; involving a silane and a polyelectrolyte technique. The capillary used was a

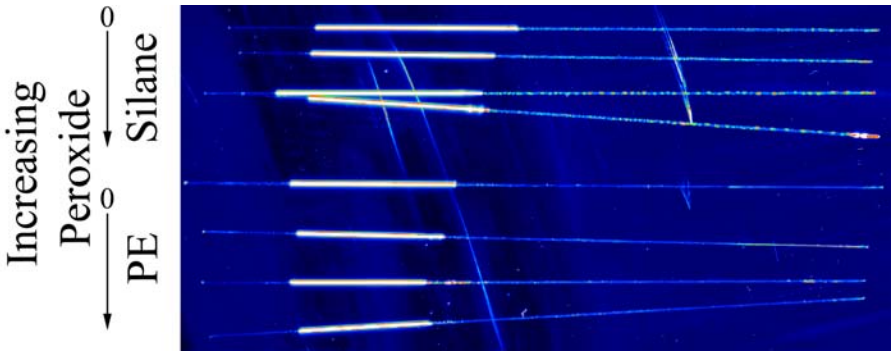

Figure 195: Silica capillary coating trial with biotin/avidin/PEG-NHS-Biotin coating technique.

commercial silica 300 µm outer diameter 100 µM inner diameter with a total length of approximately 70 cm. Here the pressure filling setup was not used, instead the capillaries were first cut in to short lengths and inserted into the septum of a small vial. By using a 30 mL syringe a pressure could then be applied to the vial, and due to a combination of the short length of the capillaries and their large internal diameter large volumes of liquid could then be flushed through. For this trial the deprotected ARD without piperidine had been synthesised, so this was used during the process

For the silane capillaries 2% Aminopropyltriethoxy Silane (APTES) was filled in the fibre, and allowed to react overnight. This is a silane that gives a free amine group on the surface for interaction with the biotin. The polyelectrolytes capillaries first had 2 mg/ml Poly(allylamine hydrochloride) (PAH) deposited overnight, then alternating layers of poly(sodium styrene sulfonate) (PSS) and PAH for a total of 5 separate layers. Between polyelectrolytes water was flushed through the fibres.

The remainder of the coating protocol was the same for all capillaries, and was as follows with washing and drying steps between each solution -

1. 1 µM biotin + EDC + NHS 2 hours
2. Avidin 1 µM 3 hours
3. NHS-PEG-Biotin 1 µM 2 hours
4. 10 µM fluorophore 2 hours

The capillaries were then filled with hydrogen peroxide solutions, and recorded using the typhoon imager. The concentrations used were 20 mM, 200 µM, 2 µM & 0 µM. The results of this trial are shown in Figure 195.

The silane coated capillaries showed a large amount of silane deposited in a non-uniform fashion on the external surfaces of the capillaries. This made measurements on these capillaries unreliable, as

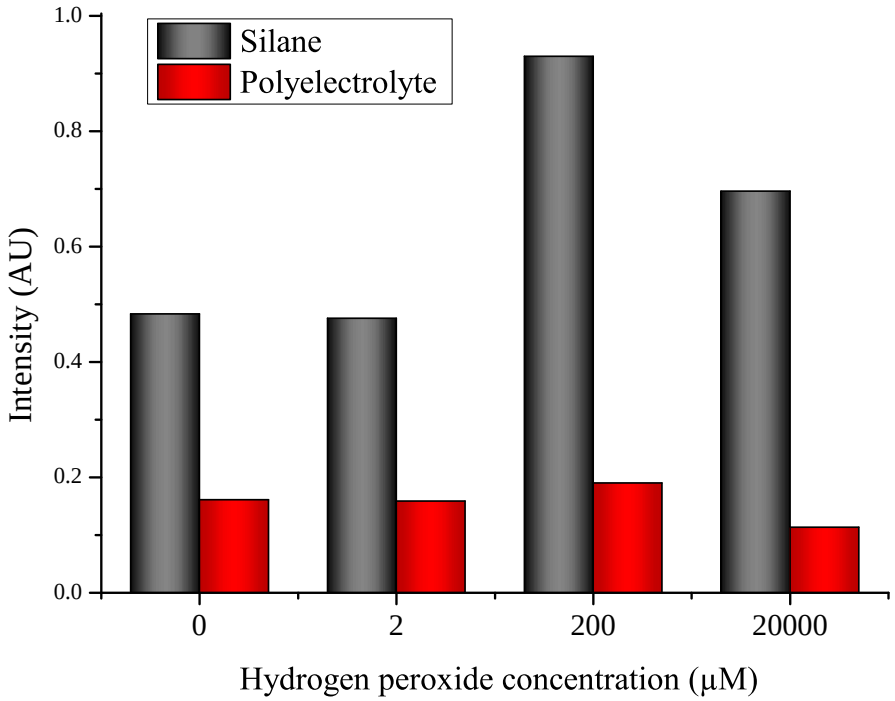

Figure 196: Volume analysis for silica capillaries coated using biotin/avidin process.

the majority of the obtained fluorescence signal appeared to originate from these points on the outside of the capillaries. The analysis for this measurement is shown in Figure 196.

This demonstrates no clear correlation between the hydrogen peroxide concentration and the fluorescence intensity. As mentioned the silane coated capillary results are unreliable due to the contamination of the external surfaces so those results are considered unreliable. The polyelectrolyte coated fibres show no statistically significant difference in the observed fluorescence regardless of the hydrogen peroxide concentration.

Due to the limited availability of silica capillaries, the next trial was performed using the same F2 capillaries as the first capillary coating trial. The aim of this trial was to determine the coupling reagent that would be used for fibre-based experiments, and to repeat the biotin/avidin/PEG-NHS-Biotin procedure.

A similar coating procedure was again used, with CEST used for all coupling reagent trials and APTES or PAH for the biotin/avidin/PEG-NHS-Biotin trials. These were allowed to react overnight with further layers deposited on top of this. Three coupling reagents were trialled here -

1. 2-(1H-7-Azabenzotriazol-1-yl)–1,1,3,3-tetramethyl uronium hexafluorophosphate Methanaminium (HATU) in DMF

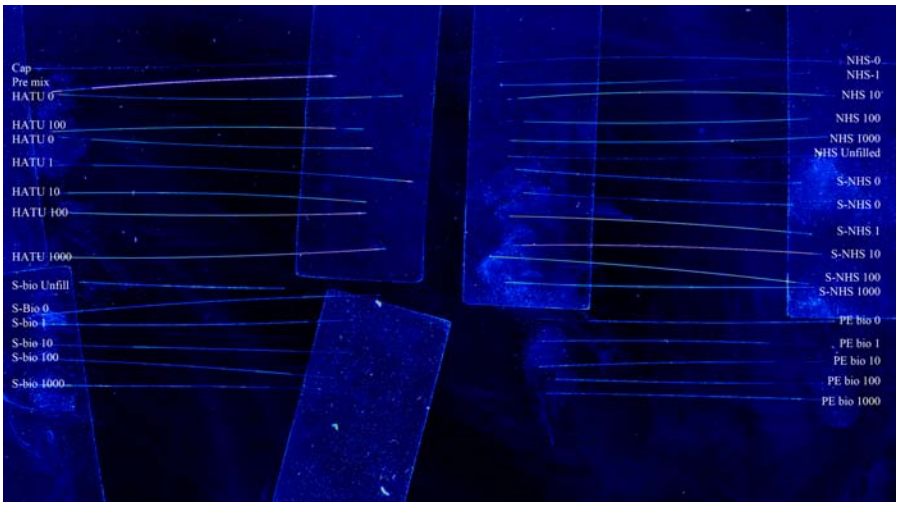

Figure 197: Typhoon image for capillaries coating using various methods. Red shows the regions of highest intensity. This result shows that nil results are obtained using the polyelectrolyte/silane + biotin.

2. N-hydroxysulfosuccinimide (Sulfo-NHS) + ethyl(dimethylaminopropyl) carbodiimide (EDC) 2 mg/mL

3. N-hydroxysuccinimide (NHS) + EDC

The coated fibres were cut to length and filled with hydrogen peroxide + HRP solutions with concentrations of 0, 1 nM, 10 nM, 100 nM & 1 µM. These were then placed on the typhoon imager plate, with the results shown in Figure 197, with the analysis shown in Figure 198.

For the measurements in Figure 197 the signal was significantly above the background level so it was possible to perform reasonably accurate measurements. The fine spots on the image arise from dust on the screen, but are infrequent enough and low enough in intensity that they did not significantly affect the final measurement.

This trial demonstrates a statistically significant increase for HATU, NHS + SNHS. It is unclear as to why the trials with the biotin process both with the polyelectrolyte and silane were unsuccessful, and due to time constraints the reasons behind this failure were not examined. This trial showed that capillaries using HATU as the coupling reagent showed an increase from 10 nM, NHS+EDC from 10 nM and sulfo-NHS from 1 nM. This is a significant improvement over earlier trials, both in the magnitude of the fluorescence increase as well as the concentration of hydrogen peroxide required to observe this change.

Additional trials after this demonstrated that the observed fluorescence intensity from capillaries in which the coupling reagent was not included was significantly lower than those in which the standard coating process was used. This strongly supports the hypothesis that the fluorophore is being covalently bound to the surface. The removal of the coupling reagent prevents the amine:carboxylic interac-

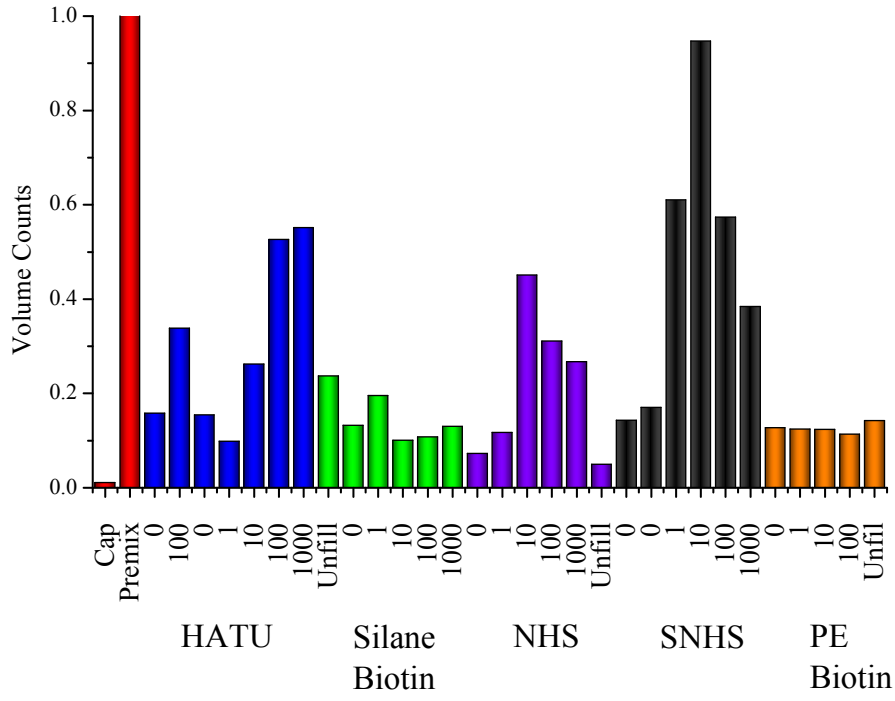

Figure 198: Analysis of Figure 197, considering the summation of the observed counts after subtraction of the background signal for capillaries coated using various techniques with differing concentrations of hydrogen peroxide.

tion from forming an amide bond, so if the observed fluorescence intensity is higher with the coupling reagent than without this strongly suggests that the covalent bond is being formed as intended.

For the next fibre trial it was decided to attempt the coating process using a silane layer, and HATU as the coupling reagent even though the sulfo-NHS shows a higher total fluorescence signal. With the issues previously noted with the NHS significantly increasing the loss of the fibre the Sulfo-NHS presents a somewhat unknown factor, while for the HATU we were confident that the molecules should not crash out of the solution forming crystals. Additionally, at this point the long term stability of the fluorophore was unknown, and the effects of HATU on the fluorophore had already been characterised. As such no additional measurements were required to conclude that in bulk solutions at least the HATU had no effect on the fluorescent properties of the ARD or the way that it interacts with the hydrogen peroxide molecules.

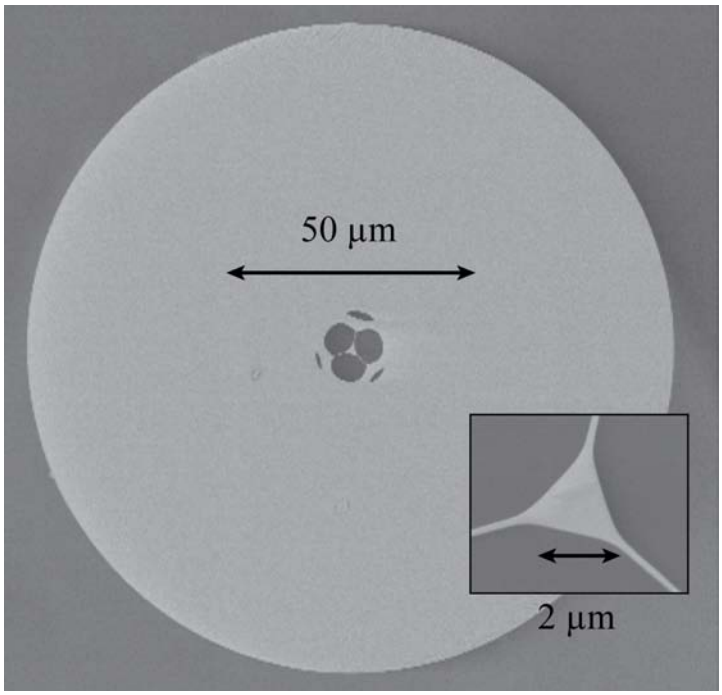

Figure 199: F2HT wagon-wheel fibre used for coating trials.

7.6.9 *Fibre coating*

7.6.9.1 *First trial*

With the capillary measurements complete it was desirable to attempt to perform hydrogen peroxide detection in fibre to observe how repeatable and reliable this technique could be. The fibre used for previous measurements had been depleted, so a slightly different fibre was used for these trials. A SEM of this fibre is shown in Figure 199.

The process used for coating the F2 wagon-wheel fibres was as follows.

1. CETS Silane 5% 17 hours.
2. Nitrogen 15 mins.
3. Water 2 hours.
4. Nitrogen 15 mins.
5. Fluorophore 2 1/2 hours.
6. Nitrogen 15 mins.
7. Water 30 mins.
8. Nitrogen 15 mins.

At the completion of filling the fibre was then cut in to 15 cm length using a mechanical cleaver. Each of these fibres was then placed on

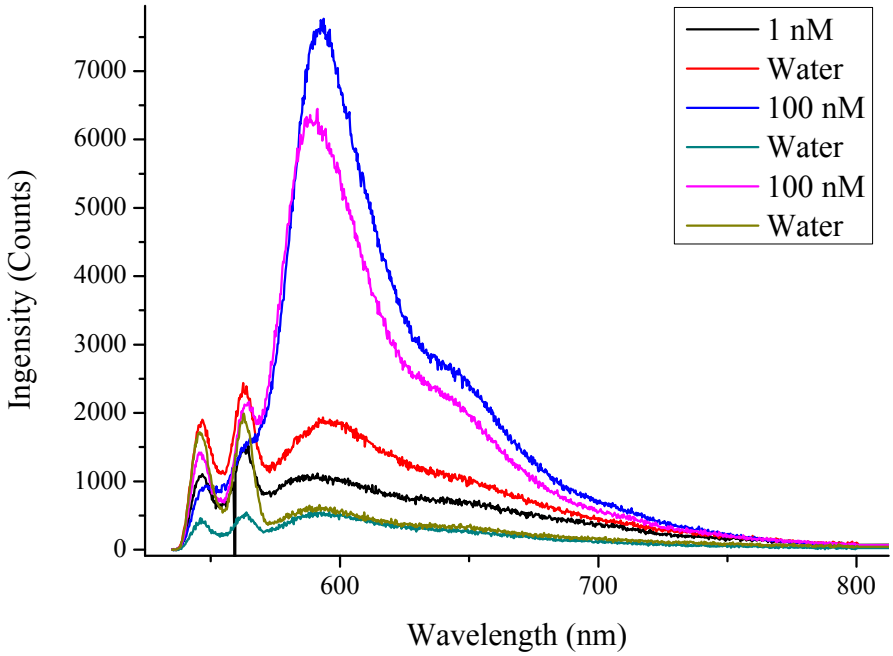

Figure 200: Fluorescence results from coating of deprotected ARD in F2 WW fibres, filled with different concentrations of hydrogen peroxide after coating.

the translation stages, and aligned using the minimal possible power level. The fibre was then filled for 10 minutes at which point the fibre tip was removed from the solution. The fibre was then left for a further 12 minutes, and a scan performed. The results of this measurement for 6 separate fibres filled alternately with water + HRP and hydrogen peroxide solutions are shown in Figure 200. The input power used for these measurements was 2.5 µW.

Since this fibre was cut in to such short pieces (~150 mm) this made it difficult to measure the loss directly with a cutback measurement. We can however indirectly estimate the loss of the fibre, by assuming that the coupling efficiency between fibres is the same. A 150 mm length of wagon wheel fibre was filled with water, and the input coupling optimised using a power meter. The transmitted power through this length was measured as 840 µW for approximately 2.5 mW input. The power transmitted through the fibre used for the photobleaching measurements in Figure 201 was 550 µW for the same input power. Assuming that the coupling efficiency was similar for both fibres, we can therefore estimate that the additional loss induced by both the coating process and the absorption of the fluorophore is 12 dB/m. This amount of loss is acceptable for a dip sensor since the fibre lengths are so short, but would be prohibitive for any sort of distributed measurements over longer lengths of fibre.

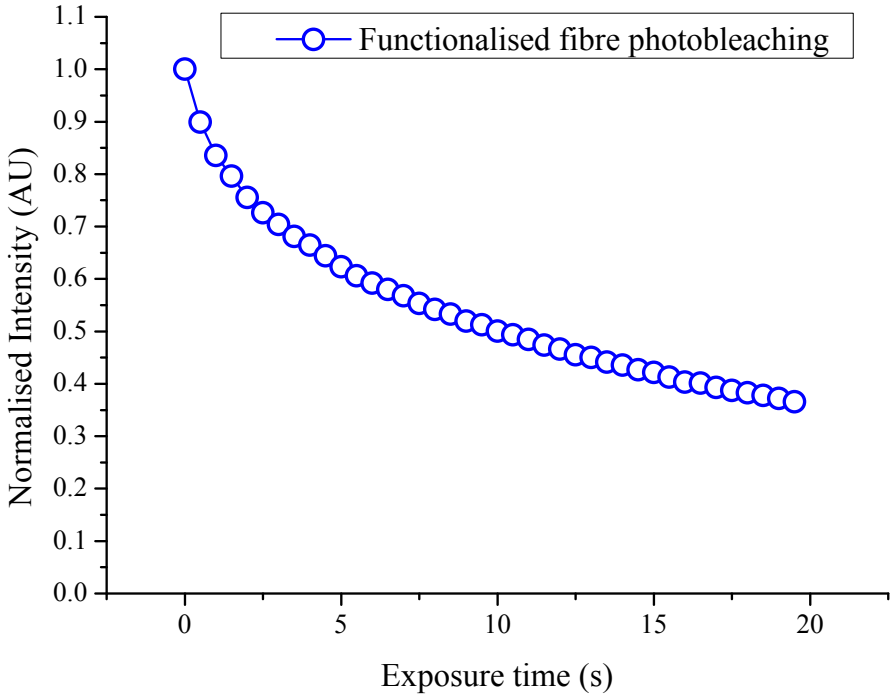

Figure 201: Photobleaching rate for coating fibre filled with 100 µM H_2O_2 + HRP solution. The input power used here was 25 µW.

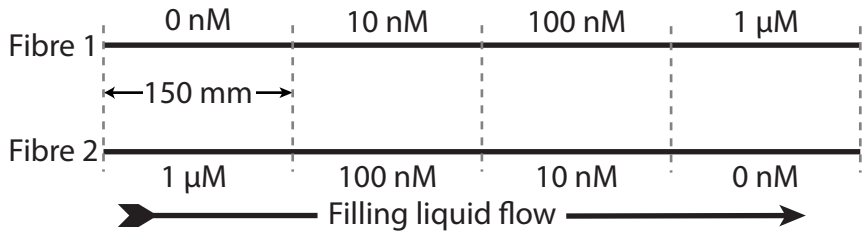

Figure 202: Order of peroxide concentration used in the two fibres coated.

7.6.9.2 *Second Trial*

This trial was then repeated using the same coating protocol with two fibres with an initial length of approximately 700 mm. Again the fibres were cut into 150 mm lengths and filled with various concentrations of H_2O_2 and HRP solutions. One of the drawbacks to filling longer lengths of fibre is that at the opposite end of the fibre from which the liquid is filled some depletion of the chemicals used could occur. This could possibly reduce the observed fluorescence signals at this end of the fibre due to a reduced surface density of fluorophores. To minimise any possible effects arising from variations in the density of the surface coating along the length of the fibre, the two fibres were filled with hydrogen peroxide solutions in a different order, as shown in Figure 202. If the observed fluorescence intensity is a product of the fibre length then an inverse correlation to the peroxide concentration should be observed with one of the fibres.

The results of this trial are shown in Figure 203, which shows a reasonable dependence on the fluorescence intensity, and more importantly both of the fibres show a trend in the same direction so we can conclude that the length dependence of the fluorescence is not the reason behind the increase in fluorescence signal. If the difference in fluorescence signal was solely due to variations of the coating density, then it would be reasonable to assume that the higher fluorescence signal would be observed at the end with the highest fluorophore density which is likely the end from which the liquid was inserted.

Filling hydrogen peroxide solutions in the order shown in Figure 202 allows fluorescence from the increase in the hydrogen peroxide signal to be distinguished from the length dependence. Since the two fibres are filled with peroxide concentrations in opposite orders the two should show the inverse dependence if the difference in fluorescence is due to the length dependence of the surface density. Since this is clearly not the case, it can be reasonably concluded that this is not true for this coating trial.

The reduced signal at 1 µM solution is either due to an issue with the surface coating, or alternatively could also be due to oxidation to a non-fluorescent compound at high peroxide levels as was seen earlier with AUR in bulk solutions. Both fibres show a large increase in the fluorescence signal between the water filled and 10 nM, with the smallest increase for the first fibre at one hour of 1.8 × and the largest 5.3 × for the same fibre after four hours. Part of this is likely due to variations in the coupling both in and out of the fibre, and part due to variations in the actual emitted fluorescence intensity over time.

It was not possible to study the kinetics of each individual fibre due to concerns about the time stability of the coated fibres. This meant that fibres were removed from the stages between the measurements and thus could not be monitored for the duration. The fibre could have been monitored from filling to the time of the first measurement, however it was decided to minimise the exposure of the fluorophore to light to reduce any impact of this on the final result. Indeed for the entire filling process once the fluorophore was introduced the fibres were kept in the dark for the maximum possible amount of time, with the lights only turned on when required to check the progress of the filling or to change the solution.

At the conclusion of these measurements issues were raised about the structure of the compound, which will be examined in more detail in the following discussion section.

7.6.10 *Discussion and summary*

With the results from the previous chapter it can be concluded that hydrogen peroxide has been successfully detected in solution using a

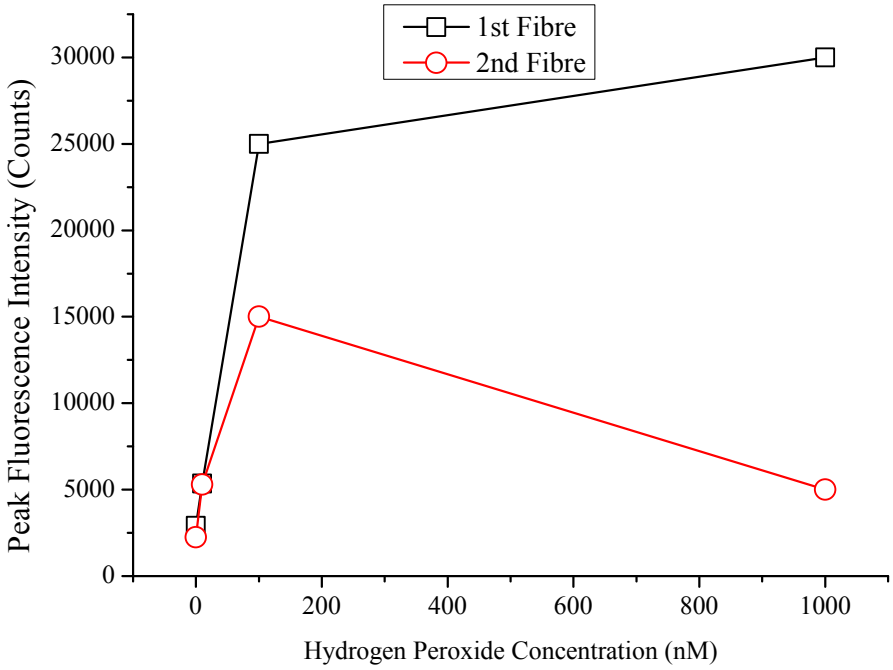

(a) Fluorescence intensity measured approximately 1 hour after fibre filling.

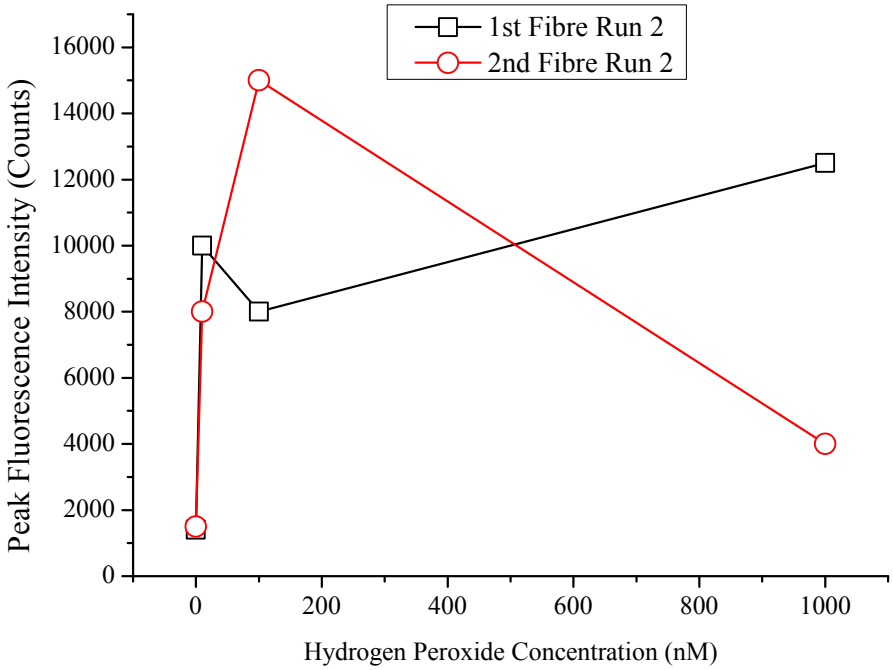

(b) Fluorescence intensity measured approximately 4 hours after fibre filling.

Figure 203: Second WW fibre coating trial with deprotected ARD.

microstructured optical fibre. Pre-mixing of the solutions of amplex red and horseradish peroxidase demonstrated a detection limit of approximately 20 nM after the solution was filled into the fibre. This limit was below the minimum desired concentration required for both the wine and IVF applications, and as such no specific effort was made to improve the sensitivity beyond this. This sensing method had the drawback that the volume of liquid required was still relatively large, with >10 µL of sample still required to perform a measurement. This large sample size prevents the main advantage of the fibre-based sensing system, the low (<50 nL) volume of the fibre to be effectively utilised.

This was improved on with the low-volume bulk mixing, reducing the required sample size to only 1 µL by diluting the sample 9:1 with the fluorophore and then taking care with the experimental procedure to be able to fill the fibre from this small reservoir. The sample size could potentially be reduced further by increasing the magnitude of this dilution, however this would come at the cost of the sensitivity of the sensor.

Significant effort has been invested in developing a fluorophore that can be surface functionalised, concluding with the successful synthesis of an amplex red derivative with an amine tether. The reactivity of this fluorophore to hydrogen peroxide has been conclusively shown in bulk solutions, and demonstrated with good results in both capillaries and in fibre when attached to the glass surface. This has demonstrated a fluorescence signal that is dependent on the hydrogen peroxide concentration filled into the functionalised fibre.

Exactly how the fluorophore is attached to the surface here has not been confirmed. NMR of the deprotected compound could not conclusively show that the compound showed the expected structure, and mass spectrometer results had a similar issue. Clear results were obtained at the start of the process both for NMR and mass spectrometer for the protected compound. The reaction of piperidine with the FMOC group is a well studied reaction, and the successful deprotection of the molecule to expose the amine group can reasonably assumed. Over the subsequent weeks some white particles were seen in the container holding the dry sample, even though the sample was kept in the dark at -20 °C. The impurities were removed from the compound, and the sample rechecked with the mass spectrometer result again showing a clear signal for the protected fluorophore. This however produced questions about the stability of the compound, as to how long the compound could be used for before it began to break down. The likely conclusion here is that the FMOC protective group was breaking off from the rest of the molecule, but this was not confirmed due to the limited amount of compound that was available at this point.

Due to equipment issues beyond our control, we were unable to perform any mass spectrometry measurements on the fluorophore between the initital characterisation, and the final measurements. A mass spectrometer measurement performed on the day of the final fibre coating trial (Figure 203) was unable to observe the expected peak at 314.29, instead only showing the mass of the base amplex red molecule at 264.2. This was further complicated when a measurement was performed using a high resolution mass spectrometer - Orbitrap 3000 RSL HPLC, which again did not show the expected peak. It did however show a peak at 338.34 which aligns well with the compound plus sodium. However due to inconsistencies between these mass spectrometer results, as well as NMR results not showing the expected results it is impossible to conclusively say what the structure of this molecule actually is.

Initial functionalisation trials were promising, but not conclusive as to whether peroxide was able to be detected in fibre. Most trials demonstrated a small increase in fluorescence with high concentrations of peroxides, however these increases were significantly less than the fluorescence increase observed from bulk samples of Amplex Red. Issues with the surface functionalisation technique with the NHS blocking the holes and problems with the polyelectrolyte produced delays in obtaining low-loss coated fibres. By the time the functionalisation protocol had been developed the stability of the fluorophore had come into question.

Further characterisation of the bulk chemicals demonstrated that the NHS, EDC and piperidine were likely interfering with the fluorophore. Although in theory the EDC and NHS should be washed from the fibre during the coating process, in practice it is likely that small quantities of these compounds will remain in the fibre. Likewise the excess piperidine should be washed from the fibre, but again some will likely be electrostatically bound to the surface in the fibre. The capillary trials shown in Figures 197 and 198 show that high fluorescence signals are indeed obtained when EDC and NHS are used the coating process. This suggests that, for these large capillaries at least, residual amounts of these molecules remaining on the surface have minimal impact on the behaviour of the fluorophore. This trial did not address the issues observed earlier with the NHS degrading the loss of the fibre, and due to time constraints the possibility of using sulfo-NHS in the coating process was not examined outside of capillaries.

In the future significant time will need to be invested developing a repeatable, reliable, low loss protocol for fibre functionalisation. There are a vast number of choices for coupling reagents, including the HATU with which was used with success for the later trials. Alternatively the solvent for the NHS/EDC/fluorophore could be changed from water to DMF or DMSO, as this should increase

the solubility off all components of the reaction reducing the amount of product that precipitates out of the solution which is likely what induces the additional loss.

More quantitative measurements of the surface density using both silanes and polyelectrolytes are also required in addition to measurements related to the coupling reagents. Again there are more options as to the choice of chemicals and conditions used here. As previously mentioned the issue with obtaining quantitative measurements begin with ensuring that the initial surface quality of the glass is the same as in fibre, then pass on to exactly how to make measurements as to what the surface density actually is. It can be indirectly measured by binding a fluorophore such as a quantum dot to the surface, and looking at the amount of observed fluorescence [41, 234]. This however does not give a direct measurement of the density of the silane or polyelectrolyte layer, and to obtain this requires further assumptions about the efficiency of the coupling reaction between the amine and carboxylic groups. Additionally this assumes that the quantum efficiency of the fluorophore remains the same, and also does not consider that the fluorescence emission will likely not be homogeneous this close to the glass surface [241, 242].

Once the fluorophore had been cleaved and the piperidine removed more successful trials of the surface functionalisation process were obtained. Control trials showed that the fluorescence intensity was higher when a coupling reagent was included, suggesting that the fluorophore was binding to the silane layer as desired. Due to the amount of variability in the obtained fluorescence intensity it was not possible to use this fluorophore to check the surface density.

It is also important to note here that the concentration of fluorophore that was used for the surface functionalisation was particularly high at 1 µM. So for a 15 cm length of fibre, we have 1.5×10^{10} fluorophores inside the fibre at any one time, assuming that the volume is 24 nL. During the filling process, a constant pressure is maintained, such that the amount of liquid flushed through the fibre over the 2-3 hours of the coating step is multiple times that of the total volume of the fibre. As such with this high number of fluorophores present in the fibre this suggests that even if 99% of the fluorophore has degraded from the tethered amplex red to standard amplex red there should still be a sufficient amount of fluorophore molecules available to be bound to the surface. The mass spectrometer results should be sensitive to low concentrations of fluorophore, but the inconsistency of the results makes it difficult to reach a conclusion as to the success of the binding process.

So although measurements to determine that the structure of ARD was as desired, we have indirect evidence as to the successful synthesis of the fluorophore from the control trials with both the fibres

(Figure 184) and capillaries showing low fluorescence signals for coating processes without the coupling reagents.

The final two fibre coating trials, which bring together the refinements in the coating process along with the removal of piperidine, show a good dependence on the hydrogen peroxide concentration, with a minimum detectable concentration of approximately 10 nM. This technique is almost at the point of being a single-step process to take a measurement, as the only external addition at this point is HRP. This can either be introduced by adding small quantities to the entire sample which is to be sampled, or ideally the HRP itself could be functionalised. This has previously been demonstrated to work [229] using silane coatings, and the primary reason that it was not included in these measurements was a desire to minimise the complexity of the experiments arising from concerns about the stability of the fluorophore.

So with these results sensing for hydrogen peroxide has been demonstrated in fibre, however it is also clear that refinements of both the fluorophore and the coating procedure will be required before this can find effective use as a sensing platform. This is an important step towards this goal. Control trials showed that the fluorophore is likely bound to the surface, but unfortunately mass spectrometer and NMR results were unable to conclusively show the structure of the fluorophore that was used. Nonetheless significant progress has been made towards developing a process that can successfully bind fluorophores with amine functional grounds to the glass surface, which to this point had not been demonstrated to the best of our knowledge.

8

CONCLUSIONS

This thesis shows development towards creating a practical fluorescence based fibre dip sensor both for detection of low concentrations of fluorophores for use as a biosensor, as well as for hydrogen peroxide detection in aqueous solutions. A method for the surface functionalisation of hydrogen peroxide reactive fluorophores has been developed, resulting in preliminary results indicating the successful detection of hydrogen peroxide in solution using only ~20 nL of sample volume. This has expanded on the previously developed methods for surface functionalisation, demonstrating that the fibres can be coated with an acceptable increase in loss of only 6.5 dB/m at 532 nm.

This work has covered the development and optimisation of both the sensor and detector architecture, reducing the minimum detectable concentration of Quantum Dots in solution by two orders of magnitude over what had previously been demonstrated in fibre to 10 pM. This was further improved through the use of lanthanide doped nanocrystals, showing a reduction in the detectable concentration of Erbium doped nanocrystals to 660 fM limited by the background fluorescence from the glass. The use Thulium doped nanocrystals allowed this detection limit to be lowered further still, as the emission spectra from these nanoparticles is distinctly changed from that of the background signal from the glass, allowing easier differentiation between the signal and background fluorescence. Both the Quantum Dots and nanocrystals can find use as fluorescent labels for biological detection via surface functionalisation processes, so it can be inferred from this that with the developments here more sensitive biosensors can be created using these optical fibres.

A range of soft glasses has also been characterised for their background fluorescence at various visible wavelengths, which should allow more reasoned choices of glasses for sensing applications in the future. This work also involved the development of a new optical fibre, with lower intrinsic background fluorescence, and work is proceeding on the characterisation of a novel multi core structure that potentially can reduce the effect of glass fluorescence on the measurements (Appendix A).

A range of practical improvements to fibre optic sensors have been developed, with the primary goal of creating a sensor platform which can be used for real world measurements. This has covered splicing the soft-glass microstructured fibres to conventional silica core:clad fibres for easier integration with existing systems, as well as tapering to create a probe tip that can easily be integrated with a wagon-wheel

fibre based dip sensor. A theoretical model has also been employed to analyse the prospective performance of these splices, both in terms of the amount of light coupled into them as well as the amount of fluorescent light that can be expected to be observed after transmission through the spliced region.

This goal of improving the practicality of these wagon-wheel fibre dip sensors has also involved initial development on microfluidic techniques that, once fully realised should allow sensing to be performed with sub-microlitre sample sizes that does not require the development of specialised fluorophores that can be functionalised to the surface of the fibre. As such this work, once fully developed should present an alternative to developing fluorophores for surface functionalisation, as through optimisation of the methods it should be possible to perform multiple measurements without drawing enough liquid to significantly affect IVF samples.

Additionally progress has been made both on the use of a new glass for fibre fabrication, FK5, which shows reduced photodarkening rates in bare fibre compared to what is observed using F2 fibres. This work has also included development in die materials that can find use at higher temperatures, opening up new possibilities of glasses that can be extruded, partially bridging the gap between what is currently achievable and the temperatures required for silica extrusion.

Finally characterisation of various hydroperoxide and hydrogen peroxide sensitive molecules both in cuvette and in fibre has been performed, culminating in the aforementioned detection of hydrogen peroxide using a surface functionalised fibre. Several molecules were characterised in the process of these developments, leading to a greater understanding of the requirements and ideal characteristics of a fluorophore intended for use in optical fibre sensors. This has given a better understanding of the desired characteristics of a fluorophore for use in this type of dip sensor, primarily in the area of photostability needed to perform measurements. During the course of this work the methods used for detection of this fluorescence have been greatly improved, leading to a reduced requirement in the stability of the molecules.

Initial work on hydroperoxide detection in fuel was unable to obtain a clear signal when the fluorophore was filled into the fibre due to the long scan times and high illumination intensities required. When repeated using the optimised detection system developed over the course of this thesis measurements were able to be performed demonstrating a photobleaching rate that now would not preclude this fluorophore from use in a sensor.

This project has covered applications beginning in fuel sensing, and progressing through wine sensing and finally embryo sensing. A commercial fluorophore, Amplex Ultrared has successfully been employed in fibre, showing a good linearity over the desired concen-

tration range. A version of this fluorophore has also been modified for surface attachment, demonstrating likely detection of hydrogen peroxides down to 10 nM. This last example should provide an ideal application especially suited for sampling using optical fibres, since the low volume required for sensing with these microstructured fibres integrates well with the low sample sizes available for detection on IVF samples. The typical buffer volume around an embryo that can be sampled is approximately 20 µL. So using a 20 cm length of functionalised fibre with an internal volume of 20-30 nL as a dip sensor results in minimal reduction in the available sample volume, such that a series of measurements can be performed on a single embryo to monitor the peroxide concentration around the embryo as it develops.

The work presented here has produced developments in both the sensitivity and practicality of fluorescence-based microstructured optical fibre detection methods, which potentially will lead to more real world applications being explored to find new uses for these types of sensors.

Part IV

APPENDICES

A

TRIPLE CORE WAGON WHEEL FABRICATION

Another approach that was investigated to reduce the effect of the intrinsic glass fluorescence by altering the geometry of the fibre, rather than by changing the glass or the wavelengths of the excitation/emission. The proposed concept in the most general form is shown in Figure 204. Here it is proposed to utilise one core for excitation of the fluorescent molecules within the holes, and the second for recapture. This type of multi-core concept has been used in the past for coupling both with solid [243, 244] and microstructured fibres [245] including work done applying this to sensing applications [246]. The technique used in Ref [246] utilised interferometric methods to observe pressure and strain by monitoring the coupling between the cores.

On average the fluorophores will be closer to the collection core (i.e. between the launch and collection cores) than the emitters responsible for the background emission from the glass, which resides within the launch core. This should in theory mean that the capture of the signal photons will be of a higher efficiency than those emitted from the excitation core.

Some preliminary modelling was performed, suggesting that there would be some fluorescence capture into the second core. For 0.85 µm cores the modelled fluorescence capture drops by approximately 500 × when the offset distance (see Figure 204) is increased to 1 µm when considering a single mode excitation and capture in to all modes of the collection fibre (see Section 2.11). Since this was a completely new fibre geometry requiring a new die design rather than performing extensive theoretical modelling to determine the precise ideal geometry it was instead decided to attempt to fabricate some test fibres, and determine from these fibres what modifications then needed to be made to the die to obtain a useful fibre. The die used is shown in Figure

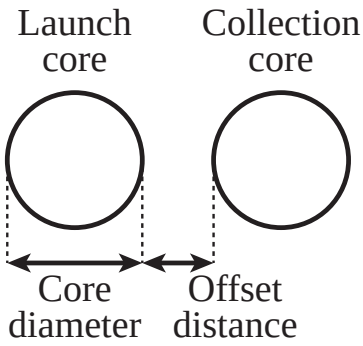

Figure 204: Concept for excitation and capture with separated cores.

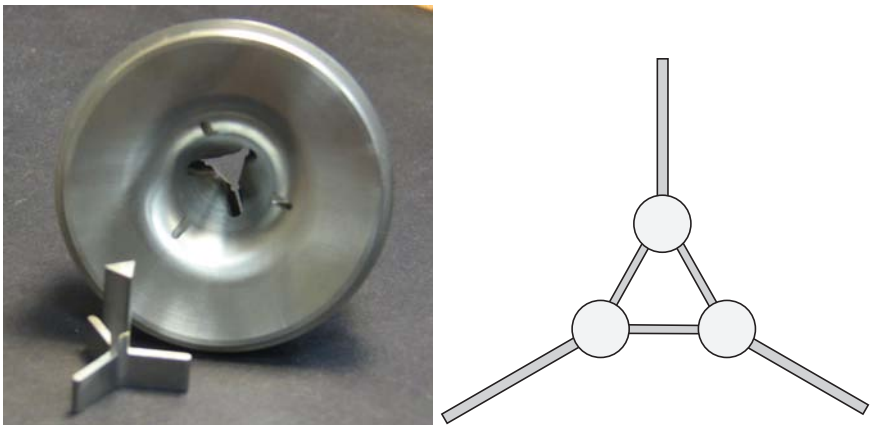

Figure 205: (left) Extrusion die used for triple core preform fabrication (right) Sketch of proposed structure.

205. It was decided to make three cores rather than two, primarily because this simplified the fabrication process. Fabricating three cores meant that the basic die design and flow structure could remain, as the three cores should be adequately supported by three long struts. Changing to two cores would likely require four struts which would require extensive modifications to the existing die design, in addition to presents additional challenges during the drawing process.

The die design was modified from that used normally for large wagon-wheel extrusion. Typically the central region of this die consists of a hole in the centre for the core, with slots for the struts. Here the central hole was replaced by a torpedo structure which acted both to separate the central region from one large triangular hole in to three separate cores linked by thin struts. A preform was extruded using the standard technique, with the results shown in Figure 206.

This preform unfortunately showed extensive deformations from the ideal structure. The initial section of the preform shows "ribbing" in the outer wall with a period of 3-5 cm, which has occurred previously when the glass flow through the die is unstable. This effect is minimal after approximately 20 cm of the extruded structure has pass through the die. When the preform was cut to length it was clear that the internal structure had deformed, with the struts bent inside the preform. This likely arises from excessive glass flow through this region.

The internal flow design of the die was modified slightly to improve the stability of the glass flow, and the extrusion repeated. Past experience had shown that this instability was due to differing flow rates of the glass through the internal struts, and external walls. Since it can be observed that the core emerges a significant time before the walls, it can be concluded that the flow rate for the glass going to the walls is too low and thus needs to be increased by modifying the die. The results of this trial are shown in Figure 207.

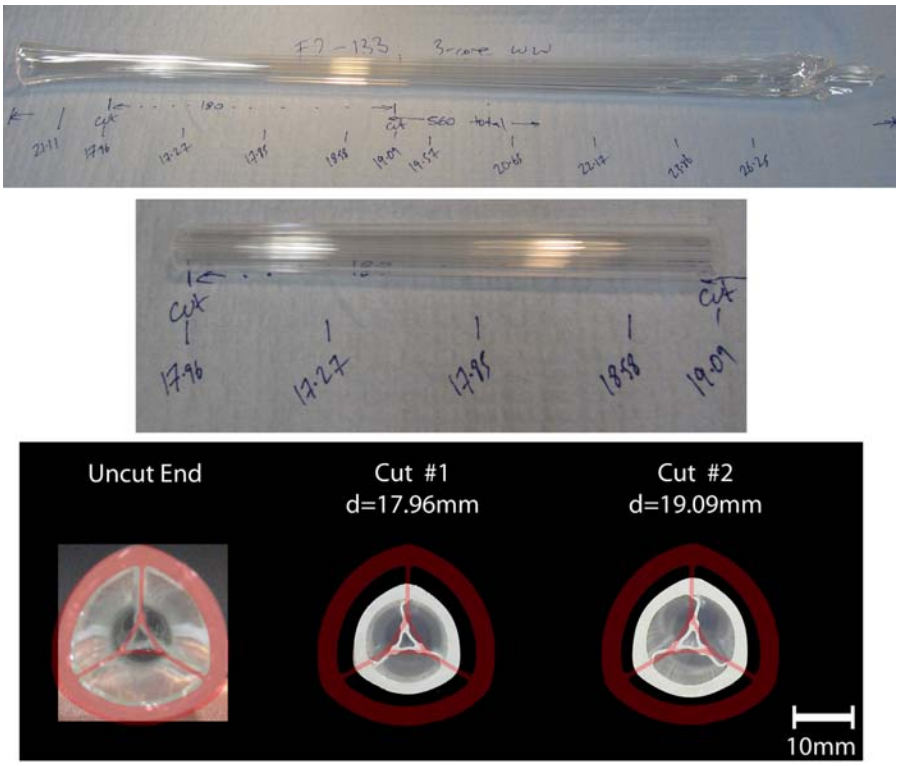

Figure 206: F2 triple core extrusion trial #1 (top) Full preform, showing periodic deformation (middle) Central extrusion region, the draw has stabilised and the surface is now smooth (bottom) Comparison between die exit (red) and preform cross-section at either end of the cut region.

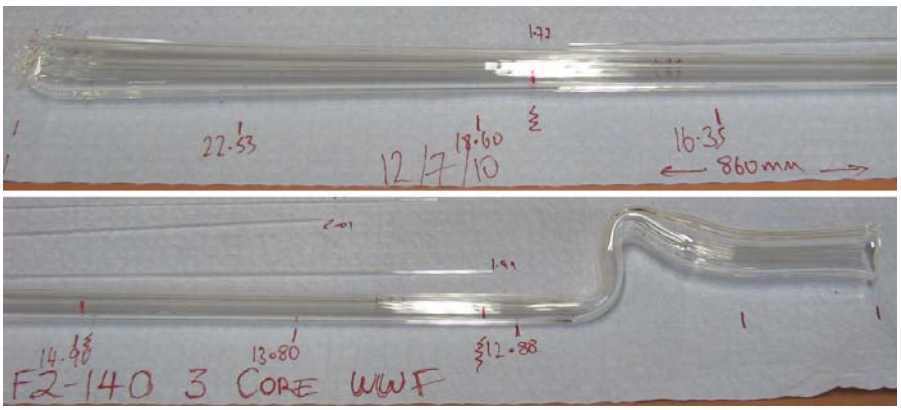

Figure 207: F2 triple core extrusion trial #2.

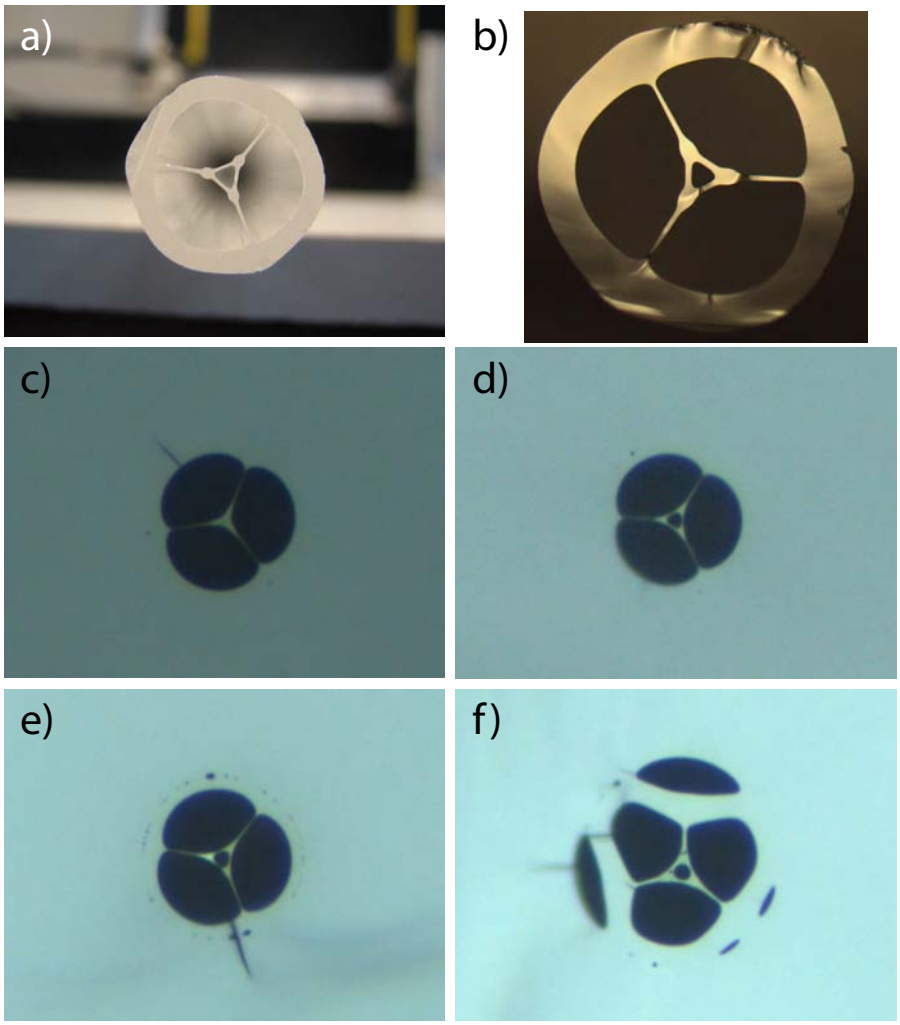

Figure 208: Triple core fibre fabrication process (a) Preform (b) Cane (c) Start of fibre draw, cores merged (d,e) Continuation of draw, centre hole opened holes progressively inflating (f) End of draw, interface gap opening up and strut length significantly decreased.

This extrusion showed significantly less deformation than the initial trial, both in regards to the "ribbing" at the start of the extrusion as well as the deformation of the struts (Figure 208a). This result was sufficient to proceed with the remainder of the fabrication process to observe how further deformations affect the final geometry of the fibre.

The fibre was drawn using a cane-in-tube technique (see Section 2.3.1), which involves first caning the preform down to ~1 mm diameter (Figure 208), and then inserting this in a tube with an inner diameter approximately equal to the outer diameter of the cane. This assembly is then drawn down to a fibre with a typical outer diameter of 125-200 µm.

This trial resulted in the successful fabrication of a triple core fibre, which to the best of our knowledge is the first demonstration of a

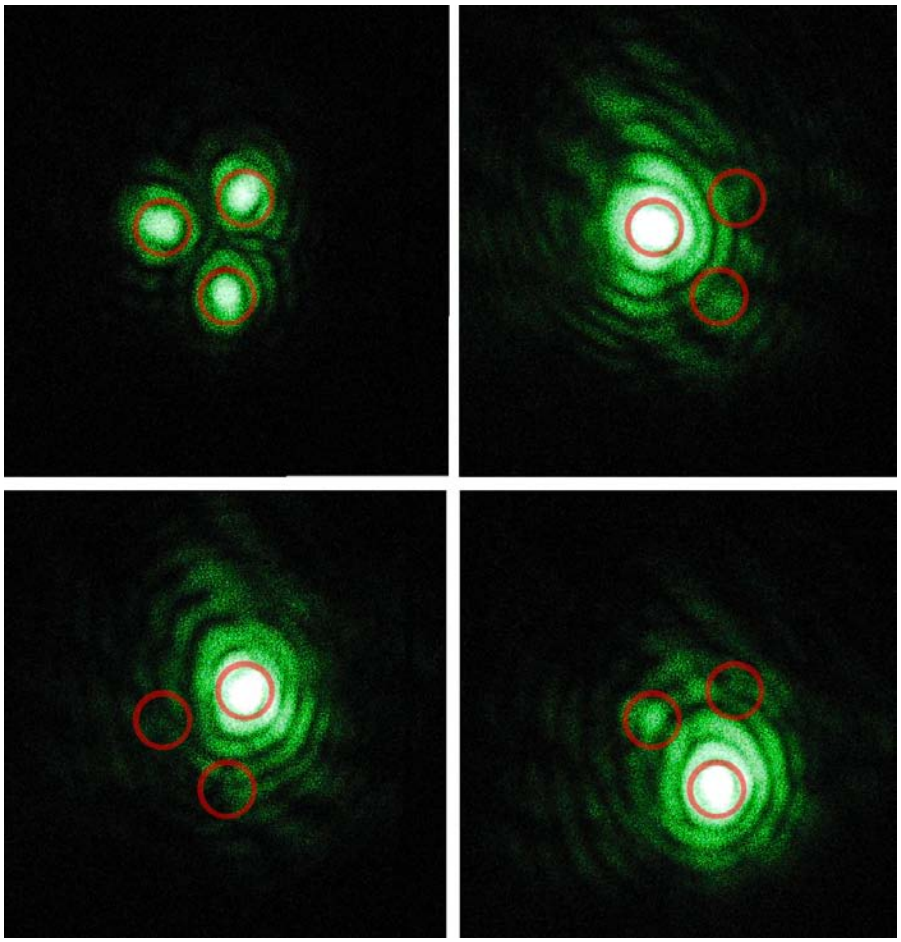

Figure 209: Individual mode coupling in first successfully fabricated triple core structure. The red circles show the approximate locations of all of the cores in each image.

multi-core fibre using the extrusion technique. It was demonstrated using a 532 nm laser source that the light could be individually coupled in to each core, which is obviously a requirement if this fibre is to be used as a sensor. This is shown in Figure 209, and displays similar results to what was demonstrated by Baggett et al. [247] for a multi-core silica fibre.

These images were obtained firstly by de-focussing the light, and adjusting such that the light was coupled approximately equally into all cores. The alignment was then adjusted to couple in to each core in sequence, and an image recorded without moving the camera. This successfully demonstrated that the light can be coupled in to each core, with almost 3 orders of magnitudes more power in the desired core than is present in the secondary cores. With 3.8 ± 0.1 mW coupled into core 1 (arbitrary designation) only 13 ± 1 µW is observed from core number 2.

Unfortunately due to issues in the fibre drawing process (Figure 208c,f) only limited amounts of fibre (<2 m usable) were actually ob-

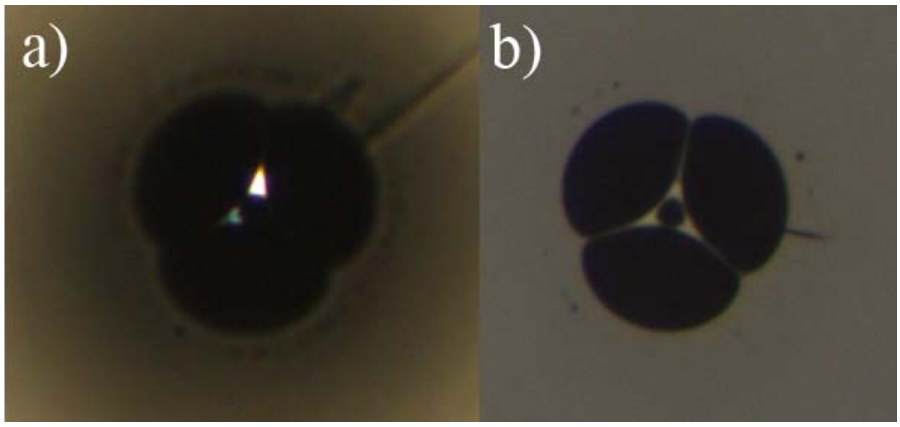

Figure 210: Second fabricated triple-core fibre (a) Transmission microscope image through ~10 cm of fibre (b) Reflection image at the same magnification.

tained from this trial, which was not enough to perform systematic measurements on the fluorescence capture.

A new tube was fabricated and the draw repeated, however it was shown here that although one core possessed a relatively low loss, the loss in the second two cores was progressively higher. This is shown qualitatively in Figure 210.

Here the observed images are compared between the transmission through ~210 cm of fibre using an external light source for excitation, and the standard reflection image using the microscope's light source. It can clearly be seen that good transmission is obtained through one of the cores, a small amount through a second and virtually none through the third. It is unlikely that this is due to any sort of resonant process, as the same cores always display higher losses. This was checked using sections of fibre that showed a single air gap between the strut and the cane (such as that seen in Figure 208f) which gave an orientation key for each piece of fibre. A spot loss measurement at 532 nm was performed on these two cores, giving a result of 1.4 ± 0.2 dB/m for the top core and 4 ± 0.4 dB/m for the bottom left core. The transmission through the bottom right core was too weak to be observed using reasonable lengths of fibre.

A third fibre draw again resulted in poor transmission. At this point it was considered that contamination of the cane or preform could possibly have caused the increased loss, either through chemical contamination or from water damaging the surface. An extrusion was performed with the third and final triple-core die. The results of this trial are shown in Figure 211.

Extrusion parameters used here were identical to the first two trials, using the same die design as the second trial with the modifications for improved glass flow. Although it is not completely clear from the image here, the preform showed significant misting along the length from defects on the internal surfaces of the preform. This degradation

Figure 211: Triple core extrusion trial #3.

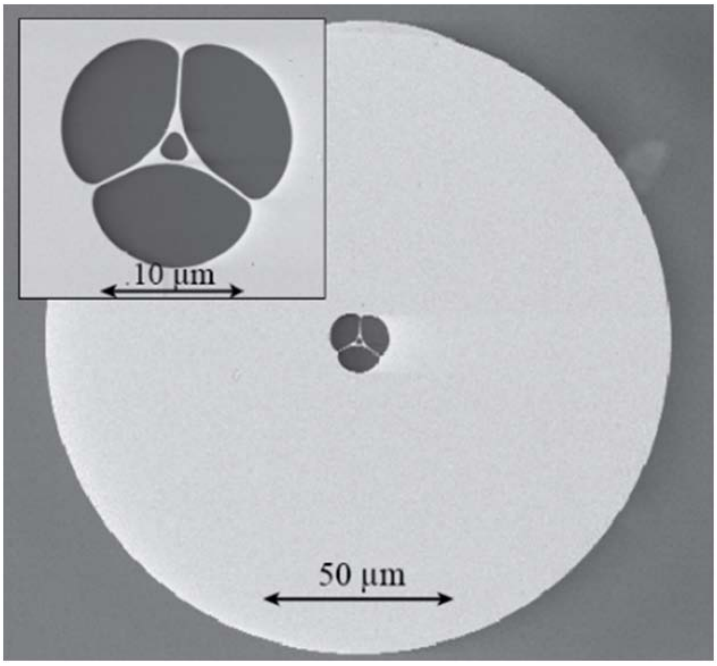

Figure 212: SEM image of fourth triple-core wagon-wheel fibre trial.

in the surface quality has been shown in the past to result in fibres that are both lossy and fragile, so it was decided that there was no practical reason to proceed any further with the fabrication process of this preform.

A fourth fibre was fabricated using a cane from the second extrusion, which showed good transmission through all three cores, reasonable (~30 m) yield and no interface gaps as seen with earlier trials. A SEM image of this fibre is shown in Figure 212.

Unfortunately the successful fibre draw occurred simultaneously with new fluorescent compounds (see Section 7.6.7), and due to the uncertainty in regards to the stability of the compound these measurements took precedence over trials with the triple-core fibre. As a result only preliminary measurements were performed using this fibre, involving coupling sequentially in to each core as demonstrated for the first fibre and an attempt to measure the fluorescence capture into the secondary cores.

To measure the fluorescence capture the fluorescence was measured in the forward direction with the experimental configuration shown in Figure 30, as was used for the initial Qdots experiments. Here the only change was rather than having the OSA positioned at

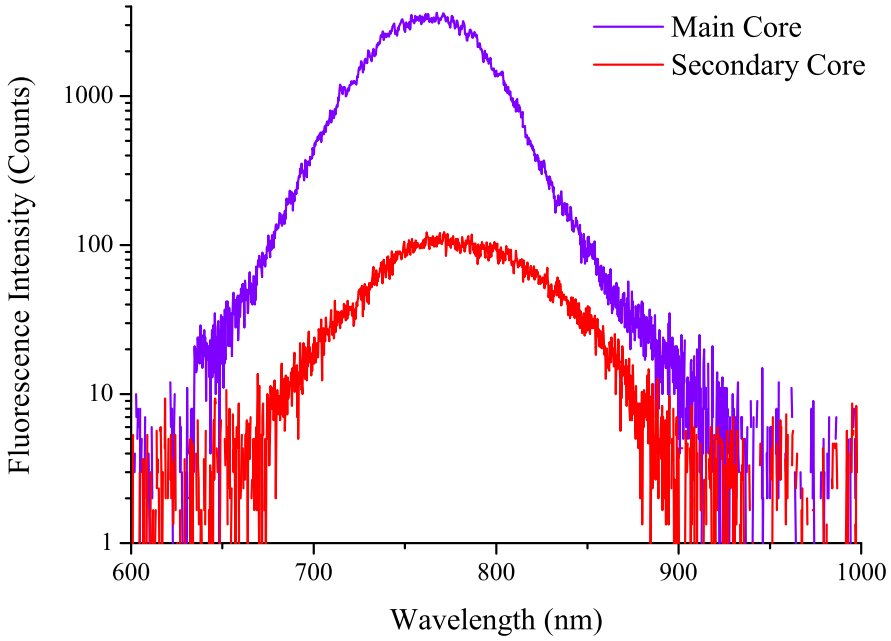

Figure 213: Observed fluorescence from excitation (Main) and collection (Secondary) cores in triple-core fibre.

the focus of the output light, instead a large diameter (200 µm) core multi-mode fibre connected to the monochromator was located for collection of the light. The collection fibre was located approximately 75 cm from the end of the end of the wagon-wheel fibre. A variable aperture was used to ensure that only the emission from the intended core was being observed. Once the position of the image of the core was optimised dichroic filters were added after the fibre output to reduce the excitation power such that damage to the CCD in the monochromator was prevented. The observed fluorescence light from both the excitation core (Main) and collection core (Secondary) is shown in Figure 213.

The power coupled into each of these cores when aligned into the main core was measured before filling at 3600 µW for the main core, 50 µW for the secondary. Due to experimenter's error the coupling into each of these cores after filling was not measured, as the fibre was broken when attempting to align into the third core.

With this fibre we have demonstrated preliminary results of fluorescence recapture using a multi-core fibre, however this result does not demonstrate whether this signal arises from capture using the launch and collection core scheme described above, or if it is simply due to a small amount of unavoidable coupling of laser light into the collection core which then excites fluorescence directly.

This fibre could also find interesting applications multiplexing sensing for different compounds within the same fibre. Even if the fluorescent labels had similar or identical emissions it should be possible to coat different holes with different fluorophores, thus making it pos-

sible to use the two collection cores for detection of different species. Initial concerns were raised that this would greatly complicate the coating process, as although it is possible [248, 249] to individually fill holes it is time consuming to ensure that the hole is completely blocked. However coating different fluorophores in each hole should only require modification to one step of the coating process; when the fluorophore itself is added (see Section 7.6.2). The remainder of the coating procedure is performed as per the usual technique, so this only results in one addition step as two separate fluorophores must be flushed through the fibre.

B

SENSORS PAPER

Sensors **2011**, *11*, 1-x manuscripts; doi:10.3390/s110x0000x

OPEN ACCESS

sensors

ISSN 1424-8220

www.mdpi.com/journal/sensors

Article

Driving down the Detection Limit in Microstructured Fiber-Based Chemical Dip Sensors

Erik P. Schartner *, Heike Ebendorff-Heidepriem, Stephen C. Warren-Smith, Richard T. White and Tanya M. Monro

Institute for Photonics & Advanced Sensing, School of Chemistry & Physics, University of Adelaide, Adelaide, SA 5005, Australia; E-Mails: heike.ebendorff@adelaide.edu.au (H.E.-H.); stephen.warrensmith@adelaide.edu.au (S.W.-S.); richard.white@adelaide.edu.au (R.T.W.); tanya.monro@adelaide.edu.au (T.M.M.)

* Author to whom correspondence should be addressed; E-Mail: erik.schartner@adelaide.edu.au.

Received: 25 November 2010; in revised form: 17 January 2011 / Accepted: 21 February 2011 / Published:

Abstract: We present improvements to fluorescence sensing in soft-glass microstructured optical fibers that result in significantly improved sensitivity relative to previously published results. Concentrations of CdSe quantum dots down to 10 pM levels have been demonstrated. We show that the primary limitation to the sensitivity of these systems is the intrinsic fluorescence of the glass itself.

Keywords: soft glass; dip sensing; microstructured optical fiber; quantum dots

1. Introduction

Optical fibers are ideal for environmental sensing applications because of their ability to transmit optical signals to and from the sensing region without the use of free-space optics. By accessing the evanescent field, the fiber itself can be the sensing element and long interaction lengths can be achieved [1]. Microstructured optical fibers (MOFs) are particularly suited to such applications as the air spaces inside the fiber form natural cavities for locating the material to be detected. These types of fibers have a significant advantage over conventional core-clad fibers, in that they can be fabricated from a single material, so issues involving thermal and chemical compatibility between different glasses can be avoided [2].

By tailoring both the MOF material and the geometry, the light-matter overlap can be increased to values much larger than with conventional fibers. Through varied structure geometries such as photonic band-gap fibers (PBGF) [3,4] or suspended nanowires [5-8], the overlap between the guided light and the analyte located within the holes of the fiber can be increased significantly over that which can be obtained using multi-mode bare fibers or D-shaped fibers [9]. However, due to the relatively limited bandwidth of most PBGFs [7], the excitation and emission wavelengths must be relatively close to enable detection with the fiber. Here we employ the suspended nanowire design [10] that provides the high evanescent overlap of a standard nanowire [11] with the large interaction length and robust handling comparable to conventional fibers.

The extremely small transverse structures that are possible in MOFs allow very small samples to be measured, with total volumes of less than 10 nL being easily obtainable with practical (~20 cm) lengths of fiber using the fiber shown in Section 3 below.

Through the use of fluorescent molecules that interact with target species these fibers can be applied to diverse applications including hydrogen peroxide detection [12] or aluminum detection [10]. The detection of biomolecules attached to fluorescent labels has recently been demonstrated in suspended-core MOFs [3,13], yielding a detection sensitivity down to 1 nM for antibodies labelled with quantum dots (Qdots).

The fluorescence-detection approach is attractive because of its simplicity. When one end of the fiber is dipped into the sample, capillary forces draw the liquid into the voids within the fiber. The evanescent field of the pump light excites the fluorescent labels and a portion of the fluorescence is captured by the fiber core and propagates to the fiber tips. Captured fluorescence can be detected at either end of the fiber, although backward detection provides the convenience of single-ended devices and an improved signal-to-pump ratio [14].

This can be done either for labelled biomolecules in solution [3,13], or, if specificity is required, by attaching recognition antibodies to the internal fiber surface [15,16]. In the later case, fluorescence is detected when antigens bind to their corresponding immobilized antibodies and non-bound antigens are flushed out of the fiber. In either case, efficient fluorescence-based MOF sensors require a large evanescent field in the fiber holes, such as in band-gap fibers, liquid-core fibers or suspended core fibers.

Suspended-core fibers are clearly a powerful platform both for chemical and biological sensing [10]. The aim of this work is determine the factors currently restricting the detection limit in this type of sensor and to improve this sensing architecture to increase the sensitivity of the dip sensor.

2. Glass Choices for Fluorescent Sensing Architectures

Various glasses were examined to test their suitability as a material for fabricating sensing fibers. The primary consideration here was the amount of fluorescence that was generated within the glass itself when light at the fluorophore's absorption wavelength is guided within the fiber, as this has been identified as the primary limitation to the sensitivity of this type of sensor. The glass choice was restricted to soft glasses that can currently be fabricated into optical fibers through extrusion at temperatures less than 650 °C [2], so that suspended-core fibers could be fabricated via use of extruded preforms.

To measure the glass background fluorescence spectra, a 25 mW 532 nm laser source was used to illuminate a range of bulk glass samples, and the fluorescence captured using a multi-mode fiber and recorded using an iHR 320 monochromator with the pump blocked with a long-pass filter. The results for various soft-glasses are shown in Figure 1 below. This fluorescence is believed to originate from trace metal impurities within the glass, although the exact origin of this fluorescence has not been studied in detail.

Figure 1. Bulk glass fluorescence measurements with 532 nm excitation.

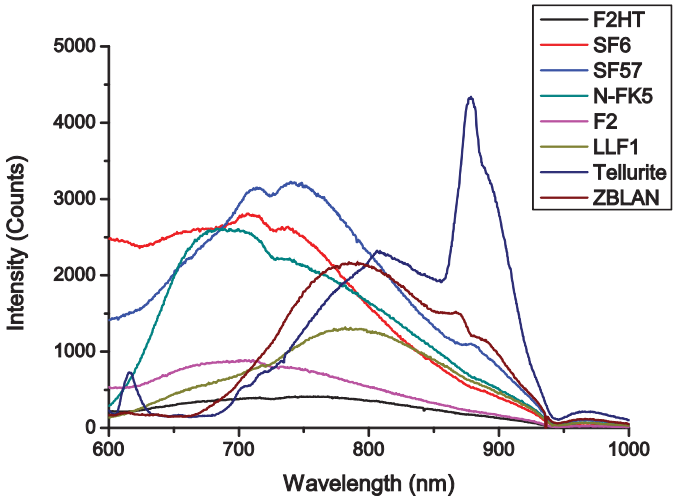

Of greatest interest to this work is the glass fluorescence background in the region of the Qdot 800 emission (as described below), which is between 700 and 900 nm, with a peak at 780 nm. These results suggest that the best two glasses are both commercial lead-silicate glasses from Schott; the F2 glass used in earlier [17] work, and the F2HT glass proposed for use here. A third candidate in LLF1, another Schott lead silicate which has also found extensive use in fabricating soft glass fibers and is considered in the modeling results shown in Section 7.

The bulk measurements suggest that since all other relevant material parameters are virtually identical between the two different glasses, changing glass from F2 to F2HT should result in almost a 50% reduction in the observed glass fluorescence.

3. Experimental Design

A commercially available CdSe quantum dot Qdot® 800 ITK™ from Invitrogen was selected for use in this research. Unlike conventional organic fluorophores, quantum dots are virtually immune to the effects of photobleaching, meaning that direct comparisons between samples can be readily made as the fluorescence signal does not decrease over time. Additionally, due to the optical characteristics of Qdots, it is possible to excite the molecules at a wavelength that is significantly shorter than their fluorescence emission wavelength (Δ~250 nm separation in this case: excitation at 532 nm, emission peak at 780 nm), which reduces the need to spectrally filter out residual pump light. Finally, they have a relatively high absorption coefficient (~4×10^6 M^{-1} cm^{-1} at 532 nm) compared to other organic

flurophores such as Rhodamine B which has an absorption coefficient of 8.2×10^4 at 532 nm. The Qdots in this case were unconjugated, and suspended in decane (CH_3-$(CH_2)_8$-CH_3). Note that conjugated Qdots could readily be used, and indeed protein detection down to 1 nM has previously been demonstrated in fiber using a similar system to that described here [13].

The fiber used for these experiments was an in-house fabricated suspended core MOF as shown in Figure 2, referred to hereafter as a wagon-wheel (WW) fiber. The fiber was fabricated via preform extrusion and subsequent fiber drawing performed using a cane-in-tube technique [17] to allow the production of a relatively small core within a robust fiber geometry (core diameter ~1.7 μm, outer diameter 130 μm). To the best of our knowledge this is the first MOF reported to have been fabricated from Schott F2HT glass [18], with the primary difference between this glass and the more commonly used F2 [14,19,20] being improved UV transmission [18] and a reduced intrinsic glass fluorescence, which was discussed in detail in Section 2. F2HT glass was used as the material for the central cane, with the outer tube being fabricated from standard F2 glass. As the thermal and chemical properties of the two glasses are virtually identical, no issues were seen to arise from this. The fabricated fiber had a loss of 0.9 dB/m at 532 nm.

Figure 2. Scanning Electron Microscope (SEM) image of the soft glass MOF used for these experiments. The central, structured region of the fiber was made from F2HT glass, and the cladding from F2 glass.

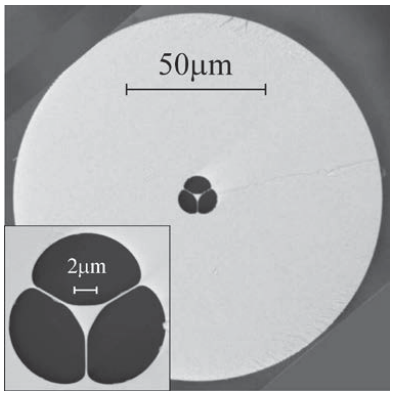

4. System Characterization

Initial characterization was performed on the MOF using two different samples: a 1 nM Qdot 800 solution in decane, and plain decane without added Qdots. The fibers were filled simply by dipping the tip in the solution and allowing capillary forces to draw the liquid within the holes along the fiber length. Before measurements were taken the fiber was removed from the solution, and its alignment optimized by monitoring the laser power from the distal end of the fiber using a power meter as shown in Figure 3. Due to the small size of the holes within the fiber (~4 μm) compared to the filled length (~ 19 cm) it was observed that the effects from evaporation of the solvent were negligible as minimal amounts were lost even over a period of several days.

Figure 3. Experimental configuration for fiber-based fluorescence measurements.

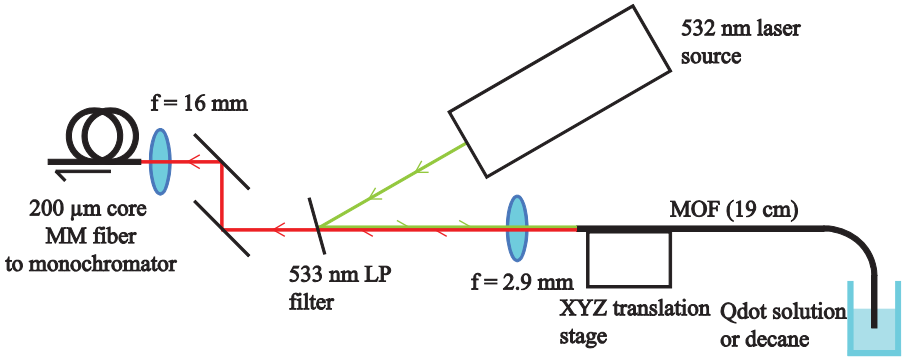

Results (as shown in Figure 4) were taken using a 25 mW 532 nm laser source, an iHR 320 monochromator and 533 nm long pass filter to remove any scattered or reflected pump light from the system. The filter was used as close to normal incidence as possible, and even when misaligned still demonstrated a greater than OD4 reduction for the pump light. The fiber was aligned by optimizing the output power. Minimizing the path length of the laser ensured that the alignment stability of the light coupled into the fiber was good, with a maximum power reduction of 10% being recorded over a period of one hour. Here we define the output power as the total pump power recorded from the distal end of the fiber. For reference the total coupling efficiency from the laser source to the core of the WW fiber is in the range 35–40%.

The aim of these experiments was to investigate and characterize the power dependence of both the background glass fluorescence and Qdot fluorescence to determine the optimal excitation power for the sensor.

Figure 4. Peak fluorescence counts at 780 nm of both a fiber filled with a solution of Qdots in Decane (black squares) and a F2HT-core WW fiber filled with plain decane (red triangles) without Qdots added. The fluorescence counts have been normalized to 1 at 8.95 mW output power.

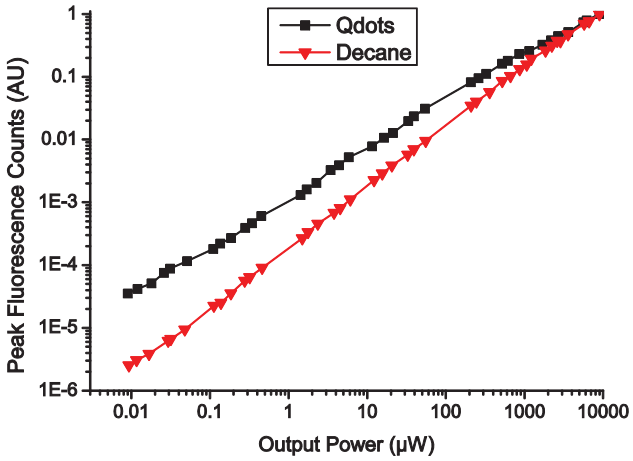

The results in Figure 4 show that while the background glass fluorescence, as shown by the red symbols in Figure 4, increases almost linearly with the output power of the fiber, as might be expected, the Qdot signal is not linear with the output power. Note the logarithmic scale of the axes in Figure 4. As can be seen from Figure 4, as the power within the fiber increases, the Qdot signal decreases relative to the background glass fluorescence. A similar effect is observed using laser excitation on a 1 nM Qdot sample in cuvette giving a result that agrees within the error margin of the experiments with the result shown above. As such, when the power launched in to the fiber increases, the net sensitivity of the sensor decreases.

Previously published results [13] employed an optical spectrum analyzer, whereas this paper uses a monochromator/CCD setup, resulting in a significant improvement in the signal to noise ratio. As a result, it is now possible to perform measurements with less than 30 nW of input power (*i.e.*, less than 10 nW output), whereas previous results required several milliwatts of input power to record any significant signal. This gives an immediate improvement to the Qdot fluorescence : glass fluorescence ratio of at least 5× which likewise corresponds to a 5× increase in the sensitivity of the system. Section 5 explores the improvements derived from these results.

5. Sensing Results

A spectrum was taken of the unfilled fiber to ensure consistency between results to eliminate any possible variations in the signal arising from cleave-related reductions in the coupling efficiency, and the fiber filled with Qdots (or decane for the background signal) for a range of different concentrations. The results of these measurements are shown in Figure 5.

Figure 5. In-fiber fluorescence measurements with varied Qdot concentrations. As per previous results, a fiber filled with a plain decane solution was used to give a background reference signal (in this case the fluorescence comes from the glass itself).

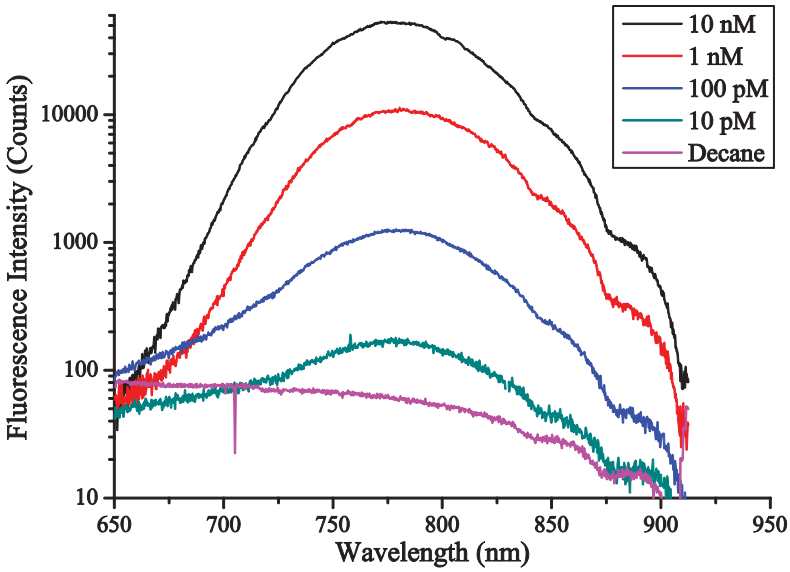

These results demonstrate that with a relatively high (compared to that shown in Figure 4) input power of 2.5 μW for all measurements, the minimum detectable Qdot signal using this configuration is 10 pM, which is a significant improvement over the 1 nM concentration previously reported in [13]. Given that the total volume of the fluid within the fiber used in this experiment is approximately 9 nL for the 19 cm fiber length, this implies that for the 10 pM minimum concentration demonstrated here there are in the order of 5×10^4 Qdots located within the fiber.

6. Theoretical Modelling

Previous work [13] demonstrated that the fundamental limitation to the sensitivity of fiber-based fluorescence sensors is the background fluorescence from the glass itself, which was discussed in detail in Section 2. To better understand the behaviour of these sensors, we chose to model the system using the analytic vectorial solutions of a simple step-index fiber, as opposed to a FEM model [21], making the reasonable assumption that the supporting struts within the WW fiber have a negligible impact on the field distributions and fluorescence recapture. We define the effective core size as the diameter of the circle with an area equivalent to the largest triangle that fits wholly within the core [17]. For the purposes of this modeling, the fiber loss was ignored, as since both the glass fluorescence and Qdot signal fluorescence are located in the same spectral region, they both experience a comparable reduction in signal under transmission. As such, the primary effect of loss on this system is a reduction in the measured signal to noise ratio.

We seek to gain an understanding of how the impact of the undesirable glass fluorescence on the sensor performance can be minimized. To do this, we define a figure of merit (FOM) for both the background glass fluorescence (FOM_{glass}) and for the Qdot signal fluorescence (FOM_{signal}) as a measure of the intensity of the fluorescence that is captured into the backward propagating modes of the fiber. These FOMs give a measure of the total amount of fluorescence photons that are initially emitted and then recaptured in to the modes of the fiber. The former is a result of the amount of incident laser power on the fluorophores, and the latter due to the efficiency that photons emitted by the fluorophore are recaptured.

For the Qdot fluorescence, FOM_{signal} is defined as the product of the power fraction (PF) of the fundamental mode at the excitation wavelength located within the holes of the fiber (PF_{clad}) [19] and the fluorescence capture fraction (FCF) of the emitted fluorescent light back in to all guided modes of the fiber [19].

Only the fundamental mode was considered for the excitation of the fluorescence, as through proper lens choice and careful alignment the laser light can be preferentially coupled into the fundamental mode of the fiber, even though the waveguide is capable of supporting higher order modes (HOMs) unless impractically small core sizes are considered.

For the fluorescence capture, it has been demonstrated that higher order modes must be included in the model, as the fluorescence capture into these modes has a significant impact on the total FCF, especially once the core size is increased well beyond the cut-off for single mode guidance [20]. Further supporting this, the experimentally measured mode images (Figure 6 below) show that while the excitation at 532 nm [Figure 6(a)) is well confined to the core and displays no obvious HOM content, the fluorescence emission around 780 nm [Figure 6(b)] clearly has substantial HOM content.

Figure 6. (a) Mode image of 532 nm excitation. Fiber filled with decane to ensure correct mode profile for comparison to fluorescence mode image. **(b)** Mode image of very high concentration (1 μM) Qdot 800 fluorescence mode excited with 532 nm source. Scales are directly comparable between (a) and (b).

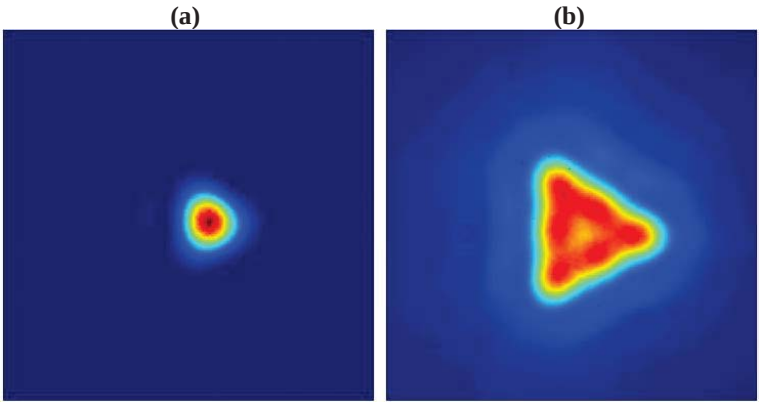

Similarly for the glass fluorescence, the same definitions and assumptions are made, with FOM_{signal} being defined as the product of the PF within the glass (*i.e.*, $1 - PF_{clad}$) and the FCF of the glass emitted light captured by all backward travelling modes of the waveguide.

These quantities can now be brought together to provide a better understanding of the overall performance of the sensor. This is done by defining a figure of merit, $FOM_{total} = FOM_{signal}/FOM_{glass}$. The primary constraint currently limiting the minimum detectable concentration of the sensor is the amount of Qdot signal fluorescence relative to the glass fluorescence. FOM_{total}, shown in Figure 7(d), is a direct measure of the relative magnitude of detected Qdot signal relative to the glass that is observed by the sensor.

As can be seen from Figure 7, reducing the core size fiber has a significant impact on FOM_{total} (regardless of the glass choice), and thus on the performance of the sensor, with improving performance predicted for the smallest core sizes. However, it is important to note that loss mechanisms were not included in this study. It has been previously shown [17] that the loss increases significantly due to scattering from surface roughness both in tapered nanowires and suspended nanowires once the core size becomes sufficiently small. Additionally, modes close to cutoff also experience significant confinement loss [20], resulting in both a reduction in signal at small core sizes where FOM_{total} is predicted to be largest using the simple model derived here, and a reduction in signal at each point where an additional mode is guided as modes close to cutoff are generally spread out and not well confined.

The final parameter examined within this theoretical study was the effect of the index contrast between the glass and the cladding (Figure 7). Three glasses were examined: F2, LLF1 and Tellurite. The first two are commercially available lead silicates, with the third an in-house fabricated glass, with refractive indices at 532 nm of 1.63, 1.55 and 2.02 respectively. The refractive index used for the decane within the holes was 1.41, giving Δn values of 0.22, 0.14 and 0.61 respectively.

Figure 7. (a) Power fraction at the excitation wavelength located within the cladding or core for various glasses, decane filled. **(b)** Figure of Merit (FOM) for fluorescent photons excited within the core of the fiber, this represents the intrinsic glass fluorescence. **(c)** FOM for fluorescent photons excited within the holes—this represents the Qdot fluorescence **(d)** Total FOM for the sensing system, with a higher value corresponding to a higher Qdot signal fluorescence relative to the background glass fluorescence.

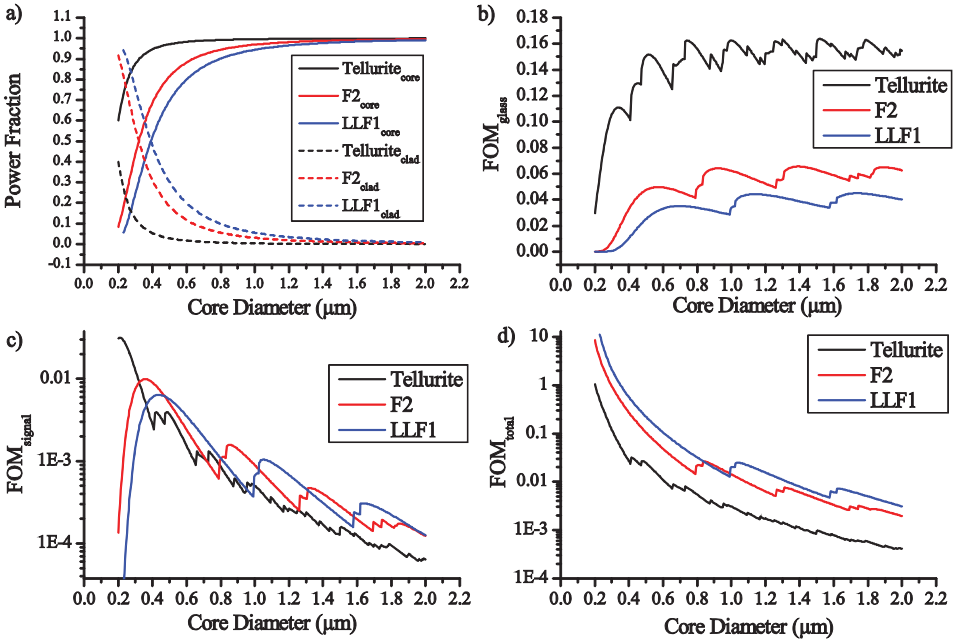

As shown from the plots in Figure 7 reducing the index contrast results in an increase in FOM_{total} which corresponds to an increase in the amount of Qdot signal fluorescence observed relative to the background glass levels. However when the intensity of the glass fluorescence for each of the three glasses (as shown in Figure 1) is considered the F2 or F2HT glasses will in practice show the lowest background glass signals and therefore the best sensitivity. This is a consequence of the F2HT fluorescence intensity being 3.3× lower than LLF1 at 780 nm, and 4.6× lower than the Tellurite fluorescence at the same wavelength. So even though the overall capture of the fluorescence photons is reduced for the LLF1 glass, since the efficiency with which they are generated within the glass is significantly higher the net result in fiber is a higher glass fluorescence signal. This is further exacerbated by using a higher index glass such as Tellurite, as more fluorescence is generated in the first place and since FOM_{total} is significantly lower with the higher index glass this results in a very large glass fluorescence signal relative to the Qdot signal.

These results demonstrate that a reduction in the index contrast results in a decrease in FOM_{glass}, and depending on the core size can also show an increase in FOM_{signal} leading to an overall increase in FOM_{total}.

7. Conclusion

We have demonstrated significant improvements in the sensitivity of fiber based fluorescence sensors, resulting in a large decrease in the minimum detectable concentration to 10 pM from the previously published result of 1 nM. This has been enabled through improvements to the experimental configuration and the use of low-fluorescence glass for the fiber fabrication, although we have demonstrated theoretically that this could be improved further by modifications to the fiber structure.

Although improvements in FOM_{total} can be obtained by reducing the core size, this also has the effect of making the experiment highly dependent on the coupling alignment, making reproducible results more difficult to come by as well as increased loss arising from surface roughness as mentioned earlier. Additionally, since the next phase of this work will involve splicing to conventional Silica SMF for easier integration and field deployability using extremely small core (*i.e.*, single mode at the fluorescence wavelength) results in a significantly reduced coupling efficiency between the silica fiber and the WW fiber.

By building on the improvements discussed within this paper, it should be possible to further reduce the lowest detectable concentration using MOF sensors of this type significantly beyond the results that have been demonstrated here. If a relatively low loss fiber with a smaller core size than used above were fabricated, the amount of observed glass fluorescence would drop significantly, enabling a further reduction in the detectable concentration to be observed. At present with a 10 pM concentration approximately 5×10^4 Qdots are filled within the holes, and we anticipate that reducing the core size well below a micron would enable a drop in concentration to at least 1 pM with as few as 500 total Qdots within the fiber.

Notes added in proof

Page 4 line 6 – added reference to figure 2

Page 4 line 25 – added reference to figure 3

Acknowledgements

We acknowledge Schott Glass Co. for the supply of F2HT glass. The authors acknowledge the support of DSTO for research within the Centre of Expertise in Photonics. T. M. Monro acknowledges the support of an ARC Federation Fellowship, and the support of ARC Discovery, Linkage and LIEF grants.

References

1. Monro, T.; Belardi, W.; Furusawa, K.; Baggett, J.; Broderick, N.; Richardson, D. Sensing with microstructured optical fibres. *Meas. Sci. Technol.* **2001**, *12*, 854.
2. Ebendorff-Heidepriem, H.; Monro, T. Extrusion of complex preforms for microstructured optical fibers. *Mater. Res.* **2006**, *36*, 467-495.
3. Jensen, J.; Pedersen, L.; Hoiby, P.; Nielsen, L.; Hansen, T.; Folkenberg, J.; Riishede, J.; Noordegraaf, D.; Nielsen, K.; Carlsen, A., Photonic crystal fiber based evanescent-wave sensor for detection of biomolecules in aqueous solutions. *Opt. Lett.* **2004**, *29*, 1974-1976.
4. Smolka, S.; Barth, M.; Benson, O., Highly efficient fluorescence sensing with hollow core photonic crystal fibers. *Opt. Express* **2007**, *15*, 12783-12791.

5. Monro, T.; Richardson, D.; Bennett, P. Developing holey fibres for evanescent field devices. *Electron. Lett.* **2002**, *35*, 1188-1189.
6. Webb, A.; Poletti, F.; Richardson, D.; Sahu, J. Suspended-core holey fiber for evanescent-field sensing. *Opt. Eng.* **2007**, *46*, 010503.
7. Ritari, T.; Tuominen, J.; Ludvigsen, H.; Petersen, J.; Sørensen, T.; Hansen, T.; Simonsen, H., Gas sensing using air-guiding photonic bandgap fibers. *Opt. Express* **2004**, *12*, 4080-4087.
8. Cordeiro, C.; Franco, M.; Chesini, G.; Barretto, E.; Lwin, R.; Brito Cruz, C.; Large, M. Microstructured-core optical fibre for evanescent sensing applications. *Opt. Express* **2006**, *14*, 13056-13066.
9. Henry, W. Evanescent field devices: a comparison between tapered optical fibres and polished or D-fibres. *Opt. Quant. Electron.* **1994**, *26*, 261-272.
10. Monro, T.; Warren-Smith, S.; Schartner, E.; Francois, A.; Heng, S.; Ebendorff-Heidepriem, H.; Afshar V, S. Sensing with suspended-core optical fibers. *Opt. Fiber Technol.* **2010**, *16*, 343-356.
11. Lou, J.; Tong, L.; Ye, Z. Modeling of silica nanowires for optical sensing. *Nanotechnology* **2003**, *14*, 907-912.
12. Schartner, E.; Pietsch, M.; Abell, A.; Monro, T. A Hydrogen Peroxide Fibre Optic Dip Sensor for Aqueous Solutions. In *Proceedings of ACOLS ACOFT 09 Conference*, Adelaide, SA, Australia, 29 November–3 December 2009.
13. Ruan, Y.; Schartner, E.; Ebendorff-Heidepriem, H.; Hoffmann, P.; Monro, T. Detection of quantum-dot labelled proteins using soft glass microstructured optical fibers. *Opt. Express* **2007**, *15*, 17819-17826.
14. Afshar, S.; Ruan, Y.; Warren-Smith, S.; Monro, T. Enhanced fluorescence sensing using microstructured optical fibers: a comparison of forward and backward collection modes. *Opt. Lett* **2008**, *33*, 1473-1475.
15. Ruan, Y.; Foo, T.; Warren-Smith, S.; Hoffmann, P.; Moore, R.; Ebendorff-Heidepriem, H.; Monro, T. Antibody immobilization within glass microstructured fibers: a route to sensitive and selective biosensors. *Opt. Express* **2008**, *16*, 18514-18523.
16. Jensen, J.; Hoiby, P.; Emiliyanov, G.; Bang, O.; Pedersen, L.; Bjarklev, A. Selective detection of antibodies in microstructured polymer optical fibers. *Opt. Express* **2005**, *13*, 5883-5889.
17. Ebendorff-Heidepriem, H.; Warren-Smith, S.; Monro, T. Suspended nanowires: fabrication, design and characterization of fibers with nanoscale cores. *Opt. Express* **2009**, *17*, 2646-2657.
18. Schott F2HT Datasheet. Available online: http://www.schott.com/advanced_optics/us/abbe_datasheets/schott_datasheet_f2.pdf (accessed on 1 June 2010).
19. Afshar, S.; Warren-Smith, S.C.; Monro, T.M. Enhancement of fluorescence-based sensing using microstructured optical fibres. *Optics Express* **2007**, *15*, 17891-17901.
20. Warren-Smith, S.; Afshar, S.; Monro, T. Fluorescence-based sensing with optical nanowires: a generalized model and experimental validation. *Opt. Express* **2010**, *18*, 9474-9485.
21. Mescia, L.; Prudenzano, F.; Allegretti, L.; Calò, G.; De Sario, M.; D'Orazio, A.; Maiorano, L.; Palmisano, T.; Petruzzelli, V. Design of silica-based photonic crystal fiber for biosensing applications *J. Non-Cryst. Solids* **2009**, *355*, 1163-1166.

BIBLIOGRAPHY

[1] Schott. Optical glass catalogue may 2011. Retrieved 6-2011. http://www.schott.com/advanced_optics/english/our_products/materials/data_tools/index.html.

[2] G. Keiser. Optical fiber communications. *Encyclopedia of Telecommunications*, 2000.

[3] B. Culshaw. Optical fiber sensor technologies: opportunities and-perhaps-pitfalls. *Journal of lightwave technology*, 22(1):39, 2004.

[4] T.M. Monro, W. Belardi, K. Furusawa, J.C. Baggett, NGR Broderick, and D.J. Richardson. Sensing with microstructured optical fibres. *Measurement Science and Technology*, 12:854, 2001.

[5] J.M. Lopez-Higuera. *Handbook of optical fibre sensing technology*. John Wiley & Sons Inc, 2002.

[6] A.W. Snyder and J.D. Love. *Optical waveguide theory*, volume 190. Springer, 1983.

[7] T. Ritari, J. Tuominen, H. Ludvigsen, J. Petersen, T. Sørensen, T. Hansen, and H. Simonsen. Gas sensing using air-guiding photonic bandgap fibers. *Optics Express*, 12(17):4080–4087, 2004.

[8] B. Culshaw, F. Muhammad, G. Stewart, S. Murray, D. Pinchbeck, J. Norris, S. Cassidy, M. Wilkinson, D. Williams, I. Crisp, et al. Evanescent wave methane detection using optical fibres. *Electronics Letters*, 28(24):2232–2234, 1992.

[9] B. Culshaw, G. Stewart, F. Dong, C. Tandy, and D. Moodie. Fibre optic techniques for remote spectroscopic methane detection–from concept to system realisation. *Sensors and actuators B: chemical*, 51(1-3):25–37, 1998.

[10] G. Stewart, W. Jin, and B. Culshaw. Prospects for fibre-optic evanescent-field gas sensors using absorption in the near-infrared. *Sensors and Actuators B-Chemical*, 38(1-3):42–47, Jan-Feb 1997.

[11] Z. Hale and F. Payne. Demonstration of an optimised evanescent field optical fibre sensor. *Analytica Chimica Acta*, 293:49–54, 1993.

[12] V. Afshar et al. Enhanced fluorescence sensing using microstructured optical fibers: a comparison of forward and backward collection modes. *Optics letters*, 33(13):1473–1475, 2008.

[13] J.B. Jensen, L.H. Pedersen, P.E. Hoiby, L.B. Nielsen, T.P. Hansen, J.R. Folkenberg, J. Riishede, D. Noordegraaf, K. Nielsen, A. Carlsen, et al. Photonic crystal fiber based evanescent-wave sensor for detection of biomolecules in aqueous solutions. *Optics Letters*, 29(17):1974–1976, 2004.

[14] J. Jensen, P. Hoiby, G. Emiliyanov, O. Bang, L. Pedersen, and A. Bjarklev. Selective detection of antibodies in microstructured polymer optical fibers. *Optics Express*, 13(15):5883–5889, 2005.

[15] P. H. Paul and G. Kychakoff. Fiberoptic evanescent field absorption sensor. *Applied Physics Letters*, 51(1):12–14, Jul 6 1987.

[16] BD Gupta and DK Sharma. Evanescent wave absorption based fiber optic ph sensor prepared by dye doped sol-gel immobilization technique. *Optics communications*, 140(1-3):32–35, 1997.

[17] M. D. Degrandpre and L. W. Burgess. Long path fiber-optic sensor for evanescent field absorbance measurements. *Analytical Chemistry*, 60(23):2582–2586, Dec 1 1988.

[18] P. V. Preejith, C. S. Lim, A. Kishen, M. S. John, and A. Asundi. Total protein measurement using a fiber-optic evanescent wave-based biosensor. *Biotechnology Letters*, 25(2):105–110, Jan 2003.

[19] E. Scorsone, S. Christie, K. C. Persaud, and F. Kvasnik. Evanescent sensing of alkaline and acidic vapours using a plastic clad silica fibre doped with poly(o-methoxyaniline). *Sensors and Actuators B-Chemical*, 97(2-3):174–181, Feb 1 2004.

[20] W. Q. Cao and Y. X. Duan. Optical fiber evanescent wave sensor for oxygen deficiency detection. *Sensors and Actuators B-Chemical*, 119(2):363–369, Dec 7 2006.

[21] B. D. Gupta and N. K. Sharma. Fabrication and characterization of u-shaped fiber-optic ph probes. *Sensors and Actuators B-Chemical*, 82(1):89–93, Feb 1 2002.

[22] S. K. Khijwania and B. D. Gupta. Fiber optic evanescent field absorption sensor with high sensitivity and linear dynamic range. *Optics Communications*, 152(4-6):259–262, Jul 1 1998.

[23] P. K. Choudhury and T. Yoshino. On the ph response of fiber optic evanescent field absorption sensor having a u-shaped probe: An experimental analysis. *Optik*, 114(1):13–18, 2003.

[24] H. Golnabi, M. Bahar, M. Razani, M. Abrishami, and A. Asadpour. Design and operation of an evanescent optical fiber sensor. *Optics and Lasers in Engineering*, 45(1):12–18, Jan 2007.

[25] G. Brambilla, F. Xu, P. Horak, Y. Jung, F. Koizumi, N.P. Sessions, E. Koukharenko, X. Feng, G.S. Murugan, J.S. Wilkinson, et al. Optical fiber nanowires and microwires: fabrication and applications. *Advances in Optics and Photonics*, 1(1):107–161, 2009.

[26] L. M. Tong, R. R. Gattass, J. B. Ashcom, S. L. He, J. Y. Lou, M. Y. Shen, I. Maxwell, and E. Mazur. Subwavelength-diameter silica wires for low-loss optical wave guiding. *Nature*, 426(6968):816–819, Dec 18 2003.

[27] W. Henry. Evanescent field devices: a comparison between tapered optical fibres and polished or d-fibres. *Optical and quantum electronics*, 26(3):261–272, 1994.

[28] F. Warken, E. Vetsch, D. Meschede, M. Sokolowski, and A. Rauschenbeutel. Ultra-sensitive surface absorption spectroscopy using sub-wavelength diameter optical fibers. *Optics Express*, 15(19):11952–11958, Sep 17 2007.

[29] L. Tong, L. Hu, J. Zhang, J. Qiu, Q. Yang, J. Lou, Y. Shen, J. He, and Z. Ye. Photonic nanowires directly drawn from bulk glasses. *Optics Express*, 14(1):82–87, 2006.

[30] P. Russell. Photonic crystal fibers. *Science*, 299(5605):358, 2003.

[31] JC Knight, TA Birks, P.S.J. Russell, and DM Atkin. All-silica single-mode optical fiber with photonic crystal cladding. *Optics Letters*, 21(19):1547–1549, 1996.

[32] P. Yeh, A. Yariv, and E. Marom. Theory of bragg fiber. *JOSA*, 68(9):1196–1201, 1978.

[33] RF Cregan, BJ Mangan, JC Knight, TA Birks, P.S.J. Russell, PJ Roberts, and DC Allan. Single-mode photonic band gap guidance of light in air. *Science*, 285(5433):1537, 1999.

[34] D.J. Richardson, F. Poletti, JJY Leong, X. Feng, H.E. Heidepreim, HV Finazzi, K.E. Frampton, S. Asimakis, R.C. Moore, J.C. Baggett, et al. Advances in microstructured fiber technology. In *Fibres and Optical Passive Components, 2005. Proceedings of 2005 IEEE/LEOS Workshop on*, pages 1–9. IEEE.

[35] JC Knight, TA Birks, RF Cregan, P.S.J. Russell, and J.P. De Sandro. Photonic crystals as optical fibres-physics and applications. *Optical materials*, 11(2-3):143–151, 1999.

[36] A. M. Cubillas, M. Silva-Lopez, J. M. Lazaro, O. M. Conde, M. N. Petrovich, and J. M. Lopez-Higuera. Methane detection at 1670-nm band using a hollow-core photonic bandgap fiber and a multiline algorithm. *Optics Express*, 15(26):17570–17576, Dec 24 2007.

[37] A. M. Cubillas, J. M. Lazaro, M. Silva-Lopez, O. M. Conde, M. N. Petrovich, and J. M. Lopez-Higuera. Methane sensing at 1300 nm band with hollow-core photonic bandgap fibre as gas cell. *Electronics Letters*, 44(6):403–405, Mar 13 2008.

[38] F. Brechet, P. Roy, J. Marcou, and D. Pagnoux. Single-mode propagation into depressed-core-index photonic-bandgap fibre designed for zero-dispersion propagation at short wavelengths. *Electronics Letters*, 36(6):514–515, 2000.

[39] Y.L. Hoo, W. Jin, C. Shi, H.L. Ho, D.N. Wang, and S.C. Ruan. Design and modeling of a photonic crystal fiber gas sensor. *Applied Optics*, 42(18):3509–3515, 2003.

[40] YL Hoo, W. Jin, H.L. Ho, DN Wang, and R.S. Windeler. Evanescent-wave gas sensing using microstructure fiber. *Optical Engineering*, 41:8, 2002.

[41] Y. Ruan, T.C. Foo, S. Warren-Smith, P. Hoffmann, R.C. Moore, H. Ebendorff-Heidepriem, and T.M. Monro. Antibody immobilization within glass microstructured fibers: a route to sensitive and selective biosensors. *Optics Express*, 16(22):18514–18523, 2008.

[42] S. Konorov, A. Zheltikov, and M. Scalora. Photonic-crystal fiber as a multifunctional optical sensor and sample collector. *Optics Express*, 13(9):3454–3459, 2005.

[43] X. Yu, Y. Sun, GB Ren, P. Shum, NQ Ngo, and YC Kwok. Evanescent field absorption sensor using a pure-silica defected-core photonic crystal fiber. *Photonics Technology Letters, IEEE*, 20(5):336–338, 2008.

[44] C. Cordeiro, C.J.S. de Matos, E.M. dos Santos, A. Bozolan, J.S.K. Ong, T. Facincani, G. Chesini, A.R. Vaz, and C.H. Brito Cruz. Towards practical liquid and gas sensing with photonic crystal fibres: side access to the fibre microstructure and single-mode liquid-core fibre. *Measurement Science and Technology*, 18:3075, 2007.

[45] H. Lehmann, S. Bruckner, J. Kobelke, G. Schwotzer, K. Schuster, and R. Willsch. Toward photonic crystal fiber based distributed chemosensors. *Proc. SPIEE*, 5855:419–422, 2005.

[46] Y. Lai, K. Zhou, L. Zhang, and I. Bennion. Microchannels in conventional single-mode fibers. *Optics Letters*, 31(17):2559–2561, Sep 1 2006.

[47] C. Martelli, P. Olivero, J. Canning, N. Groothoff, B. Gibson, and S. Huntington. Micromachining structured optical fibers using

focused ion beam milling. *Optics Letters*, 32(11):1575–1577, Jun 1 2007.

[48] F.M. Cox, R. Lwin, M.C.J. Large, and C. Cordeiro. Opening up optical fibres. *Optics Express*, 15(19):11843–11848, 2007.

[49] S.C. Warren-Smith, E. Sinchenko, P.R. Stoddart, and T.M. Monro. Distributed fluorescence sensing using exposed core microstructured optical fiber. *Photonics Technology Letters, IEEE*, 22(18):1385–1387, 2010.

[50] Y. K. Lize, E. C. Magi, V. G. Ta'eed, J. A. Bolger, P. Steinvurzel, and B. J. Eggleton. Microstructured optical fiber photonic wires with subwavelength core diameter. *Optics Express*, 12(14):3209–3217, Jul 12 2004.

[51] E. C. Magi, H. C. Nguyen, and B. J. Eggleton. Air-hole collapse and mode transitions in microstructured fiber photonic wires. *Optics Express*, 13(2):453–459, Jan 24 2005.

[52] V. P. Minkovich, D. Monzon-Hernandez, J. Villatoro, and G. Badenes. Microstructured optical fiber coated with thin films for gas and chemical sensing. *Optics Express*, 14(18):8413–8418, Sep 4 2006.

[53] T. M. Monro, D. J. Richardson, and P. J. Bennett. Developing holey fibres for evanescent field devices. *Electronics Letters*, 35(14):1188–1189, Jul 8 1999.

[54] T. M. Monro, W. Belardi, K. Furusawa, J. C. Baggett, N. G. R. Broderick, and D. J. Richardson. Sensing with microstructured optical fibres. *Measurement Science & Technology*, 12(7):854–858, Jul 2001.

[55] A.S. Webb, F. Poletti, D.J. Richardson, J.K. Sahu, et al. Suspended-core holey fiber for evanescent-field sensing. *Optical Engineering*, 46:010503, 2007.

[56] G. Emiliyanov, J. B. Jensen, O. Bang, P. E. Hoiby, L. H. Pedersen, E. M. Kjaer, and L. Lindvold. Localized biosensing with topas microstructured polymer optical fiber. *Optics Letters*, 32(5):460–462, Mar 1 2007.

[57] K. M. Kiang, K. Frampton, T. M. Monro, R. Moore, J. Tucknott, D. W. Hewak, D. J. Richardson, and H. N. Rutt. Extruded singlemode non-silica glass holey optical fibres. *Electronics Letters*, 38(12):546–547, 2002.

[58] X. A. Feng, T. M. Monro, P. Petropoulos, V. Finazzi, and D. J. Richardson. Extruded single-mode high-index-core one-dimensional microstructured optical fiber with high index-

contrast for highly nonlinear optical devices. *Applied Physics Letters*, 87(8):–, Aug 22 2005.

[59] Y. N. Zhu, H. Du, and R. Bise. Design of solid-core microstructured optical fiber with steering-wheel air cladding for optimal evanescent-field sensing. *Optics Express*, 14(8):3541–3546, Apr 17 2006.

[60] S. Afshar, S. C. Warren-Smith, and T. M. Monro. Enhancement of fluorescence-based sensing using microstructured optical fibres. *Optics Express*, 15(26):17891–17901, Dec 24 2007.

[61] Y. Ruan, E.P. Schartner, H. Ebendorff-Heidepriem, P. Hoffmann, and T.M. Monro. Detection of quantum-dot labelled proteins using soft glass microstructured optical fibers. *Optics Express*, 15(26):17819–17826, 2007.

[62] H. Ebendorff-Heidepriem and T.M. Monro. Extrusion of complex preforms for microstructured optical fibers. *Optics Express*, 15(23):15086–15092, 2007.

[63] M.H. Frosz, A. Stefani, and O. Bang. Highly sensitive and simple method for refractive index sensing of liquids in microstructured optical fibers using four-wave mixing. *Optics Express*, 19(11):10471–10484, 2011.

[64] G. Emiliyanov, J.B. Jensen, O. Bang, P.E. Hoiby, L.H. Pedersen, E.M. Kjær, and L. Lindvold. Localized biosensing with topas microstructured polymer optical fiber. In *Optical Fiber Sensors*. Optical Society of America, 2006.

[65] T. Izawa and S. Sudo. Optical fibers: materials and fabrication. *KTK Scientific Publishers, 1987,*, page 186, 1987.

[66] T. Miya, Y. Terunuma, T. Hosaka, and T. Miyashita. Ultimate low-loss single-mode fibre at 1.55 ã â¿ m. *Electronics Letters*, 15(4):106–108, 1979.

[67] JB MacChesney and KL Walker. An overview of the modified chemical vapor deposition(mcvd) process and performance. *IEEE Transactions on Microwave Theory and Techniques*, 82(4):305–322, 1982.

[68] KL Walker, FT Geyling, and SR Nagel. Thermophoretic deposition of small particles in the modified chemical vapor deposition (mcvd) process. *Journal of the American Ceramic Society*, 63(9-10):552–558, 1980.

[69] J.C. Knight. Photonic crystal fibres. *Nature*, 424(6950):847–851, 2003.

[70] TA Birks, JC Knight, and P.S.J. Russell. Endlessly single-mode photonic crystal fiber. *Optics Letters*, 22(13):961–963, 1997.

[71] K. Mukasa, M.N. Petrovich, F. Poletti, A. Webb, J.R. Hayes, A. van Brakel, R. Amezcua Correa, L. Provost, J. Sahu, P. Petropoulos, et al. Novel fabrication method of highly-nonlinear silica holey fibres. In *Conference on Lasers and Electro-Optics*. Optical Society of America, 2006.

[72] X. Feng, A.K. Mairaj, D.W. Hewak, and T.M. Monro. Non-silica glasses for holey fibers. *Lightwave Technology, Journal of*, 23(6):2046–2054, 2005.

[73] T.M. Monro and H. Ebendorff-Heidepriem. Progress in microstructured optical fibers. *Annu. Rev. Mater. Res.*, 36:467–495, 2006.

[74] JS Wang, EM Vogel, and E. Snitzer. Tellurite glass: a new candidate for fiber devices. *Optical Materials*, 3(3):187–203, 1994.

[75] M.R. Oermann, H. Ebendorff-Heidepriem, Y. Li, T.C. Foo, and T.M. Monro. Index matching between passive and active tellurite glasses for use in microstructured fiber lasers: Erbium doped lanthanum-tellurite glass. *Optics Express*, 17(18):15578–15584, 2009.

[76] H. Ebendorff-Heidepriem, T.C. Foo, R.C. Moore, W. Zhang, Y. Li, T.M. Monro, A. Hemming, and D.G. Lancaster. Fluoride glass microstructured optical fiber with large mode area and mid-infrared transmission. *Optics Letters*, 33(23):2861–2863, 2008.

[77] P. Lucas, M.R. Riley, C. Boussard-Plédel, and B. Bureau. Advances in chalcogenide fiber evanescent wave biochemical sensing. *Analytical biochemistry*, 351(1):1, 2006.

[78] J.S. Sanghera, L. Brandon Shaw, and I.D. Aggarwal. Chalcogenide glass-fiber-based mid-ir sources and applications. *Selected Topics in Quantum Electronics, IEEE Journal of*, 15(1):114–119, 2009.

[79] K.Y. Song, K.S. Abedin, K. Hotate, M. González Herráez, and L. Thévenaz. Highly efficient brillouin slow and fast light using as2 se3 chalcogenide fiber. *Optics Express*, 14(13):5860–5865, 2006.

[80] H. Ebendorff-Heidepriem and T. M. Monro. Progress in the fabrication of soft glass microstructured optical fibres with complex and new structures. In *Proc. Australian Conf. Optical Fibre Technology/Australian Optical Society ACOFT/AOS 2006*, pages 69–71, 2006.

[81] H. Ebendorff-Heidepriem, Y. Li, and T. M. Monro. Reduced loss in extruded soft glass microstructured fibre. *Electronics Letters*, 43(24):1343–1345, 2007.

[82] H. Ebendorff-Heidepriem and T. M. Monro. Soft glass microstructured optical fibres: Recent progress in fabrication and opportunities for novel optical devices. In *Proc. 11th Int. Conf. Transparent Optical Networks ICTON '09*, pages 1–4, 2009.

[83] M. Benounis, T. Aka-Ngnui, N. Jaffrezic, and J. P. Dutasta. Nir and optical fiber sensor for gases detection produced by transformation oil degradation. *Sensors and Actuators a-Physical*, 141(1):76–83, Jan 15 2008.

[84] J. Y. Y. Leong, S. Asimakis, F. Poletti, P. Petropoulos, X. Feng, R. C. Moore, K. E. Frampton, T. M. Monro, H. Ebendorff-Heidepriem, W. H. Loh, and D. J. Richardson. Towards zero dispersion highly nonlinear lead silicate glass holey fibres at 1550 nm by structured-element-stacking. In *Proc. 31st European Conf. Optical Communication ECOC 2005*, volume 6, pages 45–46, 2005.

[85] J. Y. Y. Leong, S. Asimakis, F. Poletti, P. Petropoulos, X. Feng, R. C. Moore, K. E. Frampton, T. M. Monro, H. Ebendorff-Heidepriem, W. H. Loh, and D. J. Richardson. Nonlinearity and dispersion control in small core lead silicate holey fibers by structured element stacking. In *Proc. and the 2006 National Fiber Optic Engineers Conf. Optical Fiber Communication Conf. OFC 2006*, 2006.

[86] F. Prudenzano, L. Mescia, L. Allegretti, V. Moizan, V. Nazabal, and F. Smektala. Theoretical study of cascade laser in erbium-doped chalcogenide glass fibers. *Optical Materials*, 2010.

[87] J. Heo, M. Rodrigues, S.J. Saggese, and G.H. Sigel Jr. Remote fiber-optic chemical sensing using evanescent–wave interactions in chalcogenide glass fibers. *Applied optics*, 30(27):3944–3951, 1991.

[88] H. Ebendorff-Heidepriem, P. Petropoulos, S. Asimakis, V. Finazzi, R. Moore, K. Frampton, F. Koizumi, D. Richardson, and T. Monro. Bismuth glass holey fibers with high nonlinearity. *Optics Express*, 12(21):5082–5087, 2004.

[89] J.A. Buck. *Fundamentals of optical fibers*. Wiley-IEEE, 2004.

[90] M. Liao, C. Chaudhari, G. Qin, X. Yan, C. Kito, T. Suzuki, Y. Ohishi, M. Matsumoto, and T. Misumi. Fabrication and characterization of a chalcogenide-tellurite composite microstructure fiber with high nonlinearity. *Optics Express*, 17(24):21608–21614, 2009.

[91] FG Omenetto, NA Wolchover, MR Wehner, M. Ross, A. Efimov, AJ Taylor, V.V.R.K. Kumar, AK George, JC Knight, NY Joly, et al. Spectrally smooth supercontinuum from 350 nm to 3 μm in sub-centimeter lengths of soft-glass photonic crystal fibers. *Optics Express*, 14(11):4928–4934, 2006.

[92] VV Kumar, A. George, W. Reeves, J. Knight, P. Russell, F. Omenetto, and A. Taylor. Extruded soft glass photonic crystal fiber for ultrabroad supercontinuum generation. *Optics Express*, 10(25):1520–1525, 2002.

[93] M. Liao, C. Chaudhari, G. Qin, X. Yan, T. Suzuki, and Y. Ohishi. Tellurite microstructure fibers with small hexagonal core for supercontinuum generation. *Optics Express*, 17(14):12174–12182, 2009.

[94] G. Barton, M.A. van Eijkelenborg, G. Henry, M.C.J. Large, and J. Zagari. Fabrication of microstructured polymer optical fibres. *Optical Fiber Technology*, 10(4):325–335, 2004.

[95] H. Ebendorff-Heidepriem, T. Monro, M. A. van Eijkelenborg, and M. J. C. Large. Extruded polymer preforms for high-na polymer microstructured fiber. In *Proc. and the 2006 National Fiber Optic Engineers Conf. Optical Fiber Communication Conf. OFC 2006*, 2006.

[96] M. van Eijkelenborg, M. Large, A. Argyros, J. Zagari, S. Manos, N. Issa, I. Bassett, S. Fleming, R. McPhedran, C.M. de Sterke, et al. Microstructured polymer optical fibre. *Optics express*, 9(7):319–327, 2001.

[97] E. Roeder. Extrusion of glass. *Journal of Non-Crystalline Solids*, 5(5):377–388, 1971.

[98] Heike Ebendorff-Heidepriem, Stephen C. Warren-Smith, and Tanya M. Monro. Suspended nanowires: fabrication, design and characterization of fibers with nanoscale cores. *Opt. Express*, 17(4):2646–2657, Feb 2009.

[99] A.B. Seddon, D. Furniss, and A. Motesharei. Extrusion method for making fiber optic preforms of special glasses. 3416:32, 1998.

[100] S.C. Warren-Smith, S. Heng, H. Ebendorff-Heidepriem, A.D. Abell, and T.M. Monro. Fluorescence-based aluminum ion sensing using a surface-functionalized microstructured optical fiber. *Langmuir*, 2011.

[101] T.M. Monro, S. Warren-Smith, E.P. Schartner, A. François, S. Heng, H. Ebendorff-Heidepriem, V. Afshar, et al. Sensing with suspended-core optical fibers. *Optical Fiber Technology*, 2010.

[102] A. Vahid, S. Warren-Smith, and T.M. Monro. Enhancement of fluorescence-based sensing using microstructured optical fibres. *Optics Express*, 15(26):17891–17901, 2007.

[103] S.C. Warren-Smith, S. Afshar, and T.M. Monro. Fluorescence-based sensing with optical nanowires: a generalized model and experimental validation. *Optics Express*, 18(9):9474–9485, 2010.

[104] Comsol multiphysics. Retrieved 8-2011. www.comsol.com.

[105] S. Atakaramians, V. Afshar, et al. Porous fibers: a novel approach to low loss thz waveguides. *Optics Express*, 16(12):8845–8854, 2008.

[106] S. Atakaramians, V. Afshar, et al. Thz porous fibers: design, fabrication and experimental characterization. *Optics Express*, 17(16):14053–15062, 2009.

[107] C. Cordeiro, M.A.R. Franco, G. Chesini, E. Barretto, R. Lwin, CH Brito Cruz, and M.C.J. Large. Microstructured-core optical fibre for evanescent sensing applications. *Optics Express*, 14(26):13056–13066, 2006.

[108] L. Rindorf, J.B. Jensen, M. Dufva, L.H. Pedersen, P.E. Høiby, and O. Bang. Photonic crystal fiber long-period gratings for biochemical sensing. *Optics Express*, 14(18):8224–8231, 2006.

[109] B.N.G. Giepmans, S.R. Adams, M.H. Ellisman, and R.Y. Tsien. The fluorescent toolbox for assessing protein location and function. *Science*, 312(5771):217, 2006.

[110] H. Mattoussi, J.M. Mauro, E.R. Goldman, G.P. Anderson, V.C. Sundar, F.V. Mikulec, and M.G. Bawendi. Self-assembly of cdse-zns quantum dot bioconjugates using an engineered recombinant protein. *Journal of the American Chemical Society*, 122(49):12142–12150, 2000.

[111] J.V. Frangioni. In vivo near-infrared fluorescence imaging. *Current opinion in chemical biology*, 7(5):626–634, 2003.

[112] L. Song, EJ Hennink, I.T. Young, and H.J. Tanke. Photobleaching kinetics of fluorescein in quantitative fluorescence microscopy. *Biophysical Journal*, 68(6):2588–2600, 1995.

[113] L. Song, CA Varma, JW Verhoeven, and H.J. Tanke. Influence of the triplet excited state on the photobleaching kinetics of fluorescein in microscopy. *Biophysical journal*, 70(6):2959–2968, 1996.

[114] H. Giloh and J.W. Sedat. Fluorescence microscopy: reduced photobleaching of rhodamine and fluorescein protein conjugates by n-propyl gallate. *Science*, 217(4566):1252, 1982.

[115] RI Ghauharali, JW Hofstraat, and GJ Brakenhoff. Fluorescence photobleaching-based shading correction for fluorescence microscopy. *Journal of Microscopy*, 192(2):99–113, 1998.

[116] H. Du, R.C.A. Fuh, J. Li, L.A. Corkan, and J.S. Lindsey. Photochemcad: A computer-aided design and research tool in photochemistry. *Photochemistry and Photobiology*, 68(2):141–142, 1998.

[117] L. Brus. Quantum crystallites and nonlinear optics. *Applied Physics A: Materials Science & Processing*, 53(6):465–474, 1991.

[118] Invitrogen. Retrieved 5-2011. www.invitrogen.com.

[119] MA Reed, JN Randall, RJ Aggarwal, RJ Matyi, TM Moore, and AE Wetsel. Observation of discrete electronic states in a zero-dimensional semiconductor nanostructure. *Physical review letters*, 60(6):535–537, 1988.

[120] W.C.W. Chan and S. Nie. Quantum dot bioconjugates for ultrasensitive nonisotopic detection. *Science*, 281(5385):2016, 1998.

[121] W.C.W. Chan, D.J. Maxwell, X. Gao, R.E. Bailey, M. Han, and S. Nie. Luminescent quantum dots for multiplexed biological detection and imaging. *Current Opinion in Biotechnology*, 13(1):40–46, 2002.

[122] D.R. Larson, W.R. Zipfel, R.M. Williams, S.W. Clark, M.P. Bruchez, F.W. Wise, and W.W. Webb. Water-soluble quantum dots for multiphoton fluorescence imaging in vivo. *Science*, 300(5624):1434, 2003.

[123] X. Wu, H. Liu, J. Liu, K.N. Haley, J.A. Treadway, J.P. Larson, N. Ge, F. Peale, and M.P. Bruchez. Immunofluorescent labeling of cancer marker her2 and other cellular targets with semiconductor quantum dots. *Nature biotechnology*, 21(1):41–46, 2002.

[124] J.K. Jaiswal, H. Mattoussi, J.M. Mauro, and S.M. Simon. Long-term multiple color imaging of live cells using quantum dot bioconjugates. *Nature biotechnology*, 21(1):47–51, 2002.

[125] X. Michalet, FF Pinaud, LA Bentolila, JM Tsay, S. Doose, JJ Li, G. Sundaresan, AM Wu, SS Gambhir, and S. Weiss. Quantum dots for live cells, in vivo imaging, and diagnostics. *Science*, 307(5709):538, 2005.

[126] H.X. Mai, Y.W. Zhang, R. Si, Z.G. Yan, L. Sun, L.P. You, and C.H. Yan. High-quality sodium rare-earth fluoride nanocrystals: controlled synthesis and optical properties. *Journal of the American Chemical Society*, 128(19):6426–6436, 2006.

[127] F. Meiser, C. Cortez, and F. Caruso. Biofunctionalization of fluorescent rare-earth-doped lanthanum phosphate colloidal nanoparticles. *Angewandte Chemie International Edition*, 43(44):5954–5957, 2004.

[128] I.I. Slowing, B.G. Trewyn, S. Giri, and V.S.Y. Lin. Mesoporous silica nanoparticles for drug delivery and biosensing applications. *Advanced Functional Materials*, 17(8):1225–1236, 2007.

[129] M. Wang, C.C. Mi, W.X. Wang, C.H. Liu, Y.F. Wu, Z.R. Xu, C.B. Mao, and S.K. Xu. Immunolabeling and nir-excited fluorescent imaging of hela cells by using nayf4: Yb, er upconversion nanoparticles. *ACS nano*, 3(6):1580–1586, 2009.

[130] F. Enrichi, E. Trave, and M. Bersani. Acid synthesis of luminescent amine-functionalized or erbium-doped silica spheres for biological applications. *Journal of Fluorescence*, 18(2):507–511, 2008.

[131] F. Enrichi. Luminescent amino-functionalized or erbium-doped silica spheres for biological applications. *Annals of the New York Academy of Sciences*, 1130(1):262–266, 2008.

[132] J.C. Boyer, F. Vetrone, L.A. Cuccia, and J.A. Capobianco. Synthesis of colloidal upconverting nayf4 nanocrystals doped with er3+, yb3+ and tm3+, yb3+ via thermal decomposition of lanthanide trifluoroacetate precursors. *Journal of the American Chemical Society*, 128(23):7444–7445, 2006.

[133] G. Yi, H. Lu, S. Zhao, Y. Ge, W. Yang, D. Chen, and L.H. Guo. Synthesis, characterization, and biological application of size-controlled nanocrystalline nayf4: Yb, er infrared-to-visible upconversion phosphors. *Nano Letters*, 4(11):2191–2196, 2004.

[134] S. Heer, K. Kompe, H.U. Gudel, and M. Haase. Highly efficient multicolour upconversion emission in transparent colloids of lanthanide-doped nayf4 nanocrystals. *Advanced Materials*, 16(23-24):2102–2105, 2004.

[135] F. Wang, D.K. Chatterjee, Z. Li, Y. Zhang, X. Fan, and M. Wang. Synthesis of polyethylenimine/nayf4 nanoparticles with upconversion fluorescence. *Nanotechnology*, 17:5786, 2006.

[136] Sigma-Aldrich. Retrieved 5-2011. www.sigmaaldrich.com.

[137] L.R. Fisher and P.D. Lark. An experimental study of the washburn equation for liquid flow in very fine capillaries. *Journal of Colloid and Interface Science*, 69(3):486–492, 1979.

[138] E.W. Washburn. The dynamics of capillary flow. *Physical Review*, 17(3):273, 1921.

[139] F.L. Pedrotti and L.S. Pedrotti. Introduction to optics 2nd edition. *Introduction to Optics 2nd Edition by Frank L. Pedrotti, SJ, Leno S. Pedrotti New Jersey: Prentice Hall, 1993*, 1, 1993.

[140] J.W. Fleming and D.L. Wood. Refractive index dispersion and related properties in fluorine doped silica. *Applied optics*, 22(19):3102–3104, 1983.

[141] Schott. Borofloat products and applications. Retrieved 5-2011. http://www.us.schott.com/borofloat/english/.

[142] V. Poncon, M. Bouderbala, A.M. Boulon, et al. Laser spectroscopy of chromium (iii) in gahnite crystals and transparent gahnite-type glass-ceramics. *Chemical physics letters*, 130(5):444–447, 1986.

[143] T.T. Basiev, P.G. Zverev, V.V. Fedorov, and S.B. Mirov. Multiline, superbroadband and sun-color oscillation of a lif: F2 color-center laser. *Applied optics*, 36(12):2515–2522, 1997.

[144] Schott. Fluorescence of optical glass. Retrieved 5-2011. http://www.schott.com/advanced_optics/english/download/tie-36_fluorescence_of_optical_glass.pdf.

[145] W. Geffcken. Mehrstoffsysteme zum aufbau optischer glaser. *Glastechn. Ber*, 34:91–101, 1961.

[146] J.W. Stouwdam and F.C.J.M. van Veggel. Near-infrared emission of redispersible er3+, nd3+, and ho3+ doped laf3 nanoparticles. *Nano letters*, 2(7):733–737, 2002.

[147] P.R. Selvin. Principles and biophysical applications of lanthanide-based probes. *Annual review of biophysics and biomolecular structure*, 31(1):275–302, 2002.

[148] R. Abdul Jalil and Y. Zhang. Biocompatibility of silica coated nayf4 upconversion fluorescent nanocrystals. *Biomaterials*, 29(30):4122–4128, 2008.

[149] M. Nyk, R. Kumar, T.Y. Ohulchanskyy, E.J. Bergey, and P.N. Prasad. High contrast in vitro and in vivo photoluminescence bioimaging using near infrared to near infrared up-conversion in tm3+ and yb3+ doped fluoride nanophosphors. *Nano letters*, 8(11):3834–3838, 2008.

[150] D.K. Chatterjee, A.J. Rufaihah, and Y. Zhang. Upconversion fluorescence imaging of cells and small animals using lanthanide doped nanocrystals. *Biomaterials*, 29(7):937–943, 2008.

[151] J. Yuan and G. Wang. Lanthanide-based luminescence probes and time-resolved luminescence bioassays. *TrAC Trends in Analytical Chemistry*, 25(5):490–500, 2006.

[152] X. Wang and Y. Li. Rare-earth-compound nanowires, nanotubes, and fullerene-like nanoparticles: Synthesis, characterization, and properties. *Chemistry–A European Journal*, 9(22):5627–5635, 2003.

[153] W. Wang, M. Wu, and GK Liu. Analysis of upconversion fluorescence dynamics in nayf4 codoped with er3+ and yb3+. *Spectroscopy Letters*, 40(2):259–269, 2007.

[154] Y. Wang, L. Tu, J. Zhao, Y. Sun, X. Kong, and H. Zhang. Upconversion luminescence of β-nayf4: Yb3+, er3+@ β-nayf4 core/shell nanoparticles: Excitation power density and surface dependence. *The Journal of Physical Chemistry C*, 113(17):7164–7169, 2009.

[155] S. Wu, G. Han, D.J. Milliron, S. Aloni, V. Altoe, D.V. Talapin, B.E. Cohen, and P.J. Schuck. Non-blinking and photostable upconverted luminescence from single lanthanide-doped nanocrystals. *Proceedings of the National Academy of Sciences*, 106(27):10917, 2009.

[156] H. Jiang, G. Wang, W. Zhang, X. Liu, Z. Ye, D. Jin, J. Yuan, and Z. Liu. Preparation and time-resolved luminescence bioassay application of multicolor luminescent lanthanide nanoparticles. *Journal of fluorescence*, 20(1):321–328, 2010.

[157] M. Xiao and P.R. Selvin. Quantum yields of luminescent lanthanide chelates and far-red dyes measured by resonance energy transfer. *Journal of the American Chemical Society*, 123(29):7067–7073, 2001.

[158] N. Hildebrandt, L. Charbonnière, R.F. Ziessel, and H.G. Löhmannsröben. Quantum dots as resonance energy transfer acceptors for monitoring biological interactions. In *Proceedings of SPIE*, volume 6191, page 61910W, 2006.

[159] N. Hildebrandt and H.G. Lohmannsroben. Quantum dot nanocrystals and supramolecular lanthanide complexes-energy transfer systems for sensitive in vitro diagnostics and high throughput screening in chemical biology. *Current Chemical Biology*, 1(2):167–186, 2007.

[160] A.D. Yablon. *Optical fiber fusion splicing*, volume 103. Springer Verlag, 2005.

[161] B. Bourliaguet, C. Paré, et al. Microstructured fiber splicing. *Optics express*, 11(25):3412–3417, 2003.

[162] F.V. Englich, E.P. Schartner, D.F. Murphy, H. Ebendorff-Heidepriem, and T.M. Monro. Fusion splicing soft-glass sus-

pended core fibers to solid silica fibers for optical fiber sensing. In *Australian Institute of Physics Congress (19th: 2010: Melbourne, Australia) Australian Conference on Optical Fibre Technology (35th: 2010: Melbourne, Australia) ACOFT/AIP 2010*. version: http://www. aip. org. au/Congress2010/Posters. htm, 2010.

[163] PJ Bennett, T.M. Monro, and DJ Richardson. Toward practical holey fiber technology: fabrication, splicing, modeling, and characterization. *Optics letters*, 24(17):1203–1205, 1999.

[164] X. Chen, F. Shen, Z. Wang, Z. Huang, and A. Wang. Micro-air-gap based intrinsic fabry-perot interferometric fiber-optic sensor. *Applied optics*, 45(30):7760–7766, 2006.

[165] H. Bach and N. Neuroth. *The properties of optical glass*. Springer Verlag, 1995.

[166] T. Yanagawa, H. Nakano, Y. Ishida, and K. Kubodera. Host glass dependence of photodarkening in colored filter glasses. *Optics communications*, 100(1-4):118–123, 1993.

[167] M. Engholm and L. Norin. Preventing photodarkening in ytterbium-doped high power fiber lasers; correlation to the uv-transparency of the core glass. *Optics Express*, 16(2):1260–1268, 2008.

[168] A. Chandonnet, P. Laperle, S. LaRochelle, and R. Vallée. Photodegradation of fluoride glass blue fiber laser. In *Proc. SPIE*, volume 2998, pages 70–81. Citeseer, 1997.

[169] Y. Ikeda and K. Shimakawa. In situ simultaneous measurements of photodarkening and photoinduced volume changes in chalcogenide glasses. *Journal of non-crystalline solids*, 352(9-20):1582–1586, 2006.

[170] K. Shimakawa, N. Nakagawa, and T. Itoh. The origin of stretched exponential function in dynamic response of photodarkening in amorphous chalcogenides. *Applied Physics Letters*, 95:051908, 2009.

[171] C.R. Schardt, J.H. Simmons, P. Lucas, L.L. Neindre, and J. Lucas. Photodarkening in ge3se17 glass. *Journal of non-crystalline solids*, 274(1-3):23–29, 2000.

[172] JF White and WB Silverman. Some studies on the solarization of glass. *Journal of the American Ceramic Society*, 33(8):252–257, 1950.

[173] H. Jia, G. Chen, Z. Hou, L. Liu, W. Wang, M. Affatigato, and S. Feller. Uv-visible absorption changes of lead silicate

glasses after uv laser irradiation. *Journal of non-crystalline solids*, 319(3):322–326, 2003.

[174] X.C. Long and SRJ Brueck. Composition dependence of the photoinduced refractive-index change in lead silicate glasses. *Optics letters*, 24(16):1136–1138, 1999.

[175] X.C. Long and SRJ Brueck. Large photosensitivity in lead–silicate glasses. *Applied physics letters*, 74:2110, 1999.

[176] Corning. Macor data sheet. Retrieved 5-2011. http://www.corning.com/docs/specialtymaterials/pisheets/Macor.pdf.

[177] Special metals corporation inconel technical datasheet. Retrieved 5-6-2011. www.specialmetals.com/documents/MSDS_Inconel.pdf.

[178] B.J. Todd. Outgassing of glass. *Journal of Applied Physics*, 26(10):1238–1243, 1955.

[179] MM Broer, DM Krol, and DJ DiGiovanni. Highly nonlinear near-resonant photodarkening in a thulium-doped aluminosilicate glass fiber. *Optics letters*, 18(10):799–801, 1993.

[180] R. M. Sutherland, C. Dahne, J. F. Place, and A. S. Ringrose. Optical-detection of antibody antigen reactions at a glass liquid interface. *Clinical Chemistry*, 30(9):1533–1538, 1984.

[181] S. Zabarnick. Chemical kinetic modeling of jet fuel autoxidation and antioxidant chemistry. *Industrial & Engineering Chemistry Research*, 32(6):1012–1017, Jun 1993.

[182] N. J. Kuprowicz, S. Zabarnick, Z. J. West, and J. S. Ervin. Use of measured species class concentrations with chemical kinetic modeling for the prediction of autoxidation and deposition of jet fuels. *Energy & Fuels*, 21(2):530–544, Mar-Apr 2007.

[183] Z. J. West, S. Zabarnick, and R. C. Striebich. Determination of hydroperoxides in jet fuel via reaction with triphenylphosphine. *Industrial & Engineering Chemistry Research*, 44(10):3377–3383, May 11 2005.

[184] L. M. Balster, S. Zabarnick, R. C. Striebich, L. M. Shafer, and Z. J. West. Analysis of polar species in jet fuel and determination of their role in autoxidative deposit formation. *Energy & Fuels*, 20(6):2564–2571, Nov 15 2006.

[185] G. Y. Tian, D. H. Xia, and F. T. Zhan. The oxidation of tetralin and its effect on the stability of fluidized catalytic cracked diesel. *Energy & Fuels*, 18(1):49–53, Jan-Feb 2004.

[186] B. Beaver, L. Gao, C. Burgess-Clifford, and M. Sobkowiak. On the mechanisms of formation of thermal oxidative deposits in jet fuels. are unified mechanisms possible for both storage and thermal oxidative deposit formation for middle distillate fuels? *Energy & Fuels*, 19(4):1574–1579, Jul-Aug 2005.

[187] S. Zabarnick and D. K. Phelps. Density functional theory calculations of the energetics and kinetics of set fuel autoxidation reaction. *Energy & Fuels*, 20(2):488–497, Mar-Apr 2006.

[188] S. Zabarnick and M. S. Mick. Inhibition of jet fuel oxidation by addition of hydroperoxide-decomposing species. *Industrial & Engineering Chemistry Research*, 38(9):3557–3563, Sep 1999.

[189] A. L. Perkel, L. V. Krutskaya, and B. G. Freidin. Application of triphenylphosphine to the gas-chromatographic determination of peroxides in the oxidation-products of organic-compounds. *Journal of Analytical Chemistry*, 49(7):693–697, Jul 1994.

[190] K. Akasaka, H. Ohrui, and H. Meguro. Normal-phase high-performance liquid-chromatography with a fluorometric post-column detection system for lipid hydroperoxides. *Journal of Chromatography*, 628(1):31–35, Jan 1 1993.

[191] Y. Okimoto, E. Warabi, Y. Wada, E. Niki, T. Kodama, and N. Noguchi. A novel method of following oxidation of low-density lipoprotein using a sensitive fluorescent probe, diphenyl-1-pyrenylphosphine. *Free Radical Biology and Medicine*, 35(6):576–585, Sep 15 2003.

[192] A. Kazuaki, S. Ijichi, K. Watanabe, H. Ohrui, and H. Meguro. High-performance liquid chromatography and post-column derivatization with diphenyl-1-pyrenylphosphine for fluorimetric determination of triacylglycerol hydroperoxides. *Journal of Chromatography A*, 596(2):197–202, 1992.

[193] Y. Okimoto, A. Watanabe, E. Niki, T. Yamashita, and N. Noguchi. A novel fluorescent probe diphenyl-1-pyrenylphosphine to follow lipid peroxidation in cell membranes. *Febs Letters*, 474(2-3):137–140, Jun 2 2000.

[194] C. Chotimarkorn, R. Nagasaka, H. Ushio, T. Ohshima, and S. Matsunaga. Development of novel fluorescent probe 3-perylene diphenylphosphine for determination of lipid hydroperoxide with fluorescent image analysis. *Biochemical and Biophysical Research Communications*, 338(2):1222–1228, Dec 16 2005.

[195] C. Chotimarkorn, T. Ohshima, and H. Ushio. Fluorescent image analysis of lipid hydroperoxides in fish muscle with 3-perylene diphenylphosphine. *Lipids*, 41(3):295–300, 2006.

[196] N. Soh, O. Sakawaki, K. Makihara, Y. Odo, T. Fukaminato, T. Kawai, M. Irie, and T. Imato. Design and development of a fluorescent probe for monitoring hydrogen peroxide using photoinduced electron transfer. *Bioorganic & Medicinal Chemistry*, 13(4):1131–1139, Feb 15 2005.

[197] N. Soh, T. Ariyoshi, T. Fukaminato, H. Nakajima, K. Nakano, and T. Imato. Swallow-tailed perylene derivative: a new tool for fluorescent imaging of lipid hydroperoxides. *Organic & Biomolecular Chemistry*, 5(23):3762–3768, 2007.

[198] M. Onoda, S. Uchiyama, A. Endo, H. Tokuyama, T. Santa, and K. Imai. First fluorescent photoinduced electron transfer (pet) reagent for hydroperoxides. *Organic Letters*, 5(9):1459–1461, 2003.

[199] A.P. de Silva, HQ Gunaratne, J.L. Habib-Jiwan, C.P. McCoy, T.E. Rice, and J.P. Soumillion. New fluorescent model compounds for the study of photoinduced electron transfer: the influence of a molecular electric field in the excited state. *Angewandte Chemie International Edition in English*, 34(16):1728–1731, 1995.

[200] Y. Yamamoto, M. H. Brodsky, J. C. Baker, and B. N. Ames. Detection and characterization of lipid hydroperoxides at picomole levels by high-performance liquid-chromatography. *Analytical Biochemistry*, 160(1):7–13, Jan 1987.

[201] S. Baj and T. Krawczyk. Chemiluminescence detection of organic peroxides in a two-phase system. *Analytica Chimica Acta*, 585(1):147–153, Feb 28 2007.

[202] C. A. Marquette and L. J. Blum. Applications of the luminol chemiluminescent reaction in analytical chemistry. *Analytical and Bioanalytical Chemistry*, 385(3):546–554, Jun 2006.

[203] G. Y. Tian, D. H. Xia, and F. T. Zhan. Formation of hydroperoxides and their effect on the stability of fcc diesel product. *Abstracts of Papers of the American Chemical Society*, 223:C13–C13, Apr 7 2002.

[204] D. Barnard and K. Wong. The determination of small amounts of organic hydroperoxides with triphenylphosphine. *Analytica Chimica Acta*, 84:355–361, 1976.

[205] IM Kolthoff and AI Medalia. Determination of organic peroxides by reaction with ferrous iron. *Analytical Chemistry*, 23(4):595–603, 1951.

[206] B. Mihaljevi, B. Katuin-Raem, and D. Raem. The reevaluation of the ferric thiocyanate assay for lipid hydroperoxides with spe-

cial considerations of the mechanistic aspects of the response. *Free Radical Biology and Medicine*, 21(1):53–63, 1996.

[207] M.P. Richards and Y. Feng. Choosing the proper organic solvent for the determination of lipid hydroperoxides by the ferric thiocyanate assay. *Analytical Biochemistry*, 278(2):232–234, 2000.

[208] R. Budwig. Refractive index matching methods for liquid flow investigations. *Experiments in fluids*, 17(5):350–355, 1994.

[209] A.P. de Silva, H.Q.N. Gunaratne, T. Gunnlaugsson, A.J.M. Huxley, C.P. McCoy, J.T. Rademacher, and T.E. Rice. Supramolecular photoionic devices: Photoinduced electron transfer (pet) systems with switchable luminescence output. *Advances in Supramolecular Chemistry*, 4:1, 1997.

[210] A. Prasanna de Silva, HQ Nimal Gunaratne, and T. Gunnlaugsson. Fluorescent pet (photoinduced electron transfer) reagents for thiols. *Tetrahedron Letters*, 39(28):5077–5080, 1998.

[211] A.P. de Silva, T. Gunnlaugsson, and T.E. Rice. Recent evolution of luminescent photoinduced electron transfer sensors. a review. *Analyst*, 121(12):1759–1762, 1996.

[212] A.P. De Silva, H.Q.N. Gunaratne, T. Gunnlaugsson, A.J.M. Huxley, C.P. McCoy, J.T. Rademacher, and T.E. Rice. Signaling recognition events with fluorescent sensors and switches. *Chemical reviews*, 97(5):1515–1566, 1997.

[213] F. Geiss and Commission of the European Communities. *Fundamentals of thin layer chromatography (planar chromatography)*. A. Huthig, 1987.

[214] P. Guerin, S. El Mouatassim, and Y. Menezo. Oxidative stress and protection against reactive oxygen species in the preimplantation embryo and its surroundings. *Human Reproduction Update*, 7(2):175, 2001.

[215] GH Thorpe, LJ Kricka, SB Moseley, and T.P. Whitehead. Phenols as enhancers of the chemiluminescent horseradish peroxidase-luminol-hydrogen peroxide reaction: application in luminescence-monitored enzyme immunoassays. *Clinical chemistry*, 31(8):1335, 1985.

[216] M.H. Johnson and M.H. Nasresfahani. Radical solutions and cultural problems: could free oxygen radicals be responsible for the impaired development of preimplantation mammalian embryos in vitro? *Bioessays*, 16(1):31–38, 1994.

[217] M. Zhou, Z. Diwu, N. Panchuk-Voloshina, and R.P. Haugland. A stable nonfluorescent derivative of resorufin for the fluorometric determination of trace hydrogen peroxide: Applications in detecting the activity of phagocyte nadph oxidase and other oxidases* 1. *Analytical biochemistry*, 253(2):162–168, 1997.

[218] JG Mohanty, J.S. Jaffe, E.S. Schulman, and D.G. Raible. A highly sensitive fluorescent micro-assay of h202 release from activated human leukocytes using a dihydroxyphenoxazine derivative. *Journal of immunological methods*, 202(2):133–141, 1997.

[219] G.H. Seong, J. Heo, and R.M. Crooks. Measurement of enzyme kinetics using a continuous-flow microfluidic system. *Analytical chemistry*, 75(13):3161–3167, 2003.

[220] A.L. Waterhouse. Wine phenolics. *Annals of the New York Academy of Sciences*, 957(1):21–36, 2002.

[221] A. Caputi Jr, M. Ueda, and T. Brown. Spectrophotometric determination of ethanol in wine. *American Journal of Enology and Viticulture*, 19(3):160, 1968.

[222] U. Fischer and A.C. Noble. The effect of ethanol, catechin concentration, and ph on sourness and bitterness of wine. *American journal of enology and viticulture*, 45(1):6, 1994.

[223] S.Y. Wang and H. Jiao. Scavenging capacity of berry crops on superoxide radicals, hydrogen peroxide, hydroxyl radicals, and singlet oxygen. *Journal of Agricultural and Food Chemistry*, 48(11):5677–5684, 2000.

[224] B.R. Behr, CJ Stratton, WD Foote, V. Knutzen, and G. Sher. In vitro fertilization (ivf) of mouse ova in hepes-buffered culture media. *Journal of Assisted Reproduction and Genetics*, 7(1):9–15, 1990.

[225] A. Stea and CA Nurse. Contrasting effects of hepes vs hco3–buffered media on whole-cell currents in cultured chemoreceptors of the rat carotid body. *Neuroscience letters*, 132(2):239–242, 1991.

[226] J. Church. A change from hco3 (-)-co2-to hepes-buffered medium modifies membrane properties of rat ca1 pyramidal neurones in vitro. *The Journal of physiology*, 455(1):51, 1992.

[227] C.A. Benadiva, B. Kuczynski-Brown, T.G. maguire, L. Mastroianni, and G.L. Flickinger. Bovine serum albumin (bsa) can replace patient serum as a protein source in an in vitro fertilization (ivf) program. *Journal of Assisted Reproduction and Genetics*, 6(3):164–167, 1989.

[228] C.A. Goss, D.H. Charych, and M. Majda. Application of (3-mercaptopropyl) trimethoxysilane as a molecular adhesive in the fabrication of vapor-deposited gold electrodes on glass substrates. *Analytical chemistry*, 63(1):85–88, 1991.

[229] J. Hernando, T. Pourrostami, J.A. Garrido, O.A. Williams, D.M. Gruen, A. Kromka, D. Steinmuller, and M. Stutzmann. Immobilization of horseradish peroxidase via an amino silane on oxidized ultrananocrystalline diamond. *Diamond and related materials*, 16(1):138–143, 2007.

[230] JD Mendelsohn, CJ Barrett, VV Chan, AJ Pal, AM Mayes, and MF Rubner. Fabrication of microporous thin films from polyelectrolyte multilayers. *Langmuir*, 16(11):5017–5023, 2000.

[231] A. Francois, J. Boehm, SY Oh, T. Kok, et al. Collection mode surface plasmon fiber sensors: a new biosensing platform. *Biosensors and Bioelectronics*, 2010.

[232] M.J.E. Fischer. Amine coupling through edc/nhs: a practical approach. *Methods Mol. Biol*, 627:55–73, 2010.

[233] H. Maeda, Y. Fukuyasu, S. Yoshida, M. Fukuda, K. Saeki, H. Matsuno, Y. Yamauchi, K. Yoshida, K. Hirata, and K. Miyamoto. Fluorescent probes for hydrogen peroxide based on a non-oxidative mechanism. *Angewandte Chemie International Edition*, 43(18):2389–2391, 2004.

[234] A. Francois, H. Ebendorff-Heidepriem, and T.M. Monro. Comparison of surface functionalization processes for optical fibre biosensing applications. In *Proceedings of SPIE*, volume 7503, page 75030U, 2009.

[235] XH Yang and LL Wang. Fluorescence ph probe based on microstructured polymer optical fiber. *Optics Express*, 15(25):16478–16483, 2007.

[236] M. Rutowska, F. Garcia Gunning, W. Urbanczyk, and A. Ellis. Dna immobilisation and hydrogel matrix formation in suspended-core optical fibre. In *The European Conference on Lasers and Electro-Optics*. Optical Society of America, 2011.

[237] D. Li and L. Wang. Fluorescence hydrogen peroxide probe based on a microstructured polymer optical fiber modified with a titanium dioxide film. *Applied spectroscopy*, 64(5):514–519, 2010.

[238] E. Coscelli, M. Sozzi, F. Poli, D. Passaro, A. Cucinotta, S. Selleri, R. Corradini, and R. Marchelli. Toward a highly specific dna biosensor: Pna-modified suspended-core photonic crystal

fibers. *Selected Topics in Quantum Electronics, IEEE Journal of*, (99):1–6, 2010.

[239] Nanocs. Retrieved 9-2011. www.nanocs.com.

[240] Piercenet. Retrieved 8-2011. www.piercenet.com.

[241] M.R. Henderson, S. Afshar V, A.D. Greentree, and T.M. Monro. Dipole emitters in fiber: interface effects, collection efficiency and optimization. *Optics Express*, 19(17):16182–16194, 2011.

[242] X. Brokmann, L. Coolen, J.P. Hermier, and M. Dahan. Emission properties of single cdse/zns quantum dots close to a dielectric interface. *Chemical physics*, 318(1-2):91–98, 2005.

[243] R. Vallée and D. Drolet. Practical coupling device based on a two-core optical fiber. *Applied optics*, 33(24):5602–5610, 1994.

[244] N.F. Smyth and A.L. Worthy. Dispersive radiation and nonlinear twin-core fibers. *JOSA B*, 14(10):2610–2617, 1997.

[245] WEP Padden, MA van Eijkelenborg, A. Argyros, and NA Issa. Coupling in a twin-core microstructured polymer optical fiber. *Applied physics letters*, 84:1689, 2004.

[246] M.K. Szczurowski, T. Martynkien, G. Statkiewicz-Barabach, W. Urbanczyk, and D.J. Webb. Measurements of polarimetric sensitivity to hydrostatic pressure, strain and temperature in birefringent dual-core microstructured polymer fiber. *Optics Express*, 18(12):12076–12087, 2010.

[247] J.C. Baggett, T.M. Monro, W. Belardi, K. Furusawa, and D.J. Richardson. Assorted core air-clad fibre. *Electronics Letters*, 36(25):2065–2066, 2000.

[248] L. Xiao, W. Jin, M. Demokan, H. Ho, Y. Hoo, and C. Zhao. Fabrication of selective injection microstructured optical fibers with a conventional fusion splicer. *Optics Express*, 13(22):9014–9022, 2005.

[249] Y. Huang, Y. Xu, and A. Yariv. Fabrication of functional microstructured optical fibers through a selective-filling technique. *Applied physics letters*, 85:5182, 2004.